NAVAL POSTGRADUATE SCHOOL

MONTEREY, CALIFORNIA

THESIS

HYPERVELOCITY IMPACT ANALYSIS OF INTERNATIONAL SPACE STATION WHIPPLE AND ENHANCED STUFFED WHIPPLE SHIELDS

Michael E. Kalinski

December 2004

Thesis Advisor:	Eric Christiansen
Second Readers:	Terry McNelley
	Daniel Bursch

Approved for public release; distribution is unlimited.

THIS PAGE INTENTIONALLY LEFT BLANK

REPORT DOCUMENTATION PAGE		Form Approved OMB No. 0704-0188

1. AGENCY USE ONLY *(Leave blank)*	2. REPORT DATE December 2004	3. REPORT TYPE AND DATES COVERED Master's Thesis

4. TITLE AND SUBTITLE: Hypervelocity Impact Analysis of International Space Station Whipple and Enhanced Stuffed Whipple Shields	5. FUNDING NUMBERS
6. AUTHOR(S) Michael E. Kalinski	
7. PERFORMING ORGANIZATION NAME(S) AND ADDRESS(ES) Naval Postgraduate School Monterey, CA 93943-5000	8. PERFORMING ORGANIZATION REPORT NUMBER
9. SPONSORING /MONITORING AGENCY NAME(S) AND ADDRESS(ES) N/A	10. SPONSORING/MONITORING AGENCY REPORT NUMBER

11. SUPPLEMENTARY NOTES The views expressed in this thesis are those of the author and do not reflect the official policy or position of the Department of Defense or the U.S. Government.

12a. DISTRIBUTION / AVAILABILITY STATEMENT Approved for public release; distribution is unlimited	12b. DISTRIBUTION CODE

13. ABSTRACT (maximum 200 words)

The International Space Station (ISS) must be able to withstand the hypervelocity impacts of micrometeoroids and orbital debris that strike its many surfaces. In order to design and implement shielding which will prevent hull penetration or other operational losses, NASA must first model the orbital debris and micrometeoroid environment. Based upon this environment, special multi-stage shields called Whipple and Enhanced Stuffed Whipple Shields are developed and implemented to protect ISS surfaces. Ballistic limit curves that establish shield failure criteria are determined via ground testing. These curves are functions of material strength, shield spacing, projectile size, shape and density, as well as a number of other variables. The combination of debris model and ballistic limit equations allows NASA to model risk to ISS using a hydro-code called BUMPER. This thesis modifies and refines existing ballistic limit equations for U.S. Laboratory Module shields to account for the effects of projectile (debris/ micro-meteoroid) densities. Using these refined ballistic limit equations this thesis also examines alternative shielding materials and configurations to optimize shield design for minimum mass and maximum stopping potential, proposing alternate shield designs for future NASA ground testing. A final goal of this thesis is to provide the Department of Defense a background in satellite shield theory and design in order to improve protection against micrometeoroid and orbital debris impacts on future space-based national systems.

14. SUBJECT TERMS orbital debris, hyper-velocity impact, International Space Station, Whipple Shield, Enhanced Stuffed Whipple Shield, NASA, ballistic limit equations	15. NUMBER OF PAGES 299
	16. PRICE CODE

17. SECURITY CLASSIFICATION OF REPORT	18. SECURITY CLASSIFICATION OF THIS PAGE	19. SECURITY CLASSIFICATION OF ABSTRACT	20. LIMITATION OF ABSTRACT
Unclassified	Unclassified	Unclassified	UL

NSN 7540-01-280-5500

Standard Form 298 (Rev. 2-89)
Prescribed by ANSI Std. 239-18

THIS PAGE INTENTIONALLY LEFT BLANK

Approved for public release; distribution is unlimited.

HYPERVELOCITY IMPACT ANALYSIS OF INTERNATIONAL SPACE STATION WHIPPLE AND ENHANCED STUFFED WHIPPLE SHIELDS

Michael E. Kalinski
Lieutenant, United States Navy
B.S., Illinois Institute of Technology, 1998

Submitted in partial fulfillment of the
requirements for the degree of

MASTER OF SCIENCE IN ASTRONAUTICAL ENGINEERING

from the

NAVAL POSTGRADUATE SCHOOL
December 2004

Author: Michael E. Kalinski

Approved by: Dr. Eric Christiansen
Thesis Advisor

Dr. Terry R. McNelley
Co-Advisor

CAPT Daniel Bursch, USN
Second Reader

Dr. Anthony J. Healey
Chairman, Department of Astronautics and Mechanical Engineering

THIS PAGE INTENTIONALLY LEFT BLANK

ABSTRACT

The International Space Station (ISS) must be able to withstand the hypervelocity impacts of micrometeoroids and orbital debris that strike its many surfaces. In order to design and implement shielding which will prevent hull penetration or other operational losses, NASA must first model the orbital debris and micrometeoroid environment. Based upon this environment, special multi-stage shields called Whipple and Enhanced Stuffed Whipple Shields are developed and implemented to protect the ISS surfaces. Ballistic limit curves that establish shield failure criteria are determined via ground testing. These curves are functions of material strength, shield spacing, projectile size, shape and density, as well as a number of other variables. The combination of debris models and ballistic limit equations allows NASA to model risk to the ISS using a hydro-code called BUMPER. This thesis modifies and refines existing ballistic limit equations for U.S. Laboratory Module shields to account for the effects of the projectile (debris/ micro-meteoroid) densities. Using these refined ballistic limit equations this thesis also examines alternative shielding materials and configurations to optimize shield design for minimum mass and maximum stopping potential, proposing alternate shield designs for future NASA ground testing. A final goal of this thesis is to provide the Department of Defense a background in satellite shield theory and design in order to improve protection against micrometeoroid and orbital debris impacts on future space-based national systems.

THIS PAGE INTENTIONALLY LEFT BLANK

TABLE OF CONTENTS

THIS PAGE INTENTIONALLY LEFT BLANK

LIST OF FIGURES

THIS PAGE INTENTIONALLY LEFT BLANK

LIST OF TABLES

THIS PAGE INTENTIONALLY LEFT BLANK

LIST OF EQUATIONS

THIS PAGE INTENTIONALLY LEFT BLANK

ACKNOWLEDGMENTS

I'd like to acknowledge the selfless assistance of all the analysts and support personnel at NASA Johnson Space Center's Hypervelocity Impact Technology Facility (JSC HITF) for the time and effort they expended in providing me research materials and personal knowledge of hypervelocity impact testing and analysis. I'd particularly like to thank my sponsor, Dr. Eric Christiansen, who provided expert tutelage and timely counsel throughout the research and analysis. His support of joint NPS/ JSC student theses has been invaluable. I'd also like to thank Mr. Ron Bernhard, also of JSC HITF. He provided expert assistance in raw data collection and was a wonderful sounding board for some of my preliminary ideas for revising the ballistic limit equations. Mr. Tom Prior of Lockheed Martin Space Operations at JSC HITF provided me with the best possible explanation of the International Space Station Integrated Threat Assessment and the relationship that debris models, shield components, and the ballistic limit equations share. His detailed discussions with me were particularly useful in preparing the introductory material for this thesis and in helping me understand how my work would fit into the greater framework with regards to evaluating the space station's ability to operate safely. Without my Naval Postgraduate School co-sponsors, Dr. Terry McNelley and CAPT Daniel Bursch, United States Navy, I would not have been able to pursue this interesting research. For their willingness to co-sponsor my work, I am eternally grateful. And to my wife, Karen, and my son, Brandon, thank you for your support throughout the research, analysis and report processes. I couldn't have done it without you.

THIS PAGE INTENTIONALLY LEFT BLANK

I. INTRODUCTION

A. FRAMEWORK OF RESEARCH

As the world's space-faring nations continue to launch satellites, missiles, and other spacecraft into orbit, the threat of damage resulting from orbital or micrometeoroid debris impacts will continue to loom large. This is particularly true for manned spacecraft, whether it be the Space Shuttle, Chinese manned capsules or the International Space Station (ISS). The International Space Station, in particular, is a spacecraft for which hypervelocity impacts by orbital debris and micrometeoroids could prove costly, both in terms of functionality and in terms of human lives. For this reason, NASA and its international partners in manned spaceflight must pay particular attention to and understand the debris and micrometeoroid environment when designing future spacecraft.

For the case of the International Space Station, the problem is three-fold. First, one must understand the ISS operating environment, including the threat presented by orbiting debris. One must understand the range of impact velocities, the debris composition, size and flux. Based on these traits, one must develop means of mitigating the damage caused by these impact events when they occur. This can be in the form of active maneuvering measures to reduce the number of impacts or passive debris protection techniques (shielding) to mitigate damage. Lastly, one must use a current model of the micrometeoroid/ orbital debris (MM/OD) environment in conjunction with the shield performance characteristics to accurately determine the risk involved in order to ensure the ISS is operating in the most safe, benign MM/OD condition possible.

The research and analysis contained herein specifically addresses the second of the three problems mentioned above, the performance characteristics of the ISS flight shielding. A new data series examining the projectile density effects on spacecraft shielding has been collected. Current ballistic performance equations are problematic

because they are semi-deterministic equations derived using pure Aluminum projectiles in ground tests. Pure Aluminum is much less dense, hence less damaging then heavier materials like Steel, Titanium, and Alumina which are other common on-orbit debris materials that may impact the ISS. Consequently, a density effects test series using 440C Stainless Steel and Ruby Sapphire Aluminum Oxide projectiles was ordered in order to determine the effects that projectile density has on the predicted and actual shield performance. These two materials were selected because they are both more dense and likely more destructive than pure Aluminum. Additionally, they makeup a statistically significant sample of known orbit debris materials, as will be shown later in Chapter I. Until this test series was ordered, NASA had not conducted testing with impact materials other than pure Aluminum, so this was a necessary experiment. These new test results are compared to predictive performance equations for two types of ISS shielding: the Whipple Shield and the Enhanced Stuffed Whipple Shield. Iterative processes to refine the original Ballistic performance equations and to improve their prediction accuracy will be the prime focus of this report. With this accomplished, the risk assessment process will become more accurate and meaningful, allowing design and safety engineers to optimize conditions for the ISS operation. With improved ballistic limit equations input into the BUMPER code, greater fidelity risk assessments can be output. The ultimate goal of this research is to improve NASA's risk assessment by addressing the fidelity of the ballistic limit equations input.

While the scope of this research is meant to specifically address NASA's needs for the International Space Station, there is additional value for the Department of Defense and its space-minded military partners. A better understanding of the performance of multi-stage shielding and debris mitigation techniques can lead to improved satellite engineering that incorporates Whipple or Enhanced Stuffed Whipple Shields. The addition of these components to unmanned national assets, whether imaging, signals intelligence, or communications satellites, would not only improve protection against accidental impact from debris and micrometeoroids, it would also protect against the emerging threat of deliberate kinetic kill attempts by "smart pebbles."

By utilizing NASA's multi-stage shielding and leveraging their hard-won knowledge of ballistic performance of these shields, the Department of Defense could easily incorporate Whipple and Enhanced Stuffed Whipple Shields into its unmanned satellites to maintain assured access to space-based assets even if they are attacked or accidentally impacted by space debris. This is a logical follow-on research and design effort for the National Reconnaissance Office, or similar organizations.

Before addressing the performance equations of the ISS shields themselves, it is helpful to discuss the International Space Station's orbital environment. This allows for a better understanding of the velocities and geometries with which analysts will be dealing, as well as the debris and micrometeoroid environment the ISS will be experiencing. This is followed by a discussion of debris mitigation techniques. Debris mitigation is a means by which engineers may actively or passively reduce risk to functionality and safety. A detailed discussion of NASA's Risk Assessment techniques is undertaken next. An understanding of the risk analysis process allows for a better understanding of how improved shield performance equations will translate into higher fidelity risk assessments. Once this framework is established, Whipple and Enhanced Stuffed Whipple Shields will be described, along with the new data set and accompanying analysis used to develop improved performance equations.

B. THE INTERNATIONAL SPACE STATION AND ITS ORBIT

The International Space Station (ISS) is a multi-nation endeavor whose mission is scientific research. Its total cost when complete will be measured in the billions of dollars. Launched and assembled over a period of years, the ISS incorporates some of the most advanced space technologies developed to date in its modular design. The ISS is the largest manmade object ever to be placed into orbit. Due to budgetary reasons and the grounding of the United States' fleet of space shuttles subsequent to the COLUMBIA disaster, it is not yet complete. However, the ISS is presently orbiting the earth with a

crew of international partners. Upon completion of construction, it will have a total surface area of over 11,000 square meters (m^2) (Ref 5, p3). On a daily basis, the ISS and its crew are carrying out hundreds, if not more, scientific experiments ranging from medical research to agricultural experimentation.

The ISS is in a low earth orbit (LEO). The LEO orbital regime is generally held to be from the earth's atmosphere to altitudes up to 2000 kilometers above the earth's surface. ISS flies in a circular orbit having a 51.6-degree inclination at an altitude of 400 kilometers. As a result of atmospheric drag, the altitude may vary considerably. The ISS will, from time to time, require a thruster burn to boost its altitude back to a nominal 400 kilometers.

Using Kepler's Equations, one can determine the orbital velocity of the Space Station as follows:

$$V_{CIRC} = [\ \mu_e / (R_e + h)\ ]^{1/2} \qquad \text{Equation 1}$$

Where:

μ_e is 398601 km^3/sec^2, the earth's gravitational parameter;

h is the orbital altitude in kilometers; and

R_e is the mean radius of the earth, 6378 kilometers.

For an orbital altitude of 400 kilometers, this translates into an orbital velocity of 7.669 kilometers per second (km/s). Figure 1 below shows the ISS' velocity versus a number of altitudes, as determined from Equation 1. These velocities are on the order of 7 km/s, which are considered to be hypervelocity. Over small altitude variations on the order of 150 kilometers or less, the curves are very nearly linear.

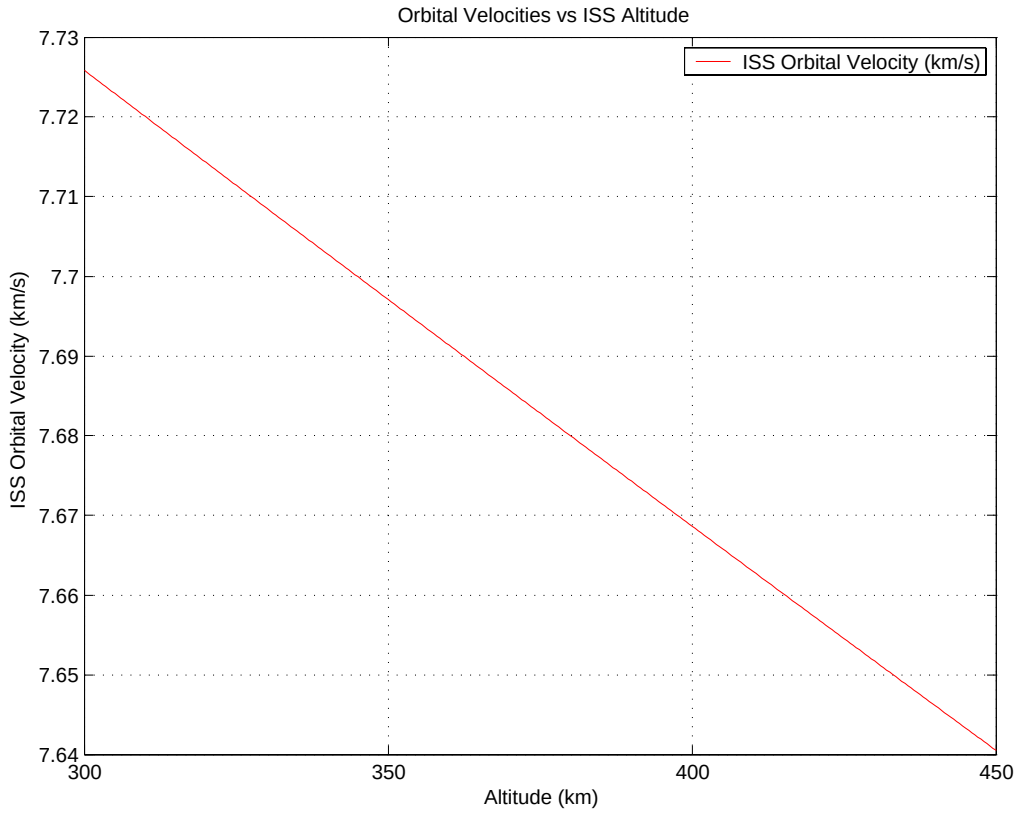

Figure 1. The ISS Orbital Velocity.

From the orbital velocity determined above, estimates as to the impact speeds if the ISS were to collide with space debris or micrometeoroids can be made. For simplicity, assume that an object in retrograde orbit that is symmetric to ISS' orbit collides with ISS. The impact velocity would be twice the orbital velocity, or 15.337 km/s. Alternatively, a root-mean-square (RMS) case, in which the collision occurs at $2^{½}$ times the orbital speed, or 10.845 km/s. While these values don't accurately predict all impact speeds and geometries, they do provide the illustrative point that impact velocities can be very large. In fact, impact velocities could be significantly higher, especially when they involve the faster heliocentric meteoroid particles. Figure 2 shows these characteristic impact velocities over a number of altitudes.

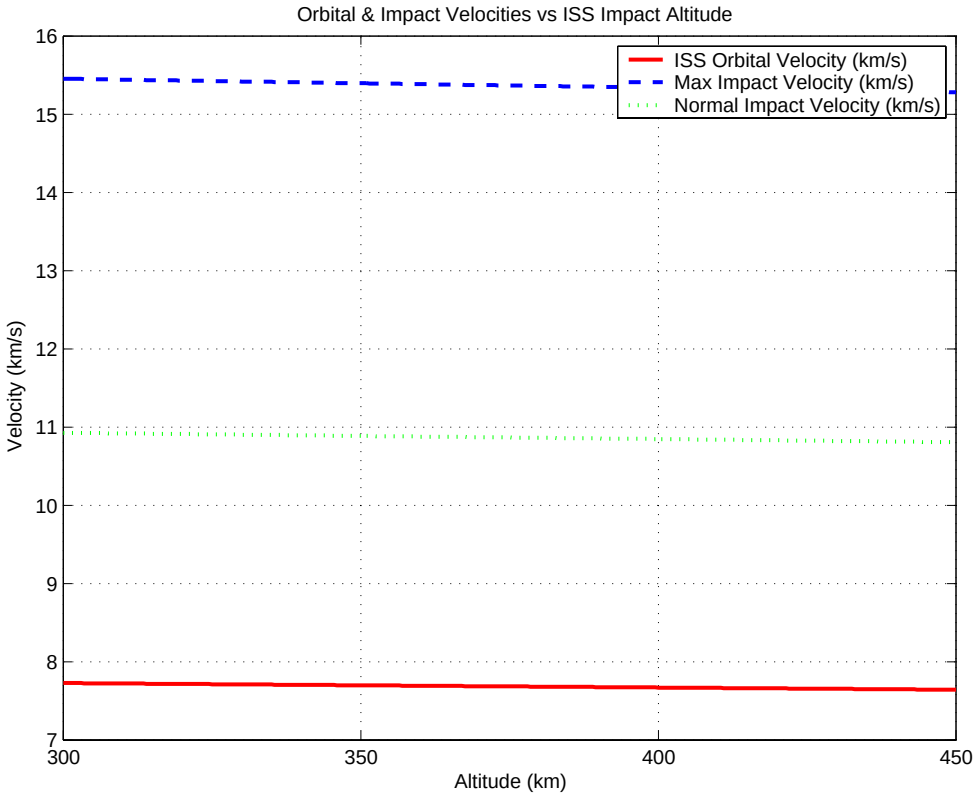

Figure 2. Maximum Impact Velocity (2x V_{ISS}); RMS Impact Velocity (1.41x V_{ISS}); and V_{ISS} Versus Orbit Altitude in Kilometers.

C. MICROMETEOROIDS AND ORBITAL DEBRIS

Having developed a good approximation of International Space Station's orbital speeds, an understanding of the micrometeoroid and orbital debris environment that the ISS will experience is the next logical step. Due to potential hypervelocity impact speeds on the order of those discussed above, orbital debris and micrometeoroids constitute a very real and very severe risk to the safety and functionality of the space station.

Micrometeoroids are naturally occurring objects in space. They are generally made up of small particles from comets or asteroids. The micrometeoroid environment is characterized by objects traveling in orbits around the sun with speeds as high as 70 km/s.

The mean velocity of these micrometeoroids is 20 km/s and is the predicted value that an object in a LEO orbit like the ISS might encounter. Other estimated micrometeoroid speeds range from 11 – 72 km/s. (Ref 3, p8). There are an estimated 40,000 metric tons of micrometeoroid material that enter the atmosphere every year (Ref 14, p1). Generally, though, the micrometeoroids are smaller and less dense than orbital debris in low earth orbit, having densities from 0.5 – 2.0 g/cm^3. Because micrometeoroids orbit around the sun and not the earth, they tend to impact upon the top face of spacecraft, with a somewhat lesser likelihood of striking the front or sides of the satellite (Ref 10, p13).

Orbital Debris, on the other hand, is manmade. At altitudes less than 2000 kilometers, i.e., in the LEO regime, the orbital debris population dominates the micrometeoroid population for objects greater in diameter than one-millimeter. For particles less than one millimeter in diameter, the objects are roughly equally divided between manmade debris and micrometeoroids. The average impact speed predicted for any LEO hypervelocity collisions is ten kilometers per second (Ref 20). Because orbital debris orbits the earth, it more frequently tends to impact spacecraft on the front and sides, with lesser numbers of impacts occurring on the top face (Ref 10, p13).

Sources and sizes of orbital debris are wide and varied. Some of the most common sources of orbital debris are fragmented rocket bodies; debris resulting from explosions or collisions in space; stray nuts and bolts lost during space walks; paint chips and other insulating materials that degraded off spacecraft surfaces; nozzle slag; motor casings; and Aluminum Oxide (Al_2O_3) exhaust particles. There are countless others, including: dead, inert, or discarded hardware; pyrotechnic separation bolts; lens caps; momentum flywheels; nuclear reactor cores; clamp bands; auxiliary motor fairings from launch vehicles; adapter shrouds; motor liner residuals; solid fuel fragments; exhaust cone fragments and particles from erosion during rocket burn; and, finally, assorted debris resulting from on-orbit collisions or breakup. In the history of the space age, there have been over 124 verified breakups that have resulted from spacecraft collisions or

explosions (Ref 20). Collisions occur when the orbital path of two or more objects intersect, a predictable point if the objects are tracked and monitored, as is the case for all operational satellites and many large debris objects. Explosions, on the other hand, are not predictable. Explosions can occur because of the inadvertent mixing of propellant and oxidizer or the over-pressurization of residual propellant due to spacecraft heating. Over-pressurized batteries may also cause explosions. Based on statistical analysis of known hypervelocity impact events on orbit, one source classifies the percentages of orbital debris from numerous sources as follows (Ref 14, p3):

Fragmentation Material	40.0%
Nonfunctional Spacecraft	25.3%
Rocket Bodies	19.4%
Mission Related Items	13.3%
Unknown Sources	2.0%

The most common materials that are found in orbital debris and micrometeoroids are Aluminum, Aluminum Oxide, Steel, and paint chips. These materials, in their various alloys, are the most common engineering materials used in space applications, hence their prevalence. There are surely many other materials and substances to be found in orbital debris, although there are too many to list here. The above materials are a statistically significant sample of common on-orbit debris materials, as verified by returned spacecraft and spaceflight components from which impacts surfaces were analyzed chemically to determine the impacting materials. While there is no precise way of determining the total debris material content on orbit, chemical analysis of impacted surfaces can be conducted to provide a reasonable indication of the most common impacting materials. This chemical analysis to determine material composition has been done on a number of returned systems including the Space Shuttle's windows, radiator face sheet, and other shuttle surfaces, as well as on the Long Duration Exposure Facility

(LDEF) satellite, the Hubble Space Telescope (HST) solar arrays, and many other components and satellites. Post-mission analysis of STS COLUMBIA in 1996 revealed two 1-2 mm impacts by Stainless Steel debris that caused marked damage, while a similar post-mission analysis of STS ATLANTIS in 1997 revealed a 2-mm hole resulting from an Aluminum debris impact (Ref 21, p8). An impact material analysis of the Space Shuttle's windows for fifty missions revealed that Aluminum, Aluminum Alloys, Paint and Steel were the most common impacting debris. A separate analysis of the shuttle's radiator face sheet showed that Steel and paint comprised 95 percent of the on-orbit impacts examined. The figures below summarize the debris material composition from these two post-mission analyses.

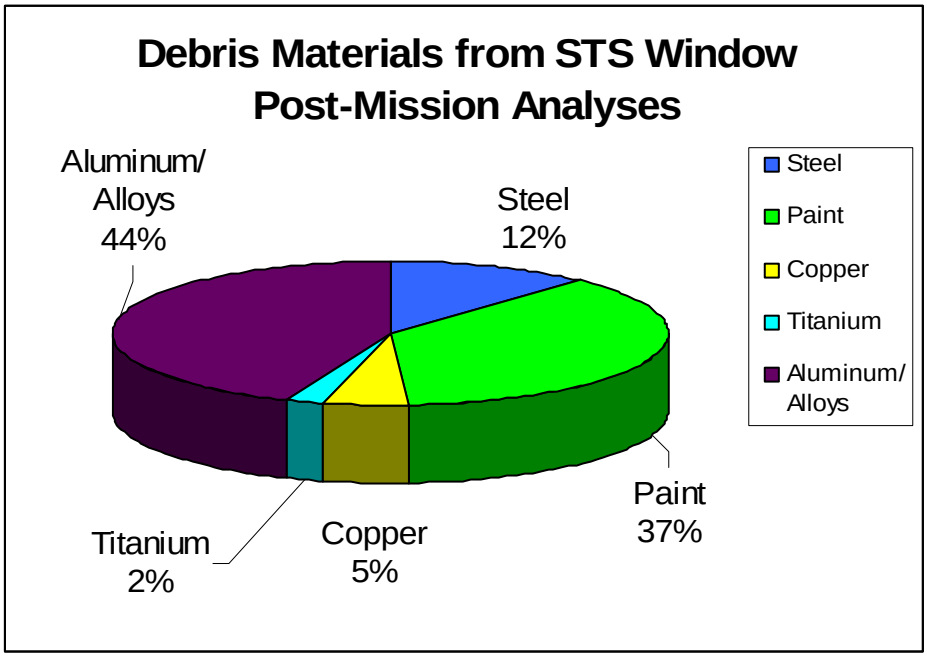

Figure 3. STS Post-Mission Impact Material Analysis of Windows, as Reported in Ref 3.

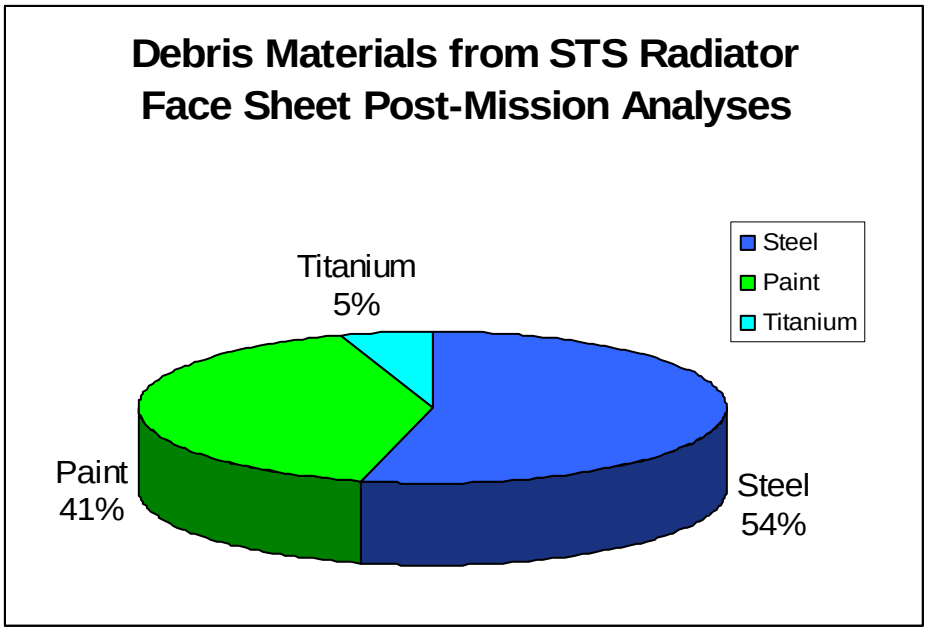

Figure 4. STS Post-Mission Impact Material Analysis of Radiator Face Sheet, as Reported in Ref 3.

Of these materials, a large sample are more dense than Aluminum, the most common ground impact-tested debris material to date. Despite there being significant percentages of other on-orbit debris materials, including Steel and Aluminum Oxide, Aluminum remains the most-widely ground-tested debris material. This is problematic because the results of ground tests using Aluminum impactors are used to design ISS' shielding. Of these materials, pure Aluminum is significantly less dense (2.8 g/cm^3 for pure Aluminum) than Aluminum Oxide (3.9 g/cm^3) and common Steels (7.8 g/cm^3). Of these materials in Figures 3 and 4, only paint, with an average density of 1.14 g/cm^3, is less dense than pure Aluminum. Higher density debris has the potential to be more penetrating than lower density materials because of the added mass (momentum and kinetic energy) for projectiles with equal diameters. Consequently, more dense materials must be ground-tested in order to design shields to counter the most statistically significant and most penetrating debris threats on orbit, the Aluminum, Aluminum Oxide and Steel. This is the major reason why the density effects test series was ordered and why revised ballistic limit equation are required. 440C Stainless Steel and Ruby

Sapphire Aluminum Oxide were chosen as representative materials for testing. This choice is based upon their densities and their abundance in the known debris catalog.

Commonly, orbital debris is classified by size. Debris particles range in size from sub-millimeter diameter objects to bodies having diameters larger than thirty centimeters. Generally speaking, objects less than one millimeter in diameter pose little risk to the functionality of the spacecraft. Objects that range in size between one millimeter and ten centimeters in diameter may or may not penetrate the spacecraft. This size range of debris has the potential to cause loss of satellite functionality or the outright loss of the satellite. Objects greater in size than ten centimeters in diameter will penetrate those objects they strike and will likely cause catastrophic losses of satellites.

Debris having a mean diameter greater than ten centimeters is considered large. Orbital debris with a mean diameter less than one millimeter is classified as small. Finally, debris that varies in size from one millimeter to ten centimeters in diameter is classified as medium. There is no standard convention, but this seems to be the accepted definition in most literature consulted (Refs 4, 7, 10, 18 and 20).

Estimates of the total amount of debris in orbit vary greatly. There are an estimated 100,000 or more objects in space with sizes up to one centimeter in diameter (Ref 23). Some sources believe there are between 30,000 and 100,000 objects in space that range in size between one and ten centimeters in diameter (Ref 4, p1). Other sources state that there are up to 150,000 pieces of debris littering the LEO environment at altitude less than 1500 kilometers (Ref 17, p1). There are even estimates that put these numbers as high as 1,000,000 for objects larger than one millimeter and 1,000,000,000 for objects larger than 0.1 millimeters (Ref 5, p2).

The number of orbital debris objects in space is growing. As a result of new launches and the debris they introduce, as well as collisions, breakup and degradation involving existing spacecraft, the number of debris particles increases every year. Both the LEO and GEO environments are debris-dense orbits because they are so heavily populated by manmade satellites and the leftover components resulting from orbital insertion. An object in LEO orbit is nearly one hundred times more likely to collide with debris or another satellite than a GEO satellite. This a function of the total volume of space present in which objects can orbit, as well as the total number of objects orbiting in that particular regime. Satellites in highly inclined LEO orbits often experience much harsher debris environments for longer times due to the orbital pathway these satellites must fly along.

D. ORBITAL DEBRIS IMPACT RISK MITIGATION

To protect the ISS from the threat of destructive collisions with other orbiting objects, mitigation techniques are employed. These measures reduce risk and help protect the ISS from the potentially crippling effects of a hypervelocity impact with debris, meteoroids, or other satellites. The threat of orbital debris hypervelocity impacts is a growing international problem that affects all the space-faring nations around the globe. Thus, international cooperation is required to address the risk and to take action to curtail or prevent the generation of new orbital debris. Such is the case for the ISS, where sixteen partner nations are involved.

There are four factors that determine the effects of debris, and comprise the main risk factor inputs. They are the time on orbit, the projected spacecraft area to be impacted (a function of geometry and attitude), the altitude, and the orbital inclination (Ref 18, p14). These four factors are at the root of risk reduction and debris mitigation. Optimizing all four factors or, at the very least, improving upon any one of these factors will significantly reduce the risk to spacecraft functionality over the operational lifetime

of the spacecraft. The International Space Station, by virtue of its large size and its anticipated fifteen-year lifetime is an inherently risk-laden spacecraft. Thus mitigation measures are necessary to ensure the ISS maintains its functionality for its entire design life.

There are two basic categories of mitigation techniques – active mitigation and passive mitigation. As the names imply, active mitigation most commonly involves the maneuvering and reorienting of the spacecraft to reduce impact risk. Active mitigation may also include the removal of orbital debris from space. Passive mitigation is designed into the spacecraft in the form of impact shielding or structural support. These two types of mitigation will be discussed in more depth in the following paragraphs.

Before discussing active and passive measures that mankind can take to mitigate the orbital debris threat, it is important to discuss the naturally occurring mechanisms that assist in the removal of these undesirable particles. For altitudes less than 400 kilometers, the debris lifetime is on the order of a few months. The process of orbital decay caused by atmospheric drag removes both orbital debris and micrometeoroids from low earth orbit. Eventually, orbital decay will cause the debris particles to re-enter the earth's atmosphere and burn-up. At altitudes near 400 kilometers, i.e. in the ISS characteristic altitudes, the friction with the upper earth atmosphere acts as a vacuum cleaner, slowing the debris particles and causing reentry. The rate of orbital decay also relies upon the density and projected surface areas of the debris particles themselves. The larger the projected surface area-to-mass ratio, the shorter the orbital lifetime of the debris (Ref 14, p6). This implies that less dense particles will decay more quickly than more dense orbital debris. The orbital altitudes and the effects of atmospheric drag vary with the solar cycle. Increased solar activity causes the earth's atmosphere to heat up and expand. This increases the cleaning effect of the atmosphere and the drag it imparts on orbiting objects at low altitudes (Ref 5, 14).

This is a very useful phenomenon, but it alone will not remove the full orbital debris polluting the LEO environment. This is true for two reasons. First, as debris in the lowest LEO environment is pulled into the atmosphere by friction and drag, debris in slightly higher orbits is pulled into lower LEO orbits, replenishing some of the orbital debris that has already reentered earth's atmosphere. Secondly, and most significantly, the historic rate of debris removal due to atmospheric drag is much less than the debris growth rate resulting from new launch-related debris or collision ejecta. In fact, orbital debris grows at an average rate of five percent per year in low earth orbits (Ref 20).

Active debris mitigation is usually accomplished by maneuvering the spacecraft to avoid known debris or satellite threats. Using the ability to catalog and track threat objects, ground station operators for the ISS may define an "approach-no-closer-than" safe zone around the space station. If orbital analysis shows that any known object will pass within this zone in the near future, the astronauts or ground control will fire the spacecraft's thrusters to reposition the ISS so that the danger object passes well clear. This is called a collision avoidance maneuver. The collision avoidance maneuver is the preferred means of debris mitigation for large objects like satellites or orbital debris greater than 10 centimeters in size, as impacts by these objects would cause the most severe damage. Another active mitigation step involves flying the spacecraft in an orientation or attitude that reduces the exposed cross-sectional area to known debris threat directions. This, in itself, reduces the probability of impact and limits the need for expensive propellant burns to move the spacecraft to a new orbit. Additionally, it allows operators to place the heavier shields used to passively protect the station in a few localized areas, instead of over the entire surface of the spacecraft. This saves on mass and volume, hence on cost as well, without appreciably increasing risk. Further, the selection of orbital regimes that are known to have less orbital debris in them is considered an active measure. If astrodynamicists choose to fly a satellite in a lightly populated orbital regime, they will be less likely to encounter manmade debris.

There are a number of other proposed active mitigation measures that would remove the debris from the orbit altogether. These concepts involve either the "space vacuum cleaner" or a laser system that would cause the debris in LEO orbit to decay and re-enter the earth's atmosphere, wherein it would burn up. Progress in these fields will be discussed near the conclusion of this report in the section discussing future concepts and designs. For the interim though, this discussion will be shelved.

By far, passive forms of debris impact mitigation are the most common mitigation technique practiced today. The most common means of passively mitigating the risk associated with MM/OD hypervelocity impacts is to add shielding to the spacecraft. For this measure to be effective, the shielding must be capable of withstanding hypervelocity impacts without loss of satellite operation and functionality. The International Space Station alone incorporates between 200 and 300 individual shield types to withstand impact by projectiles up to one to two centimeters in size (Ref 21, p9; Ref 1). Based upon ISS' estimated completed mass of 250 metric tons, nearly ten percent (over 20 metric tons) of ISS' mass will be MM/OD shielding. It is possible to design passive shielding of significant strength to withstand hypervelocity impact events by very large particles impacting at very high-speed, however such shields would be prohibitively massive. Hence, a combination of passive shielding and active maneuvering and spacecraft attitude to mitigate the debris threat and reduce overall risk to the mission is used.

While the above mitigation measures provide the most common on-orbit solutions to the debris problem, they fail to account for other design methodologies that, over the long term, will reduce the threat posed by orbital debris. With the growing debris threat, greater international cooperation has been required to minimize risk. The United Nations Committee on the Peaceful Uses of Space often provides a medium for voicing concerns of the space-faring nations related to debris mitigation. The largest spaceflight agencies, namely NASA, the European Space Agency (ESA), Russia, and Japan have already

agreed to common guidelines for spacecraft design and development, as they relate to mitigating orbital debris risk (Ref 15). These common guidelines grew out of the mutual understanding that one nation's debris could destroy or damage another nation's spacecraft, hence the beneficial nature of cooperating to reduce overall risk. Additionally, all the parties to the agreement realized that debris mitigation in the design of satellites and launch vehicles, while reducing risk, increases cost. To minimize cost, it is best to incorporate debris mitigation measures very early into the design. All modern satellites are being designed to these common guidelines, in the hopes that orbital debris growth can be halted. These guidelines can be found, in part, in two NASA standard publications, the *NASA Safety Standard 1740.14* and the *NASA JSC Orbital Debris Mitigation Standard Practices*. Some of the common design practices now used include improvements to booster and payload designs to prevent explosions of spacecraft and rocket bodies; the incorporation of particle-free propellants; the addition of tethers and pyro-catchers to deployment hardware and explosive bolts; and the increase in passive shields. Additionally, the movement of critical functional components within the spacecraft bus to locations in the geometric shadow of the prevailing direction of debris flux reduces risk and ensures better vehicle survivability and functionality when it sustains an impact (Ref 18, p34). Not only is this technique used for debris impact mitigation on the ISS, it is incorporated into the designs of most unmanned satellites designed after 1996.

There are also operational mitigation techniques that are incorporated into modern spacecraft design to reduce the risk of explosion and hence the introduction of more debris into the environment at the satellite end-of-life. These include venting or burning propellant to total depletion and battery passivation at satellite end-of-life. These measures ensure that no inadvertent explosions occur as a result of heat and over-pressurization. Lastly, to reduce the risk of collision once the satellite has reached the end of its operational life, an allotment is made to remove the satellite to a graveyard orbit for higher altitude satellites, like those in GEO. Alternately for LEO satellites, allowances are made to place the spacecraft into a very low earth orbit so that

atmospheric drag will cause the rapid orbital decay and atmospheric reentry of the spacecraft. By removing the old spacecraft from orbit, the number of large objects that the ISS could collide with is reduced. This also removes the risk that the dead satellite will degrade or will be impacted, creating many new, smaller debris objects.

Since the early 1980's, when this problem began receiving the attention it deserved from all the space-faring nations, satellite fragmentation and explosions have been dramatically reduced. Engineering improvements resulting in the reduction of explosions and spacecraft fragmentation have consequently slowed down the rate of orbital debris growth. This is largely related to improved designs and ground testing that flow from increasing engineering expertise since the early days of the space age.

E. MICROMETEOROID AND ORBITAL DEBRIS TRACKING AND MODELING

A great deal of information regarding the space debris and micrometeoroid environment has come from years of scientific observation and study. To make a proper MM/OD model, one must first measure and record as much debris data as can be captured. Observed objects are counted, with a record of their size and ephemeris data made. These results are used to build models that classify the current debris environment and predict the future debris environment. These models are then applied to risk analysis measures in order to design or assess spacecraft ability to minimize the risk associated with impacting debris and micrometeoroid particles. Before discussing orbital debris modeling itself, one should first examine how the data that comprises the model is found. This leads to a discussion of tracking space objects.

Tracking of space objects is accomplished by either space-based or ground-based systems. These include radars, electro-optical imagers, and infrared sensors. Generally, ground-based radar outperforms similarly based optical telescopes when observing

objects in LEO (Ref 18, p4). Space-based observations, radar or optical, would have higher resolutions. These space-based systems are ideal for observing and cataloging debris and micrometeoroid characteristics. Unfortunately, this is a technology yet to be fielded in space specifically for the purpose of debris monitoring and classification. From time to time, space-based telescopes have been used to examine objects of interest. However, the space telescopes were only used after being cued from another tracking sensor, usually ground-based. Debris and micrometeoroids have also been measured by analyzing impact surfaces that have been returned from space. These include the Hubble Space Telescope solar array, Space Transportation System (STS) (Space Shuttle) panels, and the Long Duration Exposure Facility (LDEF) satellite, which was a satellite launched specifically to examine debris impacts and impact characteristics.

Presently, objects greater than ten centimeters in diameter are tracked and cataloged by the United States Space Command (USSPACECOM) (Ref 8). USSPACECOM passes this catalog onto agencies like NASA whenever it is updated. The U.S. Space Surveillance Network, still referred to as "The Fence" despite its operational control being passed from Navy control to U.S. Air Force control, is a ground-based tracking network that uses radar, electro-optical, and infrared sensors to track over 7500 objects in space, of which, forty percent consist of old satellites and discarded upper stages of boosters. This network can track objects down to ten centimeters in diameter as well (Ref 4, p1).

The Haystack radar in Massachusetts often conducts debris observations, being used for this purpose since 1990. NASA uses Haystack and its X-band radar to detect small objects in space at altitudes up to 1000 kilometers (Ref 16). The Haystack radar is capable of tracking objects from five millimeters in diameter up to sizes of twenty centimeters in diameter (Ref 12, p8). It utilizes a fixed-stare observation methodology, whereby it stares at a slice of space and counts and classifies the objects that fly across its fixed field of view. This capability allows Haystack to track and report up to 100,000

observable objects with sizes down to one centimeter (Ref 16). The Goldstone radar has a similar capability, tracking objects larger than five millimeters in diameter (Ref 18, p5).

It goes without saying that large objects are easy to track using existing observation technologies. In all, there are over 9000 objects larger than a softball orbiting the earth that are tracked and monitored by the agencies and facilities listed above (Ref 1). There are millions of objects smaller than one millimeter in diameter in orbit that we do not have the capability to track and monitor. However, these particles are not particularly damaging when they impact a spacecraft. Moderate shielding can account for these particles. The real difficulty occurs in the 0.5- to 10-centimeter objects. These objects are too small to track, but large enough to do significant damage to any spacecraft they encounter.

The data collected by each of the facilities is passed to NASA, who then generates an updated model that describes the debris and micrometeoroid environment. These models are then used in engineering risk assessments to ensure spacecraft like the Space Shuttle and the ISS are adequately designed to operate within this environment. The reason for creating and utilizing these models is quite simple. Models provide mathematical descriptions of the distribution of objects in space. They describe the movement, flux and physical characteristics of the space objects. Characteristics of interest include density, size, shape, mass, and material composition of the debris or micrometeoroid objects. Models can be deterministic, statistical, or a hybrid of the two types of common model. Many models are very robust and even account for the added debris contribution of new spacecraft launches, breakup, de-orbit maneuvers, and fragmentation. Models can also be discrete or engineering approximations, focusing on predicting short-term or long-term environmental characteristics. However, all models are limited in their precision due to the sparsity of deterministic data. Because of the inability to track many smaller objects, existing catalogs are only populated with a small fraction of the total number of debris and micrometeoroids in orbit. Therefore, most

models rely on statistical predictions based on deterministic data. For this reason, the hybrid model is commonly used.

NASA's Orbital Debris Program Office is the lead NASA center for orbital debris research, taking the international lead in measuring the orbital debris environment. NASA debris models use deterministic catalog data from USSPACECOM, Russia and other U.S. organizations. Statistical data and/or ground-based simulated or predicted data may be incorporated into the models as well (Ref 18, p19). Circa 1997, NASA used the EVOLVE model to predict the current debris environment and the short-term future environment. EVOLVE was used in conjunction with real measurements to derive a simplified model for the ISS design engineers (Ref 16). This model eventually morphed into the more current ORDEM series of debris models. The ORDEM2000 orbital debris model is the most current model used by NASA in its debris risk assessments. It replaced the older ORDEM96 model in 2002 (Ref 3, p4). ORDEM2000 is a semi-empirical engineering model that was developed by NASA JSC. It is based on extensive in-situ and remote observation of orbital debris and micrometeoroids. NASA uses the ORDEM2000 model to predict the anticipated particle flux for given ISS and STS mission parameters. Flux is defined simply as the number of impacts per square meter of spacecraft area exposed per year. Debris and micrometeoroid flux provides a direct proportionality to the probability of impact. This model is used in NASA's BUMPER code to predict and assess risk for the International Space Station. Risk assessment and the BUMPER code will be discussed next.

F. HYPERVELOCITY IMPACT RISK ANALYSIS

The goal of NASA design and safety engineers is to build and operate the International Space Station so that its shields will withstand the predicted MM/OD environment. To ensure the station's ability to withstand hypervelocity impacts, NASA conducts a detailed risk assessment of the ISS. Based on the results of this assessment,

NASA engineers and management make determinations on the feasibility and safety of various components and systems of the ISS. This risk assessment incorporates orbital debris/ micrometeoroid models; finite element models of the ISS; ballistic limit equations for the many shielding configurations flown on the spacecraft; and other material property data.

Hydrocodes are large, complex computer analysis algorithms that require supercomputers to process and to characterize simulated impact events. These hydrocodes refer to physics-based simulations of dynamic impact events. They solve conservation of momentum, mass, and energy equations, as well as shock and material failure equations for a large number of elements in a two- dimensional or three-dimensional grid as a function of time. They may also model material performance, yielding graphical representations of the state of a material after it is impacted. Suffice it to say that hydrocodes are robust and may be used to output a wide variety of significant data to risk assessors. NASA evaluates risk and models impact events using a code called BUMPER. It integrates results from hydrocode simulations and predicts the probability of certain events occurring, like the probability of no penetration (PNP), the probability of no impact (PNI), or the probability of critical failure (PCF) over the entire ISS mission duration. Ultimately, it provides an estimate of the overall risk to the ISS from micrometeoroid and orbital debris penetration.

The current code NASA employs is BUMPER II version 1.92a (Ref 6, p 10), which assesses critical impact risk. BUMPER uses a combination of an I-DEAS-based finite element model of the International Space Station inclusing all its components and different configurations; current ballistic limit equations for each shield configuration; and orbital debris and micrometeoroid models to model risk. Each of these models is embedded within in the BUMPER code. Ultimately, the results of the analysis are reported in terms of Probability of No Penetration (PNP), the ultimate predictor of a shield's effectiveness. These values, along with the risk summaries for each component,

each element and each configuration of the ISS are reported in NASA's *Integrated Threat Assessment of the International Space Station, ITA-10C.*

BUMPER conducts two types of assessments, the performance assessment and the requirements assessment. Requirements assessments are based on a set of input parameters, namely a fixed altitude, constant solar flux, and the SSP 30425 debris environment models, which dates from 1991. These provide a baseline set of results for ITA-10C, presenting data to compare with earlier assessments. Performance assessments, on the other hand, reflect the most accurate results that can be calculated based upon currently available data at the time of analysis. This usually involves present ISS orientation and configuration (attitude and stage of assembly), as well as solar cycle data and up-to-date debris and micrometeoroid models. To model the debris environment for the performance assessment, BUMPER uses the ORDEM2000 model, which replaced the ORDEM96 model in the latest Integrated Threat Assessment, ITA-10C. For the requirements assessment, BUMPER uses the SSP 30425 model, an older model. To model the micrometeoroid environment, BUMPER uses the SSP 30425 model, for both the performance and requirements assessments (Ref 6, p10), as it remains the most recent model that is widely accepted. Each debris and micrometeoroid model includes debris size, velocity, and flux predictions, which are applied to the finite element models and ballistic limit equations that further comprise BUMPER, to yield probabilities of shield failure and risk of impact.

The finite element model embedded in BUMPER consists of 156,007 individual elements, both triangular and quadrilateral in shape (Ref 6, p 6). The model is built using the I-DEAS computer software, a commonly used engineering modeling suite. Each element is assigned a property identifier (PID) to act as an index for shielding. This delineates which shield configuration is physically flown in that space, ensuring that BUMPER applies the correct ballistic limit equation to that particular element during analysis. The BUMPER code used to produce the most recently published Integrated

Threat Assessment, ITA-10C, utilized 386 separate PID's to differentiate between the many shielding types used over the entire body of the space station. Due to the large on-orbit time, as well as the fact that long periods of time elapsed between the addition of new components of the space station or reconfiguration of existing elements, the BUMPER code evaluates risk based on twenty-three different assembly stages of the station, incorporating the sections' arrival date on orbit and the movement of the elements once in orbit. Additionally, BUMPER accounts for the altitude and attitude of the station. Spacecraft geometry, shield configurations, flight parameters like inclination, altitude, time of analysis, etc. are all accounted for in the risk assessment completed by the code. This provides the most accurate risk assessment based on the most current input information available.

The assessment types are further broken down into spacecraft exposure regimes. The first regime is the system regime. This is risk calculated based upon an analysis start date equaling the date of first element launch. In other words, it uses the analysis start date that reflects the date upon which the first element of the ISS was placed in orbit. The second regime is the element regime. It is based on an analysis start date equaling the date upon which the particular module was launched. This yields a total of four specific assessments conducted by the BUMPER code – Performance/System, Performance/Element, Requirements/System, and Requirements/Element, each of which is be delineated and summarized separately in ITA-10C, and will be broken out similarly in later threat assessment summaries.

BUMPER uses the finite element model in conjunction with the debris models and the shield ballistic prediction equations, as well as ninety different debris threat directions and 149 different micrometeoroid threat directions per element to predict the Probability of No Penetration (PNP). New PNP calculations are completed using BUMPER after every major ISS configuration change; changes to ballistic limit curves; or updates to the environmental models are completed, with results being released in a

new Integrated Threat Assessment. BUMPER determines the number of failures by finding the number of debris and micrometeoroid particles that exceed the predicted ballistic limits for each element of the finite element model. The code sums the number of failures for each element of the finite element model over the lifetime of the space station. It then outputs PNP values for each element, core module, and the complete station, for each of the four assessment types discussed in the paragraphs above.

Since the research contained in this document specifically examines the shield types and configurations used on the U.S. Laboratory Module of the ISS, some pertinent PNP results are included in the table below. These PNP values are summarized in below purely for illustrative purposes, demonstrating the type of data yielded by the BUMPER code in NASA's most recent Integrated Threat Assessment. The data shown is PNP values broken down for debris, micrometeoroids, and a combination of the two for the U.S. Laboratory Module only. Further, data is presented for both the ten-year and fifteen-year exposure times. Each of the four assessment types is represented in this sample table. As a practical matter, the differences between performance and requirements parameters will be discussed in greater depth when defining the format of the ballistic limit equations. At this point, it should suffice to say that the fundamental difference is that a performance parameter analysis uses the ballistic limit equation that predicts shield performance based upon a defined shield configuration. The requirements parameter analysis relies upon ballistic limit equations that predict the shield configurations needed to meet the debris impact requirements.

Performance Parameter/ System Exposure		
PNP	**10-Yr Exposure**	**15-Yr Exposure**
Orbital Debris	0.999461	0.998970
Micrometeoroid	0.999829	0.999765
Total PNP	0.999289	0.998736

Requirements Parameter/ System Exposure		
PNP	**10-Yr Exposure**	**15-Yr Exposure**
Orbital Debris	0.993795	0.990891
Micrometeoroid	0.999853	0.999802
Total PNP	0.993649	0.990695

Performance Parameter/ Element Exposure		
PNP	**10-Yr Exposure**	**15-Yr Exposure**
Orbital Debris	0.999281	0.998794
Micrometeoroid	0.999801	0.999737
Total PNP	0.999081	0.998532

Requirements Parameter/ Element Exposure		
PNP	**10-Yr Exposure**	**15-Yr Exposure**
Orbital Debris	0.992549	0.989410
Micrometeoroid	0.999830	0.999779
Total PNP	0.992381	0.989191

1st Element Launch (FEL) to DEC '02 Performance Parameters	
PNP	**U.S. Lab Module Only**
Orbital Debris	0.999895
Micrometeoroid	0.999941
Total PNP	0.999836

1st Element Launch (FEL) to DEC '02 Requirements Parameters	
PNP	**U.S. Lab Module Only**
Orbital Debris	0.998137
Micrometeoroid	0.999948
Total PNP	0.998086

U.S. Laboratory Module Probability of No Penetration (PNP) values as found in the Integrated Threat Assessment for the International Space Station, ITA-10C, copied from Tables 4.1 through 4.6, pages 147-152.

Table 1. ITA-10C Probability of No Penetration (PNP) predictions for ISS U.S. Laboratory Module.

The third component of the BUMPER code is the family of ballistic limit equations. These predictive equations in BUMPER represent the most accurate and current ballistic performance equations for each specific shield configuration. As will be discussed in more detail in the following chapters, the ballistic limit equations are largely determined from experimental data obtained during ground testing of hypervelocity impacts. Therefore, as new ground tests are conducted and ballistic limit equations are modified and improved, they must be incorporated anew into BUMPER.

It is obvious that, in order to effectively evaluate risk, accurate ballistic limit prediction equations, plus updated debris/ micrometeoroid models and finite element

models are necessary inputs to the BUMPER code. Without continuous improvement of these models to reflect the changing engineering and environmental realities, the risk assessment will yield outdated data and will not accurately reflect the hypervelocity impact threats to or the shield performance of the ISS. The goal of NASA's Hypervelocity Impact Technology Facility and this report based upon their raw data collection is to improve the ballistic limit equations input into the BUMPER model, thereby improving the BUMPER code fidelity and improving NASA's risk assessment capability. ITA-10C includes BUMPER input data from December 2002. ITA-11 will be the next iteration. Its release in the near future is greatly anticipated. It will incorporate all the modeling improvements and ballistic limit equation improvements since December 2002. The results of ballistic limit equation improvements found in the data analysis chapter of this report will likely be incorporated into the BUMPER code and reflected in future Integrated Threat Assessments.

II. SHIELD AND HYPERVELOCITY IMPACT THEORY

A. UTILITY OF IMPACT AND WHIPPLE SHIELD THEORY

Before attempting to revise the ballistic limit equation (BLE) curves subsequent to the collection of the density effects raw data, one should first develop a clear understanding of the physical phenomenon that occurs during the hypervelocity impact event. Next, one should examine the existing multi-plate penetration equations to understand how and why the entering BLEs were chosen. Finally, one should understand the desirable material and configuration characteristics so that intelligent suggestions for alternate shields can be made.

B. WHIPPLE SHIELDS AND IMPACT PHENOMENA

Perhaps the best place to begin is with the physical phenomena that occur during a hypervelocity impact event on a double plate shield. In 1947, Dr. Fred Whipple proposed placing a thin metal plate outboard of the spacecraft hull to improve protection (Ref 13, p1). This outboard plate would be a staged or double plate structure whose purpose was to breakup the projectile at the first stage bumper into smaller, less massive, slower projectiles that could be stopped by the rear wall of the shield (the spacecraft hull). The shield was called the Whipple Shield. The outboard, sacrificial plate is called the bumper, while the spacecraft hull is called the rear wall. The ISS incorporates a vast number of different Whipple Shield configurations on its many modules.

When the first plate, the bumper plate, is impacted, it will likely be perforated. If perforation occurs, a cloud of debris is propelled out the rear of the plate. This debris cloud may consist of both projectile and wall material. The debris cloud may have projectile and shield material in solid, liquid and gaseous states depending upon the angle of impact, the shape of the projectile, the impact velocity and a number of other factors.

The phase of the debris cloud materials can play a significant role in whether the rear wall can stop them or not. Generally, solids in the debris cloud are more penetrating in the rear wall than the liquid or gaseous phase materials. This observation has implications in the bumper plate material selection. It demonstrates that the bumper plate should be made of a material that will undergo a phase shift to liquid or gaseous form upon impact so that it will be less likely to penetrate the rear wall (Ref 10, p43). Other desirable characteristics of the bumper plate are low weight; good projectile breakup qualities; large dispersion angles of the debris cloud; low expansion speed of the debris cloud; and minimal secondary ejecta (Ref 10, p27). The bumper should be adequately thick for the majority of the projectile to be shocked (melted) to a level initially experienced upon impact, however, the bumper should also be optimally thin so that a less dense debris cloud is created. A thinner bumper has the benefit of spreading the debris out over a larger area downrange. This yields smaller, less energetic particles that strike the rear wall. The ideal bumper material is one that is flexible, i.e. that can be easily fashioned around the ISS component bodies. It should be lightweight to reduce launch costs. Ground testing has shown that the shockwave produced is greatest when the density of the bumper plate and the impacting projectile (orbital debris) are the same. These two idealities are reasons why Aluminum alloy shields have been used for the bumper plate. A large portion of the orbital debris the ISS will be impacted by is Aluminum. Also, Aluminum is very lightweight, having a density of approximately 2800 kg/m^3.

As the debris cloud exits through the rear face of the bumper plate, the debris cloud spreads the broken wall material and fractured projectile outward radially in an expanding conical shape. It is accompanied by a pressure pulse (shock wave) and light emission (Ref 14, p9). The hypervelocity impact that caused the shock wave to form also causes the metals to behave like fluids for short periods of time, exhibiting hydrodynamic flow properties. The shockwaves induce millions of pounds-per-square-inch stresses. This is because the impact stress (shock wave) travels through the shielding material

supersonically (Ref 7). An ejecta cloud, consisting of the same materials as those in the debris cloud, is expelled through the perforation in the bumper plate and back out toward the front face of the bumper. The proof of this can often be seen in the crater observed on the bumper plate of the multi-stage shield. The crater may often exhibit a frozen, raised lip around its perimeter. Much like in the debris cloud itself, the extreme kinetic energy from the hypervelocity impact causes the high-pressure shock waves to momentarily melt the projectile and shield materials and forces them to flow back through the plate as ejecta. The material then quickly refreezes and deposits itself back on the plate. This can be seen on a monolithic (single plate), thick shield in Figure 3. Figure 4 depicts some of the flash radiography images of the debris cloud and ejecta after striking the bumper plate.

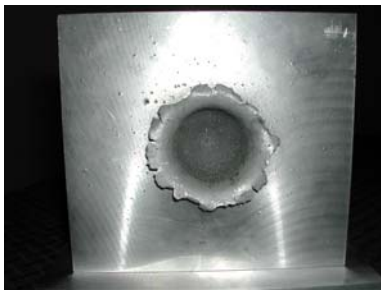

Figure 5. Frozen Lip on Front Face of Monolithic Shield, Resulting from Hydrodynamic Flow of Ejecta Materials from NASA JSC HITF Display, as Analyzed by the Author.

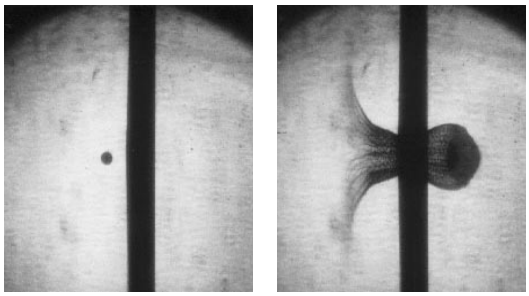

Figure 6. Flash Radiography Images of the Debris Cloud and Ejecta Formation After the Projectile Impacts the Bumper Plate from Ref 7.

As the debris cloud expands radially, it loses kinetic energy. The particles are reduced in mass, as well as in velocity, by the bumper plate. The conical expansion of the debris cloud forces the smaller, less energetic particles to impact the rear wall over a much larger area than would have been impacted if not for the bumper plate. This spreads the damage over a larger area, but with less effect than if all the particles struck in a small area, causing cascading damage.

The size of the impact area is largely a function of the standoff distance between the bumper plate and the rear wall. The larger the standoff distance, the more the debris cloud can expand radially. This further reduces projectile velocity while increasing the impact area. To improve protection, standoff distances that are fifteen to thirty times the size of the impacting projectile are required (Ref 3, p50). Large standoff distances between the stages of the shield are ideal, but not always achievable. Unfortunately, greater standoff ranges force the addition of mass for the structural attachment of one stage to the other. Up to eight percent of total shield mass is composed of the support structure mass for multi-stage shields (Ref 13, p25). Increased standoff distances may also cause launch volumes to increase, which may restrict selection of launch vehicles or payload containers. This is less an issue if the bumper plate and support structure are installed on orbit; however, it increases risk because a lesser shielded component must fly until the installation is completed; the installation must be completed by spacewalk; and the materials must still be launched into space. Thus, mass and volume constraints necessitate shield optimization which trades standoff distances, mass (thickness of plates), and predicted shield strength (stopping power). As a matter of practical design though, standoff distance between multi-plated shields is increased on the end cone portions of the ISS' modules due to the higher probability of impact at these locations (Ref 10, p58).

Once the debris cloud strikes the rear wall, some level of damage must be expected. However, the rear wall must not sustain damage that allows hull perforation of

any kind. For a shield to perform effectively on orbit or to pass a ground test, there must be no holes nor light leaks. After the impact, the rear wall should continue to completely separate the space and interior spacecraft atmospheres from one another. Additionally, there should be no detached spall on the back face of the rear wall, the surface that is also the inside bulkhead of the International Space Station.

Spalling is usually produced when cratering penetrates approximately seventy percent of the rear wall thickness being struck (Ref 14, p9). Spalling or spallation is the result of reflected shock waves inside the wall thickness causing internal cracking (Ref 7). The compressive shock wave that has propagated through the wall thickness becomes a tensile shock wave when it reflects from the back face of the rear wall. Often times, that tensile wave is strong enough to pull some material away from the back face and cause internal cracking (Ref 7).

A spall can either be attached or detached. In the case of attached spall, there are no light penetrations or perforations on the back face of the shield. Additionally, the wall material appears to bulge outward, but there are no overt material defects otherwise. A shield is considered to pass if only attached spall is present. Detached spall, on the other hand, is indicated by shield material being expelled off the back face of the shield. Although detached spalling can occur without perforation and light leaks present, it is still considered a failing indicator of a shield. This is because the material that separates from the rear wall face is energetic and hot. It can be forced into the interior of the ISS, causing damage to equipment or injury to personnel. Obviously, shield testing and design is based on preventing both perforations of the rear wall and detached spalling from occurring. An example of both detached spall and attached spall are shown in the figure below. These examples are from a thick monolithic plate that was impacted by a high-speed projectile. The cross-sectional photographs show the material separation inside the plate thickness.

a.  b. 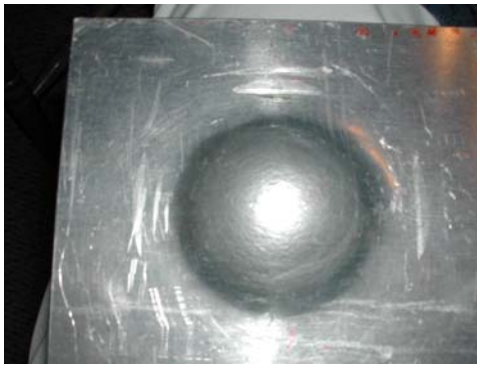

c.  d. 

Figure 7. 1100 Aluminum Monolithic Shields with Normal 0-degree Impact by 3/8" 2017 Aluminum Sphere from NASA JSC HITF Display, as Analyzed by the Author. The Back Face of Monolithic Shields Showing: (a) Detached Spall Resulting from a Hypervelocity Impact (7.0 km/s Impact, 2.5cm Shield Thickness) ; (b) The Back Face of a Different Monolithic Shield (7.1 km/s Impact, 3.7 cm Shield Thickness) Showing Attached Spall; (c) The Cross-sectional View of the Shield in (a) Showing the Internal Material Yielding Detached Spall (1.4" Diameter Hole in Front Face and 1.4" Diameter Spall Area on Rear Face); and (d) The Cross-sectional View of the Shield in (b) Showing the Internal Material Yielding Attached Spall (1.6" Diameter Hole in Front Face with 1" Penetration Depth).

C. ENHANCED STUFFED WHIPPLE SHIELDS AND IMPACT PHENOMENA

With the invention of high-strength, lightweight materials many years after the introduction of the Whipple Shield, the basic Whipple Shield was modified so that 3M Nextel ceramic fiber and Dupont Kevlar sheets were placed between the bumper plate

and rear wall to provide further protection. This shield configuration was named the Enhanced Stuffed Whipple Shield. One major advantage of the Enhanced Stuffed Whipple Shield over the conventional Whipple Shield is that, as a result of the impulsive loading at the rear wall, the Enhanced Stuffed Whipple Shield is more likely to yield a bulge shape after impact, vice cratering or cracking, as is more commonly observed in conventional Whipple Shields (Ref 23). Detached Spalling is less likely to occur in an Enhanced Stuffed Whipple Shield than in a standard Whipple Shield. The Whipple Shield is more likely to experience perforation instead of or in conjunction with detached spalling (Ref 10, p43). The basic physical phenomena described above still apply for the Enhanced Stuffed Whipple Shield. The presence of the Nextel and Kevlar between the two stages of the Whipple Shield helps shock and pulverize the debris cloud even further prior to the cloud striking the rear wall, reducing the projectile mass and velocity even more than already done by the bumper plate. The Kevlar also serves the role of catching many of the smallest debris cloud particles, stopping them from striking the rear wall altogether.

The selection of Kevlar and Nextel for the intermediate stage of the Enhanced Stuffed Whipple Shield was based on the material characteristics and performance of each of these materials. Nextel is a woven ceramic fabric produced by 3M Corporation. It consists of Alumina-Boria–Silica fibers that induce shockwaves into any particles impacting upon it. Nextel is a series of continuous polycrystalline metal oxide fibers (Ref 24). In fact, the Nextel is actually better at shocking the projectile fragments than Aluminum. On the Enhanced Stuffed Whipple Shield, the Nextel ceramic cloth generates greater shock pressures and greater disruption of the impactor than an Aluminum bumper of equal mass (Ref 10, p39), stopping fifty percent to three-hundred percent more massive projectiles than an equal mass Aluminum plate (Ref 23).

Kevlar is a high-strength, lightweight material produced by Dupont. Kevlar is used in many high-stress applications because of its superior resistance to heat and wear.

It is much stronger than any other reinforcing material currently on the market. People are most familiar with Kevlar being used in ballistic (or bulletproof) vests. Kevlar consists of long molecular chains produced from polyparaphenylene teraphthalamide (Ref 22). The molecular chains are highly oriented with strong inter-chain bonding. This provides Kevlar's high tensile strength versus its low mass. Kevlar also has significant structural rigidity and toughness (work to break). Kevlar has a greater strength-to-weight ratio than Aluminum. It possesses a superior ability to slow the particles in the debris cloud. Additionally, when Kevlar is impacted and penetrated, it produces less damaging particles than those metal fragments that are added to the debris cloud when an Aluminum sheet is impacted.

D. PHYSICAL PHENOMENA AND BALLISTIC PERFORMANCE DESCRIPTIONS

Hundreds of ground-based impact tests were conducted to understand the physical phenomena associated with hypervelocity impacts. Over a large range of projectile sizes and impact velocities, some common performance characteristics emerged. Most notably, there are three distinct impact velocity regimes, each possessing characteristic physical phenomena. These regions are the ballistic range, the shatter range, and the melting/ vaporization range (Ref 13, pp3-4).

The ballistic range, sometimes called the deforming projectile regime (Ref 10, p43), occurs at low impact speeds, usually less than three kilometers per second. Generally low shock pressures characterize this regime. The projectile remains basically intact after striking and penetrating the bumper plate. It travels too slowly to create the shock wave necessary to fragment it (Ref 13, pp3-4). This deformed, but intact projectile then propagates along into the rear wall or through the Nextel/ Kevlar and then to the rear wall in the case of the enhanced Stuffed Whipple Shield. Because the projectile particle remains large and intact, it maintains most of its momentum. Because the projectile

remains highly energetic after perforating the bumper, the slow impact may cause more damage than if the impact velocity was greater and the projectile broke up.

The shatter range occurs at intermediate impact speeds, usually between three and seven kilometers per second. This regime is often known as the projectile fragmentation regime (Ref 10, p43). In this impact regime, the projectile fragments upon striking the bumper plate and breaks up. Above impact speeds of 5.5 kilometers per second, the projectile may begin to melt due to shock pressure for Aluminum bumpers and impactors. For other shield and projectile material configurations, melting due to shock pressure will be associated with greater impact speeds. The liquid phase of the projectile and shield material in the debris cloud is less penetrating of the rear wall than the remaining sold phase material. Thus, the shield may actually perform better when it is struck by a fixed-size particle at a faster speed.

The melt/ vaporization range occurs at high speeds, typically greater than seven kilometers per second. The high speed of the impact causes very large shock pressures, which, in turn, leads to the formation of a mixed phase debris cloud. This combined solid, liquid and gaseous cloud impacts the rear wall of the shield. At some lower speeds in this regime, this multi-phasing of impact material may help the rear wall withstand the impact. Unfortunately, the speed is often enough to perforate the rear wall regardless of the phase of the debris cloud. Due to the inability to duplicate such high-speed impacts in the laboratory, most analysts have modeled this regime using hydrocode to arrive at predictive equations that describe the highest-speed impact events.

These three regimes and the characteristic shape of double-plate ballistic limit equations are shown in the figure below. Any data points corresponding to a particle of the given diameter at the specified impact velocity that fall above the curve predict shield failure, while data points falling below the curve predict that the shield will not

experience failure despite the hypervelocity impact by a particle of the specified size and velocity.

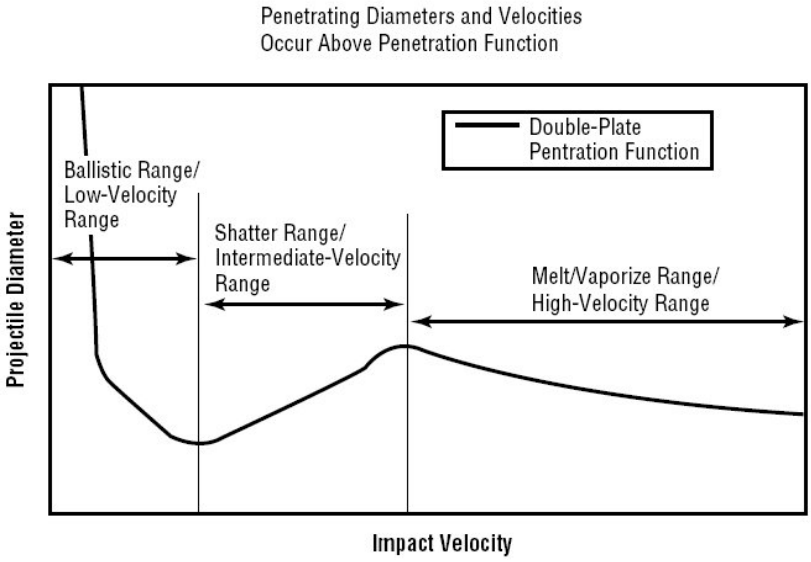

Figure 8. Ballistic Limit Performance Regimes for Double Plate Shields, from of *Double Plate Penetration Equations, NASA/TM-2000-209907*, p3.

E. CREATION OF DOUBLE PLATE PENETRATION PREDICTOR EQUATIONS

With the introduction of double plate shields to space applications, a number of double plate penetration equations were developed to describe or predict shield performance. There are seven commonly used predictor equations. These are the Nysmith, Wilkinson, Original Cour-Palais, Modified Cour-Palais, New Cour-Palais (or Christiansen), Burch, and Lundeberg-Stern-Bristow Equations (Ref 13, p iii). These various types of predictor equations are largely empirical. They are based on a number of different tests performed on the shield and only apply to the specific shield materials and configurations tested (Ref 14, p12). Commonly, these predictor equations are called Ballistic Limit Equations (BLEs). These equations are semi-empirical, and are developed from hypervelocity impact test data and analysis (Ref 10, p42). There are two basic types of Ballistic Limit Equations – the design equation and the performance equation (Ref 10,

p42). The design equation yields the minimum plate thickness for the bumper and the rear wall based upon material selection and impact characterization. These equations allow engineers to design shields so that they will withstand a hypervelocity impact. The performance equations predict the shield's ability to withstand a hypervelocity impact based upon the impacting projectile's diameter and the impact velocity. These performance equations will be the ones examined when determining the effectiveness of current equations to predict damage based upon projectile density effects data. Further, it is these performance equations that are used in NASA's risk analysis, so they are of the most direct interest to us.

A detailed comparison of the seven double plate penetration equations can be found in Ref C. While no detailed comparison of the seven existing equations will be conducted here, some necessary conclusions should be stated with regards to the best equation to use when predicting the ISS Whipple and Enhanced Stuffed Whipple Shield performance. Several hundred hypervelocity impact tests were conducted using double plate shields at Marshall Space Flight Center during the ISS shielding design. Fifty-eight of these tests were compared with predictions to determine which of the double plate penetration equations most accurately predicted the shield performance. As a consequence of these test results, the New Cour-Palais equation, sometimes called the Christiansen equation, was chosen as the best overall predictor equation for the ISS double plate shielding. The New Cour-Palais equation evolved from the Modified Cour-Palais equation in order to encompass the effects of all three impact regimes for velocities between two and fifteen kilometers per second. It is the only one of the seven, predictor equations that includes all three impact regimes. It is a semi-empirical/ semi-analytical performance equation that uses coefficients and exponents that were derived from test data. The test data anchors the predictions at the highest attainable laboratory impact speeds and then conservatively extrapolates higher impact velocity data (Ref 10, p25).

For the high velocity range of impacts, the New Cour-Palais equation is the most conservative. This is very desirable for flight crew and equipment safety. The equation encompasses all failures, providing a thorough and comprehensive range of predictions. The downside of this equation is that some data points that may actually withstand the impact will inaccurately be predicted as failures. The new Cour-Palais equation is also the only equation that directly determines the ballistic limit projectile size. It provides an analysis-oriented equation vice a design-oriented one. This equation is the most effective at balancing conservatism (more massive shields) with non-conservatism (more risk). For this reason, the New Cour-Palais equation became the starting point for analyzing the Whipple and Enhanced Stuffed Whipple Shields.

Over time, this equation has been further refined to reflect newly collected data that has accounted for such things as the projectile shape and material. Based upon the projectile density effects data collected recently, it will be further modified to more accurately reflect all possible factors contributing to shield performance. The series of equations below reflect the existing Ballistic Limit Equations prior to conducting the density effects test series. NASA provided these equations prior to the commencement of the density effects test series, and describe both the Whipple and Enhanced Stuffed Whipple Shield predicted performances respectively. The figures following the equations summarize the predicted shield performance for the test Whipple and Enhanced Stuff Whipple Shields. An expanded graphical analysis of these curves is found in Appendix E. Equations 2, 3 and 4 are the entering ballistic limit equations for the U.S. Laboratory Module Whipple Shield.

For $V \leq V_{lo}(\cos\varphi)^{Xlo}$ Equation 2

$$d_{crit} = K_L\left(t_{rw}(\sigma_Y/40)^{1/2} + C_L t_b \rho_b\right)(\cos\varphi)^{-11/6}\ \rho_p^{-1/2}\ V^{-2/3}$$

For $V_{lo}(\cos\varphi)^{Xlo} < V < V_{hi}(\cos\varphi)^{Xhi}$ Equation 3

$$d_{crit} = \left[K_H V_{hi}^{-2/3} \rho_p^{-1/3} \rho_b^{-1/9} S^{1/2} (t_{rw} \rho_{rw})^{2/3} (\sigma_Y/70)^{1/3}\right] x$$

$$\left[(V - V_{lo}(\cos\varphi)^{Xlo}) / (V_{hi}(\cos\varphi)^{Xhi} - V_{lo}(\cos\varphi)^{Xlo})\right] +$$

$$K_L V_{lo}^{-2/3} \left(t_{rw}(\sigma_Y/40)^{1/2} + C_L t_b \rho_b\right) \rho_p^{-1/2} (\cos\varphi)^{(-11/6 - 2/3 \cdot Xlo)} x$$

$$\left[(V_{hi}(\cos\varphi)^{Xhi} - V) / (V_{hi}(\cos\varphi)^{Xhi} - V_{lo}(\cos\varphi)^{Xlo})\right]$$

For $V \geq V_{hi}(\cos\varphi)^{Xhi}$ Equation 4

$$d_{crit} = K_H \rho_p^{-1/3} \rho_b^{-1/9} (V \cos\varphi^{-2/3} S^{1/2} (t_{rw} \rho_{rw})^{2/3} (\sigma_Y/70)^{1/3}$$

Where:

V = projectile velocity in km/s;

d_{crit} = the maximum projectile diameter, in cm, if the shield is predicted to pass at a given impact velocity;

V_{hi} = 7, in km/s;

V_{lo} = 3, in km/s;

X_{lo} = -3/2;

X_{hi} = -1;

K_L = 1.8;

$K_H = 1.35$ unless $\left[t_b/(t_{rw}^{2/3}S^{1/3})\right] < 0.126$. In this case, it equals

$$\left[7.451\ t_b/(t_{rw}^{2/3}S^{1/3})\right]+0.411;$$

$C_L = 0.37$, in cm^3/g;

S = the standoff distance in cm, between the rear wall and bumper plate;

φ = the impact angle in degrees;

σ_Y = yield strength, in ksi, of the rear wall plate;

t_{rw} = rear wall plate thickness in cm;

t_b = bumper plate thickness in cm;

ρ_{rw} = rear wall plate density, in g/cm^3;

ρ_b = bumper plate density, in g/cm^3; and

ρ_p = projectile density, in g/cm^3.

Equations 5, 6 and 7 are the entering ballistic limit equations for the U.S. Laboratory Module Enhanced Stuffed Whipple Shield.

For $V \leq [V_{LO}/(\cos\varphi)^{1/2}]$ Equation 5

$$d_{crit} = C_L(\cos\varphi)^{-5/3}\ \rho_p^{-1/2}\ V^{-2/3}$$

For $[V_{HI}/(\cos\varphi)^{1/3}] < V < [V_{LO}/(\cos\varphi)^{1/2}]$ Equation 6

$$d_{crit} = C_{li}\ \rho_p^{-1/2}(\cos\varphi)^{-4/3}\left[([V_{HI}/(\cos\varphi)^{1/3}]- V)/\ \delta\right] +$$

$$C_{hi}\ \rho_p^{-1/3}(\cos\varphi)^{-7/18}\left[(V - [V_{LO}/(\cos\varphi)^{1/2}])/\delta\right]$$

For $V \geq [V_{HI}/(\cos\varphi)^{1/3}]$ Equation 7

$$d_{crit} = C_H(\cos\varphi)^{-1/2} \rho_p^{-1/3} V^{-1/3}$$

Where:

V = projectile velocity in km/s;

d_{crit} = the maximum projectile diameter, in cm, if the shield is predicted to pass at a given impact velocity;

V_{HI} = 6.5, in km/s;

V_{LO} = 2.7, in km/s;

C_H = 3.642;

C_L = 2.063;

$C_{hi} = C_H \cdot V_{HI}^{-1/3}$;

$C_{li} = C_L \cdot V_{LO}^{-2/3}$;

φ = the impact angle in degrees;

ρ_p = projectile density, in g/cm^3; and

$\delta = [V_{HI}/(\cos\varphi)^{1/3}] - [V_{LO}/(\cos\varphi)^{1/2}]$.

The units of many of the coefficients used in the equations above are quite complex, and reflect units with fractional exponents. As the ballistic limit performance equations are refined, these numerical, coefficients and their respective units will change, rendering the discussion of them above of very limited utility. Thus, the units were excluded above to avoid later confusion, as the new ballistic limit equations replace these eqution s above.

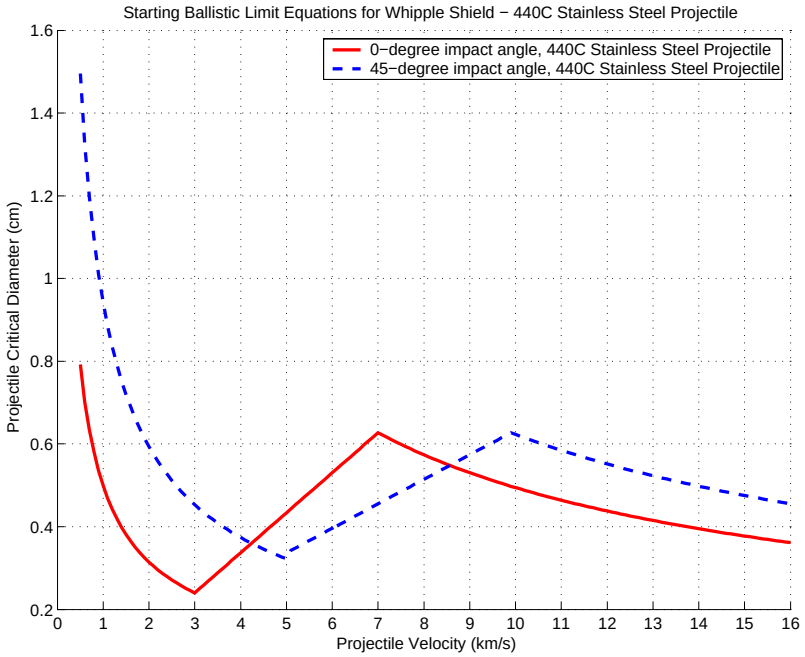

Figure 9. Original Whipple Shield Ballistic Limit Equations for the 440C Stainless Steel Projectile.

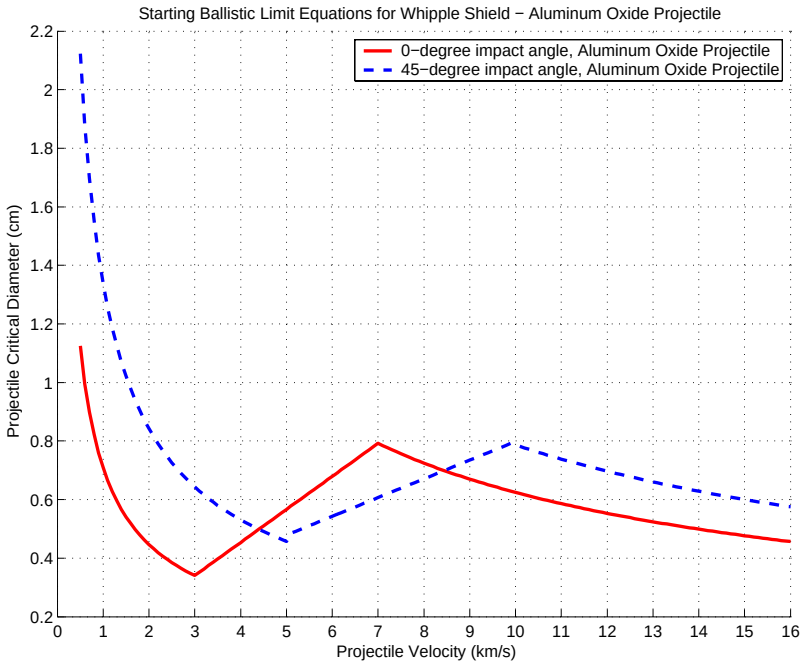

Figure 10. Original Whipple Shield Ballistic Limit Equations for Aluminum Oxide Projectiles.

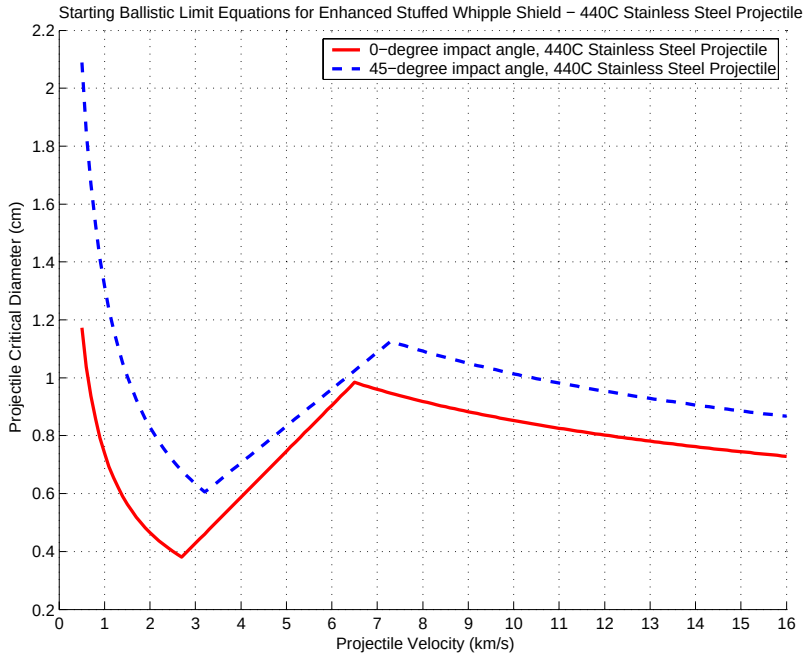

Figure 11. Original Enhanced Stuffed Whipple Shield Ballistic Limit Equations for 440C Stainless Steel Projectiles.

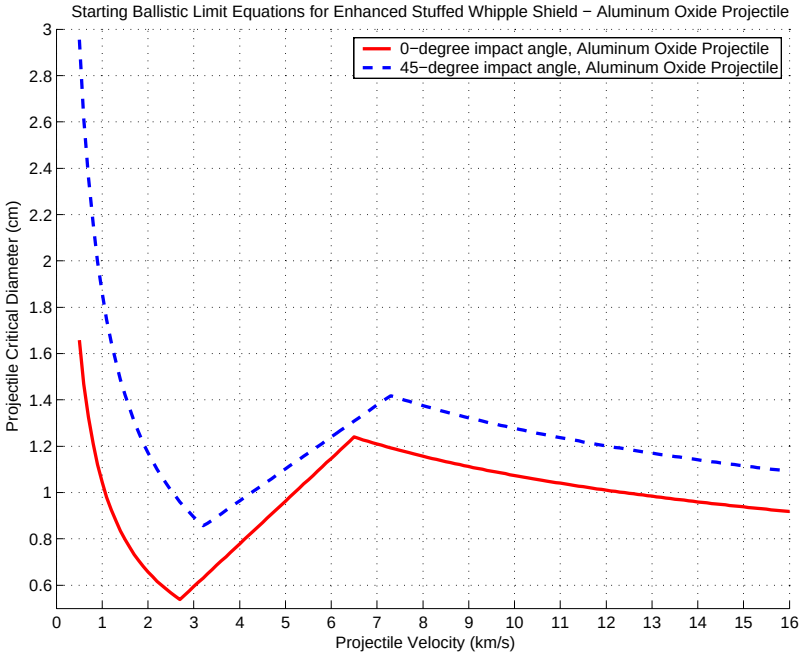

Figure 12. Original Enhanced Stuffed Whipple Shield Ballistic Limit Equations for Aluminum Oxide Projectiles.

Figures 7, 8, 9 and 10 show the ballistic limit curves produced using these equations for projectiles having the given diameter, impacting with the specified speed. Notice the piecewise continuity of the curves that corresponds to the three impact regimes described earlier. The utility of these curves as shield performance predictors is immense. If a data point falls on or above the curve, the shield is predicted to fail. If the data point falls below the curve, the shield is predicted to withstand the impact. Consequently, if the environmental models can adequately predict the debris' impact speeds and projectile diameters, the ballistic limit equations can be applied to determine the risk associated with the impact. From the earlier discussion about the ISS risk assessment, it should be intuitively obvious that accurate ballistic performance equations are a necessary component of high-fidelity risk analysis. As an analysis tool, these equations and curves are invaluable. To ensure they remain an invaluable analysis tool, they should be updated to reflect the lab-based performance of the shields as new data is collected.

III. HYPERVELOCITY IMPACT GROUND TEST FOR DENSITY EFFECTS TEST SERIES

A. THE HYPERVELOCITY IMPACT GROUND TEST FACILITY

To determine the ballistic limit equations (BLEs) for a shield configuration, ground testing and evaluation is required. NASA JSC conducts its ground testing of hypervelocity impacts at the White Sands Test Facility (WSTF), located in Las Cruces, New Mexico. The White Sands Test Facility uses a remote, access-controlled hazardous test area to help NASA's Hypervelocity Impact Technology Facility (HITF), located at Johnson Space Center, acquire the experimental data necessary to determine ballistic limits of various shielding configurations. This, in turn, helps HITF develop and test lightweight, effective shields.

The facility has the capability to shoot projectiles ranging in size from 0.25 to 22.0 millimeters in diameter at speeds up to approximately 7.5 km/s (Ref 8) from its light gas gun. Using an inhibited shaped charge, the gun is capable of reaching projectile velocities of 11 km/s (Ref 3, p25). Tests are performed at ambient temperature in a chamber regulated to less than 0.05 psia pressure. The gun is a two-stage, 0.17-caliber light gas gun that launches a test projectile at a specified speed at a test shield. This light gas gun is capable of firing the projectile at many different speeds, covering roughly 40% of the anticipated, on-orbit impact speeds (Ref D, p 15).

B. HYPERVELOCITY IMPACT GROUND TEST EQUIPMENT

The first stage of the light gas gun consists of a large diameter cylinder with compressed (50 psi) Hydrogen gas. The breach contains a powder charge. The other end of the cylinder is tapered and called the pump tube. Inside the pump tube is a nylon

piston. When the charge is ignited, the piston is forced through the pump tube, where it moves toward the end of the first stage, compressing the Hydrogen to a much greater pressure as it displaces along the pump tube. The pressure builds to the order of 100,000 psi (100 ksi).

The second stage of the light gas gun consists of the barrel, the flight range, and the target chamber itself. It is separated from the first stage by a scored rupture disc. The test projectile is located at the front of the barrel, downrange from the rupture disc. This second stage is maintained at near-vacuum pressure. As a result of the charge ignition and piston displacement in the first stage, an extremely high pressure builds up, causing the rupture disc in the adjacent second stage to burst. The high pressure Hydrogen floods into the near-vacuum second-stage and propels the projectile down the barrel at speeds up to 7.5 km/s. The projectile then strikes its target, completing the impact test.

In order to measure projectile fidelity and velocity, the test bed utilizes a number of lasers and high-speed cameras. WSTF uses a Cordin 140 Infrared Ultra-High-Speed Camera to determine projectile integrity and to measure velocity. The Cordin 140 camera is shadowgraph camera rated at 2.5 Million frames per second. Besides its use in verifying projectile fidelity and velocity, the camera can also be used to examine the debris cloud and ejecta, creating a photographic record of the debris propagation after impacting the bumper plate.

A combination of intervelometers and impact flash detectors provide two more independent means of verifying velocities of interest (Ref 9, p2). Two laser curtains are used to detect disruptions upstream and downstream of the projectile path. When the projectile breaks the laser curtain plane, the time is measured. The distance between the laser curtains is fixed. When the time measurements are taken between laser curtain disruptions, a projectile velocity can be calculated.

Light detectors are also used to measure velocities of interest. Light is emitted during hypervelocity impact. Light is also emitted when the sabot pieces impact the sabot stripper. Time between light emissions is measured and compared with the fixed and known distances involved to determine velocity (Ref 7).

Lastly, flash x-rays are used to verify projectile integrity for each experimental shot fired. The x-ray itself has three heads, one for verifying integrity and two for scanning the target. The x-ray depicts the cross section of the projectile. The x-ray is examined to ensure that the projectile is in one piece at the time of launch and immediately prior to impact. This ensures the validity of the data being collected. Projectile integrity is one necessary condition of deeming a test shot as being satisfactory, hence yielding meaningful results. If the projectile breaks up prior to impacting the bumper plate, technicians will be unable to verify the accurately determine the quality of predictive ballistic performance equations for the shield configuration being tested. The two x-ray heads that scan the target are used to map the propagation of the debris cloud as it travels inside an opaque target (Ref 7).

THIS PAGE INTENTIONALLY LEFT BLANK

IV. RAW DATA COLLECTION AND MEASUREMENT

A. OVERVIEW/REQUIREMENTS

For the density effects test series examined in this thesis, a number of conditions were prescribed for testing. Both 440C Stainless Steel and Ruby Sapphire Aluminum Oxide projectiles were used, as they are representative of the more commonly encountered manmade debris materials found in low earth orbit. They are also more dense than the pure Aluminum used to formulate the original ballistic limit equations. Because less dense Aluminum was used to formulate the original BLEs, this test series was ordered to determine if existing equations accurately reflected shield performance when struck by more dense and presumably more damaging heavy materials. Test shield configurations were established as both the Whipple and Enhanced Stuffed Whipple Shields, with materials, plate thicknesses, and spacing specified in the HITF Density Effects Test Plan (Ref 2). The shields used for the ground tests were duplicates of Whipple and Enhanced Stuffed Whipple Shields presently flown on the ISS onboard the U.S. Laboratory Module. The U.S. Laboratory Module is shown in the images below. These represent the finite element models of the module, as used in NASA's BUMPER II code.

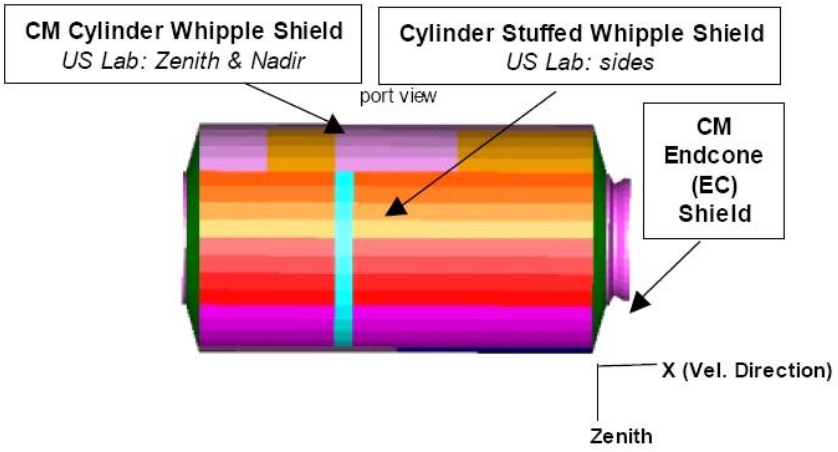

Figure 13. U.S. Laboratory Module Shielding Configuration, from *Meteoroid/ Debris Shielding, NASA TP-2003-210788*, p58.

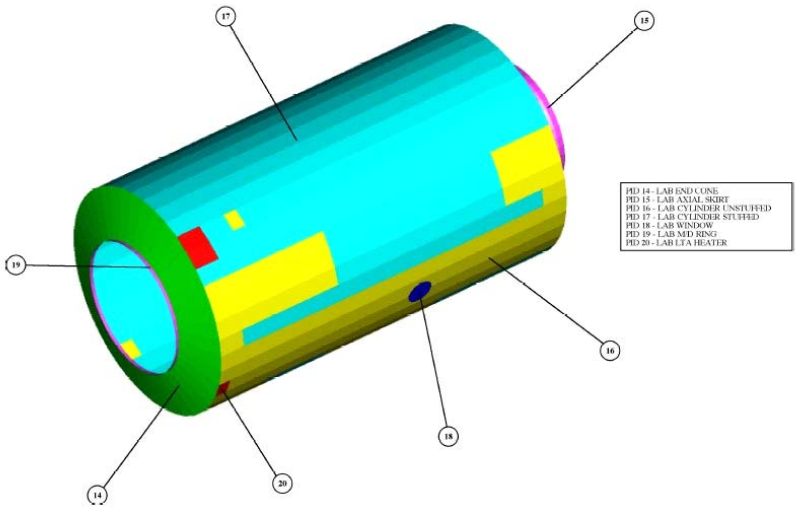

Figure 14. U.S. Laboratory Module Shielding Configuration, Showing ITA-10C FEM PID. Image from *Integrated Threat Assessment 10c (ITA-10C), LMSEAT 34102/ NASA JSC 29951*, p126.

For the Whipple Shield, the bumper was made of 6061-T6 Aluminum alloy and 0.08 inches (2.03 mm) in thickness. The rear wall, simulating the spacecraft hull, was made of 2219-T87 Aluminum alloy and was 0.19 inches (4.83 mm) thick. A witness plate was placed behind the rear wall to give us an indication of the extent of damage inside the U.S. Laboratory itself if the rear wall were penetrated or suffered detached spalling. This witness plate was made of 2024-T3 Aluminum alloy and was only 0.04 inches (1.02 mm) thick. Each plate measured twelve inches by twelve inches.

Similarly, for the Enhanced Stuffed Whipple Shield, the bumper was made of 6061-T6 Aluminum alloy, 0.08 inches in thickness. Layers of Nextel AF-62 ceramic fabric and Kevlar-120 high-strength weave were placed between the bumper and rear wall. There were six layers of the Nextel and 6 layers of the Kevlar used in this test series. The rear wall, simulating the spacecraft hull, was made of 2219-T87 Aluminum alloy and was 0.19 inches thick. A witness plate was placed behind the rear wall to give us an indication of the extent of damage inside the U.S. Laboratory itself if the rear wall was penetrated or suffered detached spalling. This witness plate was made of 2024-T3

Aluminum alloy and was only 0.04 inches thick. Each plate measured twelve inches by twelve inches.

Diagrams of the shielding configuration showing spacing between stages of the shield, as well as plate thicknesses are shown in figures below:

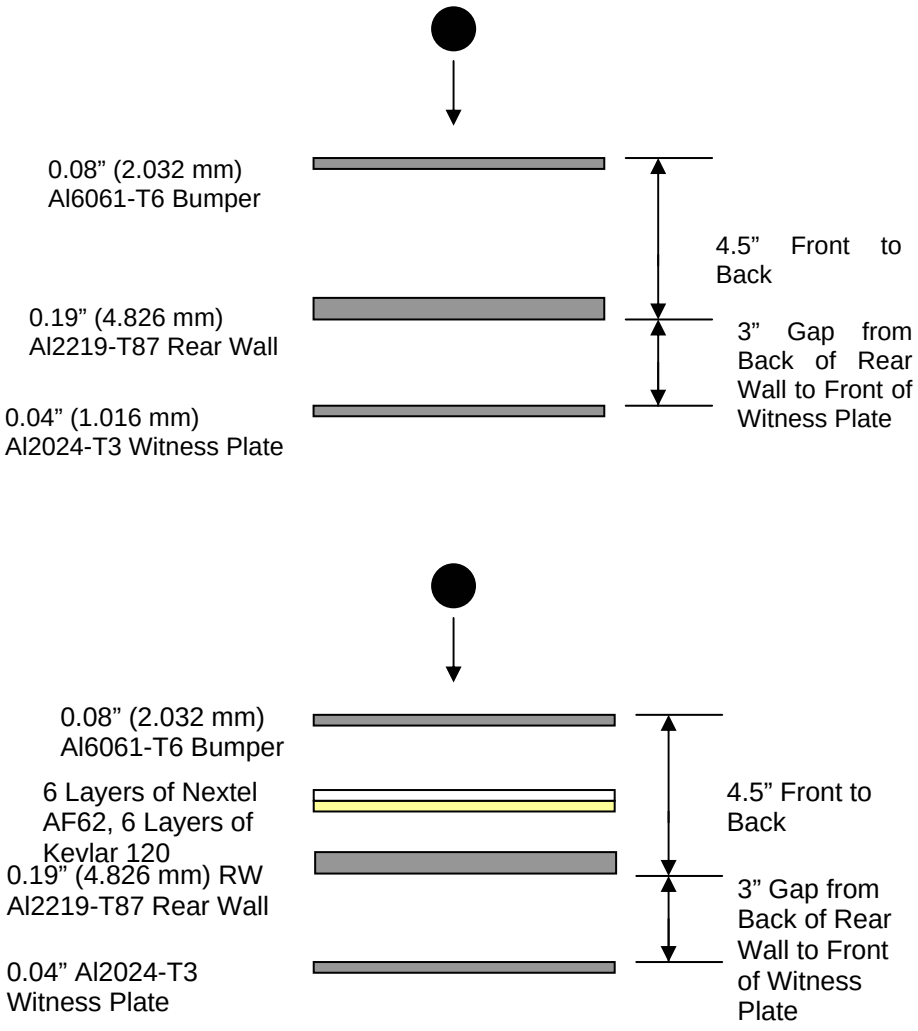

Figure 15. Density Effects Test Series Shielding Configuration to Match U.S. Laboratory Module Shield Configurations: (a) Whipple Shield Configuration and (b) Enhanced Stuffed Whipple Shield Configurations (Note that the Center of the Nextel/ Kevlar Stuffing is 2.25” from the Back of the Rear Wall.

Projectile speed, impact angle and diameter ranges were specified for each type of projectile, 440C Stainless Steel and Ruby Sapphire Aluminum Oxide. The only impact angles specified for this test series were zero-degree, normal impact and a 45-degree impact angle. Velocities and projectile sizes varied greatly within the testable range of White Sands Test Facility. Most individual tests called for speeds within the range of four to seven kilometers per second. Projectile sizes varied as well. This data can be found in Appendix C, in the detailed raw data spreadsheet. Prior to testing, plate areal densities were measured, and the masses and diameters of the projectiles were verified. This data is summarized in the raw data Tables 2 and 3, as well as in Appendix C of this report. The shield materials and configurations were not varied throughout the test series. Only projectile diameter, material, velocity, and impact angle were varied for the Density Effects Test series.

Upon completion of testing, post-impact analysis was conducted for each test in the series. The velocities were calculated and projectile integrity was verified following the basic discussion in the previous chapter. This allowed the test facility to evaluate whether the test was valid and if its data should be used in post-impact analysis of the shields' ballistic limits. Additionally, each plate and sheet within the various shields was photographed. A number of measurements and observations were made to characterize the damage resulting from the hypervelocity impact. These measurements included sizes of holes and diameters of concentrated damage areas; depths of penetration and cratering; and comments regarding the extent and character of damage. Following the approved NASA Damage Classification diagrams, rear wall damage was classified and included in the database of Density Effects Test results (Ref 9, pp 20-22). Finally each shield was evaluated to determine if it PASSED or FAILED, based upon the presence or absence of perforation or detached spall on the rear wall. Appendices C, D, and F contain the full characterization of the raw data (projectile material, diameter, velocity, impact angle, and PASS/ FAIL evaluation); post-test pictures of the rear wall and front and back faces used to determine PASS/ FAIL criteria; and the Density Effects Test Series database which includes damage classification and measurement. Although multiple pictures of every

stage of the shield were captured during raw data collection, only the images of the rear walls of the test shields are included in the Appendices. Because these were the only plates pertinent in evaluating if the shield was characterized as a "PASS" or a "FAIL," they are the only images included. Electronic copies of the 350 or more pictures of the various shields and their complete stages were forwarded separately to JSC HITF upon collection of the data. Raw data values used in the plots are summarized with the data overlay curves below. Tables 2 and 3 contain the pertinent results of the tests, showing projectile speeds, impact angles, PASS/FAIL evaluation for each projectile type and shield configuration.

B. RESULTANT RAW DATA FOR DENSITY EFFECTS SERIES

440C Stainless Steel			
Impact Angle (deg)	Velocity (km/s)	Projectile Diameter (cm)	Pass or Fail?
0	6.66	0.600	FAIL
0	6.78	0.500	FAIL
0	6.86	0.400	FAIL
0	6.73	0.318	FAIL
45	6.84	0.480	FAIL
45	4.57	0.360	FAIL
45	6.76	0.400	FAIL
45	4.30	0.320	PASS
45	6.76	0.360	FAIL

Al2O3 Aluminum Oxide			
Impact Angle (deg)	Velocity (km/s)	Projectile Diameter (cm)	Pass or Fail?
0	6.80	0.640	FAIL
0	6.83	0.560	FAIL
0	6.69	0.500	PASS
45	6.72	0.560	PASS
45	4.29	0.480	PASS
45	6.95	0.640	FAIL
45	4.45	0.560	PASS
45	4.42	0.600	PASS
45	4.74	0.754	PASS

Table 2. Density Effects Test Raw Data Summary for the Test Whipple Shield.

440C Stainless Steel			
Impact Angle (deg)	Velocity (km/s)	Projectile Diameter (cm)	Pass or Fail?
0	6.90	0.900	FAIL
0	7.00	0.900	FAIL
0	7.04	0.833	FAIL
0	7.03	0.833	FAIL
0	6.47	0.873	PASS
45	6.84	0.900	FAIL
45	6.93	0.790	PASS
45	4.55	0.790	FAIL
45	5.75	0.873	PASS

Al2O3 Aluminum Oxide			
Impact Angle (deg)	Velocity (km/s)	Projectile Diameter (cm)	Pass or Fail?
0	6.51	0.950	PASS
0	5.51	0.950	PASS
0	6.84	1.032	FAIL
45	6.77	0.950	PASS
45	6.84	0.950	PASS
45	4.50	0.950	PASS
45	6.19	0.950	PASS
45	7.07	1.000	PASS
45	6.88	1.110	PASS
45	4.48	1.191	FAIL

Table 3. Density Effects Test Raw Data Summary for the Test Whipple Shield.

With this data in hand, the next step was to overlay the results of the Density Effects Test series on the entering ballistic limit equations for the shield configurations just tested. The goal of overlaying the old and new data was to determine if the present predictive ballistic limit equations effectively addressed differences in projectile density when predicting shield performance. If the raw data overlay of points representing individual test shot's "velocity versus projectile diameter" matched the ballistic limit curve predictions for PASS/ FAIL criteria, then the curve was an accurate predictor of shield performance, and did effectively account for density effects. However, if PASS/ FAIL predictions fell on the wrong side of the ballistic limit curve, then the controlling equations for the ballistic limit curves required modification to fit the new data. This second case was the one discovered upon examining the data overlays of density effects data and entering ballistic limit equations. The following figures show that existing ballistic limit curves do not accurately predict shield failure or effectiveness, as a large majority of the experimentally obtained data points do not match the predictions of the curves. A significant number of projectile velocity/ diameter combinations that were predicted to pass actually failed in the laboratory tests. Therefore, the ballistic limit equations must be modified to reflect these results. The full complement of raw data

overlay curves can be found in Appendix F. The curves in the Appendix show individual plots and also compare materials and shields in a number of different ways.

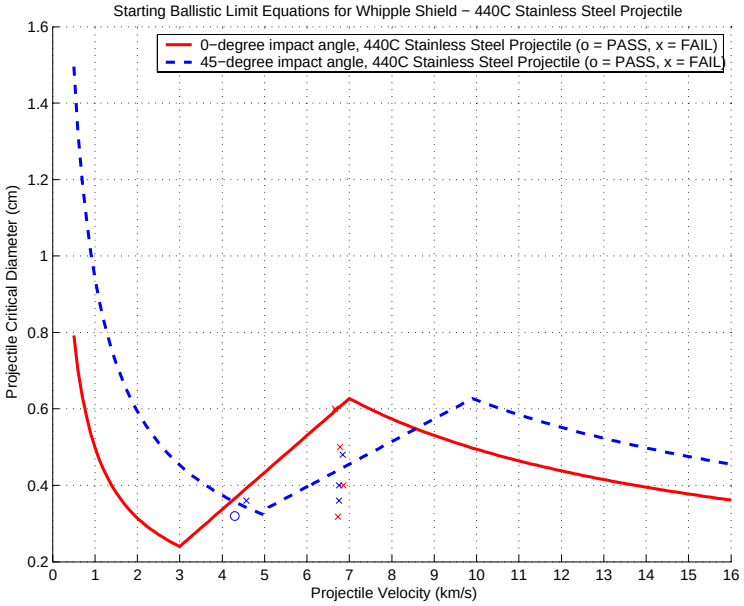

Figure 16. Density Effects Test Data Overlay on Original Ballistic Limit Equations for Whipple Shield Impacted by a 440C Stainless Steel Projectile.

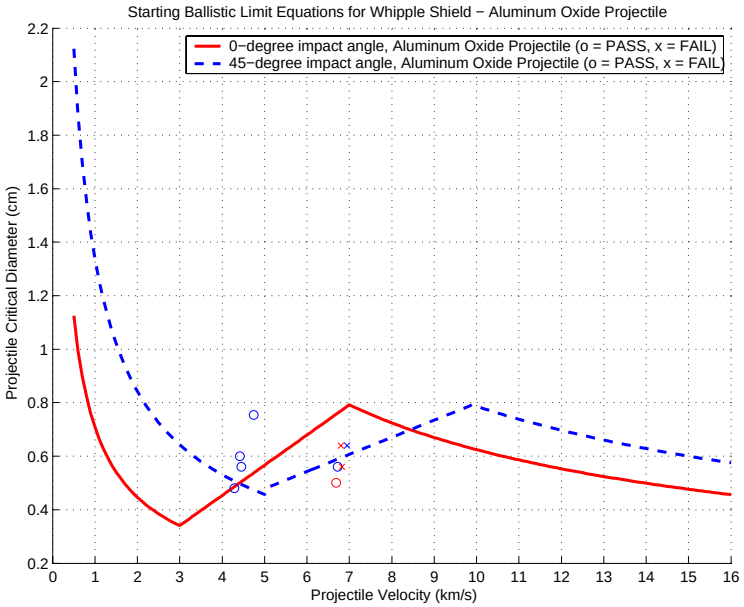

Figure 17. Density Effects Test Data Overlay on Original Ballistic Limit Equations for Whipple Shield Impacted by an Aluminum Oxide Projectile.

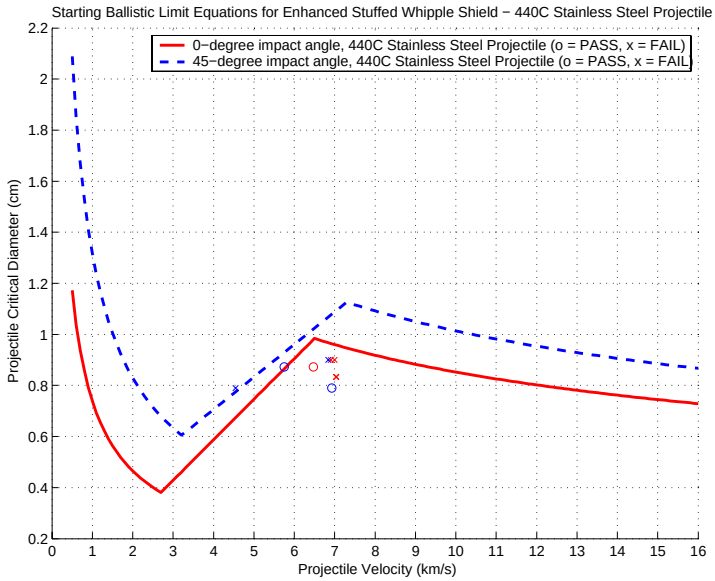

Figure 18. Density Effects Test Data Overlay on Original Ballistic Limit Equations for an Enhanced Stuffed Whipple Shield Impacted by a 440C Stainless Steel Projectile.

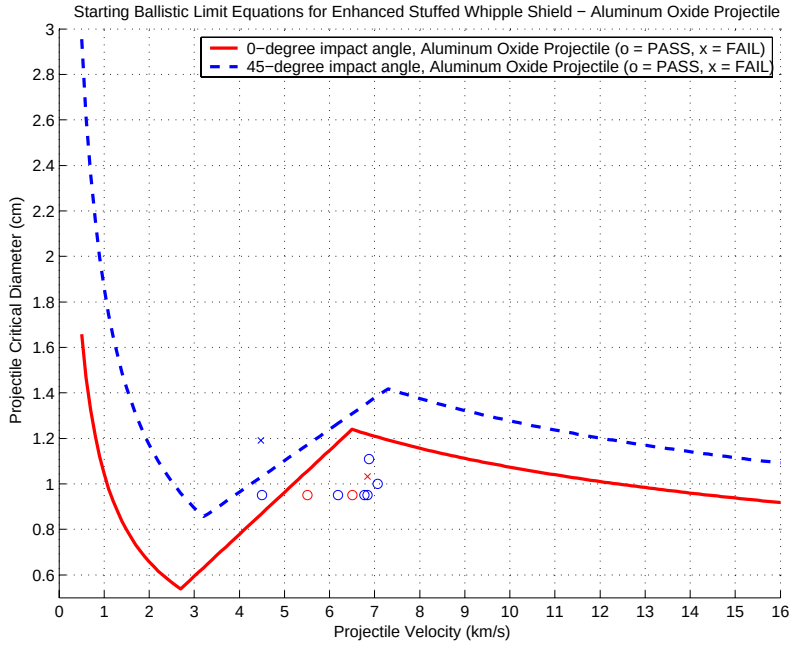

Figure 19. Density Effects Test Data Overlay on Original Ballistic Limit Equations for an Enhanced Stuffed Whipple Shield Impacted by an Aluminum Oxide Projectile.

V. DATA ANALYSIS

A. ANALYTICAL APPROACH TO REFINING THE BALLISTIC LIMIT EQUATIONS

The inability of present ballistic limit equations to accurately predict shield performance mandates that the equations must be modified to better contain the data points collected in the above test series. Because the only real difference between this test series and all the preceding test series that contributed to the development of entering ballistic limit equations was the density of the projectile, a logical place to start modifying the equations is the exponent attached to the projectile density component of the equation. Additionally, coefficients attached to the projectile density term should be varied to determine if they would improve the curve to better contain the new data. The projected best means of finding revised, more accurate predictive curves is by use of iterative processing.

The entering ballistic equations were programmed into a common engineering software suite, MATLAB. MATLAB is numerical and matrix analysis software that is commercially available from Mathworks, Inc. This software provides a numerical means of iterative analysis. Due to the simplicity of using loop structures inside the MATLAB program and its high capacity for numerical processing, one need not create overwhelmingly large MSExcel spreadsheets to accomplish the task of varying projectile density terms. Further, MATLAB's graphical interface allows for the easy creation and viewing of plots of the new ballistic limit curves. It is quite easy to overlay the old curves, as well as the individual data points collected from the Density Effects Test in order to determine which values iteratively tested yield the best new ballistic limit curves. Finally, utilizing embedded loops inside loops of computer code in a MATLAB executable script file, multiple BLE variables can be varied simultaneously. This provides the ability to examine various combinations of projectile density coefficients

and exponents at the same time. Once the loop and embedded loop are written, a matter of no more than ten lines of code, MATLAB can run without user interface to output curves representing new candidate ballistic limit equations. These curves can then be examined to find the best combination of new exponent and coefficient values to fit the Density Effects Data. This is presumably much easier than trying to use MSExcel, where a great deal of additional user input would be required to generate so many curves. Additionally, more columns of data would be needed to vary multiple variables in any meaningful way. This would require too much time and effort from the user. The MATLAB script can be written then run. The computer does all the work once the simple script file the user writes is executed. There will be associated computer processing time, but this can be accomplished while the programmers or analysts are not present in the room, thereby not adversely affecting employee or student productivity.

Appendix G includes the basic MATLAB script to program the entering ballistic limit equations into MATLAB-executable files. These files also incorporate the data overlay of the raw data collected in the Density Effects Test series. The outputs of these files are depicted graphically in the previous chapter of this report. Once these files are verified to be accurate, it is easy to modify them to integrate data loops to test the equations for various values on projectile density coefficients, then exponents, then both in combination. The first step was to give the presently coded numerical values for projectile density a variable name. This is necessary in each of the three regimes of the ballistic limit curve. As a matter of course, since most of the Density Effect data comes from the middle regime, this was the first variable to be addressed in the looping code. Once the curve was effectively moved to fit the new data, one could vary the other two piecewise curves, those portions of the ballistic limit equation in the low velocity and high velocity regimes.

Despite the ease of this solution method, the results outputted after running the program iteration were highly unreliable. Literally thousands of meaningless curves that

were discontinuous were produced. The curves produced did not adequately contain the raw data points while maintaining the basic curve features of the entering ballistic limit equations. From this failure, however, several lessons learned were captured, all of which later aided in finding accurate solutions for improved ballistic limit equations. The first major understanding developed was that the exponents of the projectile density terms had little or no impact on curve shape and position for the relatively minor adjustments needed to produce good curves. Despite varying these exponents over a wide range of values, the curve shape and position did not change appreciably. There were some adjustments made to these terms, but not in every projectile or impact angle case nor in every equation. However, varying the coefficients C_H, C_L, C_{li}, C_{hi} for the Enhanced Stuffed Whipple Shields; and K_L and K_H for the Whipple Shields did have a more dramatic impact on the curve shape shifting both the general slope of the curves and the vertical offset. This provided us a better starting point for the next analytical technique for determining the new curves. Ultimately, the reason why the MATLAB code looping method failed is that it did not account for the possibility that the V_{HI} and V_{LO} values would need to be adjusted to contain the new data in a more realistic curve. Additionally, the exponents attached to these V_{HI} and V_{LO} terms that define the boundaries of each of the three sections of the curve would need to be modified as well. These exponents are X_{lo} and X_{hi} for the Whipple Shields and were without name in the original Enhanced Stuffed Whipple equations.

Based on this failure and the subsequent realization that terms not directly related to the projectile density term could and should be varied, a reexamination of the problem was undertaken and a somewhat simpler approach to determining improved ballistic limit equations was developed. "Lines of best fit" for each segment of the curve were hand-drawn on the curves. In some cases, for some impact angles, the existing curve already fit the new data collected. In many other cases, the first segment of the curve and parts of the third segment fit the data, but the second segment needed to be modified. In virtually all cases, the entering V_{HI} value needed to be changed. While this method was quite subjective, it provided a starting place from which to mathematically analyze the new line

segments desired in the ballistic limit equations. Only those "lines of best fit" that properly predicted the new projectile density effects data without deviating dramatically from the old curve shape were accepted as candidate equations. They were also selected with an eye toward minimizing the loss of area under the curves as the new ballistic limit equations were implemented. Thus, a purely mathematical solution to the problems was begun in order to regenerate points that were still valid from the old equations, while amending the old equations in regions of the curve that needed to be shifted to fit the new data. A complete discussion of the mathematics and solutions is given below. There were multiple acceptable solutions for both projectile materials and both shield types, Whipple and Enhanced Stuffed Whipple. Those complete results are also derived below. After comparing these candidate equations to one another and the starting BLE, a single unique equation for each case will be recommended, with justification as to why it is the best choice to become the new, improved ballistic limit equation.

Because unique equations are determined for each projectile case, i.e., precise values for coefficients, exponents, and terms like V_{HI} and V_{LO} are specified, the new BLEs don't precisely predict the behavior of Aluminum projectiles, which were used to create the original, entering BLEs. Because each projectile type has a unique equation to predict ballistic performance, the original BLEs can still be used as accurate predictors of a shield's performance against pure Aluminum projectiles.

B. MODIFYING THE ENHANCED STUFFED WHIPPLE SHIELDS

The modification of the Enhanced Stuffed Whipple Shields was undertaken first because the equations were more simplistic than the Whipple Shield Equations. The 440C Stainless Steel projectile cases were analyzed first. During this analysis, several variables from the original BLEs were exploited to arrive at suitable candidate curves. Therefore, the underlying mathematical theory is first discussed in that subsection of the chapter.

1. 440C Stainless Steel Projectile Cases

There were two viable options for new BLEs in the 440C Stainless Steel projectile case. Based on the subjective "lines of best fit" for the 440C Stainless Steel projectile cases, the 0-degree impact V_{HI} value was shifted from 6.5 to 8.0. The 45-degree impact angle V_{HI} was shifted from 7.296 to 8.85 in Case 1. In Case 2, the 0-degree impact V_{HI} value was shifted from 6.5 to 8.0. The 45-degree impact angle V_{HI} shifted from 7.296 to 5.9. Recalling from Equation 5 that the minimum point on the curve (the point that separates region one from region two on the BLE curve) is defined using: $V_{LO} / (\cos\varphi)^{1/2}$, one can solve the new exponent that will replace ½. This is necessary in order to ensure the 45-degree cases have the points specified above in this paragraph. Since the V_{LO} values do not need to be shifted, the exponent will remain as ½. The same cannot be said for the maximum point of the curve (the point that separated region two from region three). Recall from Equation 7 that this point is defined as $V_{HI} / (\cos\varphi)^{1/3}$. Since the V_{HI} values have shifted for both the 0- and 45-degree cases, solutions for new values of the exponents must be found. Since cos (0) = 1, the 0-degree cases aren't particularly relevant, since the exponent can have any value without changing the value of $V_{HI} / (\cos 0)^{X}$. Thus, the focus is placed on determining the exponent based upon the requirements of the 45-degree cases. The equation is solved thusly:

$$V_{HI}/(\cos\varphi)^{X} = V_{HI\_45} \rightarrow X = [\log (V_{HI\_45} / V_{HI})] / \log (\cos(45)) \quad \text{Equation 8}$$

For the desired value of 8.85, the exponent will become -0.2914 and for the desired 5.9 case, the exponent will become -0.8786. This data will be summarized in the table below. Once these new values of exponents were incorporated, the desired new BLE points in regions one and three of the curve were created. Solving for region two in order to produce the desired output was somewhat more difficult. Of immediate note was the fact that this region of the curve was linear or very-nearly linear and have the form:

C_{li} (#) + Chi (#), where # indicates the numerical value produced from the rest of the terms found in Equation 6. Based upon this determination, solutions for new values of C_{li} and C_{hi} using simple matrix mathematics for solving systems of simultaneous equations were computed. The equation is in the form [A] [x] = [b], where the matrix [A] is made up of the numerical components of Equation 6. Vector [x] is C_{hi} and C_{li}. Vector [b] is the desired projectile critical diameters at the specified velocities within region two of the curve. One can choose only the endpoints and solve two equations for two unknowns or one can use every point along the line and solve many equations for two unknowns. In actual analysis, this last technique was the one employed, using an over-determined system to get higher fidelity solutions for C_{hi} and C_{li}. The simplified matrix Equations are shown below:

$$[\#_{11}\ \#_{12};\ \#_{N1}\ \#_{N2}] \times [C_{hi};\ C_{li}] = [d_{crit\_desired}1;\ d_{crit\_desired}N] \qquad \text{Equation 9}$$

$$[\#_{11}\ \#_{12};\ \#_{21}\ \#_{22}]^{-1} \times [d_{crit\_desired}1;\ d_{crit\_desired}2] = [C_{hi};\ C_{li}] \qquad \text{Equation 10}$$

In Case 1, C_{li} did not change from the entering value of 1.064, however the value of C_{hi} changed from 1.952 to 1.821, for both 0- and 45-degrees. In Case 2, a similar phenomenon was observed for C_{hi}, except that the 0-degree value became 1.821 and the 45-degree value became 1.643. For the 440C Stainless Steel projectile cases, neither C_H nor C_L were modified because regions one and three of the curve continued to meet requirements. The table below the Aluminum Oxide projectile discussion summarizes all changes made to the coefficients for each option discussed above.

2. Aluminum Oxide Projectile Cases

Similarly, there were two viable options for new BLEs in the Aluminum Oxide projectile case. Based on the subjective "lines of best fit" for the Aluminum Oxide projectile cases, the desired shift of the 0-degree impact V_{HI} value was from 6.5 to 8.0. Maintaining the 45-degree impact angle V_{HI} at 7.296 was also desirable. In Case 2, the 0-degree impact V_{HI} value was shifted from 6.5 to 5.7. The 45-degree impact angle V_{HI}

was maintained at 7.296. Again recalling from Equation 5 that the minimum point on the curve (the point that separates region one from region two on the BLE curve) is defined using: $V_{LO} / (\cos\varphi)^{1/2}$, a solution for the new exponent that will replace ½ was found. This was necessary in order to ensure the 45-degree cases' values are accurately generated. Since there was no need to shift the V_{LO} values, the exponent remained as ½. The same cannot be said for the maximum point of the curve (the point that separates region two from region three). Recall from Equation 7 that this point is defined as $V_{HI} / (\cos\varphi)^{1/3}$. Since the V_{HI} values for the 0-cases were shifted from the original entering value, new values of these exponents must also be found. Because cos(0) = 1, the 0-degree cases aren't particularly relevant, since the exponent can have any value without changing the value of $V_{HI}/(\cos 0)^{X}$. However, by changing the values of V_{HI} to 8.0 from 6.5, there is a need to adjust the exponent in the 45-degree cases in order to recreate the original values within the BLE curves. This is because there are no changes to the form of the curve. Thus, the focus was placed on calculating the exponent based upon the requirements of the 45-degree cases. The equation was solved thusly:

$$V_{HI}/(\cos\varphi)^{X} = V_{HI\_45} \rightarrow X = [\log (V_{HI\_45} / V_{HI})] / \log (\cos(45)) \quad \text{Equation 11}$$

To obtain the desired value of V_{HI_45}, 7.296 in Case 1, the exponent will become -0.2658; and for the desired 7.296 value in Case 2, the exponent will become 0.7123. This data will be summarized in the tables below. Once these new values of exponents were incorporated, the next step was to proceed with solving the rest of the coefficients in the Enhanced Stuffed Whipple equations using the same techniques and equations discussed in the preceding paragraphs. In Case 1, C_{li} did not change from the entering value of 1.064, however the value of C_{hi} changed from 1.952 to 1.821 for the 0-degree impact but did not change in the 45-degree impact. In Case 2, a similar phenomenon was observed for C_{hi} except that the 0-degree value became 1.788 and the 45-degree value remained 1.952. For Case 2, a new value of C_H in the 0-degree impact had to be determined because region one of the curve did not match up to the new minimum point

in region two. This was accomplished using Equation 5, replacing the entering critical diameter at that point with the desired critical diameter at the new minimum point. This yielded a C_H value of 3.050 vice the 3.642 throughout the rest of the trials.

All of these results are summarized in the table below for ease of implementation and understanding. While these represent the total number of candidate values presented in this thesis, this list is by no means complete. These are just several of the more promising candidate values. Of these, a single equation with its accompanying coefficient and exponent values will be chosen in the section below for each projectile material type, thereby becoming the new ballistic limit equation for the U.S. Laboratory Module Enhanced Stuffed Whipple Shield.

Enhanced Stuffed Whipple Shield												
440C Stainless Steel Projectile												
Case	Vhi	Vhi $(\cos)^X$ exponent	Vlo	Vlo exp.	CH_0	CH_45	CL_0	CL_45	Chi_0	Chi_45	Cli_0	Cli_45
1	8.0	0.2914	2.7	0.5	3.642	3.642	2.063	2.063	1.821	1.821	1.064	1.064
2	8.0	-0.8786	2.7	0.5	3.642	3.642	2.063	2.063	1.821	1.643	1.064	1.064
Starting BLE	6.5	0.3333	2.7	0.5	3.642	3.642	2.063	2.063	1.952	1.952	1.064	1.064
Aluminum Oxide Projectile												
Case	Vhi	Vhi $(\cos)^X$ exponent	Vlo	Vlo exp.	CH_0	CH_45	CL_0	CL_45	Chi_0	Chi_45	Cli_0	Cli_45
1	8.0	-0.2658	2.7	0.5	3.642	3.642	2.063	2.063	1.821	1.952	1.064	1.064
2	5.7	0.7123	2.7	0.5	3.050	3.642	2.063	2.063	1.788	1.952	1.064	1.064
Starting BLE	6.5	0.3333	2.7	0.5	3.642	3.642	2.063	2.063	1.952	1.952	1.064	1.064

Table 4. Summary of Candidate BLE New Coefficient and Variable Values for U.S. Laboratory Module Enhanced Stuffed Whipple Shields.

Graphical depictions of these results are included below. They show the candidate curves for new ballistic limit equations, of which the best case will be chosen to become the improved BLE. Ultimately, the ones chosen to become the new ballistic limit equations and curves will be the ones that vary the least from the entering BLEs, yet

accurately contain the density effects test data. In other words, the BLE that minimizes the reduction of area under the curve while accurately representing the latest data obtained in the lab will become the new equation. Ultimately though, the Equations 5, 6, and 7 will not need to be amended. Only the values of some of the coefficients will need to adjusting depending upon the angle of impact and the projectile material, based on the results summarized in Table 4 above. The only substantial change is making the exponents attached to the projectile density terms and the $V_{HI}(\cos\theta)^X$ term into variables as required. These changes to the equations are summarized below. Keep in mind that the values of V_{HI}, C_{li}, C_{hi}, and C_H, as well as the exponents may change, but the format of the equations will remain intact.

3. Improved Ballistic Limit Equations for the U.S. Laboratory Module Enhanced Stuffed Whipple Shield

Pictured below are the candidate curves overlaid with the density effects raw data. Using these comparison plots, along with an overlay of the entering versus candidate ballistic limit equation, a best case can be chosen for the new BLE to be incorporated for the U.S. Laboratory Module Enhanced Stuffed Whipple Shield, using the evaluation criteria discussed previously, namely good test data point containment and minimization of the variation between the old and new BLE.

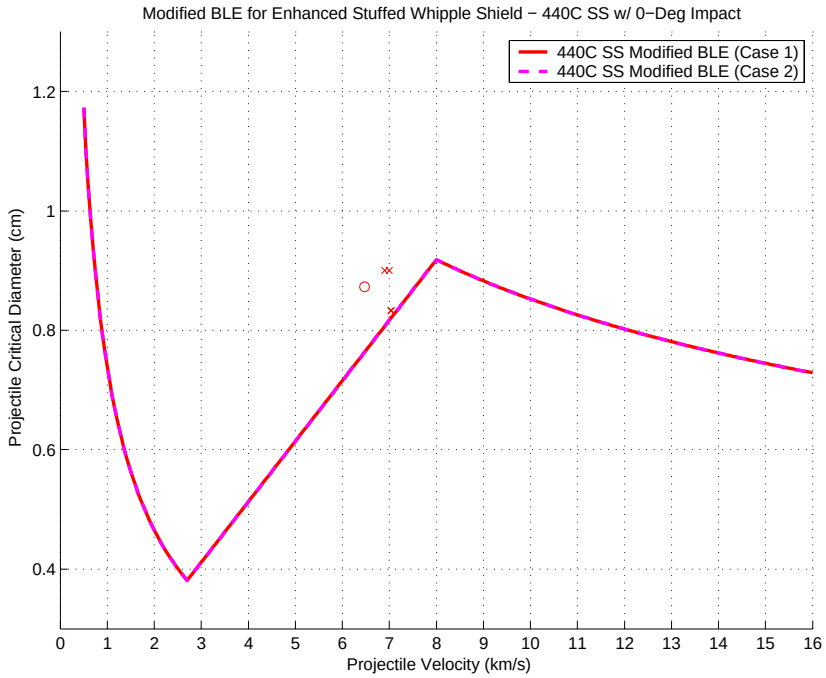

Figure 20. Overlay of Candidate BLEs with Density Effects Raw Data for Enhanced Stuffed Whipple Shield Struck by 440C Stainless Steel Projectiles at 0-degree Impact Angles.

For both cases of the Enhanced Stuffed Whipple Shield with a 440C Stainless Steel projectile at 0-degree impact angle, the resultant candidate curves are identical. Notice that the "X" indicates that the density effect data points that symbolized shield failure all fall above the new curves, whereas they did not all fall above the curve as predicted using the entering ballistic limit equations. There is one passing sample from the density effects raw data, indicated with an "o" that falls above the curve. While this is non-ideal, it is no reason to discard these curves as accurate predictors of shield failure. It is better that failure be somewhat conservatively predicted, with actual shields withstanding some impacts that were predicted to cause failure. The opposite is not true. A wayward density effects test series data point below one of the candidate new curves would be a bad thing, as a shield could fail even if predicted to pass. This alone would be reason enough to disqualify such a candidate curve from consideration as the new BLE.

Based upon the data on hand, these curves are an improvement over the entering equations, despite the one non-ideally contained point.

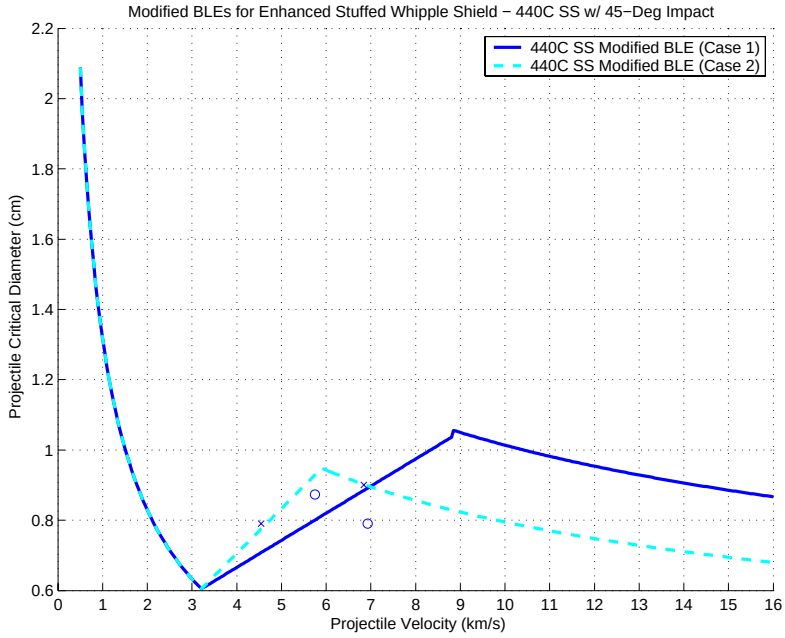

Figure 21. Overlay of Candidate BLEs with Density Effects Raw Data for Enhanced Stuffed Whipple Shield Struck by 440C Stainless Steel Projectiles at 45-degree Impact Angles.

The Enhanced Stuffed Whipple Shield with a 440C Stainless Steel projectile at a 45-degree impact angle produces two distinct, different candidate curves. Notice that the "X" indicates that the density effect data points that symbolized shield failure all fall above the new curves, whereas they did not all fall above the curve as predicted using the entering ballistic limit equations. All passing samples from the density effects raw data, indicated with an "o," fall below the curve as required in Case 2. Case 1, the solid (blue) curve does have one PASS point above the curve. However, this is not all that troubling as it yields a slightly more conservative prediction than Case 2. Both of these curves represent an improvement over the entering curves because they both accurately predict shield failure or success.

Having determined that all candidate curves contain the raw data in a meaningful and acceptable way, the new curves were examined together with the entering ballistic limit curves. In doing so, the candidate equation that also minimizes the reduction in area under the curve, i.e. that varies the least between the old and new curves, was identified. This "best" curve and the data associated with it will become the new controlling ballistic limit equation.

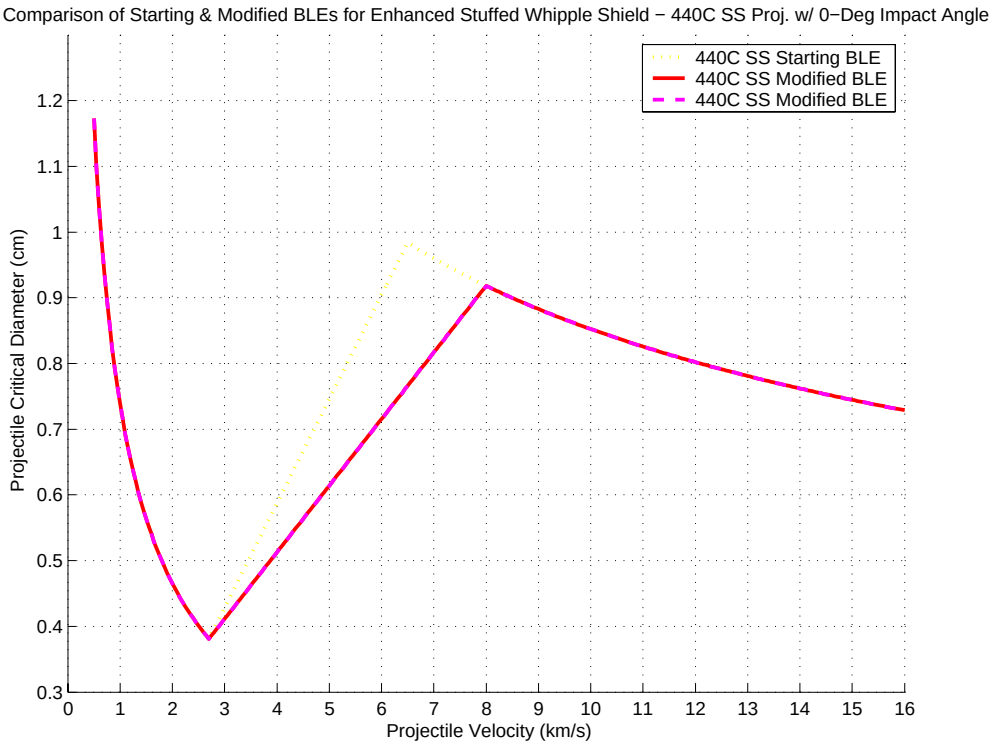

Figure 22. Overlay of Candidate BLEs with Original BLE for Enhanced Stuffed Whipple Shield Struck by 440C Stainless Steel Projectiles at 0-degree Impact Angles.

From the (yellow) dotted curve that represents the starting equation, one can see that both identical candidate equations reduce the area under the curve an equal amount. Consequently, the decision on which curve and equation to use was based upon the results from the 45-degree impact angle examination.

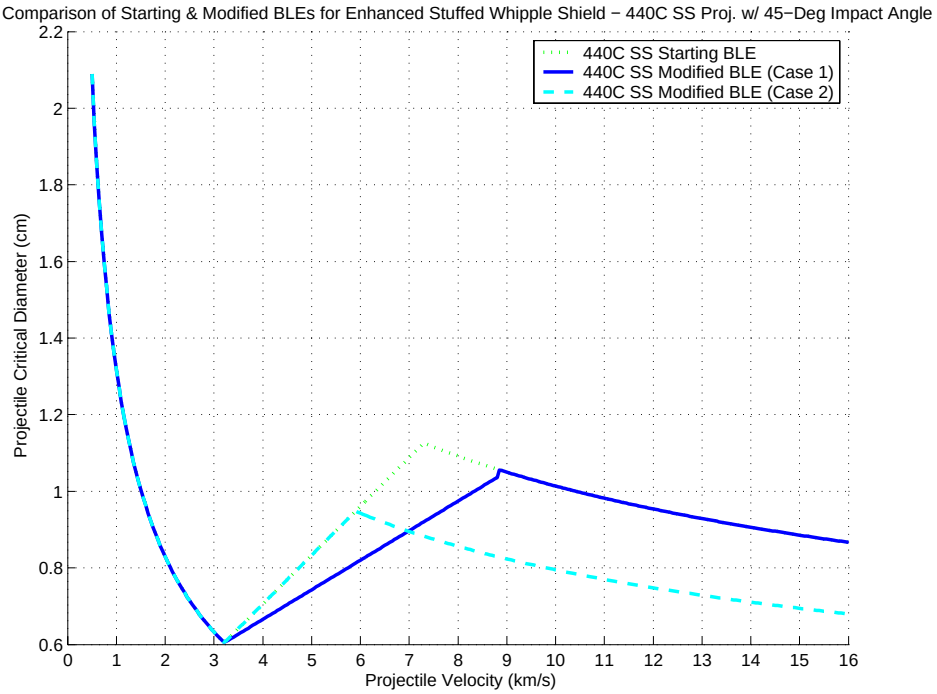

Figure 23. Overlay of Candidate BLEs with Original BLE for Enhanced Stuffed Whipple Shield Struck by 440C Stainless Steel Projectiles at 45-degree Impact Angles.

In the above plot, both candidate curves produce a reduced area under the curve from the starting (green) dotted curve. Notice though that Case 2 reduces the area under the curve more dramatically. To get the maximum point to occur at a velocity 5.9, the exponent on the projectile density term in Equation 6 must also be amended. The solution for this exponent value is found by setting Equation 6 equal to the critical diameter corresponding to a velocity of 5.9 from the entering BLE. The exponent is then computed as follows:

$$X_\rho = \log(d_{crit} / C_H(\cos\varphi)^{-1/2} V^{-1/3}) / \log (\rho_p) \qquad \text{Equation 12}$$

where X_ρ = the new value of the exponent on the projectile density term in Equation 6. Numerically, this value is computed to be 0.4516. This exponent did not require

amending in the 0-degree curves because region three of the curve remained identical to the entering ballistic limit curve.

While this produces very conservative results in the higher speed regime, an area of the hypervelocity spectrum in which NASA has little deterministic data, it also reduces predictions in the 7 – 10 kilometers per second regime, one in which NASA has the capability to test on the ground. It appears that Case 1 offers reasonable accuracy along with the most area under the curve. Hence, Case 1 appears to be a better choice. Until further tests in the 7-10 kilometers per second regime can take place, this Case's equations will be incorporated as the new, improved ballistic limit equation for the U.S. Laboratory Module Enhanced Stuffed Whipple Shield, struck by 440C Stainless Steel projectiles.

Next, the Aluminum Oxide projectile candidate curves were compared and a decision was reached as to which one would become the new BLE for the U.S. Laboratory Module Stuffed Whipple Shield impacted by an Aluminum Oxide projectile. The same methodology used in choosing the 440C Stainless Steel case to become the new ballistic limit equation was incorporated for the Aluminum Oxide case.

Notice in the figure below that, at 0-degree impact, the candidate curve that is Case 1, the (red) solid line, does have one passing data point, "o," that falls above the curve. Again, although this is a bad prediction in terms of the equations accuracy, it is a conservative prediction and one that would do no harm if an actual impact at this point occurred on orbit. Case 2 accurately contains all density effects data points.

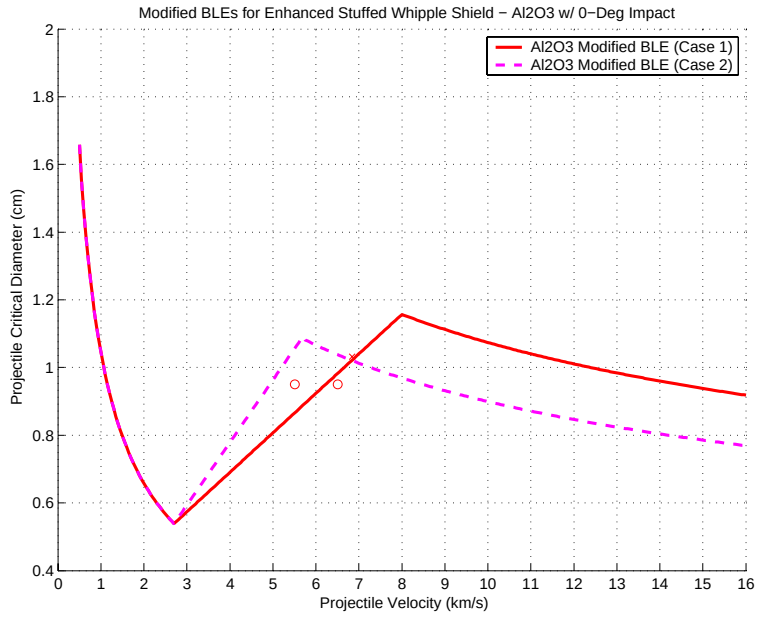

Figure 24. Overlay of Candidate BLEs with Density Effects Raw Data for Enhanced Stuffed Whipple Shield Struck by Aluminum Oxide Projectiles at 0-degree Impact Angles.

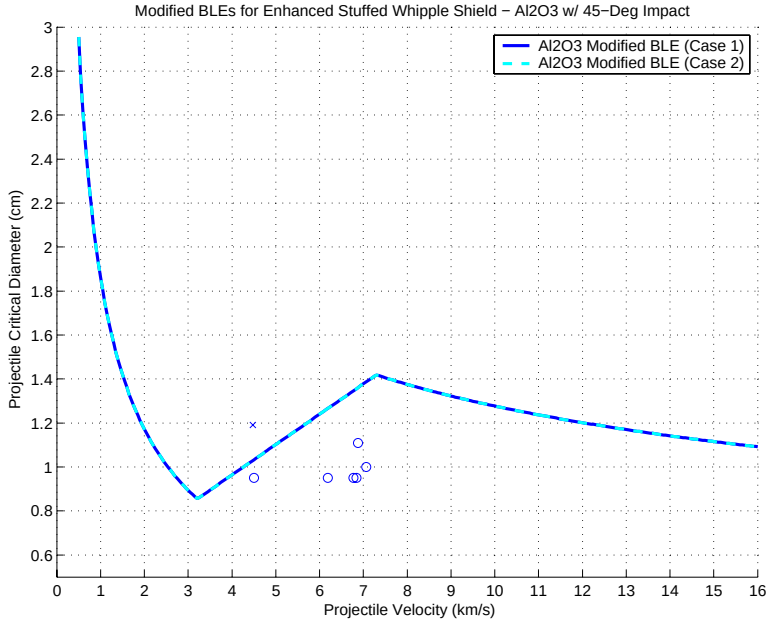

Figure 25. Overlay of Candidate BLEs with Density Effects Raw Data for Enhanced Stuffed Whipple Shield Struck by Aluminum Oxide Projectiles at 45-degree Impact Angles.

The candidate Aluminum Oxide plots at 45-degree impact angles are identical and accurately contain all the density effects raw data, therefore the determination of which curve to adopt for the new, improved BLE will rest with the 0-degree impact curves. This is the exact opposite of the 440C Stainless Steel cases, where the 0-degree curves were identical and 45-degree curves varied.

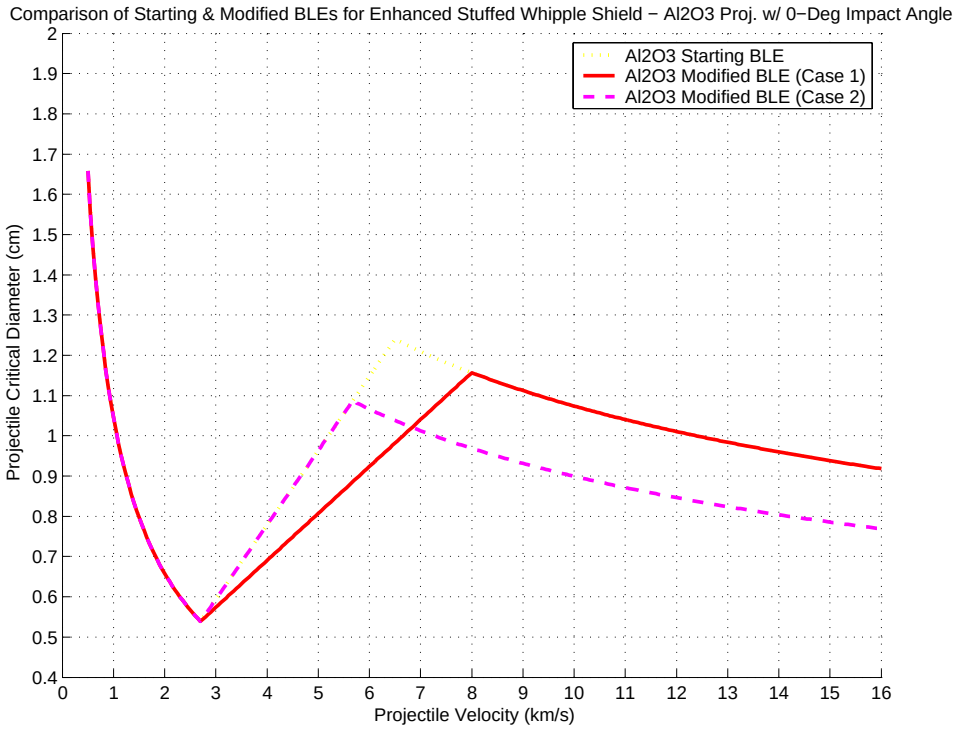

Figure 26. Overlay of Candidate BLEs with Original BLE for Enhanced Stuffed Whipple Shield Struck by Aluminum Oxide Projectiles at 0-degree Impact Angles.

The starting curve is the dotted (yellow) line. Case 2 is identical to the curve in region one and part of region two, before it deviates. However, where Case 2 deviates from the entering BLE in region three, the value of the exponent on the projectile density term in Equation 6 must be re-computed, much like that done above in the 440C Stainless Steel case. Using a similar method as in Equation 12 to solve for the new exponent value based upon the entering critical diameters at a velocity of 5.7 kilometers per second, the new exponent value was calculated to be -0.5005, on the first projectile density term that is attached to the Chi term in region two. This value was approximated as -0.5, the value

from the entering equations. Then, the second projectile density term in region two, the one attached to the Cli coefficient, shown below in Equation 13 was solved.

$$X\rho 22 = \log \left(\left[d_{crit} - C_{li}\, \rho_p^{-1/2} (\cos\varphi)^{-4/3} \left[\left([V_{HI} / (\cos\varphi)^{X\rho 22}] - V \right) / \delta \right] \right] \right) /$$

$$C_{hi}\, (\cos\varphi)^{-7/18} \left[(V - [V_{LO} / (\cos\varphi)^{1/2}]) / \delta \right] \Big) / \log \left(\rho_p \right) \qquad \text{Equation 13}$$

where $X_{\rho 22}$ = the exponent on the second projectile density term in region two of the ballistic limit curve. Computing the result yields that $X_{\rho 22}$ = -0.3621, vice -0.3333, the value used in the original BLE. By adopting this new value, the new BLE has a smooth transition point between regions two and three.

Case 1, on the other hand, is a much simpler representation. It is identical to the starting curve in region one and part of region three, but deviates throughout region two and part of three. Although it appears that Case 2 produces a somewhat more accurate prediction than Case 1, Case 1 was selected to be the new, improved BLE. Case 1 predicts a failure when a pass occurs at one of the raw data points, but this is a conservative prediction and one that is acceptable in the event of an on-orbit collision at this point. The shield will succeed even though it is predicted to fail. By choosing Case 1 to be the new BLE, the maximum area under the curve and the most duplication of original, yet still valid data points is achieved. This is particularly good because one does not want to change region three of the curve appreciably. There is little or no deterministic data to validate or refute the predictions. Instead, it is better to leave the values as they are until further capability for ground testing is developed within that range of hypervelocity impact speeds.

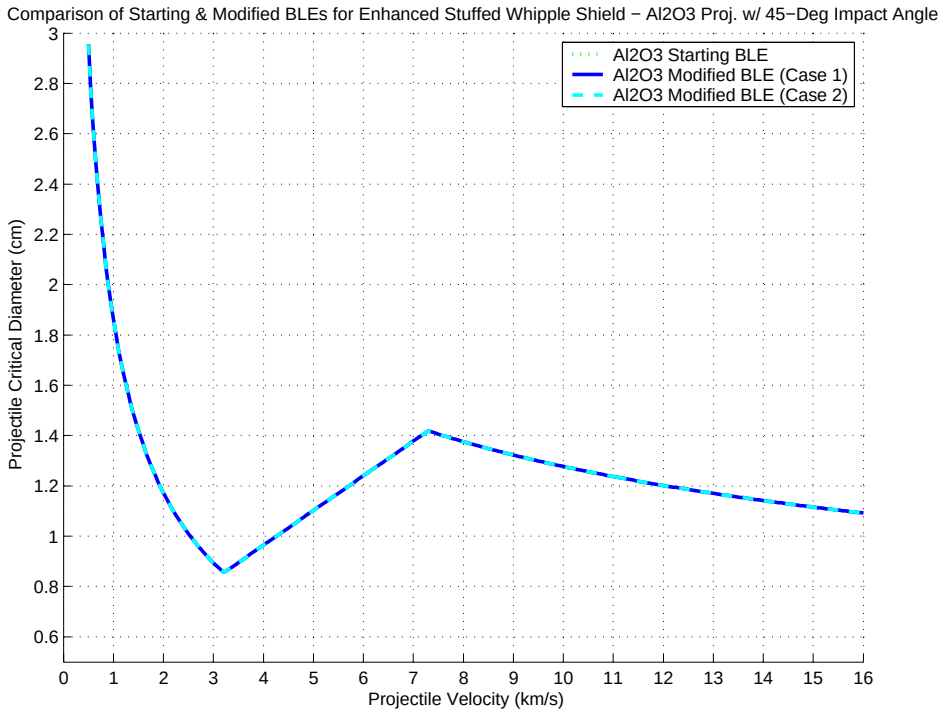

Figure 27. Overlay of Candidate BLEs with Original BLE for Enhanced Stuffed Whipple Shield Struck by Aluminum Oxide Projectiles at 45-degree Impact Angles.

The starting ballistic limit curve, the dotted (green) line, is exactly identical to both candidate curves at 45-degree impact angles. No changes are required here, thus selection of the new, improved BLE was based solely on the reduction of area under the curve in the previous plot, the 0-degree impact case.

Equations 14, 15, and 16 summarize the selection of new ballistic limit equations for the U.S. Laboratory Module Enhanced Stuffed Whipple Shields, with the most important changes noted in the comments and explanations of the variables.

For $V \leq [V_{LO}/(\cos\varphi)^{1/2}]$ Equation 14

$$d_{crit} = C_L(\cos\varphi)^{-5/3}\ \rho_p^{-1/2}\ V^{-2/3}$$

For $[V_{HI}/(\cos\varphi)^{X}] < V < [V_{LO}/(\cos\varphi)^{1/2}]$ Equation 15

$$d_{crit} = C_{li}\,\rho_p^{-1/2}(\cos\varphi)^{-4/3}\left[([V_{HI}/(\cos\varphi)^{X}] - V)/\delta\right] +$$

$$C_{hi}\,\rho_p^{X\rho 22}(\cos\varphi)^{-7/18}\left[(V - [V_{LO}/(\cos\varphi)^{1/2}])/\delta\right]$$

For $V \geq [V_{HI}/(\cos\varphi)^{X}]$ Equation 16

$$d_{crit} = C_H(\cos\varphi)^{-1/2}\,\rho_p^{-1/3}\,V^{-1/3}$$

Where:

V = projectile velocity in km/sec;

d_{crit} = the maximum projectile diameter, in cm, if the shield is predicted to pass at a given impact velocity;

V_{HI} = 8.0, in km/s;

X = -0.2914 for 440C Stainless Steel projectiles; and

= -0.2658 for Aluminum Oxide projectiles;

V_{LO} = 2.7, in km/s;

C_H = 3.642;

C_L = 2.063;

C_{hi} = 1.821 for 440C Stainless Steel projectiles at all impact angles,

= 1.821 for Aluminum Oxide projectiles at 0-degree impact, and

= 1.952 for Aluminum Oxide projectiles at 45-degree impact;

$C_{li} = C_L \cdot V_{LO}^{-2/3}$;

φ = the impact angle in degrees;

ρ_p = projectile density, in g/cm^3;

$X_{\rho 22}$ = the exponent on the 2nd projectile density term in Equation 15, which is equal to (-1/3)

$\delta = [V_{HI}/(\cos\varphi)^{1/3}] - [V_{LO}/(\cos\varphi)^{1/2}]$.

C. MODIFYING THE WHIPPLE SHIELDS

Having now determined the improved BLEs for the Enhanced Stuffed Whipple Shields, it is now appropriate to do the same thing for the U.S. Laboratory Module Whipple Shields. Because the Enhanced Stuffed Whipple and regular Whipple Shield equations differ dramatically in form and content, the same analysis approach used to determine the improved equations for the stuffed shields was not implemented when determining the regular Whipple equations. Having similarly failed to yield meaningful results from MATLAB code loops, hand-drawing "lines of best fit" on the Whipple Shield curves became the new first step in the analytical process. Having done this, new desired values of V_{HI} and V_{LO} were specified for the 0-degree curves. Similarly, desired $V_{hi}(\cos\varphi)^{Xhi}$ and $V_{lo}(\cos\varphi)^{Xlo}$ values for the 45-degree curves were selected. Much like the Enhanced Stuffed Whipple analysis, solutions for X_{lo} and X_{hi} were derived in order to produce the desired minimum point on the BLE curve (separation point between regions one and two of the curve) and maximum point on the BLE curve (separation point between regions two and three of the curve). The equations used to determine the new X_{lo} and X_{hi} are shown below, and the solutions are included in Table 5.

$$V_{LO}/(\cos\varphi)^{Xlo} = V_{LO\_45} \rightarrow X = [\log (V_{LO\_45} / V_{LO})] / \log (\cos(45)) \quad \text{Equation 17}$$

$$V_{HI}/(\cos\varphi)^{Xhi} = V_{HI\_45} \rightarrow X = [\log (V_{HI\_45} / V_{HI})] / \log (\cos(45)) \quad \text{Equation 18}$$

Having now discussed the methodology of solving for coefficients and variables of interest, a specific discussion of the actual values arrived at for the 440C Stainless Steel and Aluminum Oxide candidate equations continues below.

1. 440C Stainless Steel Projectile Cases

For the 440C Stainless Steel Projectiles, there were a total of six candidate equations from which to choose the new, improved ballistic limit equation. All six candidate equations utilized $V_{HI} = 9.5$, a change from the entering value of 7.0. The first three candidate curves all used $V_{LO} = 6.0$, while the other three equations used $V_{LO} = 6.3$. The solutions of Equations 17 and 18 for X_{lo} and X_{hi} are also found in Table 5.

Based upon the "lines of best fit" drawn for each of these six options, the coefficients K_H and K_L had to be modified to yield the desired curve shape, particularly in region two of the BLE curves. Much like the Enhanced Stuffed Whipple Shield case discussed in previous sections of this chapter, there was an interesting relationship that made determining the values of coefficients in region two fairly simple. Recall that for the stuffed shields, C_{li} (#) + C_{hi} (#) was the form of the equation describing region two, where (#) indicated the numerical value produced from the rest of the terms found in Equation 6. The same is true for the Whipple Shields, except that the variables that make up the (#) term are different values and of a different form, coming form Equation 3 instead of Equation 6. C_{li} and C_{hi} were replaced by K_H and K_L. Using the same simple matrix mathematics for solving systems of simultaneous equations utilized in the stuffed shield analysis, the same mathematical computations were copied, this time incorporating the Whipple equation and the coefficients K_H and K_L instead. The equation to be solved was in the form [A][x] = [b], where the matrix [A] was made up of the numerical components of Equation 3. Vector [x] is K_H and K_L. Vector [b] is the desired projectile critical diameters at the specified velocities within region two of the curve. One has the option of choosing only the desired endpoints of the new region two of the curve and solving two equations for two unknowns or one can use every point along the line and

solve many equations for two unknowns. In actual analysis, this second technique of using an over-determined system to get higher fidelity solutions for K_H and K_L was exercised. The simplified matrix Equations are shown below in Equations 19 and 20.

$$[\ \#_{11}\ \#_{12};\ \#_{N1}\ \#_{N2}\ ] \times [K_H;\ K_L] = [d_{crit\_desired}1;\ d_{crit\_desired}N] \qquad \text{Equation 19}$$

$$[\ \#_{11}\ \#_{12};\ \#_{21}\ \#_{22}\ ]^{-1} \times [d_{crit\_desired}1;\ d_{crit\_desired}2] = [K_H;\ K_L] \qquad \text{Equation 20}$$

Solving for the K_H and K_L values in region two, the values were found to be different from the entering values of 1.35 for K_H and 1.8 for K_L. For the 440C Stainless Steel projectile at a 0-degree impact angle, Cases 1 through 6, the desired values of K_H remained 1.35 and the desired value of K_L remained 1.8. However, for the 45-degree case, K_H values became 1.6548, while the K_L values remained 1.8.

2. Aluminum Oxide Projectile Cases

The three Aluminum Oxide cases were solved likewise. For the 0-degree impact cases, the K_H and K_L values remained 1.35 and 1.8 respectively. However, all three Aluminum Oxide projectiles with 45-degree impact cases yielded a desired K_H value of 1.5963. The desired K_L values for the Aluminum Oxide projectiles at 45-degree impact varied for each case, with the desired values being 2.1205 for Case 1, 2.5426 for Case 2 and 2.9081 for Case 3. However, the original values for K_H and K_L still worked for the curve in regions one and three because we wished to duplicate a number of points from the starting BLEs. This meant that the K_H and K_L coefficients in the region two equations had to be scaled without adjusting them in regions one or three. To accomplish this feat, new coefficients, called C_{KH2} and C_{KL2}, were created to scale K_H and K_L in region 2 of the curve. These coefficients were simply inserted into the existing form of the U.S. Laboratory Module Whipple Shield as depicted in Equation 3. The values of these new coefficients were arrived at simply by dividing the new, desired K_H and K_L values by the original values for each projectile and impact angle permutation.

A summary of all of these variables and their new and old values is contained in the Table 5 below. This list of candidate values is far from comprehensive, but it is indicative of several of the best available candidate curves and equations. Of all these values listed, only one of these solutions for each projectile type will become the values used in the new ballistic limit equation for the U.S. Laboratory Module Whipple Shield.

440C Stainless Steel Projectile										
Case	Vhi	Xhi	Vlo	Xlo	KH	KL	C_{KH2_0}	C_{KH2_45}	C_{KL2_0}	C_{KL2_45}
1	9.5	-0.1190	6.0	-0.0477	1.35	1.80	1.00	1.226	1.00	1.00
2	9.5	-0.1190	6.0	-0.2309	1.35	1.80	1.00	1.226	1.00	1.00
3	9.5	-0.1190	6.0	-0.3399	1.35	1.80	1.00	1.226	1.00	1.00
4	9.5	-0.1190	6.3	0.0931	1.35	1.80	1.00	1.226	1.00	1.00
5	9.5	-0.1190	6.3	-0.1505	1.35	1.80	1.00	1.226	1.00	1.00
6	9.5	-0.1190	6.3	-0.1991	1.35	1.80	1.00	1.226	1.00	1.00
Starting BLE	7.0	-1.0000	3.0	-1.5000	1.35	1.80	1.00	1.000	1.00	1.00
Aluminum Oxide Projectile										
Case	Vhi	Xhi	Vlo	Xlo	KH	KL	C_{KH2_0}	C_{KH2_45}	C_{KL2_0}	C_{KL2_45}
1	9.0	-0.2750	3.0	-1.8266	1.35	1.80	1.00	1.182	1.00	1.178
2	9.0	-0.2750	3.0	-2.1862	1.35	1.80	1.00	1.182	1.00	1.413
3	9.0	-0.2750	3.0	-2.4448	1.35	1.80	1.00	1.182	1.00	1.616
Starting BLE	7.0	-1.0000	3.0	-1.5000	1.35	1.80	1.00	1.000	1.00	1.000

Table 5. Summary of Candidate BLE New Coefficient and Variable Values for U.S. Laboratory Module Whipple Shields.

3. Improved Ballistic Limit Equations for the U.S. Laboratory Module Whipple Shield

The six permutations of candidate BLEs for the 440C Stainless Steel projectile at 0-degree impact angle are shown in the two figures below. For all six cases, the 0-degree candidate curves are very nearly identical. Cases 1 through 3, those where V_{LO} = 6.0, are exactly identical. Cases 4 through 6 are exactly identical as well, each having V_{LO} = 6.3. Each of the six candidate curves accurately contains all of the raw data points

collected in the density effects test series. For all six trials, the curve is well below the lowest of the failure points, corresponding to a velocity of approximately 6.8 kilometers per second, from the density effects test series. Theoretically, these BLEs could be further modified to raise the curve in this region, but is not done so here. The reasons for this are two fold. First, no tests at lower velocities, those in region 1, were conducted in the density effects test series. Therefore, dramatically shifting the curve in this region without test data to justify doing so could reduce the fidelity of the ballistic performance predictions. Secondly, a dramatic shift here will also cause a dramatic shift in the 45-degree curves, which may not be a benefit. So, these plots will remain as they are presently shown.

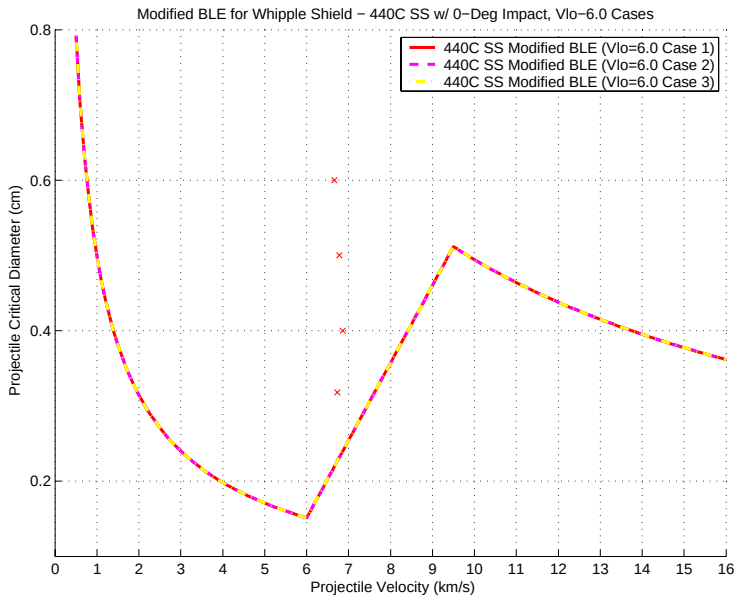

Figure 28. Overlay of Candidate BLEs (Cases 1 through 3) and Density Effects Raw Data for 440C Stainless Steel Projectile Impacting U.S. Laboratory Module Whipple Shield at 0-degree Impact Angle.

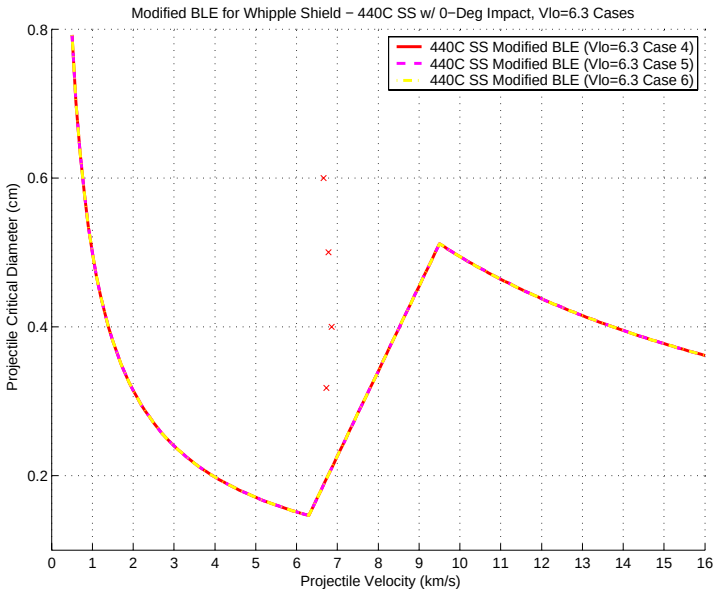

Figure 29. Overlay of Candidate BLEs (Cases 4 through 6) and Density Effects Raw Data for 440C Stainless Steel Projectile Impacting U.S. Laboratory Module Whipple Shield at 0-degree Impact Angle.

The six permutations of candidate BLEs for the 440C Stainless Steel projectile at a 45-degree impact angle are shown in the two figures below. For all six cases, the 45-degree candidate curves are not identical. Cases 1 through 3, those where V_{LO} = 6.0, have minimum points (the point separating region one from region two) at velocities of 6.1, 6.5 and 6.75 kilometers per second respectively. Cases 4 through 6, for V_{LO} = 6.3 also have minimum points (the point separating region one from region two) at velocities of 6.1, 6.5 and 6.75 kilometers per second respectively. Each of the six candidate curves accurately contains all of the raw data points collected in the density effects test series. By visual inspection, one can tell the cases for which the minimum point is located at 6.1 kilometers per second possess the most area under the curve of the three minimum point options (6.1, 6.5 and 6.75 kilometers per second). Consequently, Cases 1 or 4 would both work equally well and produce nearly identical curves if chosen to replace the starting BLEs.

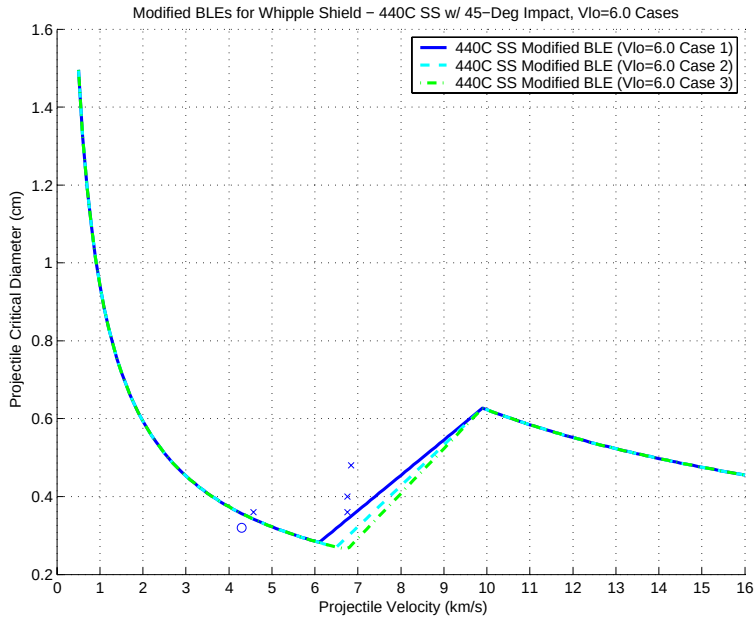

Figure 30. Overlay of Candidate BLEs (Cases 1 through 3) and Density Effects Raw Data for 440C Stainless Steel Projectile Impacting U.S. Laboratory Module Whipple Shield at 45-degree Impact Angle.

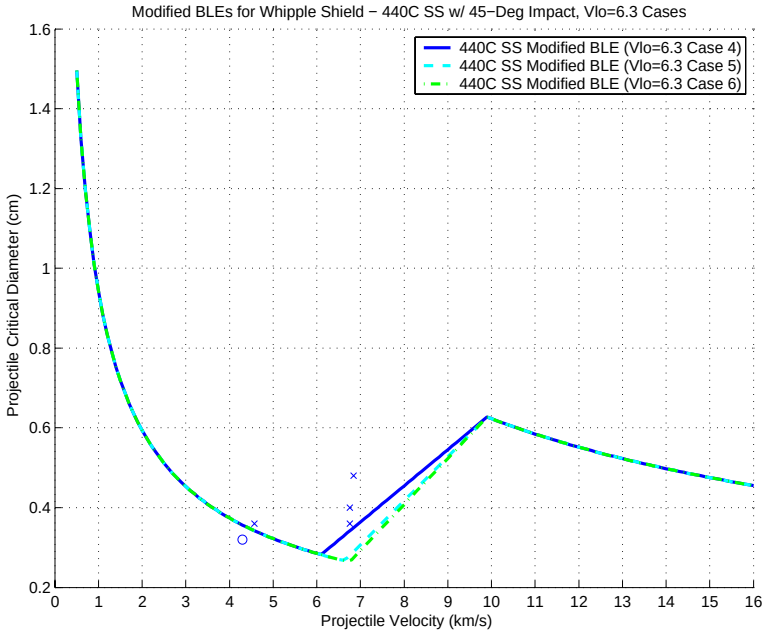

Figure 31. Overlay of Candidate BLEs (Cases 4 through 6) and Density Effects Raw Data for 440C Stainless Steel Projectile Impacting U.S. Laboratory Module Whipple Shield at 45-degree Impact Angle.

Having determined which candidate equations most accurately contain the raw data from the density effects test series, the entering ballistic limit equations were next compared with the candidate equations to determine which choice requires the least reduction in area under the curve.

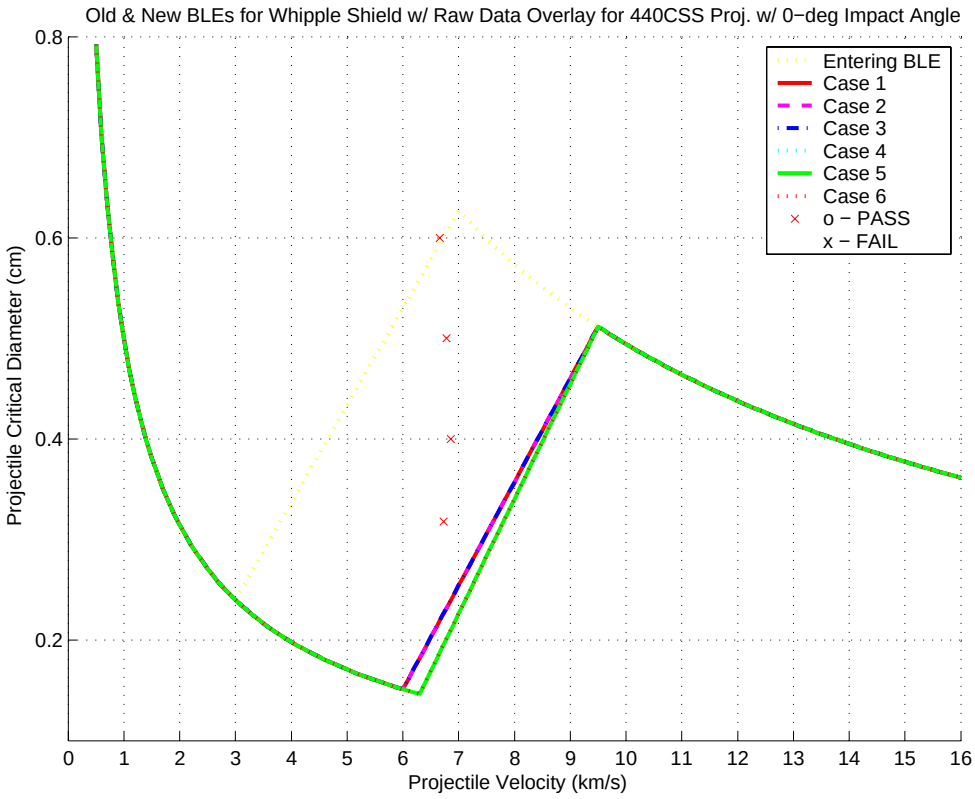

Figure 32. Overlay of Original and Candidate BLEs (Cases 1 through 6) for 440C Stainless Steel Projectile Impacting U.S. Laboratory Module Whipple Shield at 0-degree Impact Angle.

In the figure directly above, the dotted (yellow) curve represents the original BLE. All six trials for the 440C Stainless Steel projectile at 0-degree impact are very nearly identical. However, Cases 1 through 3, those with $V_{LO} = 6.0$ are slightly better in terms of maximizing the area under the curve.

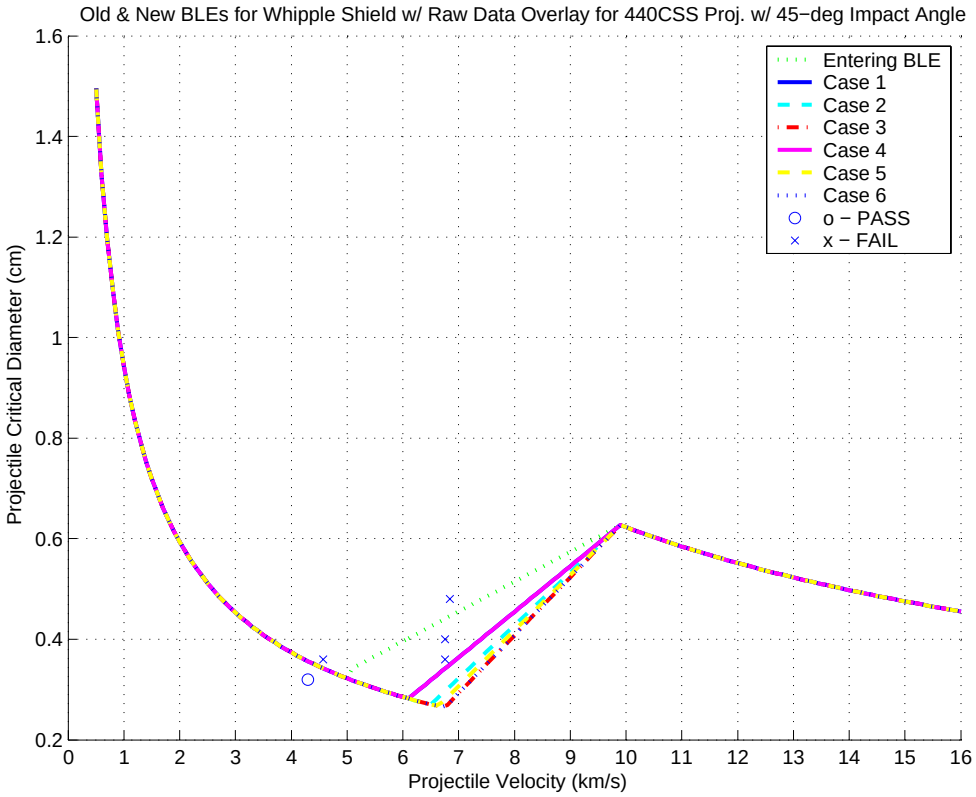

Figure 33. Overlay of Original and Candidate BLEs (Cases 1 through 6) for 440C Stainless Steel Projectile Impacting U.S. Laboratory Module Whipple Shield at 45-degree Impact Angle.

For the 45-degree impact condition of the 440C Stainless Steel projectile on the Whipple Shield, the dotted (green) line represents the entering BLE. Of the six curves shown, Case 4, the solid (magenta) line leaves the most area under the curve. Based upon the 0-degree plot, Case 1 should be the choice as the new, improved ballistic limit curve, however, the 45-degree plot shows that Case 4 should be chosen. Case 4 will be implemented as the selected equation because it leads to a relatively noticeable improvement in area under the curve in the 45-degree plot, while it is only slightly worse than Case 1 in the 0-degree plot.

The Whipple Shields for the Aluminum Oxide projectiles were next analyzed to determine the best choice for the new BLE. There were only three candidate equations to replace the entering ballistic limit equations for this category.

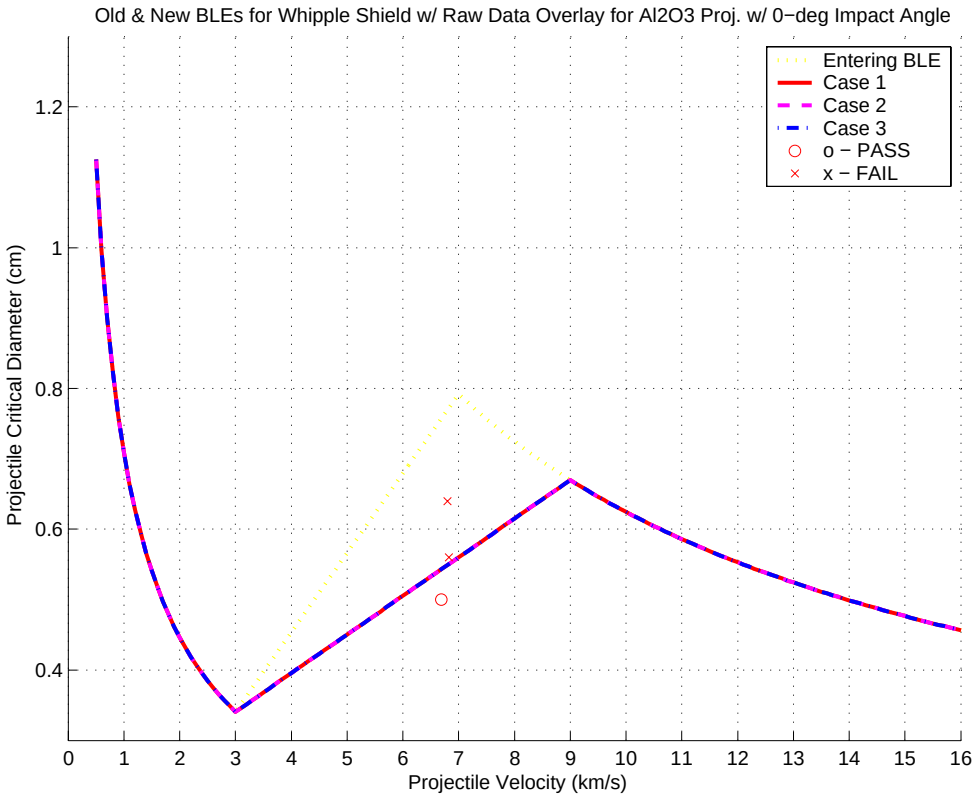

Figure 34. Overlay of Starting BLEs, Candidate BLEs (Cases 1 through 3) and Density Effects Raw Data for Aluminum Oxide Projectile Impacting U.S. Laboratory Module Whipple Shield at 0-degree Impact Angle.

The dotted (yellow) line is the entering equation, which does not adequately predict failures or successes by the shield when impacted by hypervelocity projectiles. Note that Cases 1, 2, and 3 all produce identical curves and accurately predict all the density effects test series data points. Based upon these 0-degree curves, any of the three cases would work equally well. Consequently, the 45-degree curves will be the determining factor when choosing which ballistic limit curve will be implemented as the improved BLE.

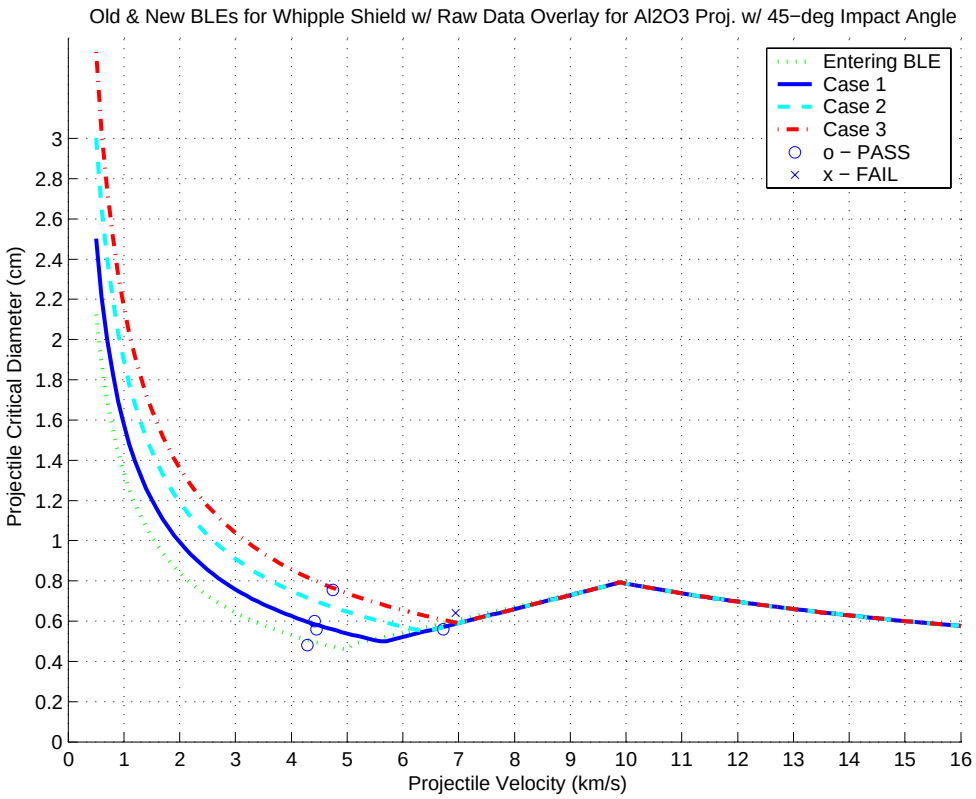

Figure 35. Overlay of Starting BLEs, Candidate BLEs (Cases 1 through 3) and Density Effects Raw Data for Aluminum Oxide Projectile Impacting U.S. Laboratory Module Whipple Shield at 45-degree Impact Angle.

Unlike the 0-degree impact plot above, all three cases yield different curves. Each case represents an improvement over the entering BLE, the dotted (green) curve. Only Case 3 accurately predicts all the density effects test series data points. In terms of accuracy and maximizing the under-curve area, it is the clear choice as the improved ballistic limit curve for Aluminum Oxide projectiles striking the U.S. Laboratory Module Whipple Shields. One significant thing to note about these candidate curves is that, while regions two and three share many points with the original BLE, region one is significantly different. In order to ensure that the outputted point separating region one from region two was the point desired, the exponent on the projectile density term in region one of the curve had to be adjusted so that the endpoint of region one matched up with the old curve's data point at the particular velocity of interest in region two.

Solving the following equation for $X_{\rho 1}$, the exponent of the projectile density in region one, one is able to update the value from the –½ value found in the starting BLE, Equation 2.

$$X_{\rho 1} = \log\left(d_{crit\_desired} / \left[K_L\left(t_{rw}(\sigma_Y/40)^{1/2} + C_L t_b \rho_b\right)(\cos\varphi)^{-11/6}\, V^{-2/3}\right]\right) / \log\left(\rho_p\right)$$

Equation 21

For Cases 1 through 3 respectively, the value of this exponent is -0.3796, -0.2452 and -0.1475. The determination of this exponent value was not required for the 0-degree cases for either projectile type, nor was it required for the 45-degree cases for the 440C Stainless Steel projectile cases. This was because the first region of the curve shifted as necessary through the changes to V_{LO} and K_L alone. Hence, no modification to the density exponents was required. The same is true for all projectile types and impact angles in region three. Region three was not altered noticeably from the old BLE data points, therefore no exponents had to be adjusted.

Based upon the selection of Case 4 for the 440C Stainless Steel projectile new BLE and the choice of Case 3 for the Aluminum Oxide projectile new BLE, the U.S. Laboratory Module Whipple Shields from Equations 2, 3, and 4 are amended in Equations 22, 23 and 24. The form of the Whipple equation was changed slightly to incorporate this multiplying coefficient that attaches itself to the K_H and K_L terms in Equation 3, C_{KH2} and C_{KL2}. Otherwise, the equations themselves underwent no further changes other than the numerical values assigned to V_{HI}, V_{LO}, X_{hi} and X_{lo}, which were updated. These changes appear in the modified ballistic limit equations that follow:

For $V \le V_{lo}(\cos\varphi)^{Xlo}$ Equation 22

$$d_{crit} = K_L\left(t_{rw}(\sigma_Y/40)^{1/2} + C_L t_b \rho_b\right)(\cos\varphi)^{-11/6}\, \rho_p^{-1/2}\, V^{-2/3}$$

For $V_{lo}(\cos\varphi)^{Xlo} < V < V_{hi}(\cos\varphi)^{Xhi}$ Equation 23

$$d_{crit} = \left[C_{KH2}\, K_H\, V_{hi}^{-2/3} \rho_p^{-1/3}\, \rho_b^{-1/9}\, S^{1/2}(t_{rw}\, \rho_{rw})^{2/3}(\sigma_Y/70)^{1/3}\right] x$$

$$\left[(V - V_{lo}(\cos\varphi)^{Xlo})/(V_{hi}(\cos\varphi)^{Xhi} - V_{lo}(\cos\varphi)^{Xlo})\right] +$$

$$C_{KL2}\, K_L\, V_{lo}^{-2/3}\left(t_{rw}(\sigma_Y/40)^{1/2} + C_L\, t_b\, \rho_b\right)\rho_p^{-1/2}(\cos\varphi)^{(-11/6 - 2/3\cdot Xlo)} x$$

$$\left[(V_{hi}(\cos\varphi)^{Xhi} - V)/(V_{hi}(\cos\varphi)^{Xhi} - V_{lo}(\cos\varphi)^{Xlo})\right]$$

For $V \geq V_{hi}(\cos\varphi)^{Xhi}$ Equation 24

$$d_{crit} = K_H\, \rho_p^{-1/3}\, \rho_b^{-1/9}(V\, \cos\varphi^{-2/3}\, S^{1/2}(t_{rw}\, \rho_{rw})^{2/3}(\sigma_Y/70)^{1/3}$$

Where:

V = projectile velocity in km/s;

d_{crit} = the maximum projectile diameter, in cm, if the shield is predicted to pass at a given impact velocity;

V_{hi} = 9.5, in km/s for the 440C Stainless Steel projectile cases and

= 9.0, in km/s for the Aluminum Oxide projectile cases;

V_{lo} = 6.3, in km/s for the 440C Stainless Steel projectile cases and

= 3.0, in km/s for the Aluminum Oxide projectile cases;

X_{lo} = -0.0930 for 440C Stainless Steel projectiles and

= -2.4448 for Aluminum Oxide projectiles;

X_{hi} = -0.1190 for 440C Stainless Steel projectiles and

= -0.2750 for Aluminum Oxide projectiles;

$K_L = 1.8$;

$K_H = 1.35$ unless $\left[t_b/(t_{rw}^{2/3}S^{1/3})\right] < 0.126$. In this case, it equals

$\left[7.451\ t_b/(t_{rw}^{2/3}S^{1/3})\right]+0.411$;

C_{KH2} = 1.000 for 0-degree impacts by all projectiles,

= 1.226 for 45-degree impacts by 440C Stainless Steel projectiles, and

= 1.182 for 45-degree impacts by Aluminum Oxide projectiles;

C_{KL2} = 1.000 for 0-degree impacts by all projectiles,

= 1.000 for 45-degree impacts by 440C Stainless Steel projectiles, and

= 1.616 for 45-degree impacts by Aluminum Oxide projectiles;

$C_L = 0.37$, in cm^3/g;

S = the standoff distance in cm, between the rear wall and bumper plate;

φ = the impact angle in degrees;

σ_Y = yield strength, in ksi, of the rear wall plate;

t_{rw} = rear wall plate thickness in cm;

t_b = bumper plate thickness in cm;

ρ_{rw} = rear wall plate density, in g/cm^3;

ρ_b = bumper plate density, in g/cm^3;

ρ_p = projectile density, in g/cm^3; and

$X_{\rho 1}$ = exponent on the projectile density term in region 1.

THIS PAGE INTENTIONALLY LEFT BLANK

VI. PROPOSED ALTERNATE SHIELD MATERIALS AND CONFIGURATIONS

A. BACKGROUND AND SCOPE OF ANALYSIS

Requirements of effective bumper and rear wall materials were mentioned in Chapter II while explaining the hypervelocity impact phenomena. In this chapter, there will be a greater explanation of the desirable characteristics that bumper materials, rear walls, and various shield configurations possess. It should be said, however, that a complete discussion of these characteristics will not be recreated here. Instead, one should consult NASA JSC HITF's publication, *Meteoroid/ Debris Shielding, TP-2003-210788*, by Dr. Eric Christiansen (Ref 10). This is an excellent reference for a full discussion of not only the mechanical, but also the thermal properties of various materials considered previously for implementation into the ISS shielding program. The goal of this chapter is merely to examine the analytical results of applying the properties of alternate shield materials and configurations into the ballistic limit equations derived in Chapter V, Data Analysis. The complete discussion of desirable material properties is therefore somewhat limited here, although a thumbnail description will be presented.

B. ENTERING ASSUMPTION AND ANALYTICAL METHODOLOGY

For the purposes of this preliminary study into feasible, alternate shield materials and configurations, the depth of analysis was limited to those values that directly link into the ballistic limit equations and those properties which are used to determine the coefficients of the BLEs. Thermal properties like melting temperature and many others that are discussed in Dr. Christiansen's publication (Ref 10, pp27-31) were therefore ignored at this time. Instead, the focus was placed on only the properties that seemed to have a direct link to shield performance within the BLEs themselves. Once the results of varying these values from the initial U.S. Laboratory Module material property values in the rear wall and bumper shields plus the standoff distance and shield thickness were

analyzed, recommendations of some promising alternate configurations for further analysis and testing could be made. At this point, one could expect to look closely at the thermal and mechanical properties of the alternate materials that don't appear directly in the BLEs, but that have a major effect on actual shield performance to determine if the recommendations as to shield material and configuration made herein are worth exploring in ground tests at White Sands.

C. CANDIDATE ALTERNATE MATERIALS AND CONFIGURATIONS

There are six basic variables in the BLEs that can be examined – shield standoff distance, bumper density, bumper thickness, rear wall density, rear wall yield strength, and rear wall thickness. Each of these terms appears directly in the ballistic limit equations or is a term in an equation used to compute the value of a coefficient in the BLE. In actuality, there are five categories that comprise these six values, namely because altering the rear wall material will account for both the density and yield strength terms. Using the newly derived BLEs from Chapter V, the results of varying the bumper thickness, rear wall thickness, and standoff distance were examined. Additionally, several alternate material choices for bumper material and rear wall material were analytically examined. For ease, only one parameter was varied from the entering shield configuration at a time. This provided a rough idea of what changes would occur in the BLEs based upon varying a single parameter. These results were computed for both shield types (Whipple and Enhanced Stuffed Whipple), at each angle of impact, for both projectile materials, 440C Stainless Steel and Aluminum Oxide. The results of these trials are shown in Appendix L and are discussed in the paragraphs below.

1. Alternate Shield Spacing

From Chapter II, it is known that increased standoff distance between the stages of the shield has a positive effect on the rear wall's ability to resist penetration and detached spalling. This is because the ejecta and debris resulting from the projectile impact with the bumper is dispersed radially outward in an expanding cone. Given more distance for the conical section to expand, the ejecta and debris will lose momentum. This allows the Nextel, Kevlar, and rear wall to absorb the force of impact with less potent force, over more of its area. Theoretically, an infinite, or at least a very large, standoff distance is ideal. In general, a standoff of fifteen to thirty times the projectile size is optimum for real world systems.

However there are imitations that preclude such a configuration from actually being implemented. Primarily, the limitation is one of module volume. If the ISS module has too large a diameter, it will not fit within the shuttle bay of the Space Shuttle, nor on conventional payload fairings for existing launch vehicles. Consequently, the limiting factor in standoff distance allowable is the diameter of the launch vehicle payload storage area.

The added structural mass needed for spacers to increase standoff distance is also a consideration. Not only does the raw material, the spacer, cost money, but any added mass in the shields will affect the launch mass and hence launch costs. With launches costing approximately $10,000 - $30,000 per kilogram, an increase in the standoff distance would most likely also increase launch costs.

Finally, the inability to alter the standoff distance on orbit via spacewalk precludes us from changing the standoff distance between stages of shields already on orbit. According to Captain Daniel Bursch, United States Navy, a NASA astronaut and

former crewmember of the ISS, any new shield and stage design with an increased standoff distance would need to incorporate new hand holds. With the present design, the hand holds used during extra-vehicular activity (EVA) are just beyond (above) the current shields. Any such changes to standoff distances would therefore best be made on the ground. Future modules could be modified to allow on-orbit access. Such modifications would allow the astronauts to replace shielding to improve performance or to repair damage caused by hypervelocity impacts by micrometeoroids or space debris. This on-orbit accessibility is desirable, but may not be an acceptable solution due to the added cost of or delays in launching newer elements of the space station with this modularity.

With these factors in mind, alternate spacing trials were conducted using relatively small increases in standoff distance. The present U.S. Laboratory Module separation distance was compared with trials for standoff values from four to eight inches. As was expected, the greater standoff distance produced ballistic limit curve which were greater than the entering values found using the improved ballistic limit equations, Equations 14 through 16 and 22 through 24. The four inch standoff distance was less than the present U.S. Laboratory Module configuration and yielded an inferior, lower ballistic limit curve. The other trial produced increasingly superior results, higher predictive curves, as the standoff distance increased. This trend was true for both shield types, both projectiles and both impact angles, and can be observed in Appendix L, Figures L1 through L8.

The changes in the ballistic limit curves were only evident in regions two and three of the curve. Region one remained the same as the baseline configuration results. This is explained by the fact that, in the first velocity regime, the projectile remains largely intact after impacting the bumper and continues to penetrate in its intact form, no matter what the separation distance between the bumper and rear wall. In the higher

velocity regimes, the projectile breaks up more upon impact and therefore disperses in the radially expanding cone previously discussed.

2. Alternate Bumper Thickness

In Chapter II, ideal characteristics of bumper were discussed. In that discussion, one learns that the bumper must be sufficiently thick that it can shock the projectile sufficiently as it penetrates through the shield thickness. NASA's design goal therefore is to pick the ideal thickness to allow this hydrodynamic shock process to occur, but to minimize the amount of shield material that is added to the debris cloud as it is ejected out the back face of the bumper. Because there is an attempt to find a "sweet spot" that is the ideal bumper thickness, a number of thicknesses were chosen as trial values, including one thinner bumper and five thicker bumpers. The following bumper thicknesses were tested against the entering value of 0.08 inches: 0.04, 0.10, 0.12, 0.16, 0.20, and 0.24 inches respectively.

Substituting these values into the bumper thickness and associated terms in Equations 14 through 16 and Equations 22 through 24, one finds that the thinner bumper plate yields lower ballistic limits. This shows that thinner plates do not possess enough distance through which the projectile can travel to be shocked into smaller, less energetic particles. Therefore, one certainly does not want to reduce the bumper to less than the initial value of 0.08 inches plate thickness.

The trials in which bumper thickness was increased predict higher ballistic limits in regions one and two of the curves, but retain the same ballistic limits in region 3, the melt/ vaporization region. These results are consistent for both shield types, impact angles, and projectile materials. This result stems from the fact that, at the highest impact velocities, the projectile will undergo a phase change to liquid or liquid/ solid as a result of the shock waves and hydrodynamic pressure resulting from the projectile's striking the

bumper. With a sufficient minimum thickness to generate these shock pressures, any additional plate thickness is overkill, as the projectile will already have been liquefied. In regions one and two of the curve, some or all of the projectile pieces will remain in solid phase because sufficient shock pressure has not been produced to completely liquefy the particles. Consequently, a thicker plate may yield better results, as there is more distance through which the projectile can travel in order to generate higher shocks and to cause projectile breakup. This added distance may allow the projectile to break into many, smaller, less energetic pieces which spread radially outward in the debris cloud. Based upon the resultant curves shown in Appendix L, Figures L9 through L16, a thicker bumper is better.

However, there is the risk that the added thickness will also produce more bumper material in the debris cloud. While this may be mitigated against by choice of bumper material, there remains some doubt as to whether these predicted curves are accurate or not. It remains to be seen if more ductile or more brittle materials are preferable. Although there is uncertainty in choosing an "ideal" bumper thickness, one thing is certain. Any increase in bumper thickness will necessitate additional mass added to the shield. Over a single 12-inch by 12-inch test plate, this may be fairly minimal, but spread over an entire ISS module, these mass increases can add up quickly and affect other things like launch costs and booster selection for launch vehicles other than the space shuttle. Additionally, on-orbit replacement of the bumper remains difficult, though not necessarily impossible. It does, however, pose a limitation to on-orbit replacements and repairs. Tentatively, though, initial analysis shows that thicker plates produce better results. Thus, ground tests may specify the use of thicker plates and eventual implementation on the ISS modules not yet flying.

3. Alternate Rear Wall Thickness

Unlike the bumper plate, where hydrodynamic shock and debris cloud contents are major issues to be considered, the rear wall thickness is actually a simpler problem. The rear wall must simply stop debris that strikes it without fracturing or causing detached spall on its own back face, the interior wall of the U.S. Laboratory Module. Consequently, the most desirable properties of the rear wall are its yield strength and ductility. However, increasing the wall's thickness is, in itself a viable means of improving the shield's performance. A greater thickness provides more material through which any debris must pass to penetrate into the hull of the ISS. There are therefore more chemical bonds that penetrating debris must break in order to make its way through the material. Breaking these bonds requires the debris to expend a large portion of its kinetic energy and lose its own momentum as it penetrates. If the rear wall material is also ductile, it can elongate while absorbing the debris' kinetic energy without actually fracturing. In conjunction with the ductility and yield strength, the thickness (distance of travel) allows the shock wave and its associated energy produced by the impact to dissipate and to not propagate all the way through the rear wall thickness to the back face, reducing the probability of detached spall occurring.

One would therefore assume that an increased rear wall thickness would show higher ballistic limits in all regions of the curve. One would also presume that this would hold true for any projectile type, both shield types, and either impact angle. Appendix L, Figures 17 through 24 shows the results of the trials for each case. Six ballistic curves were produced, corresponding to six rear wall thickness trials. These were compared with the baseline thickness of 0.19 inches. The following thicknesses were used: 0.15, 0.22, 0.25, 0.275, 0.30, and 0.39 inches.

In the case of a rear wall thickness of 0.15 inches, the curve was predictably lower than the baseline value of 0.19 inches. Conversely, the increasing rear wall thicknesses

lead to increasing ballistic limits in all three regions of the curves, with increasingly better results as plate thickness increased. This held for all cases, as was presumed. In theory, the thicker the shield, the better the stopping power and performance, however, this idea completely disregards mass restrictions and limitations. Instead, in choosing an alternate shield configuration, one must balance the performance of the shield versus the shield mass, material cost, and volume. The same lack of capability for on-orbit replacement of flying shields exists in the case of the rear wall as well, as the rear wall and hull of the U.S. Laboratory Module are the same thing. Any attempt to replace the shield rear wall in orbit would automatically cause a breach of the pressure hull and expose the module to the risk of an unprotected impact from debris or micrometeoroids. Still, it seems obviously clear that increasing the rear wall thickness is a feasible and viable option to improving shield performance if the accompanying increase in mass expense can be absorbed by the program.

4. Alternate Bumper Material Selection

Perhaps a better option than increasing the mass and thickness of the bumper is to choose an alternate, superior performing material. One would look at candidate materials that may be less dense, hence lighter weight, yet have better performance characteristics, to include higher yield strengths. The ideal bumper material characteristics are well understood and are discussed at length in Section 3 of *Meteoroid/ Debris Shielding*. NASA found that Aluminum Oxide, followed by Silicon Carbide, followed by Aluminum 6061 T6 alloy are the best bumper materials based upon the eight materials they ranked for aluminum projectiles. These results were obtained and ranked using an analytical model, based upon the highest impact pressure with bumpers of adequate thickness to shock the projectile completely (Ref 10, p29). However, these material choices don't account for other projectile types, of which steel and aluminum oxide are common types in orbit, and especially in the density effects test series. They also don't consider material thickness (hence mass and volume) or cost in the ranking. NASA also evaluated bumper materials using a figure of merit (FOM) made up of a

number of material properties including density, latent heat of fusion, melting temperature, the heat of vaporization, and the vaporization temperature. It also included the material's Brinell hardness number, speed of sound in the material, and the modulus of elasticity. The materials with the greatest figures of merit are expected to perform better a bumper. Based upon NASA's analysis of various materials, a Magnesium alloy, Tin, Lead, Cadmium, and Aluminum alloys are the top performing bumper materials, while Steel, Iron, Copper, Nickel, and Titanium are inferior (Ref 10, p30).

As a consequence of these widely different and incomplete results, more candidate bumper materials were added to the existing list from NASA in order to determine if a better, or more viable option exists than the present Aluminum 6061 T6 alloy flown on the U.S. Laboratory Module Whipple and Enhanced Stuffed Whipple Shields. With the hundreds of alloys and materials available, it was quite impossible to compile a comprehensive list of candidate materials to analyze. Instead, both NASA test data sets were compared. Only the Aluminum alloy was ranked favorably in both NASA data tables. Thus, a list of candidate materials that was primarily composed of Aluminum alloys, although ones that were less dense, but possessing greater yield strength than the baseline Aluminum 6061 T6 alloy, was created. Another reason Aluminum alloys were the ones chosen was that many of the other superior performing metals listed by NASA are significantly denser, hence heavier, plus Aluminum alloys are readily available on the commercial market at reasonable prices. The added mass and raw material costs of alternate bumper metals versus the performance improvements over Aluminum alloys they may provide was not a viable tradeoff, hence the decision to investigate only other Aluminum alloys as candidates to replace the existing bumper material on new ISS modules. The materials listed in Appendix K, Table K1 represent the total list of candidate Aluminum alloys considered. That list was pared down to six choices to test. Those materials selected for analysis and their basic material properties that are directly reflected in the ballistic limit equations are found in Table 6.

Candidate Aluminum Alloy Materials		
Bumper Material	**Density (g/cm^3)**	**Yield Strength (ksi)**
Al 2024 T351	2.770	47
Al 6061 T6	**2.713**	**40**
Al 6061 T91	2.699	57.3
Al 6061 T913	2.699	66
Al 6066 T6	2.721	52
Al 6070 T6	2.710	51
Al 6262 T9	2.721	55

Table 6. Aluminum Alloys used as Trial Bumper Materials.

Substituting these material's values into the improved BLEs, Equations 14 through 16 and 22 through 24, for each projectile type, at each impact angle, for both shield types, yields the curves shown in Appendix L, Figures L25 through L32. Because the BLEs only use the bumper density value directly within the equation, one would expect that the results for varying the bumper materials would not differ greatly from the baseline configuration using Aluminum 6061 T6 because the various Aluminum alloys all have nearly the same density, ranging from 2.699 to 2.770 grams per cubic centimeter. The Whipple Shield cases for both projectile types at both impact angles prove this supposition, producing curves which overlay the baseline ballistic limit curve nearly perfectly. This is due to the similarity in material density and the fact that only the density material term will change in the equations. Neither other values nor coefficients are affected by changes in bumper material density.

The Stuffed Whipple cases, on the other hand, show a somewhat different result. Region three of the curve, the melt/ vaporization region is identical to the baseline curves. However, the curves in regions one and two are slightly higher than the baseline curve. This can be explained by simply examining the Enhanced Stuffed Whipple Shield BLEs. While the bumper density term does not appear explicitly in the equations, it does comprise one of the factors in the equation the computes the coefficient, C_L. C_L is a value used in the equation that determines another coefficient, C_{li}. Each of these terms do

appear explicitly in the Enhanced Stuffed Whipple Shield ballistic limit equation, specifically in Equations 22 and 23, regions one and two of the curve, but not in Equation 24, region three. This explains the identical results in the higher velocity regime, yet the differences in regions one and two. While the baseline curve is lower in regions one and two than any of the trial equations, which are all virtually identical, there is little improvement noted by changing the materials. One can therefore conclude that there is no performance advantage to changing the bumper materials to one of the six candidates tested here. However, there may be a mass savings by incorporating one of these other materials and that can lead to a slight savings in mass. However, with the small deviation in densities, even this savings may be so minor that the costs of implementing the new configuration far outweigh the benefit of making any change to the existing topology.

5. Alternate Rear Wall Material Selection

Unlike the alternate bumper material selection, which proved to be unnecessary, the substitution of an alternative rear wall material can be beneficial. As mentioned in the discussion of rear wall thickness, two properties of the rear wall play directly into the BLEs, the yield strength and the density. There are thus three options for improving the shield performance by changing the rear wall material. One can select a shield that is less dense (hence lighter weight) and has equal yield strength. Performance should remain the same, but there will be a mass savings. Conversely, one can select an equally dense shield to the baseline Aluminum 2219 T87 rear wall that has greater yield strength than the 58 ksi of the Aluminum 2219 T87. This will improve performance, but not lead to any mass savings. Finally, and most efficiently, one can select a less dense material with greater yield strength. This third option will save mass while simultaneously improving shield performance. Candidate Aluminum alloy materials were chosen with an eye to following this third option. A complete listing of these materials and their associated properties is found in Appendix K, Table K2. Table 7 includes the six trial materials selected to be analyzed using the improved ballistic limit equations of Chapter V.

Candidate Aluminum Alloy Materials		
Rear Wall Material	**Density (g/cm^3)**	**Yield Strength (ksi)**
Al 2219 T87	**2.851**	**58**
Al 6061 T913	2.699	66
Al 7001 T75	2.851	71.8
Al 7050 T7451	2.823	68
Al 7075 T6	2.823	73
Al 7175 T6	2.823	78
Al 7175 T66	2.796	75.4

Table 7. Candidate Aluminum Alloys to Replace the Current U.S. Laboratory Module Rear Wall Material.

Substituting these values for the baseline values of the 2219 T87 Aluminum (58 ksi yield strength and 2.851 grams per cubic centimeter density) into each category of equations, some interesting results emerged. The plots of these trials can be found in Appendix L, Figures L33 through L40.

The results weren't as clear cut as expected. The supposition that less dense, stronger materials would be best generally held true, but not universally so. Overall, the Aluminum 7175 T6 material yielded the highest ballistic limit curves. For the Whipple Shields struck by Aluminum Oxide projectiles at all impact angles, it was the highest curve in all three regions of the plot. The same was true for the 440C Stainless Steel projectile cases for the Whipple Shield.

The Enhanced Stuffed Whipple Shield plots, on the other hand, told a different story. For the shields struck by an Aluminum Oxide projectile, the Aluminum 7175 T6 yielded the highest ballistic limit curve in region one and the first half of region two. Beyond that point though, the baseline curve yielded the best results in the later part of region two and all of region three of the curve. This was true at all impact angles. The 440C Stainless Steel projectile cases were seemingly inconsistent. For the 0-degree

impact cases, the Aluminum 7175 T6 was the superior material choice through all three regions of the ballistic limit curve. However, for the 45-degree cases, the Aluminum 7175 T6 was the best choice in regions one and two of the curve, but not in region three. In region three, the baseline material, Aluminum 2219 T87 was the ideal choice.

The reasons for these seemingly inconsistent results come from the fact that changing the rear wall material alters a number of parameters in the BLEs used. The Whipple Equations, Equations 14 through 16, have direct inputs of yield strength and density. There are no other variables or coefficients in the Whipple equations in which these values are used. Since the equations use a combination of these terms in the complex BLEs, it is not unexpected that an optimized combination of values must exist. It just so happens that in most cases, the Aluminum 7175 T6 is the best choice of those materials analyzed, but in other cases, the baseline Aluminum 2219 T87 reigned supreme. For the Enhanced Stuffed Whipple cases, the yield strength and density do not figure into the Equation 22 through 24 BLEs explicitly, however, they are components of the equations that determine the calculated values of C_H and C_L, which are subsequently used to compute the values of C_{li} and C_{hi}. These four coefficients appear in each of the three BLEs that make up the overall ballistic limit equations for Enhanced Stuffed Whipple Shields on the U.S. Laboratory Module. Much like the Whipple Shield case above, the Enhanced Stuffed Whipple Shield case must also have an optimized combination of rear wall material yield strength and density. The Aluminum 7175 T6 is the best solution in most cases, with some instances where the original Aluminum 2219 T87 is the better choice.

D. RECOMMENDED ALTERNATE SHIELDING MATERIALS AND CONFIGURATIONS FOR FURTHER TESTING

Once an understanding of the effects of varying individual parameters was ascertained, a combination of changes for all five categories was chosen for analysis. The supposition was that if one parameter change is good for shield performance, then multiple changes must be better. As will be seen below, this proved to be true. While there are literally thousands of permutations based upon the seven trials for each parameter, only one combination was chosen for further analysis in this report. This was done mainly to limit follow-on research and ground testing to more ideal alternatives to the present U.S. Laboratory Module shields. Besides improved shield performance, several other factors had to be considered. These include mass limitations, cost limitations, and volumetric limitations. While most of these limitations already figured into the choices of trial values above, they were considered again now, in the context of integration of all the parameters to vary.

Based on the results of the individual parameter variation trials for each of the five categories - standoff distance, bumper thickness, rear wall thickness, bumper material selection, and rear wall material selection, some decisions were made as to which combination of changes are worth testing on the ground to see if they can be used to improve shield performance without substantially increasing mass, volume and cost.

While increasing the standoff distance would yield the most immediate improvements in shield performance, one is limited to small increases, or else one will exceed the limits of the payload fairings and shuttle bay that will carry the modules to orbit. Consequently, a change from 4.5 inches to 6.0 inches standoff was examined. Even this small change improves shield performance measurably, without inducing too much extra cost in terms of added structural mass and launch mass related costs. It also changes the module diameter by a total three inches only. This small change should not

affect the ability to launch the modules in existing launch vehicles with existing payload fairings.

The results of the bumper thickness trials show that increasing the bumper thickness should lead to improved performance. However, the slight improvements in shield performance are outweighed by the costs associated with the additional mass, as well as the uncertainty related to the extra shield debris that can be produced upon impact and expelled into the rear wall as part of the debris cloud. To reduce uncertainty and save cost, the bumper thickness should remain at 0.08 inches. No reduction in thickness is recommended due to the shield performance's predicted limits being less than those of the baseline configuration.

Along this same line, the bumper material should not be changed. Because each of the Aluminum alloy candidates have a nearly equal density to the Aluminum 6061 T6 baseline, there is no real advantage in switching materials, particularly because the other material properties of interest, heat of vaporization, heat of fusion, speed of sound in the material, etc., should also be quite similar. There are no major cost savings in terms of mass, volume, or money, nor are there any obvious performance pluses.

The rear wall is the place upon which focus must be placed. Changes to the rear wall thickness and material have both shown improvement to the ballistic limit curves of the shield. Ideally, only small increases in shield thickness should be contemplated in order to minimize mass growth, but optimize the shield's ability to withstand hypervelocity impact. Thus, the recommended new rear wall thickness will be 0.22 inches vice the baseline 0.19 inches thickness. Although all of the other greater thickness trials outperform this 0.22 inch thick rear wall, they also represent a substantial mass growth. By increasing the shield thickness by 0.03 inches, one will still introduce a 15.8% mass growth into the rear walls. However, this cost may be worth paying, as there is a marked improvement in shield performance associated with the increase. Any

greater mass increases to improve performance, i.e. greater thicknesses, may not justify the expense.

Next to the standoff distance, the most beneficial configuration change comes from selecting an alternate rear wall material. As observed in the previous section, the Aluminum 7175 T6 outperformed the baseline Aluminum 6061 T6 in most circumstances. However, in some of the higher speed regimes for certain cases discussed above , the later half of region two of the curve and region three of the curve, the baseline Aluminum 6061 T6 was superior. This led to the dilemma over which material to choose. Ultimately the recommendation to use the Aluminum 7175 T6 is given. This material was chosen for two reasons. The first reason is that it did outperform the Aluminum 6061 T6 in most cases. The second reason Aluminum 7175 T6 is recommended over the Aluminum 6061 T6 is that, in the cases where the Aluminum 6061 T6 outperformed the Aluminum 7175 T6, it was only by a very slight amount, as indicated on the ballistic limit curves. However, in the cases where the Aluminum 7175 T6 outperformed the Aluminum 6061 T6, the difference was greater. This leads to the postulate that the Aluminum 7175 T6 will perform better in the long run.

To summarize, the single recommended configuration to be ground tested as a potential replacement for the present U.S. Laboratory Module Whipple and Enhanced Stuffed Whipple Shields, will use the same bumper thickness and material as the baseline U.S. Laboratory Module shields, but will use a standoff distance of 6.0 inches. The rear wall will be made of Aluminum 7175 T6 material and will be 0.22 inches thick. All other shield parameters will remain the same as the present parameters. This combination of changes and the predicted ballistic limit curves, based on using the improved BLEs and the substituted values of interest, are shown below in Figures 34 through 41. In each case, the ballistic limit curve for the recommended, new configuration is significantly higher than that yielded by the improved BLE for the baseline U.S. Laboratory Module shields. Thus the change in rear wall thickness, rear

wall material and standoff distance presumably will lead to actual improvements in shield performance, particularly in the higher speed regimes. It is within these higher impact velocity regimes on orbit that the majority of collisions are anticipated to occur. Based upon the empirical analysis, this configuration seems to be worthy of serious consideration for ground testing.

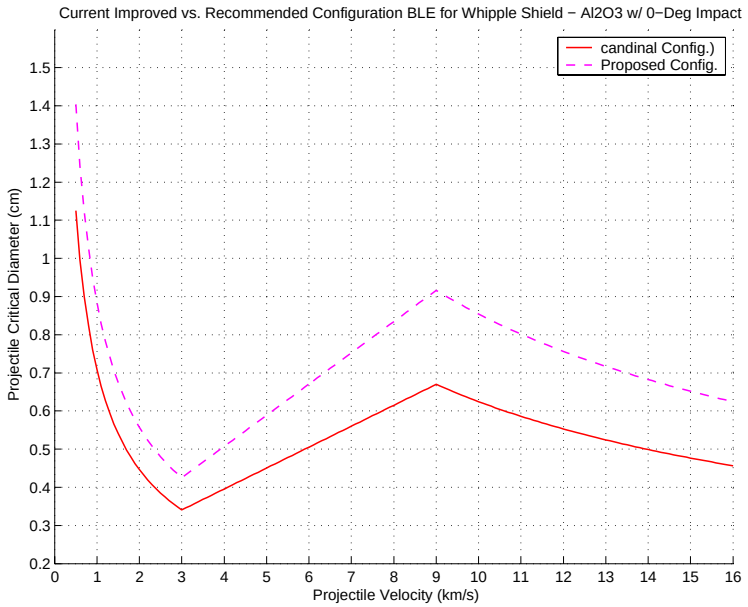

Figure 36. Comparison of Improved BLE at Original Configuration vs. Candidate Configuration BLE plots for Whipple Shield with Aluminum Oxide Projectile at 0-degree Impact Angle.

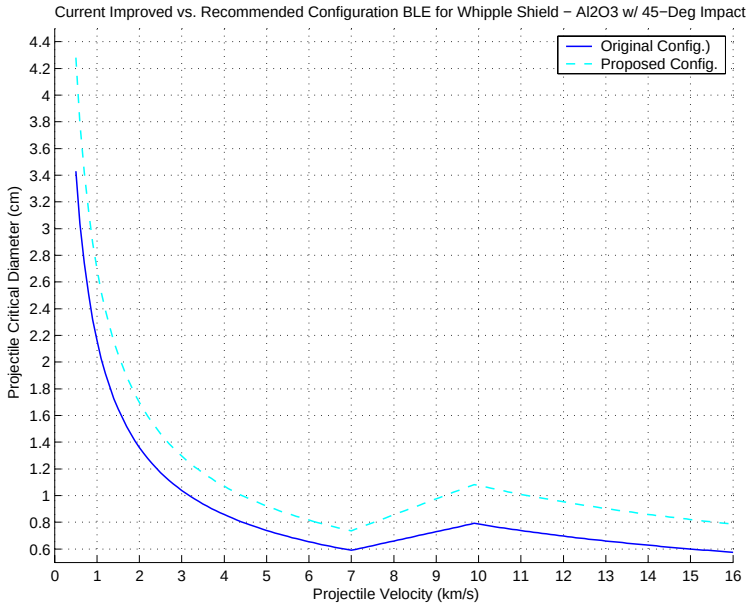

Figure 37. Comparison of Improved BLE at Original Configuration vs. Candidate Configuration BLE plots for Whipple Shield with Aluminum Oxide Projectile at 45-degree Impact Angle.

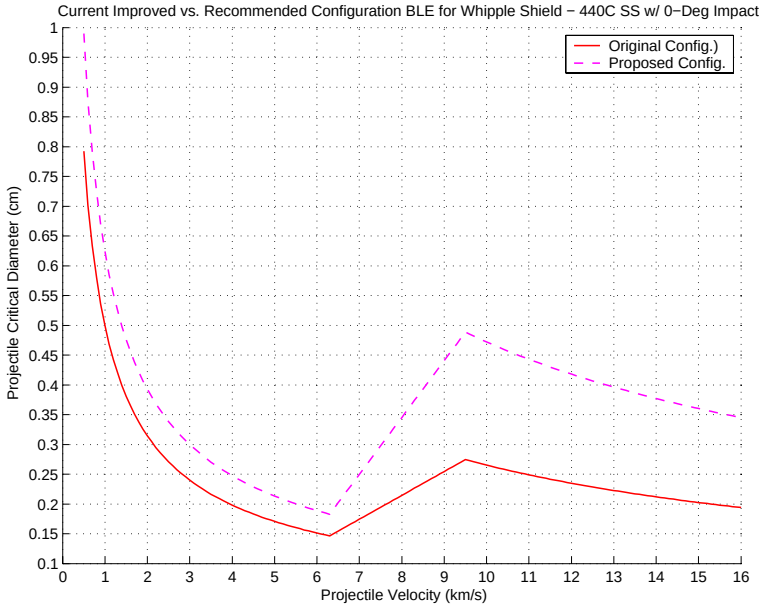

Figure 38. Comparison of Improved BLE at Original Configuration vs. Candidate Configuration BLE plots for Whipple Shield with 440C Stainless Steel Projectile at 0-degree Impact Angle.

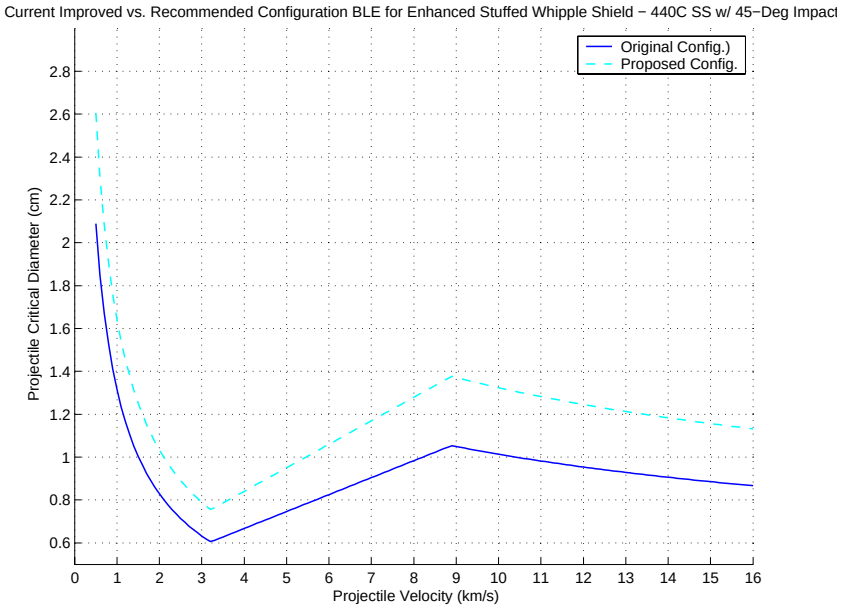

Figure 39. Comparison of Improved BLE at Original Configuration vs. Candidate Configuration BLE plots for Whipple Shield with 440C Stainless Steel Projectile at 45-degree Impact Angle.

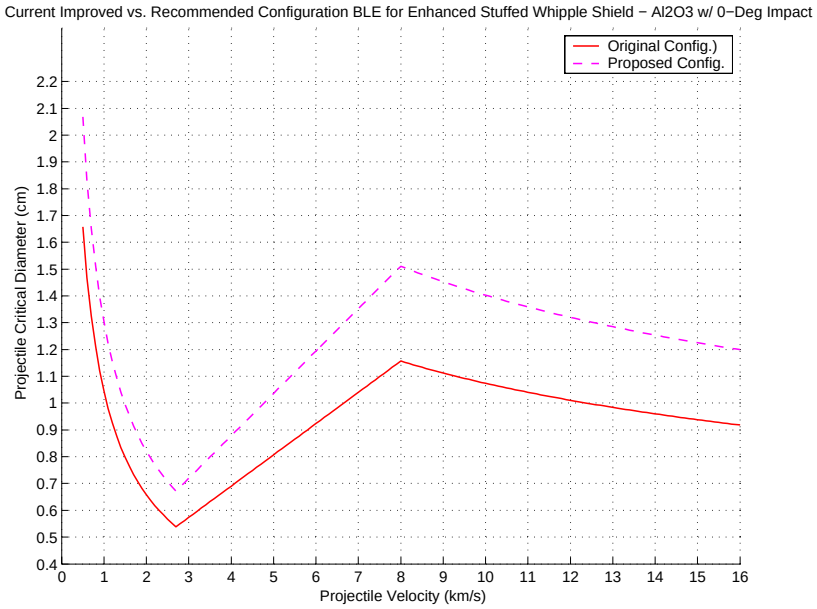

Figure 40. Comparison of Improved BLE at Original Configuration vs. Candidate Configuration BLE plot for Enhanced Stuffed Whipple Shield with Aluminum Oxide Projectile at 0-degree Impact Angle.

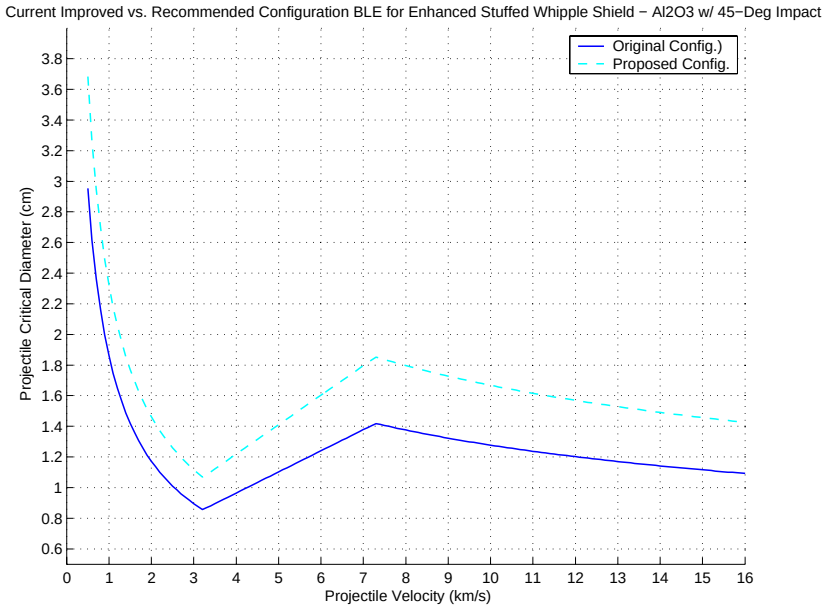

Figure 41. Comparison of Improved BLE at Original Configuration vs. Candidate Configuration BLE plot for Enhanced Stuffed Whipple Shield with Aluminum Oxide Projectile at 45-degree Impact Angle.

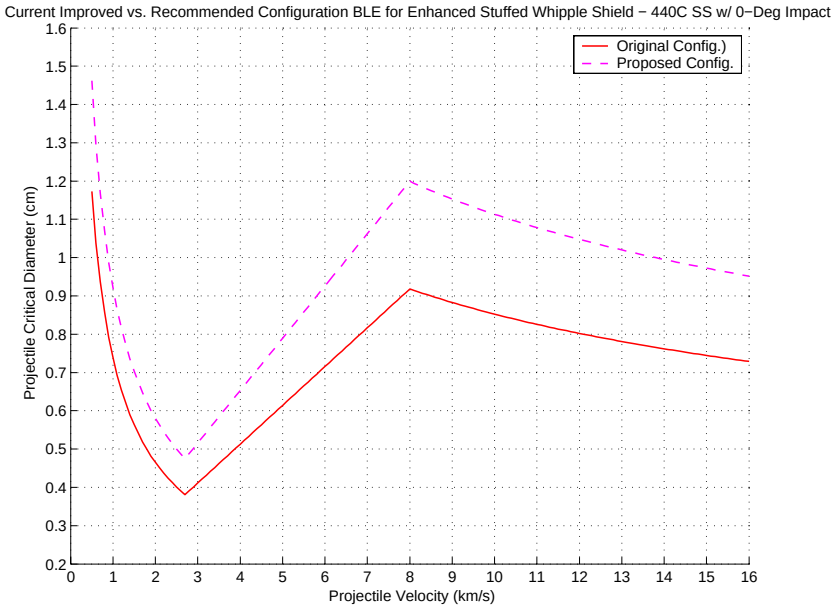

Figure 42. Comparison of Improved BLE at Original Configuration vs. Candidate Configuration BLE plot for Enhanced Stuffed Whipple Shield with 440C Stainless Steel Projectile at 0-degree Impact Angle.

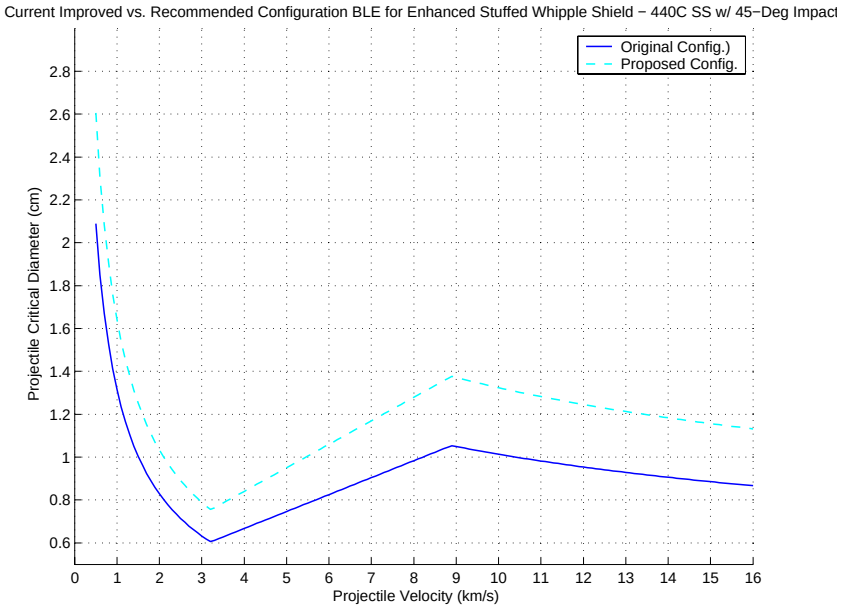

Figure 43. Comparison of Improved BLE at Original Configuration vs. Candidate Configuration BLE plot for Enhanced Stuffed Whipple Shield with 440C Stainless Steel Projectile at 45-degree Impact Angle.

No other test configurations were proposed, despite the fact that countless others could be proposed. The reasons for this are somewhat obvious. First, one must always limit their scope to a clearly defined problem, in this case, one new shield to test. Secondly, several less desirable options were already excluded because of the subjective risk assessment herein that the improvements to performance did not justify the associated costs in mass, volume and raw material, which also include the ground testing costs needed to validate the configuration. Instead, only one proposed configuration was recommended for testing, in the hope that the basic data analysis conducted in this report provides adequate justification for the time and expense of ground testing, as well as the risk versus reward benefits for operational implementation of the new shielding configuration on the International Space Station. Recommended points to test against this new configuration, using the improved ballistic limit equations, will be discussed in the next chapter, while highlighting necessary and desirable follow-on work.

THIS PAGE INTENTIONALLY LEFT BLANK

VII. FUTURE AND FOLLOW-ON WORK

A. CONTINUED GROUND TESTING AND VALIDATION

Having found new, improved ballistic limit equations to more accurately predict the performance of the U.S. Laboratory Whipple and Enhanced Stuffed Whipple Shields, the next logical step is to order additional ground tests whose results will either validate the new equations or else mandate further refinements to the equations. Because the density effects test series already provided a number of raw data points from which to formulate the improved BLEs, no duplication of these points would be necessary in future ground tests. Instead, a number of other data points is proposed for impact testing. These points are selected so that each segment of the improved curve is bracketed by new data. This new data, when collected, will either indicate that the improved equations accurately predict all failure points, or else that the curves need to be tweaked even further to optimize the shape of the curve. This tweaking process would involve a similar analysis to the one used to shift from the entering ballistic limit equations to the ones derived in Chapter V.

While the recommended points for further ground testing are not comprehensive, they do provide adequate coverage of all of the areas of deterministic uncertainty in the curve. Specifically, some of the recommended follow-on test points fall at locations between the old and new curves in order to determine if the new curves could be made less conservative, i.e. raised somewhat. Other points were selected to fall below the new curve to ensure that the improved BLEs are conservative enough. These recommended test points are shown in Table 8 below. Of particular note, test recommendations are limited to impact speeds of 7.0 kilometers per second or less. This is a result of the test apparatus' limitations and not a lack of experimental necessity. Generally speaking, the two-stage light gas gun is only capable of producing projectile speeds on the order of 7.0 kilometers per second. If the testing technology becomes available, a great deal of test

data should be collected in the higher speed regimes, the critical melt/ vaporization region of the ballistic limit curve.

Enhanced Stuffed Whipple Shield Al_2O_3 Projectile			Enhanced Stuffed Whipple Shield 440C Stainless Steel Projectile		
Test Velocity (km/s)	**Impact Angle**	**Test Diameter (cm)**	**Test Velocity (km/s)**	**Impact Angle**	**Test Diameter (cm)**
3.6	0	0.602	4.0	0	0.407
4.5	0	0.800	4.0	0	0.540
6.0	0	0.900	5.0	0	0.640
7.0	0	1.020	7.0	0	0.800
4.0	45	1.000	3.0	45	0.700
5.5	45	1.120	4.0	45	0.680
5.5	45	1.200	5.0	45	0.800
7.0	45	1.250	7.0	45	0.850
7.0	45	1.400	7.0	45	0.920
Whipple Shield Al_2O_3 Projectile			**Whipple Shield 440C Stainless Steel Projectile**		
Test Velocity (km/s)	**Impact Angle**	**Test Diameter (cm)**	**Test Velocity (km/s)**	**Impact Angle**	**Test Diameter (cm)**
5.0	0	0.400	4.0	0	0.225
5.0	0	0.425	5.0	0	0.150
5.5	0	0.500	5.0	0	0.200
6.0	0	0.425	6.6	0	0.210
6.0	0	0.500	6.6	0	0.250
3.0	45	0.800	5.5	45	0.320
3.0	45	0.950	6.0	45	0.225
6.0	45	0.450	6.0	45	0.300
6.0	45	0.600	6.5	45	0.280
7.0	45	0.500	7.0	45	0.350

Table 8. Recommended Additional Hypervelocity Impact Test Shots to be Conducted to Validate Changes to U.S. Laboratory Module Whipple and Enhanced Stuffed Whipple Shields.

While there is an associated cost with conducting additional ground impact tests, it is a cost worth paying. Because improved, higher fidelity predictive equations will be used in NASA's risk assessment and analysis models, the hydrocode and BUMPER codes will produce more realistic results. In turn, these results will help safety engineers and program managers reduce risk by choosing shield types and configurations that can withstand the worst acceptable impacts deemed likely to occur on orbit. The key to choosing sufficient shielding is having an accurate understanding of shield performance. That requires high-fidelity equations found from comprehensive laboratory testing and evaluation.

In addition to continued testing of the current shield configuration using the improved ballistic limit equations, there is also strong evidence from Chapter VI that an alternate shield configuration should be tested. The analysis conducted in Chapter VI shows that alternate configurations and materials may outperform the present U.S. Laboratory Module shields. As was predicted by empirical data analysis, a shield with an increased standoff distance of 6.0 inches and a rear wall made of Aluminum 7175 T6 alloy that is 0.22 inches thick will far exceed the performance of the present material and 4.5 inch standoff distance. However, this improvement in shield performance is predicated upon the assumption that a purely analytical solution is valid. From a purely mathematical prediction, this change in the shield topology adds significant stopping power to the shield for a nominal increase in raw material cost and mass. To decide if this is an investment worth making for real, spaceflight-ready shields, hypervelocity impact ground testing should occur in order to deterministically validate the empirical results.

Because the empirical results of an improved shield configuration were computed using the improved ballistic limit equations, it stands to reason that testing the new equations and validating them should occur first. Once these equations are validated, ground testing should continue, substituting the current shield topologies for the one

summarized above. A number of recommended test points are shown in Table 9 below. These points were also chosen in order to determine if the predicted BLEs of a newly configured shield were overly conservative, overly optimistic, or on the mark. Test velocities and diameters were proposed in order to bracket the predicted curve and to validate its position relative to the original configuration's resultant ballistic limit curve. Note that no test velocities above 7.0 kilometers per second were recommended. This was an intentional oversight. Even though this is a region of great interest for analysis, present lab conditions preclude testing in these speed regimes. Once reliable, affordable means of inducing higher velocities can be presented, NASA can expand its testing into these critical regions of the ballistic limit curves, the region in which most anticipated debris strikes against the ISS will occur.

Enhanced Stuffed Whipple Shield Al_2O_3 Projectile			Enhanced Stuffed Whipple Shield 440C Stainless Steel Projectile		
Test Velocity (km/s)	**Impact Angle**	**Test Diameter (cm)**	**Test Velocity (km/s)**	**Impact Angle**	**Test Diameter (cm)**
2.7	0	0.650	2.7	0	0.450
4.0	0	0.900	5.0	0	0.700
5.0	0	0.950	5.0	0	0.820
7.0	0	1.100	7.0	0	0.900
7.0	0	1.300	7.0	0	1.000
7.0	0	1.400	7.0	0	1.100
3.2	45	1.000	3.2	45	0.700
4.0	45	1.300	3.2	45	0.820
5.0	45	1.300	5.0	45	1.000
7.0	45	1.500	7.0	45	1.000
7.0	45	1.700	7.0	45	1.150
7.0	45	1.850	7.0	45	1.200

Whipple Shield Al_2O_3 Projectile			Whipple Shield 440C Stainless Steel Projectile		
Test Velocity (km/s)	**Impact Angle**	**Test Diameter (cm)**	**Test Velocity (km/s)**	**Impact Angle**	**Test Diameter (cm)**
3.0	0	0.400	4.0	0	0.225
4.0	0	0.550	5.5	0	0.220
5.0	0	0.520	6.3	0	0.170
7.0	0	0.625	7.0	0	0.200
7.0	0	0.700	7.0	0	0.235
7.0	0	0.775	7.0	0	0.275
3.0	45	1.200	4.0	45	0.400
3.0	45	1.400	5.0	45	0.450
4.5	45	1.100	6.1	45	0.320
5.0	45	0.800	7.0	45	0.320
7.0	45	0.670	7.0	45	0.375
7.0	45	0.800	7.0	45	0.450

Table 9. Recommended Test Shots for Alternate Shield Configuration Impact Testing.

This too would make a fine follow-on research opportunity for a student or JSC HITF representative. Positive test results could lead to NASA's incorporating a better shield than the existing U.S. Laboratory Module shields. If the ground tests are conducted and validate the predicted curves, a significant improvement to shield performance could be realized by changing the U.S. Laboratory Module type shields to the new configuration. In order to evaluate the feasibility of incorporating new shields, hypervelocity ground impact testing should follow the research conducted in this report.

B. MITIGATION TECHNOLOGY RESEARCH AND DEVELOPMENT

While the focus of the research and analysis of this report has been upon the ballistic performance equations, one cannot forget about other key parameters in reducing the threat of debris and micrometeoroid impacts. One means of mitigating against the danger is by also improving upon existing orbital debris and micrometeoroid models.

Improved models of the debris and micrometeoroid environment can combine with higher fidelity performance equations in the BUMPER II code to produce the most accurate risk assessments yet completed. While this is a difficult undertaking, it is one that can have an extremely positive impact upon how NASA designs, tests and implements shielding for the ISS. A better understanding of the debris threat, leads to a better preparation of a defense against it.

Improving the BLE predictor equations and the debris/ micrometeoroid models is the most proactive thing NASA alone can do, but it is only one part of solving or mitigating against the debris problem. Future research into mitigation technology can lead to the removal of or decreased production of orbital debris. Using a number of engineering solutions to the problem, mankind can reduce the amount of debris introduced into orbit by explosions, collisions, and jettisoning of pieces of satellites and boosters in orbit, whether by design or by accident. Research into these and other mitigation techniques are worthwhile future research opportunities, although they do comprise a very broad topic of study. Current theories in the best means of removing debris from orbit range from space-based lasers which will push the debris into lower orbits, in which the debris orbit will decay due to atmospheric drag and burn up upon atmospheric reentry; to space-based "vacuum cleaners" which will collect small debris particles and return them to the earth; to a giant "fishing net" or "catcher" apparatus that will capture particles as they pass through. While many of these ideas presently seem like something from a science fiction novel, there are several projects that have already received funding to develop systems to do these tasks. A study of debris removal and mitigation that examines each potential method would provide a great deal of value to the orbital debris community. If mankind can reduce the debris in space, he will make space a safer place in which to operate satellites, space stations, and other manned missions. Strictly speaking however, a study such as this is well outside the realm of directly related follow-on work to the analysis of hypervelocity impacts upon U.S. Laboratory Module Whipple and Enhanced Stuffed Whipple Shields. Still, it has far-reaching

scientific appeal, if not direct applicability to the projectile density effects analysis at hand.

C. WHIPPLE AND ENHANCED STUFFED WHIPPLE SHIELDS FOR OTHER APPLICATIONS

While this report has exhaustively examined alternate Whipple and Enhanced Stuffed Whipple ballistic limit equations for the U.S. Laboratory Modules, future research is not limited to this module, nor to the International Space Station as a whole. Whipple Shields and the Enhanced Stuffed Whipple Shield can be used in various forms on other earth-orbiting satellites. Protecting multi-billion dollar satellites in space with some form of Whipple shielding would reduce program risks for the commercial industry, scientific bodies, and the U.S. government. Not only could Whipple Shields and Enhanced Stuffed Whipple Shields on satellites protect against the naturally occurring space debris and micrometeoroids, it could also protect against manmade debris. Maintaining satellite functionality after an impact could save industry and government countless millions of dollars in replacement or maintenance costs (for those satellites serviced by the Space Shuttle). For the nominal cost of implementing a multi-stage shield on the bus of many satellites, a satellite may have its usable lifetime expanded considerably, or, at a minimum, may avoid having its usable life terminated abruptly as a result of damage sustained by a debris impact. An opportunity cost study or similar research should be conducted to determine the feasibility of putting the family of Whipple Shields on other earth-orbiting satellites.

In addition to the International Space Station, the shielding could be modified and used on other manned space vehicles too. With a manned mission to Mars a goal of NASA in our lifetimes, some form of shielding will be needed to protect against the heliocentric micrometeoroids that pose a great risk to any mission undertaken. The projectiles have incredibly high speeds and therefore require significant shielding to defeat their destructive power. Some configuration of Whipple or Enhanced Stuff

Whipple Shield is a more viable option than thick, heavy monolithic shields. In fact, this is an area of ballistic research that should be of particular interest to NASA as it prepares to send a man to Mars. Preliminary work should begin in earnest now. It is a logical and an ideal follow-on to the ISS shield analysis work done by JSC HITF.

From the aspect of Space Control, a topic currently of great interest in the Department of Defense, Whipple and Enhanced Stuffed Whipple Shields could provide some protection against attacks upon U.S. and allied satellites by parties using small projectiles aimed at impacting national systems and causing their disruption; reduction or loss of functionality; or outright destruction. Specifics of Space Control and the defense of U.S. satellite systems to guarantee assured access to space are typically classified, so future work in this realm would have to fuse the unclassified shield theory with classified Space Control theory. The Department of Defense would be foolish not to consider implementing some form of shields on its national systems, those satellites that provide military communications, signals-gathering, imagery, and nuclear launch warning. After all, these are strategic assets and are vulnerable enough to space debris that was not placed in space by malice. They are even more susceptible to debris put in space for the sole purpose of denying access to our satellite systems. Unfortunately, those competing states that have the ability to launch debris into orbit are also likely to know the ephemeris data of many of U.S. national asset satellites. In a known orbit, a satellite is particularly vulnerable to a dedicated, targeted attack using space debris as a kinetic kill vehicle.

As a completely theoretical example, one could assume a nation like North Korea that does not have satellites of its own in space and doesn't concern itself with the political repercussion of damaging other nation's space-based systems and satellites, could launch a missile into space that is full of ball bearings, which is promptly dispersed and becomes debris upon entering low earth orbit. At this point, North Korea has the perfect space-based weapon – it is indiscriminate, does not require guidance, and can

cause cascading damage if it impacts any manmade satellite in its path. Thus, they can impact other nations' ability to communicate, spy, or conduct scientific experiments. Such an attack could have negative effects on the entire body of manmade satellites for years to come. While this is a somewhat tenuous chain of events in modern times, it is a frightening possibility of things to come in the near future, when mankind becomes increasingly reliant on space-based systems for national defense and in our everyday lives.

To examine the possibilities of adding some form of shielding to the satellites to avoid such a devastating scenario seems a prudent decision. The work contained in this thesis merely provides an example of the ability of Whipple and Enhanced Stuffed Whipple Shields to mitigate against some of the debris that is orbiting earth. The Department of Defense can independently assess any debris threats to its satellite networks, as well as the threats of orbital debris being introduced for the sole purpose of denying the United States the ability to use space as a strategic asset. In doing so, the government must look at what defensive measures are available to counter the threats. The family of Whipple Shields is just one possible solution that springs from the research in this report. Future hypervelocity impact analysis work could become an interagency project, with NASA and the Department of Defense organizations operating in concert to mitigate against orbital debris threats to national satellite systems.

Outside of NASA and the ISS program, there is a wide customer base of potential Whipple Shield users. Future research into shield performance can and should be tailored to the commercial, civil, and military uses of these multi-stage shields. Such research would introduce this latest technological triumph of NASA into the greater world and would continue the proud tradition of technology marvels springing from the U.S. space program. This would be good for NASA and good for the space-faring community as a whole.

Continuing ballistic limit analysis and further experimentation are the best ways of ensuring all spacecraft are protected against hypervelocity impacts. If NASA is prescient enough to continue its already impressive work in this field, it will revolutionize the way in which satellites are built with debris protection in mind. NASA's work will further industry's and government's risk assessment capabilities, leading to smarter, safer business and engineering decisions on space systems.

VIII. SUMMARY AND CONCLUSIONS

A. SUMMARY OF RESEARCH FINDINGS – REVISED BALLISTIC LIMIT EQUATIONS

Ultimately, new ballistic equations were determined for both the Whipple and Enhanced Stuffed Whipple Shields. Using some subjective curve-fitting to sketch potential new ballistic limits for each projectile and shield type, as well as each angular impact, approximate curve shapes could be incorporated that best encompass the raw data from the density effects trials while minimizing the reduction in area under the ballistic limit curve. This first cut provided a starting point from which a detailed mathematical analysis was conducted to determine updated values for many variables in the equations. These revised numbers were in the form of both coefficients and exponents. Ultimately, several candidate ballistic limit equations were mathematically derived to replace the entering ones. Only the best of these candidate equations were chosen for each specific projectile, shield type and impact angle case. One result of the deviation between the raw data and the entering equations was that unique values of many of these coefficients and exponents had to be applied to the basic BLEs, meaning that there wasn't one catch-all equation that could be determined. Nevertheless, several valid equations were computed. These new, improved equations successfully predicted shield PASS/ FAIL criteria for the density effects test series once the modifications to the entering equations were completed. All that truly remains is to conduct further ground tests to validate that these equations do, in fact, more accurately predict shield performance, without being overly conservative.

As was learned in the projectile density effects experiment, the density of the impacting material does play a significant role in determining if a shield can withstand a hypervelocity impact. The entering equations were overly optimistic and only accounted for one type of projectile, Aluminum. When heavier, yet equally common debris materials like Aluminum Oxide and Steel were involved in a hypervelocity impact, the

net results were significantly more catastrophic because of the additional momentum these particles possessed upon impact. Consequently, there was a need to lower the ballistic limits in order to realistically predict shield performance under these new impact conditions. By careful mathematical manipulation and curve-fitting, one could limit the conservatism of the prediction by minimizing the amount by which the curve was lowered. The new curves fully contained the raw data density effects points in the accurate prediction region (above the curve for shield failures and below the curve for passing shields), but deviated as little as possible from the original BLE points. Changing various parameters discussed in Chapter V provided an accurate predictor of shield performance without causing an overly dramatic shift in the curve shape. Thus the goal of improving prediction accuracy without generating overly conservative ballistic limit equations was achieved.

Additional ground testing should still be conducted in order to verify that the new equations are, in fact, better predictors of shield performance than the entering equations. With these new, improved ballistic limit equations tested and validated, or, conversely, tested, invalidated and further iterated and refined in the near future, engineers will eventually arrive at fully-idealized predictive equations that can be inserted into the BUMPER II code. A firmly established and validated series of ballistic limit equations in this code will figure prominently in future risk analysis and assessment. These higher fidelity assessments will help NASA engineers improve safety and manage risk more efficiently in the International Space Station program by giving them a more accurate integrated threat assessment. With shield performance accurately predicted by new, improved ballistic limit equations, much of the danger of a debris/ micrometeoroid strike upon the ISS can be mitigated against using alternate shield configurations.

In the final estimation of the problem, ground-based hypervelocity impact tests provide the best possible means of verifying the accuracy of the predictions made by the BLEs. This deterministic approach, coupled with the empirical aspects of solving for the

ballistic limits proved to be a fine way to generate curves that accurately predict the shield performance of the U.S. Laboratory Module Whipple and Enhanced Stuffed Whipple Shields.

B. SUMMARY OF PROPOSED ALTERNATE SHIELDING MATERIALS AND CONFIGURATIONS

With new ballistic equations in place to serve as better predictors of shield performance, and, by extrapolation, risk assessment, engineers can focus their future efforts upon incorporating alternate shield configurations into future ISS modules. These new shield topologies will be more capable of withstanding characteristic hypervelocity impacts in the orbit in which the ISS flies. Having developed and refined the theory of Whipple and Enhanced Stuffed Whipple Shield performance, empirical analysis determined a combination of factors that affect the shield performance. Observing the results yielded by varying one shield property or parameter at a time (bumper thickness, rear wall thickness, standoff distance, bumper material(density), and rear wall material (yield strength and density)), multiple properties to vary simultaneously were selected, in the hopes that the combination of changes would lead to even better shield performance predictions. These iterations were then evaluated against the improved ballistic limit equations derived as part of the density effects test series. Empirically, the equations corresponding to the candidate, new configuration, predicted superior shield performance when compared with the improved BLEs determined in Chapter V. Consequently, the single configuration change that was recommended for further testing is a prime candidate to replace the existing shield topology on the U.S. Laboratory Module, pending verification from ground tests.

Before implementing the new material and design, a thorough ground impact test series that uses all shield types, projectile types and impact angles should be conducted. Only then can one claim with authority that the new shield configuration should replace the current topology in future applications. Based on the initial analysis contained in

Chapter VI, the results from changing the rear wall and standoff distance are promising. There is no appreciable increase in mass, but there is a significant increase in the shield's ability to withstand hypervelocity impacts in the higher speed regions of the curve, the velocity regimes most likely to make up the debris threat to the ISS.

C. THE NEED FOR FOLLOW-ON RESEARCH AND TESTING

These initial analytical results are very promising and offer hope that there are viable alternatives to existing shield topologies. Perhaps the greatest lesson to be gleaned from these analyses is that the work is not yet complete. There is still a great deal of impact testing to be done and refining of ballistic limit equations to be conducted. Given a reasonably limited mathematical analysis tool bag, one can still tackle this problem successfully given the time and the laboratory support to conduct further tests

It has been said many times before in this report that more testing on the ground is needed to develop the highest fidelity ballistic limit equations for the most common, predicted hypervelocity impact conditions. Accurately predicting shield performance on the ground is the best way to reduce risk to the ISS and its crew in the long run. High fidelity equations, validated by detailed and thorough ground tests, make up high fidelity models and codes. These models and codes, in turn, produce high-fidelity risk assessments that are used to make the ISS and its two- to three-man crew safe while orbiting earth at a brisk, seven kilometers per second rate. The safety of all astronauts ultimately starts with the ability to precisely predict the performance of their spacecraft. To accomplish this feat, NASA must test shields until their performance is adequately understood and the inherent risk to the astronauts is within acceptable tolerances. The cost of conducting hypervelocity ground tests in terms of time, money and manpower is a small price to pay when compared with the cost of human life, hardware and the invaluable scientific knowledge that would be lost with the failure or outright destruction

of the International Space Station as a result of hypervelocity impacts by space debris or micrometeoroids that weren't adequately shielded against.

D. OVERALL CONCLUSIONS

As a result of the research and analysis in this report, an improved understanding of ISS shield performance has been developed for high-density (440C Stainless Steel and Aluminum Oxide) hypervelocity impact threats. This knowledge, and the certainty that the improved equations developed in this work accurately predict failure, will allow NASA to improve its own risk analysis and shield design techniques. This will surely pay dividends in improving crew safety and spacecraft relaibility. Their safety is ultimately in our hands. It is far too dramatic to say that the analysis in this simple report and the accompanying changes to the ballistic limit equations will alone make our astronauts and the space station as a whole a safer place to live and work, but it is reasonable to assume that the knowledge gained today can, and will, be used to make improvements tomorrow in a number of ways that will directly or indirectly impact the men and women who fly the ISS. Someday soon, the same Whipple and Enhanced Stuffed Whipple technology that comprises the U.S. Laboratory Module may be used on other space-going systems to protect their vital payloads whether it is communications electronics, earth science experiments, or the first space tourists.

THIS PAGE INTENTIONALLY LEFT BLANK

APPENDIX A - INTERNATIONAL SPACE STATION IMPACT ORBITAL AND IMPACT VELOCITIES

Altitude (km)	Altitude (mi)	Orbital Velocity (km/s)	Orbital Velocity (mph)	Orbital Period (sec)	Orbital Period (min)
250.000	155.343	7.755	17347.287	5370.121	89.502
260.000	161.557	7.749	17334.215	5382.279	89.705
270.000	167.770	7.743	17321.173	5394.446	89.907
280.000	173.984	7.737	17308.160	5406.622	90.110
290.000	180.198	7.732	17295.177	5418.807	90.313
300.000	186.411	7.726	17282.223	5431.002	90.517
310.000	192.625	7.720	17269.298	5443.205	90.720
320.000	198.839	7.714	17256.401	5455.418	90.924
330.000	205.052	7.709	17243.534	5467.640	91.127
340.000	211.266	7.703	17230.696	5479.871	91.331
350.000	217.480	7.697	17217.886	5492.111	91.535
360.000	223.694	7.691	17205.104	5504.360	91.739
370.000	229.907	7.686	17192.351	5516.618	91.944
380.000	236.121	7.680	17179.626	5528.885	92.148
390.000	242.335	7.674	17166.930	5541.162	92.353
400.000	248.548	7.669	17154.261	5553.447	92.557
410.000	254.762	7.663	17141.621	5565.742	92.762
420.000	260.976	7.657	17129.009	5578.045	92.967
430.000	267.190	7.652	17116.424	5590.358	93.173
440.000	273.403	7.646	17103.867	5602.680	93.378
450.000	279.617	7.641	17091.338	5615.011	93.584
460.000	285.831	7.635	17078.836	5627.350	93.789
470.000	292.044	7.629	17066.361	5639.699	93.995
480.000	298.258	7.624	17053.914	5652.057	94.201
490.000	304.472	7.618	17041.494	5664.424	94.407
500.000	310.686	7.613	17029.101	5676.800	94.613

Table A1. ISS Orbital Velocity at Specified Altitudes.

THIS PAGE INTENTIONALLY LEFT BLANK

APPENDIX B - ORBITAL VELOCITY MATLAB CODE

```
%%%%%%%%%%%%%%%%%%%%%%%%%%%%%%%%%%%%%%%%%%%%%%%%%%%%%%%%%%%%%%%%%%%%%%%%
%                                                                       %
%                            APPENDIX B                                 %
%                          Thesis Figure                                %
%                                                                       %
%       ISS Orbital Velocities & Impact Geometry Speeds                 %
%                                                                       %
%                     LT Michael E. Kalinski, USN                       %
%                          11 August 2004                               %
%                                                                       %
%%%%%%%%%%%%%%%%%%%%%%%%%%%%%%%%%%%%%%%%%%%%%%%%%%%%%%%%%%%%%%%%%%%%%%%%
%
clear all;
close all;
%
% Calculate the Orbital Velocity of the International Space Station at common
% altitudes. Based on NASA data, altitude varies from 320 to 420 km, with a
% mean altitude of 360 km or 400 km.
%
% For circular orbits, the velocity is (mu/R)^(1/2) where R = Re + h & mu is the
% gravitational parameter for earth.
%
Re = 6378;            % Earth radius is km.
h = [300:0.5:450];    % ISS Altitude in km.
R = Re + h;           % Orbital Radius in km.
mu = 398601;          % Gravitational Parameter in (km^3/sec^2).
v = (mu./R).^(1/2);   % ISS Orbital Velocity in km/s.
%
% The maximum impact speed between an object and ISS would occur if an
% object was in an identical orbit, but retrograde vs. prograde. This would lead to
```

```
% impact velocities twice the normal ISS orbital velocity.
%
v_impact_max = 2 * v;      % Maximum Impact Velocity in km/s.
%
% Next assume that ISS and a micrometeoroid or debris impact with initially
% perpendicular, identical velocities so that you use the Pythagorean theorem to
% get the velocity:
%
v_impact_normal = sqrt (v.^2 + v.^2);   % normal impact velocity in km/s.
%
% Finally, generate plot of velocities of ISS and impacts to demonstrate the
% characteristic velocities with which we deal when discussing ISS
% Hypervelocity Impacts.
%
figure(1);clf reset
plot(h,v,'r-','LineWidth',2)
hold on
plot(h,v_impact_max,'b--','LineWidth',2)
hold on
plot(h,v_impact_normal,'g:','LineWidth',2),...
  xlabel('Altitude (km)'), ylabel('Velocity (km/s)'), ...
  title('Orbital & Impact Velocities vs ISS Impact Altitude'),...
  legend('ISS Orbital Velocity (km/s)','Max Impact Velocity (km/s)','Normal
  Impact Velocity (km/s)'),...
  grid on
  print -depsc -tiff -r300 Impactvel
%
%
figure(2);clf reset
plot(h,v,'r-','LineWidth',2),...
  xlabel('Altitude (km)'), ylabel(' ISS Orbital Velocity (km/s)'), ...
  title('Orbital Velocities vs ISS Altitude'),...
```

```
  legend('ISS Orbital Velocity (km/s)'),...
  grid on
  print -depsc -tiff -r300 ISSvel
%
%
figure(3);clf reset
plot(h,v_impact_max,'b-','LineWidth',2),...
  xlabel('Impact Altitude (km)'), ylabel('Maximum Impact Velocity (km/s)'), ...
  title('Maximum Impact Velocities vs ISS Impact Altitude'),...
  legend('Max Impact Velocity (km/s) = 2 x Orbital Velocity'),...
  grid on
  print -depsc -tiff -r300 MaxImpact
%
%
figure(4)
plot(h,v_impact_normal,'g-','LineWidth',2),...
  xlabel('Altitude (km)'), ylabel('Velocity (km/s)'), ...
  title('Normal Impact Velocities vs ISS Impact Altitude'),...
  legend('Normal Impact Velocity (km/s) = 1.41 x Orbital Velocity'),...
  grid on
  print -depsc -tiff -r300 RMSImpact
```

THIS PAGE INTENTIONALLY LEFT BLANK

APPENDIX C - DENSITY EFFECTS TEST SERIES RAW DATA

Legend	
	Test Plates not in lab. Partial data comes from available reports & JSC request docs
	Data points not available in any written doc.; Final masses to be measured in lab if time permits

General Comments		
Depth and Protrusion Measurement		Hole depths are measured from undisplaced flat surfaces on the rear wall plate's front and back faces. A calibration measurement was taken to zero-out the measuring device. Hole depth was then measured from this reference zero-level. Elevated areas on the front and back faces were measured in the same manner.
Depth and Protrusion Measurement		In the event of a HOLE in the plate, a max penetration depth of 0.19in (4.826mm) was recorded. In some cases, a deeper penetration depth was recorded. This occurs when there is a deep crater, that protrudes from the rear face, but doesn't puncture the material. This depth can be > 0.19in (4.826mm).
Areal Density Calculations		Areal Density (theoretical) is used in the spreadsheet above. These values were provided by Ron Bernhard. To calculate actual areal density, $\rho = m_{init} /$ (thickness x area) where area is 144 in^2 (929.0304 cm^2).
Damage Classification		Damage Classification IAW JSC 28837 ISS Ballistic Limit Study HVI Testing
Areal Density of NEXTEL & KEVLAR		Areal Density of NEXTEL is 0.1 g/cm^2 for each layer, 0.6 g/cm^2 for all six layers tested. KEVLAR is 0.034 g/cm^2 for each layer, 0.204 g/cm^2 for all six layers tested.
*	Bumper Comments	Ellipse measurements are major & minor axes respectively, annotated in the comments column. The diameters in the other columns are the MAJOR AXIS measurements only.
#	Nextel Comments	OUTER DIAMETER measurement is the MAJOR AXIS length of the widest portion of damage area, i.e. tears, piles, and rips plus holes. The INNER DIAMETER is the MAJOR AXIS length of the hole alone.
+	Kevlar Comments	OUTER DIAMETER measurement is the MAJOR AXIS length of the widest portion of damage area, i.e. tears, piles, and rips plus holes. The INNER DIAMETER is the MAJOR AXIS length of the hole alone.
**	Rear Wall Comments	IF the plate has a hole in it, the INNER DIAMETER column indicates the diameter of the hole size and the OUTER DIAMETER column is the diameter of the total damage area, i.e. the circle that contains all the assorted damage - pitting, cracking, spalling, deposits, scorch marks, etc. IF there is no hole in the rear wall, the INNER DIAMETER column is the area of most concentrated damage, while the OUTER DIAMETER is the circle of total damage containment.

##	Witness Plate Comments	IF the plate has a hole in it, the INNER DIAMETER column indicates the diameter of the hole size and the OUTER DIAMETER column is the diameter of the total damage area, i.e. the circle that contains all the assorted damage - pitting, cracking, spalling, deposits, scorch marks, etc. IF there is no hole in the rear wall, the INNER DIAMETER column is the area of most concentrated damage, while the OUTER DIAMETER is the circle of total damage containment.
++	Overall Comments	A PASS is indicated by the lack of light-leak holes or spalling on the rear wall. A FAIL is indicated if there are holes, spalling or light leaks in the rear wall. A good test is one for which cameras at White Sands Test Facility verified the projectile struck the target in once pice and did not fracture prior to impacting the bumper. Additionally, commenting is included if no supporting test documentation accompanied the shields.

Density Effects Data					
Target Setup		Projectile Data			
Test # in Series	Structure Type (Full Scale Whipple or Stuffed Whipple)	Material	Diameter (cm)	Impact Angle (deg)	Projectile Speed (km/s)
1	Stuffed Whipple	440C Stainless Steel	N/A	0	N/A
1A	Stuffed Whipple	440C Stainless Steel	N/A	0	N/A
1B	Stuffed Whipple	440C Stainless Steel	0.9	0	6.9
1C	Stuffed Whipple	440C Stainless Steel	0.9	0	7
2	Stuffed Whipple	440C Stainless Steel	0.90000	45	6.84
2C	Stuffed Whipple	440C Stainless Steel	0.90000	0	7
3	Stuffed Whipple	440C Stainless Steel	0.90000	45	4.04
4	Stuffed Whipple	Al_2O_3 Ruby Sapphire	0.95000	0	6.51
5	Stuffed Whipple	Al_2O_3 Ruby Sapphire	0.95000	45	6.77
5A	Stuffed Whipple	Al_2O_3 Ruby Sapphire	0.95000	45	6.84
6	Stuffed Whipple	Al_2O_3 Ruby Sapphire	0.95000	45	4.5
7	Full Scale Whipple	440C Stainless Steel	0.60000	0	6.66
8	Full Scale Whipple	440C Stainless Steel	0.48000	45	6.84
9	Full Scale Whipple	440C Stainless Steel	0.36000	45	4.57
10	Full Scale Whipple	Al2O3 Ruby Sapphire	0.79000	0	6.89
11	Full Scale Whipple	Al_2O_3 Ruby Sapphire	0.56000	45	6.72
12	Full Scale Whipple	Al_2O_3 Ruby Sapphire	0.48000	45	4.29
13	Stuffed Whipple	440C Stainless Steel	0.83300	0	7.04
13A	Stuffed Whipple	440C Stainless Steel	0.83300	0	7.03
14	Stuffed Whipple	440C Stainless Steel	0.79000	45	6.93
16	Stuffed Whipple	Al_2O_3 Ruby Sapphire	0.95000	0	5.51
17	Stuffed Whipple	Al_2O_3 Ruby Sapphire	0.95000	45	6.19
18	Stuffed Whipple	Al2O3 Ruby Sapphire		45	4.13
19	Full Scale Whipple	440C Stainless Steel	0.50000	0	6.78
20	Full Scale Whipple	440C Stainless Steel	0.40000	45	6.76
21	Full Scale Whipple	440C Stainless Steel	0.32000	45	4.3
22	Full Scale Whipple	Al_2O_3 Ruby Sapphire	0.64000	0	6.8
23	Full Scale Whipple	Al_2O_3 Ruby Sapphire	0.64000	45	6.95

Density Effects Data					
Target Setup		Projectile Data			
Test # in Series	Structure Type (Full Scale Whipple or Stuffed Whipple)	Material	Diameter (cm)	Impact Angle (deg)	Projectile Speed (km/s)
24	Full Scale Whipple	Al_2O_3 Ruby Sapphire	0.56000	45	4.45
24	Full Scale Whipple	Al_2O_3 Ruby Sapphire	0.56000	45	4.45
25	Stuffed Whipple	440C Stainless Steel	0.75400	0	5.69
26	Stuffed Whipple	440C Stainless Steel	0.83000	45	6.38
27	Stuffed Whipple	440C Stainless Steel	0.67500	45	4.47
28	Stuffed Whipple	Al_2O_3 Ruby Sapphire	0.10320	0	6.84
29	Stuffed Whipple	Al_2O_3 Ruby Sapphire	1.00000	45	7.07
30	Stuffed Whipple	Al_2O_3 Ruby Sapphire	1.19100	45	4.48
31	Full Scale Whipple	440C Stainless Steel	0.40000	0	6.86
32	Full Scale Whipple	440C Stainless Steel	0.36000	45	6.76
33	Full Scale Whipple	Al_2O_3 Ruby Sapphire	0.56000	0	6.83
34	Full Scale Whipple	Al_2O_3 Ruby Sapphire	0.60000	45	4.42
36	Stuffed Whipple	Nylon/ 440C Stainless Steel	0.87300	45	5.75
36A	Stuffed Whipple	440C Stainless Steel	0.87300	0	6.47
36B	Stuffed Whipple				
39	Stuffed Whipple	Al_2O_3 Ruby Sapphire	0.11100	45	6.88
39A	Stuffed Whipple				
41	Full Scale Whipple	440C Stainless Steel	0.31800	0	6.73
42	Full Scale Whipple	440C Stainless Steel	0.31800	45	6.64
43	Full Scale Whipple	Al_2O_3 Ruby Sapphire	0.50000	0	6.69
44	Full Scale Whipple	Al_2O_3 Ruby Sapphire	0.60000	45	6.72
45	Full Scale Whipple	Al_2O_3 Ruby Sapphire	0.75400	45	4.49
45A	Full Scale Whipple	Al_2O_3 Ruby Sapphire	0.75400	45	4.74

Density Effects Data							
Rear Wall **							
Test # in Series	Outer Diam. (mm) (Front)	Inner Diam. (mm) (Front)	Max. Hole Depth (mm)	Outer Diam. (mm) (Back)	Inner Diam. (mm) (Back)	Max. Spalling Depth (mm)	Max. Rear Face Bump Height (mm)
1	N/A	N/A	N/A	N/A	N/A	N/A	N/A
1A	N/A	N/A	N/A	N/A	N/A	N/A	N/A
1B	143	89	4.826	304.8	81.69	N/A	N/A
1C	163x94	163x94	4.826	163x69	163x69	N/A	N/A
2	120	19.53	4.826	105	19.53	N/A	16.415
2C							
3							
4	116	47	9.047	111	N/A	0	7.119
5	217	44	1.021	0	0	0	0
5A	70	11.88	2.176	0	0	0	0.295
6	126	63	0.636	0	0	0	0
7	55.99	24.19	4.826	52	19.78	1.847	5.484
8	64.42	22.84	4.826	28.9	24.65	1.362	6.222
9	218	53.21	5.028	5.88	0.01	0	1.465
10	320	60.09	6.614	65.81	65.81	1.682	4.238
11	197	43	2.185	0	0	0	0.54
12	202	57	1.028	0	0	0	0
13	200	97	4.826	230	112	N/A	N/A
13A	144	123	4.826	140	121	N/A	N/A
14	81	52	3.369	35.2	35.2	0	1.798
16	127	92	7.958	92.67	92.67	0	7.194
17	142	7.88	1.486	5.94	5.94	0	0.43
18							
19	182	4.9	4.826	52.64	4.9	1.922	4.754
20	236	53	4.826	15.72	9	1.337	1.194
21	239	56.95	2.753	37.94	7.48	0	0.339

Density Effects Data							
Rear Wall **							
Test # in Series	Outer Diam. (mm) (Front)	Inner Diam. (mm) (Front)	Max. Hole Depth (mm)	Outer Diam. (mm) (Back)	Inner Diam. (mm) (Back)	Max. Spalling Depth (mm)	Max. Rear Face Bump Height (mm)
22	164	69.17	2.795	58	56	1.168	4.918
22	164	69.17	2.795	58	56	1.168	4.918
23	66	52	5.162	8.55	0.01	0.27	1.729
24	226	103	2.194	0	0	0	0
25							
26							
27							
28	163	113	4.826	167	92	N/A	N/A
29	6.51	5.35	4.436	4.96	4.96	0	0.463
30	5.96	10.05	4.826	5.96	7.92	0	5.271
31	191	51	2.271	51	51	1.754	2.111
32	210	35.54	5.033	7.96	6.69	1.088	2.276
33	145	50.6	1.266	53	47	0.995	6.807
34	83	N/A	2.783	5.79	5.79	0	0.301
36							
36A							
36B	230	54	8.773	83.14	83.14	0	7.969
39	203	22	5.794	122.63	0	0	4.237
39A	24.8	24.15	4.826	27.25	21.34	0	13.015
41	172	46	1.349	48	35.89	1.605	4.133
42							
43	204	59.89	2.15	0	0	0	0.449
44							
45							
45A	220	52.95	4.912	47	11	0	3.155

Density Effects Data		
Rear Wall **		
Test # in Series	Damage Classification	Comments
1	N/A	N/A
1A	N/A	N/A
1B	F5	completely cracked and torn sheet. Explosive crowns jetting out back side; deposits all around entry hole on front face, spalling as well
1C	F5	Back face is exploded outward with several sharp, long shards sticking out. Numerous long, deep cracks in material reveal peeled back leaves of metal sheet
2	F5	19.53mm hole in front with caved in depression in impact surface of front face; 120mm damage area marked by dust/ scorch deposit plus cracking in 4 separate fault lines; back face is exploded outward with hole of 19.53mm and raised area of 105mm; hole and cracking both evident
2C		
3		
4	F3	front side cratering only with scorch deposit in diameter of 116mm; crater itself is 47mm; backside bump/ protrusion but no holes or spalling
5	F3, E1	scorch deposit in cone shape on front face; no damage on back face;
5A	E1	no damage noted on back face; front face has circle of concentrated impact with several craters and gouges, but no penetration or spalling. Deposit of black particulate in cone shape expanding from major impact point.
6	E1	no penetration or spalling evident; some very shallow cratering in three locations; with a few small divots elsewhere; some reflected deposits
7	C4, D5	Hole in top is sized in previous columns. Pitting and deposit pattern is 84mm and 173 mm diameters respectively. Spalling on back face 52mm diameter; with a hole in center of 19.77 mm. There are some smaller holes and light gaps arrayed around the main hole.
8	C1, D5	Front face has large hole in it. Deep pitting all around hole. Smaller concentration of small deposits and pits in second location along axis of projectile travel. Back face has one jagged edge sticking up due to a crack, some spalling as well around perimeter of hole, as well as dimples from deep pits on the side of sheet.
9	C1	53.21mm diameter concentrated arc of damage with deep pitting and one light leak hole of infinitesimal size. Deep pitting scattered all over the front side. Back side has two bumps from other side deep pits, one of which has <0.01mm light hole.
10	E4	Only piece of testbed available. Back side spalling with hole/ crack in middle of spall circle. Diameter 65.81 mm; some upturned edges. Front piece has central circle of damage with d =60.09mm for deep cratering and a big hairline crack. Lots of silver deposits inside the area. total damage area spreads 320mm +. with star pattern in circle. some areas of darker deposits as well, but primarily spread case of silver.

Density Effects Data		
Rear Wall **		
Test # in Series	Damage Classification	Comments
11	C1, E1	No rear face damage other than a few shallow bumps. Front face has pitting in two concentrated areas; deep pitting in one and more shallow but concentrated in another area.
12	C1, E1	no back face damage. Front face has some deep craters prior to point of primary impact, concentrated circle of deposits/ reflection with diameter of 57mm, outer damage diameter is 202mm.
13	F5	Front face - rings of black and silver deposits all around impact point. cracking and holes abound. Back face has major scorching; shards sticking out in 6 peaks with several long cracks; front is caved in with deposits at interior point of failure. Measurements taken from furthest on damage and hole width
13A	F5	cracked completely in half; major damage from cracking and hole. Back side shows burn patterns all over sheet with crown of pointed metal sticking up form 5 cracks. Metal is peeled up and out. Front side is caved in prior to cracking
14	C1, F3	no back face penetrations or spalling, only raised bump from front side impact. Front side measurements are innermost concentrated hit areas - some minor cratering, but little deep marks and outer is black deposit area. Actual shape is more elliptical like a comet shape. Other indications of metal discoloration. back measurements are bump diameter
16	D1, F3	back side has a raised center bump with diameter of 92.67mm. Front face has center ring indented with deposited material (92mm) and an outer black deposited region(102mm). Further out in concentric circles are a region of lesser deposit/ discoloration (127mm)
17	E1, F3	one small bump on back face having diameter of 5.94mm. Front has one deep crater of 7.88mm width, black residue and deposits in a roughly elliptical shape - 177mm long, 87mm wide, outer ring of grayish colored deposit as well - deposit/ damage diameter of 142 mm
18		
19	C1, D5	front face has concentric rings . Small hole in center of plate 4.9mm; outer ring of craters is concentrated to 56.56 mm diameter; outer ring of deposits is 103mm while outermost ring of less concentrated deposits is 182 mm. Back face has major spalling - 52.64 mm circle with a few outcroppings sticking up.
20	F4, D5, C1	major cluster of deep craters on front face with one large oblong hole ; another area of concentrated less shallow cratering; 236 marks outer damage bounds; and 53 indicates concentrated deep cratering in middle; hole is 10.47mm; spalling on back face plus hole. Spalling diameter is 15.72; hole is 9mm across
21	F3, C1	front face has deep cratering all along axis of projectile travel. Deepest marks are concentrated inside a diameter of 56.95mm, 98% damage ring has a diameter of 239mm. Back face as a couple of dimples sticking out. But no spalling or penetration.

Density Effects Data		
Rear Wall **		
Test # in Series	Damage Classification	Comments
22	C1, D3	flat shallow large circle of impact; concentric circle of burn and black deposit damage. central impact diameter of 69.17mm, scorched black deposit diameter of 164 with burned metal diameter of 293mm; back side has spalling in an irregular kidney shaped pattern general diameter of spall is 56-58mm; some protrusion of surface metal from spall and a little cracking as well. No holes though.
23	C1, D1, F3	major cratering in an oblique line along projectile path. Blackened material after deep impact points with other deposits and pock marks/ craters prior to this point as if debris was deflected in two principal angles. ~52x66mm area of deepest penetration leading to a small crack and light leak on back face. Back diameters based on bulge and hole size (<0.01mm). 4 distinct bulges on back due to cratering on front.
24	C1, D1	no damage noted on backside of panel. Scattered deep craters on front panel and one circular area of concentrated, but more shallow hits. Outer diameter is 98%impact circle, inner is deep crater concentration diameter
25		
26		
27		
28	F5	completely destroyed, a crack through the large hole in center completely destroyed the wall. Lots of deposited debris. 4 major leaves of peeled back jagged points sticking up on back face. Deep puncture and two other longitudinal cracks as well. Damage area is over entire panel
29	C1, F3, D1	4.81x6.51mm elliptical crater in top face, with 2 more less deep craters located prior to the point along projectile's path. Scorching evident along pathway. Scorch is ellipse of 146x138mm, scorch is deposits formed on top of metal plate. 4.96 mm bump on back face with no penetration.
30	D5, C1	1 Full circular/ elliptical penetration; 7 areas of major pitting from other impacts; some overall indentation; 154 mm diameter burn pattern of light dust. Backside clean penetration with small bulge around one end of exit. Slight cracking observed near protrusion.
31	D3, C1	Front Side pocked circle indicating concentration ring; Further particles impacts out to 98% impacts diameter listed as Outer Diameter. Backside spalling, no light penetration.
32	F3, C1	2 major areas of impact - 1 central area with deep pitting, with one tiny light hole; 2nd area is upstream and shows numerous shallow crenulations. Backside shows spalling and 2 areas on outside diameter that are bent upwards
33	E3	Front side 98% impact diameter is "Inner"; lots of black scorch marks indicating intense temperatures; large circular array of large particle impact dots outside most scorched area; deepest circle of impacts in center inner diameter. Backside there is a annulus of raised metal in a ring shape with two areas of penetration, one large fracture area (25mmx10mm) and a smaller crack on top of one of the raised portions of the annulus

Density Effects Data		
Rear Wall **		
Test # in Series	Damage Classification	Comments
34	C1, D1, F3	83mm is diameter of major pitting and crenellation. No light penetration; Many impact points along 45 degree path of projectile. Concentrated pitting in center of impact; some of deepest penetrations occur upstream of the major impact points indicating large portions of the projectile must have broken off and scattered; 1 raised 5.79 mm bump on back plate, several smaller bumps, but no signs of material puncture or failure.
36		
36A		
36B	E1, F3	rear face has bump only, no penetration or spalling; bump diameter is measured value. Front face has total damage area in form of ellipse/ expanding cone of 230mm, with a concentrated damage area of 54mm - area shows cratering, large and small plus denting of the panel. there are grayish deposits in the cone/ ellipse
39	C1, D1, F3	top face has elliptical shaped damage area with diameter of 203mm, concentrated black deposits inside this ring. Some deep cratering and silver deposits at 22mm. Cratering impacts also site of sunken in area. No penetration or spalling, bent/ raised back side only.
39A	D5, F3, D1	hole with long spiderweb cracking; sunken in where impacted, damage deposits of black expand in a conical shape/ ellipse total damage ring of 237mm, with major deposit area out to 182mm., some cratering as well on front face. Rear face has hole and some long cracks like spiderweb, some minor spalling as well.
41	D3	46mm diameter concentrated area of cratering in a circle, 68mm concentrated deposit area around the location with concentric outer ring of damage out to 172mm for98%impacts. Lots of cratering and shallow pits; back face has spalling, with outer ring sticking up - jagged edges and bubbled up material
42		
43	E1, F3, C1	59.89 marks scorch diameter; all pitting and scorch contained in outer diameter of 204mm . More numerous, but shallower pits in center, deeper, but less common pits in outer ring, with more shallow pits scattered throughout damage ring. Some small bumps on back face correspond to deepest pits on front. ~4 such bumps.
44		
45		
45A	C1, F3, D1	Some raised areas on back face with a few small bumps raised further still, but no penetration. One hairline crack but no light leak through. Deep pitting on front side. 52.95 mm diameter of major deep pits in center of plate with some areas of more scattered, less densely packed deep pits along one side. 220 mm overall diameter containing all damage. 47mm and 11 mark the diameter of the rear face raised portion with the 11 marking the bump within the bump.

Density Effects Data					
Witness Plate (WP) ##					
Test # in Series	Outer Diam. (mm) (Front)	Inner Diam. (mm) (Front)	Outer Diam. (mm) (Back)	Inner Diam. (mm) (Back)	Comments
1	N/A	N/A	N/A	N/A	N/A
1A	N/A	N/A	N/A	N/A	N/A
1B	240	104.6	127	100.45	major hole and cracking in WP, scorches on rear face; deposits and scorches on front face; with cracking and several holes
1C	147	103	147	103	Critically failed piece with several large penetrations. Large ring of deposits about central impact points, diameters measured from outlying regions of particulate deposit and scorch marks respectively. 7 individual holes including cracking between 4 central penetrations. End plate is completely warped in all three dimensions. Back face has 4 scorch marks coincident with the major penetrations of the sheet. There are also numerous jagged edges of metal sticking up.
2	76	8.94	13.11	5.98	8.94mm hole in WP; debris field area slightly offset from hole with 76mm diameter, lots of deposits on front surface with what appears to be spalliing of prior sheet wedged in WP, 2 other craters on back face
2C					
3					
4	N/A	N/A	N/A	N/A	No damage noted
5	N/A	N/A	N/A	N/A	No damage noted
5A	N/A	N/A	N/A	N/A	No damage noted
6	N/A	N/A	N/A	N/A	No damage noted
7	119	93	121	102	Explosive exit of projectile left deposits on surface of top.Some small indentations as well. Back has cracks where jagged edges of plate are forced up and forward in a "crown" shape.Tallest stands 28mm above back face surface which is warped in three dimensions anyway.

Density Effects Data					
Witness Plate (WP) ##					
Test # in Series	Outer Diam. (mm) (Front)	Inner Diam. (mm) (Front)	Outer Diam. (mm) (Back)	Inner Diam. (mm) (Back)	Comments
8	86	N/A	11.7	0.01	86x57 ellipse of deposits with some dimpling, including 4 holes and 5 other deep pock marks. Backside shows nearly 20 bumps from other side's pock marks, plus 5 small holes with some hairline cracks. Back measurements are of largest holes.
9	0	0	0	0	a couple very shallow pits, barely even noticeable with the bare eye.
10					
11	0	0	0	0	no noticeable damage
12	0	0	0	0	no damage
13	206	8.03	10.21	10.21	warped in 3 dimensions, several hols in plate - 3-9mm in diameter, one crack, dimpling in line with holes. Front face has silver and blackish deposits all over - ring of damage is 206mm across
13A	247	10.78	113	16.31	10.78 and 8.98 mm holes, numerous dents and twisting. Burn and deposit patterns all over sheet. Damage diamter on back is 113mm, biggest puncture is 16.31 and 15.65 respectively hols with jagged edges out.
14	0	0	0	0	no damage noted
16	0	0	0	0	no damage noted
17	0	0	0	0	no damage noted
18					
19	114	72	121	98	Explosive failure; back face is cracked revealing peeled layers of metal sticking out. Front face is concave. Some indications of individual large particle impacts - dents, scratches, etc.
20	22.54	7.26	14.66	0	divot in WP, but no holes or spalling
21	0	0	0	0	no damage noted

Density Effects Data					
Witness Plate (WP) [##]					
Test # in Series	Outer Diam. (mm) (Front)	Inner Diam. (mm) (Front)	Outer Diam. (mm) (Back)	Inner Diam. (mm) (Back)	Comments
22	8	8	8	8	5 major dings in front face of WP but no penetrations. Diameters of the dings match up pretty well between front and back faces. Diameter measurements are sizes of the divet/ bump.
23	27.87	27.87	0	0	Front face shows a handful of scratches only, depth is minimal. Clusterd in a circle of diameter 27.87 mm
24	0	0	0	0	no damage noted
25					
26					
27					
28	161	126.6	172	137	warped in 3 dimensions, several small holes and burn marks on metal; one large hole with shards of jagged metal sticking up from 5 areas, cracking and peeled back metal. Front side exhibits some denting and lots of deposits, plus the major hols and cracks. extent of damage is entire 12x12 plate
29	0	0	0	0	No damage noted. No impact marks, scratches, scorches or holes
30	2.34	2.34	2.21	2.21	Scorched pattern on front, dimple in plate, but no penetration of light; backside shows 2 dimples, but no scorches nor penetration; frontside "burned" area is ~70mm in diameter in semimajor axis; ~64mm in semiminor axis.
31	70	37	0	0	Hole in WP; indications of 5 separate large impacts causing deep penetrations or puncture, plus 5 other dings. FAILED.
32	0	0	0	0	Small scratch along projectile pathway, but shallow bump less than 0.02 mm in depth; no penetration of WP.
33	0	0	0	0	No indicated intrusions on WP. No holes, pitting, discoloration, puncture, etc.
34	0	0	0	0	No indicated intrusions on WP. No holes, pitting, discoloration, puncture, etc.

Density Effects Data					
Witness Plate (WP) [##]					
Test # in Series	Outer Diam. (mm) (Front)	Inner Diam. (mm) (Front)	Outer Diam. (mm) (Back)	Inner Diam. (mm) (Back)	Comments
36					
36A					
36B	0	0	0	0	a couple scratches, but not likely form test
39	0	0	0	0	no damage noted
39A	164	73	154	68	Major failure - several large puncture holes, largest is 12.89mm, damage diameter is 164mm with concetrated holes and deposits at 73mm, fronmt side scorching in expanding cone of black/ gold deposit; white/silver deposits near holes. Holes are torn open and have jagged edges - lots of cratering evidence and cracks on back face.
41	8.02	0	0	0	a ring of minor scratches on front face, but no cratering, pitting or deposits found on wither side
42					
43	0	0	0	0	Back - no Apparent Damage
44					
45					
45A	0	0	0	0	Back - no Apparent Damage

Density Effects Data			
Test Status			
Test # in Series	Rear Wall Fail?	Witness Plate Fail?	Overall Test Comment - Reason for lack of Data [++]
1			Launch package broke-up during testing causing debris to impact target and invalidate test.
1A			Projectile Impacted the stripper plate; target was impacted with launch package debris and cannot be re-tested
1B	YES	YES	Flash xray failed; otherwise good test. Target failed
1C	YES	YES	Good test
2	YES	YES	Good Test; target failed
2C	YES		Target FAILED; good test. No pieces of test in labs
3			Velocity deviation of .32+ km/s outside test requirement of +/- 0.2km/s; target failed. No pieces of test in labs.
4	NO	NO	Bad shot due to target velocity exceeded test requirement margin; however we opted to take data since it was barely outside margin. Target passed
5	NO	NO	Bad Shot - PASS; Debris cloud impacted part of the stuffed whipple metal frame. Test will be repeated. Target passed. Final mass values not contained in report. Could be measured in the lab if more time were available.
5A	NO	NO	Xray failed, but test data appears to be good. Target passed
6	NO	NO	Good test – PASS
7	YES	YES	Good test – FAIL
8	YES	YES	Good test – FAIL
9	YES	NO	Good test – FAIL
10			Data unavailable due to cordin camera, flash x-ray and Hadlin camera pre-triggered prior to firing the launcher. Projectile integrity could not be verified. Only in possession of rear wall, no other pieces are in lab.
11	NO	NO	Good Test - FAIL
12	NO	NO	velocity deviation outside test requirement of +/-0.2km/s but barely so, data looks okay. PASS
13	YES	YES	velocity deviation outside test requirement of +/-0.2km/s but barely so, data looks okay. FAIL
13A	YES	YES	velocity deviation outside test requirement of +/-0.2km/s but barely so, data looks okay. FAIL
14	NO	NO	Good test - PASS

Density Effects Data			
Test Status			
Test # in Series	Rear Wall Fail?	Witness Plate Fail?	Overall Test Comment - Reason for lack of Data ++
16	NO	NO	Good test - PASS
17	NO	NO	Good test - PASS
18			Velocity Deviation exceeded +/-0.2km/s. no data available. Pieces are not in lab
19	YES	YES	Good test – FAIL
20	YES	NO	Good test – FAIL
21	NO	NO	Good test - PASS
22	YES	NO	Good test – FAIL
23	YES	NO	Good test – FAIL
24	NO	NO	Good test - PASS
25			Launch package broke-up during testing causing debris to impact target and invalidate test. Test pieces not in lab.
26			Velocity Deviation exceeded +/-0.2km/s. no data available. Pieces are not in lab
27	YES		Good test – FAIL. Test pieces not in lab.
28	YES	YES	Good test - FAIL; no supporting test paperwork available so many measurements are unavailable. Descriptions of test pieces are discussed as well as speeds and diameters used based on requested values
29	NO	NO	Velocity deviation >=/-0.2km/s but barely, data looks okay. PASS
30	YES	NO	Good test. Target failed
31	YES	YES	Good test. Target failed
32	YES	NO	Good test. Target failed
33	YES	NO	Good test. Target failed
34	NO	NO	Good test. Target PASSED
36	NO	NO	PASSED; no data available; projectile impacted stripper plate; launch debris hit test package
36A	NO	NO	PASSED; no data available; projectile impacted stripper plate; launch debris hit test package
36B	NO	NO	No test paperwork available so many data points were undetermined. Velocities and diameters are based on requested values, not actual measurements, as they are unavailable.

Density Effects Data			
Test Status			
Test # in Series	Rear Wall Fail?	Witness Plate Fail?	Overall Test Comment - Reason for lack of Data ++
39	NO	NO	Good test. Target PASSED. No report data available so many data points were undetermined. Velocities and diameters are based on requested values, not actual measurements, as they are unavailable.
39A	YES	YES	Good test presumably, Target FAILED. No written report data was available so many data points were undetermined. Velocities and diameters are based on requested values, not actual measurements, as they are unavailable.
41	YES	NO	Good test. Target failed. No supporting test report paperwork found. No written report data was available so many data points were undetermined. Velocities and diameters are based on requested values, not actual measurements, as they are unavailable.
42	NO	NO	Good test. Target PASSED; No data available; pieces are not in lab.
43	NO	NO	Good test. Target PASSED
44	YES		Good test. Target failed; No data available, test pieces are not in lab.
45	YES		target destroyed by launch package debris; no data available. No test pieces in lab
45A	NO	NO	velocity deviation >=/-0.2km/s but barely, data looks okay. PASS

THIS PAGE INTENTIONALLY LEFT BLANK

APPENDIX D - TESTBED REAR WALL AND BUMPER SHIELD PICTURES AFTER IMPACT

(a) 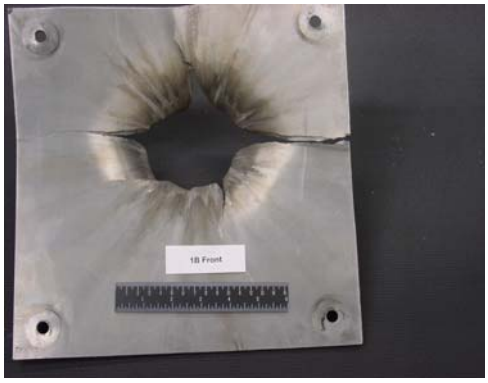

(b) 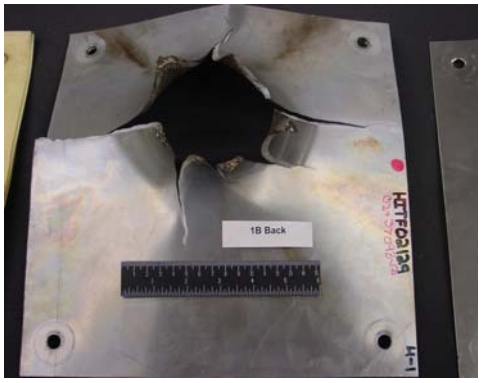

Figure D1. Sample 1B Views of Rear Wall Front (a) and Back (b) Faces after Hypervelocity Impact.

(a) 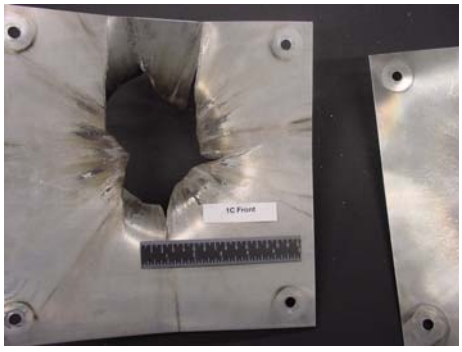

(b) 

Figure D2. Sample 1C Views of Rear Wall Front (a) and Back (b) Faces after Hypervelocity Impact.

(a) 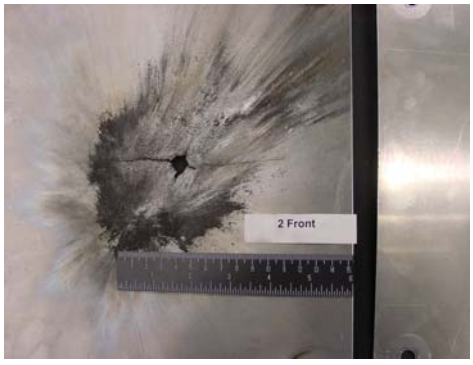

(b) 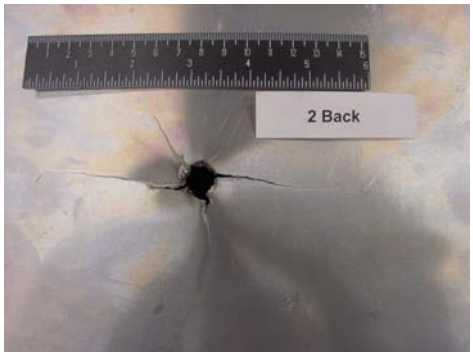

Figure D3. Sample 2 Views of Rear Wall Front (a) and Back (b) Faces after Hypervelocity Impact.

(a) 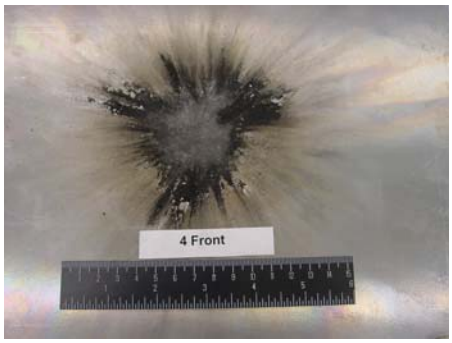

(b) 

Figure D4. Sample 4 Views of Rear Wall Front (a) and Back (b) Faces after Hypervelocity Impact.

(a) 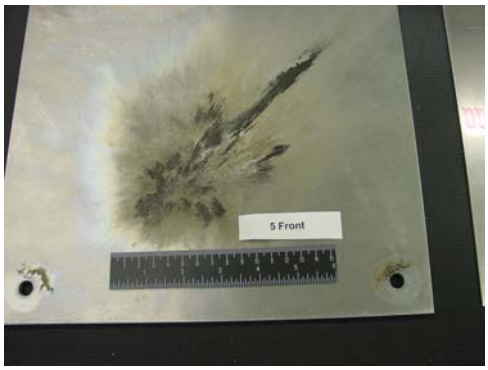

(b) 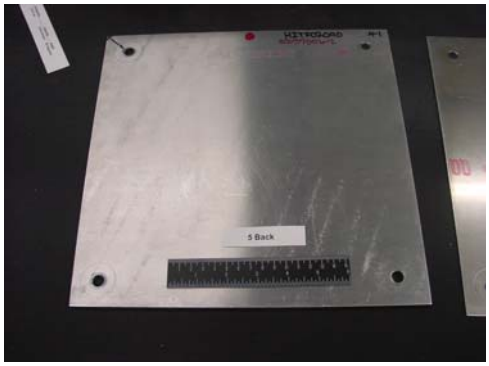

Figure D5. Sample 5 Views of Rear Wall Front (a) and Back (b) Faces after Hypervelocity Impact.

(a) 

(b) 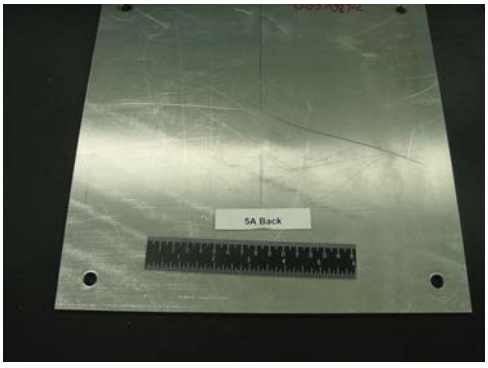

Figure D6. Sample 5A Views of Rear Wall Front (a) and Back (b) Faces after Hypervelocity Impact.

(a) 

(b) 

Figure D7. Sample 6 Views of Rear Wall Front (a) and Back (b) Faces after Hypervelocity Impact.

(a) 

(b) 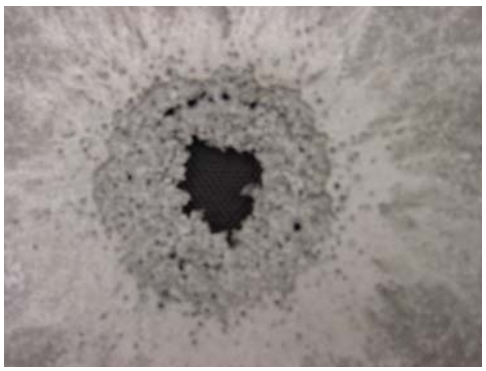

(c) 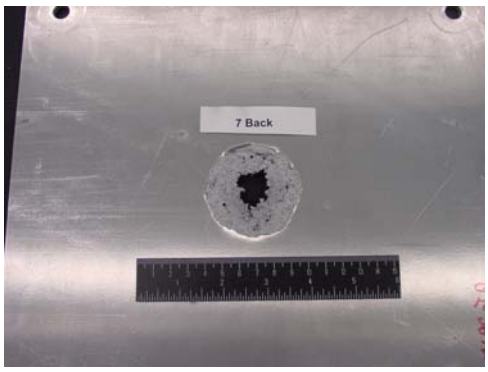

(d) 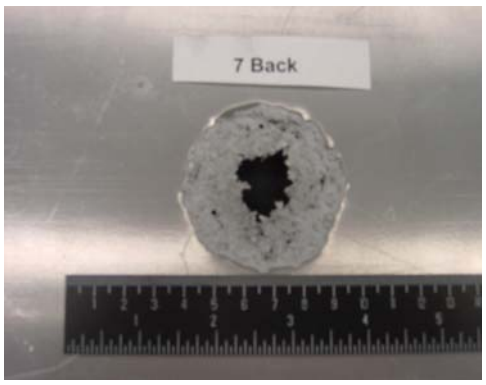

Figure D8. Sample 7 Views of Rear Wall Front (a & b) and Back (c & d) Faces after Hypervelocity Impact.

(a) 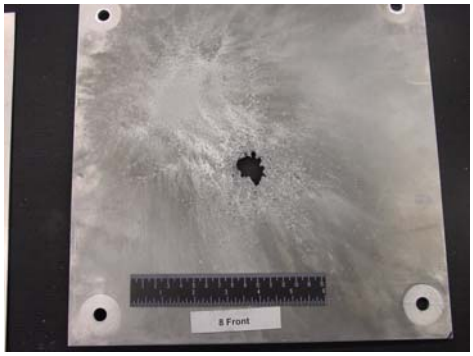

(b) 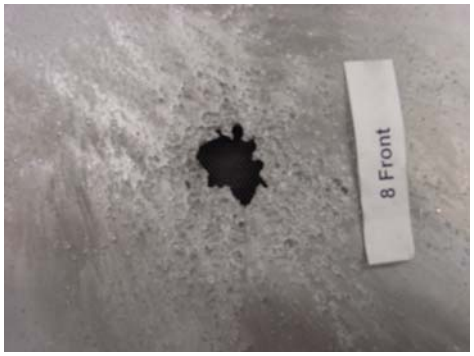

(c) 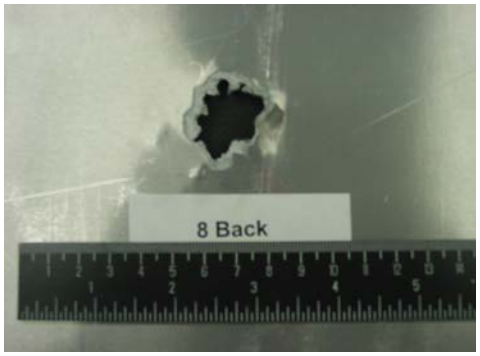

Figure D9. Sample 8 Views of Rear Wall Front (a & b) and Back (c) Faces after Hypervelocity Impact.

(a) 

(b) 

(c) 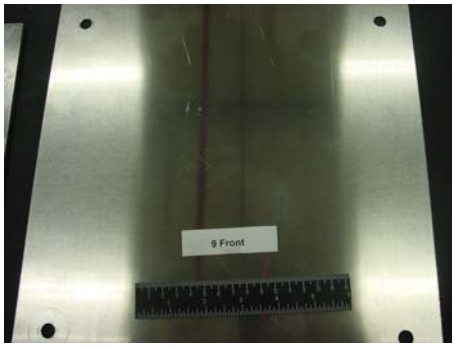

Figure D10. Sample 9 Views of Rear Wall Front (a & b) and Back (c) Faces after Hypervelocity Impact.

(a) 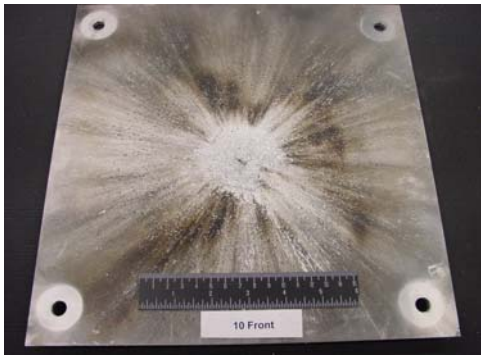

(b) 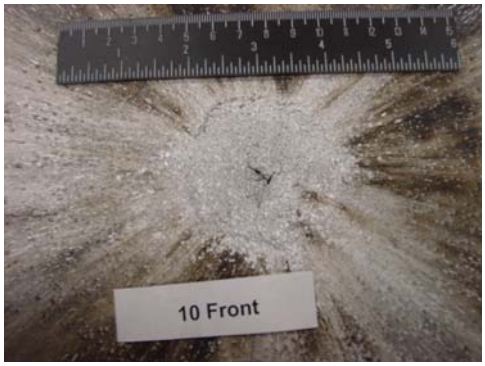

(c) 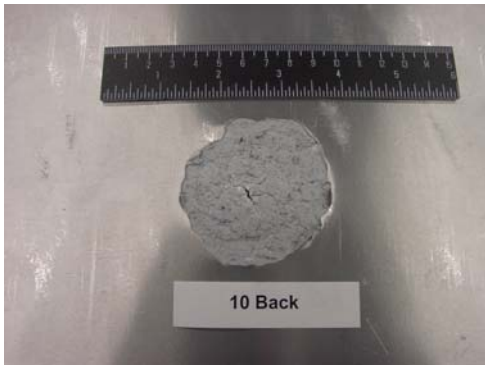

Figure D11. Sample 10 Views of Rear Wall Front (a & b) and Back (c) Faces after Hypervelocity Impact.

(a) 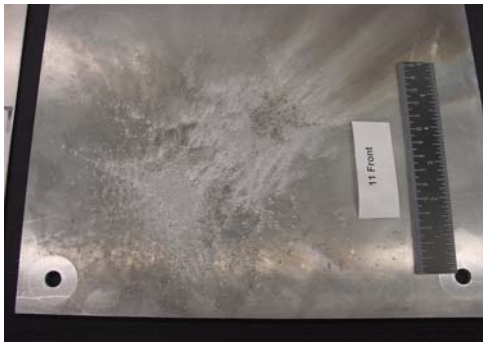

(b) 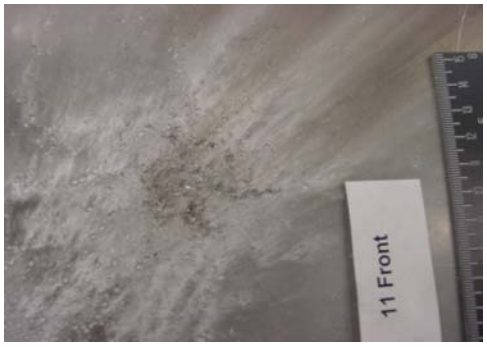

(c) 

Figure D12. Sample 11 Views of Rear Wall Front (a & b) and Back (c) Faces after Hypervelocity Impact.

(a) 

(b) 

(c) 

Figure D13. Sample 12 Views of Rear Wall Front (a & b) and Back (c) Faces after Hypervelocity Impact.

(a) 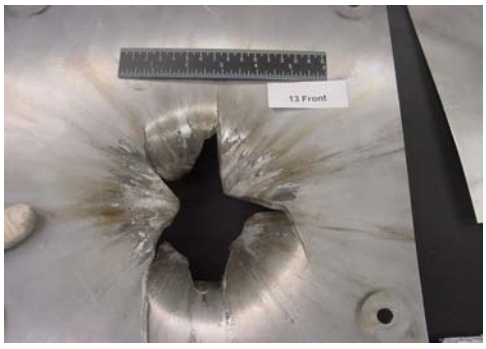

(b) 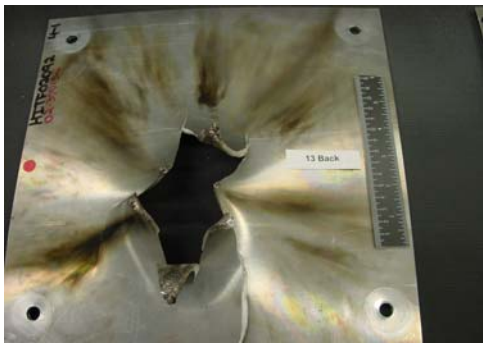

Figure D14. Sample 13 Views of Rear Wall Front (a) and Back (b) Faces after Hypervelocity Impact.

(a) 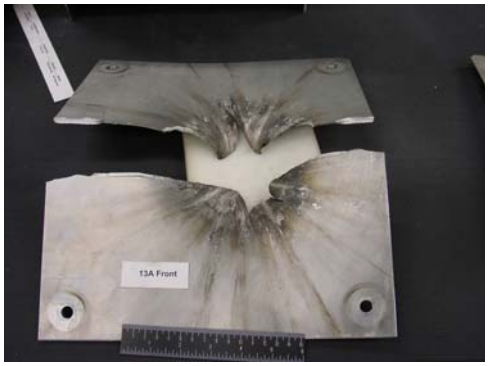

(b) 

(c) 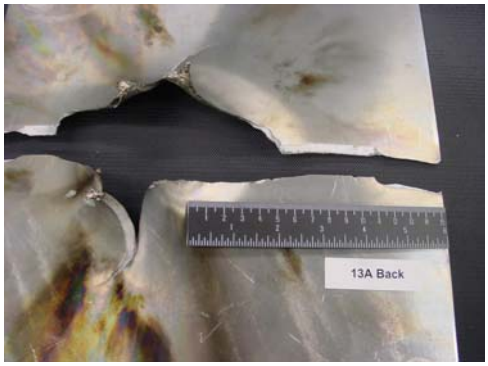

Figure D15. Sample 13A Views of Rear Wall Front (a & b) and Back (c) Faces after Hypervelocity Impact.

(a) 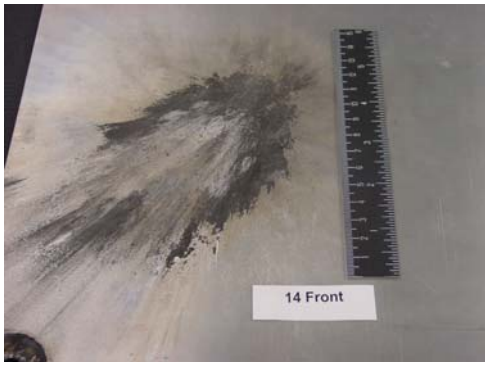

(b) 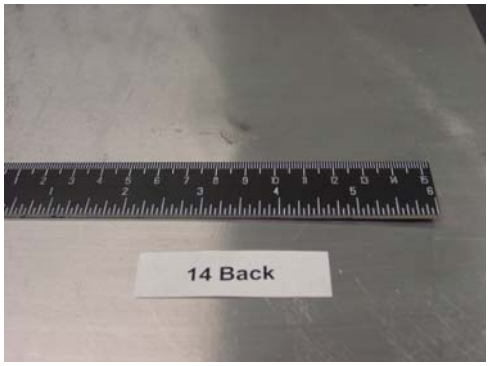

Figure D16. Sample 14 Views of Rear Wall Front (a) and Back (b) Faces after Hypervelocity Impact.

(a) 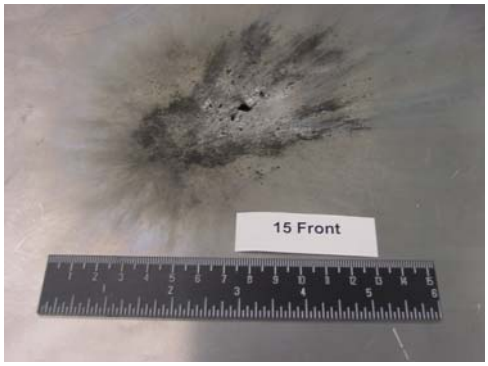

(b) 

(c) 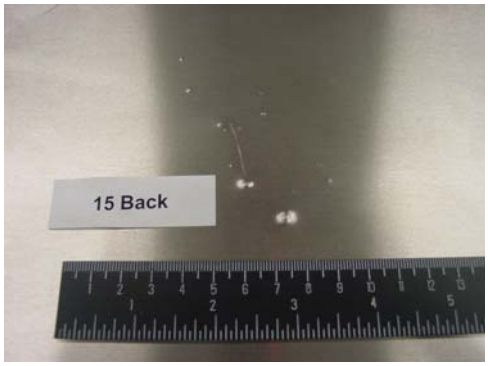

(d) 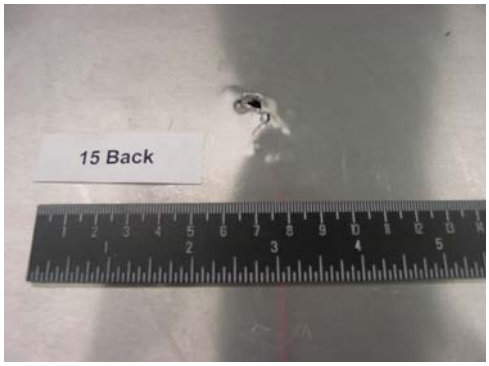

Figure D17. Sample 15 Views of Rear Wall Front (a & b) and Back (c & d) Faces after Hypervelocity Impact.

(a) 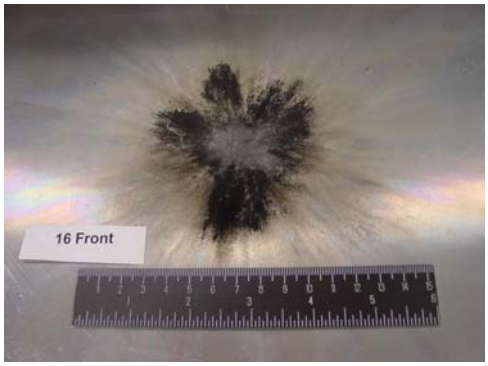

(b) 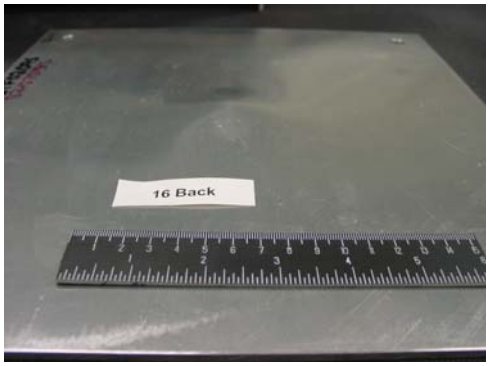

Figure D18. Sample 16 Views of Rear Wall Front (a) and Back (b) Faces after Hypervelocity Impact.

(a) 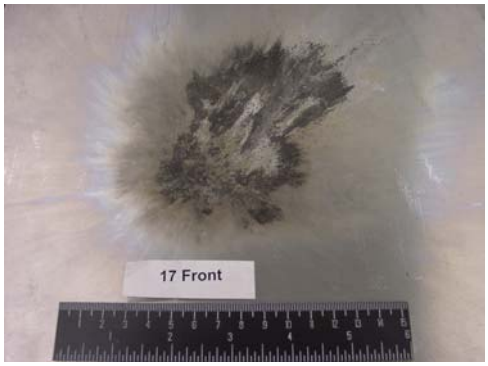

(b) 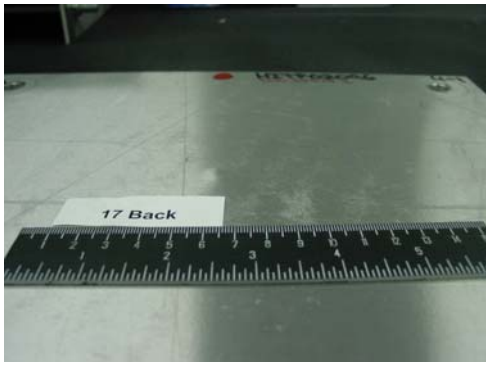

Figure D19. Sample 17 Views of Rear Wall Front (a) and Back (b) Faces after Hypervelocity Impact.

(a) 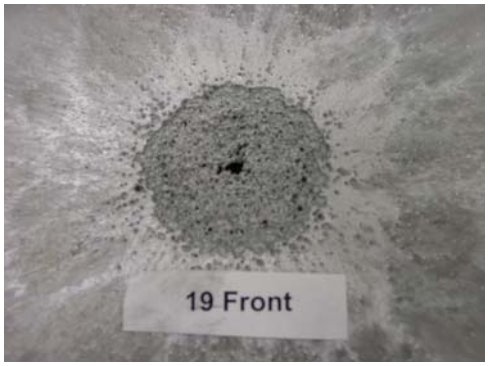

(b) 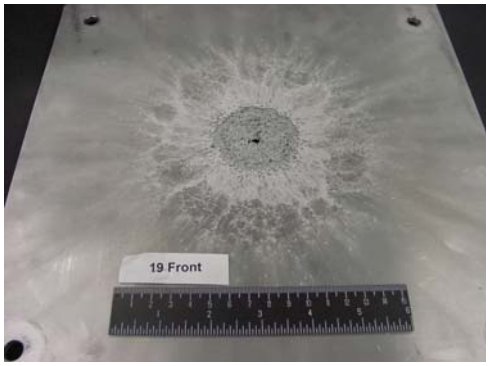

(c) 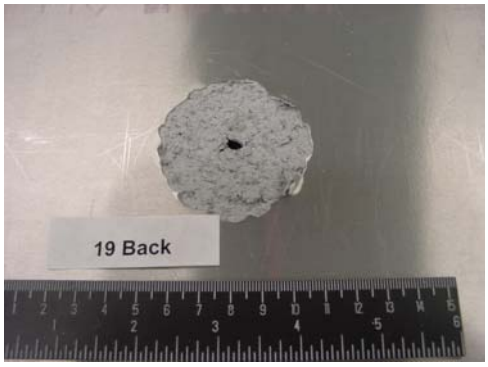

Figure D20. Sample 19 Views of Rear Wall Front (a & b) and Back (c) Faces after Hypervelocity Impact.

(a) 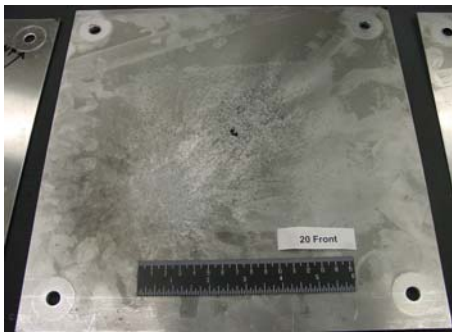

(b) 

(c) 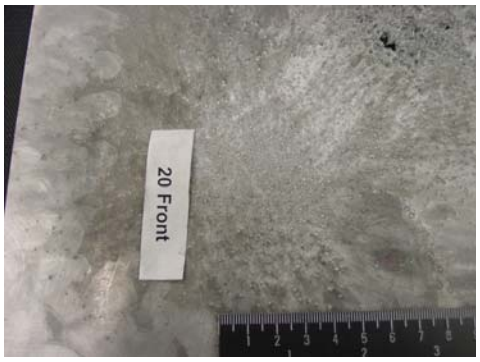

(d) 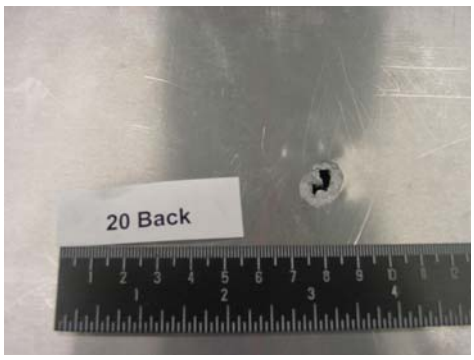

Figure D21. Sample 20 Views of Rear Wall Front (a,b, & c) and Back (d) Faces after Hypervelocity Impact.

(a) 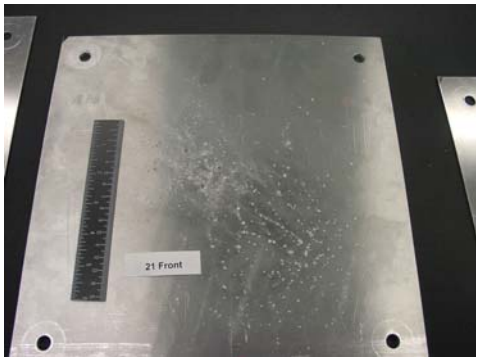

(b) 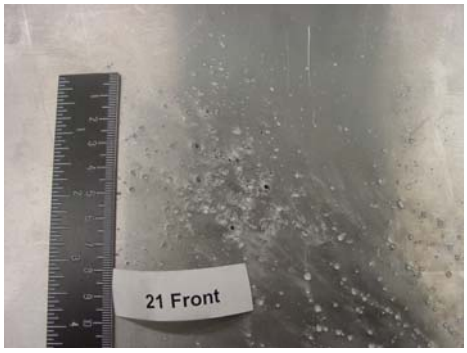

(c) 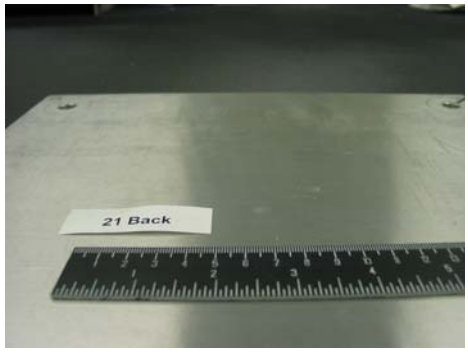

Figure D22. Sample 21 Views of Rear Wall Front (a & b) and Back (c) Faces after Hypervelocity Impact.

(a) 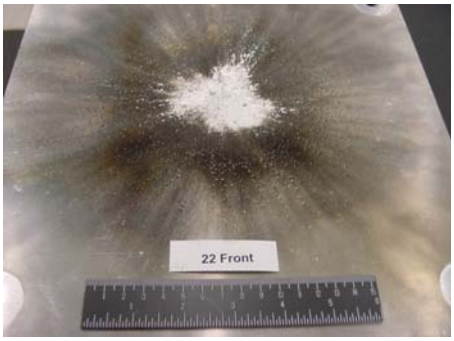

(b) 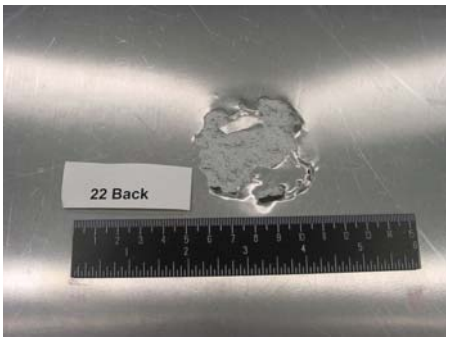

Figure D23. Sample 22 Views of Rear Wall Front (a) and Back (b) Faces after Hypervelocity Impact.

(a) 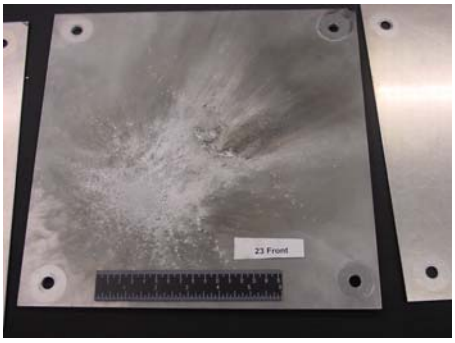

(b) 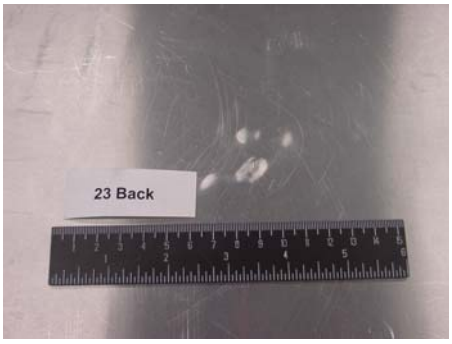

Figure D24. Sample 23 Views of Rear Wall Front (a) and Back (b) Faces after Hypervelocity Impact.

(a) 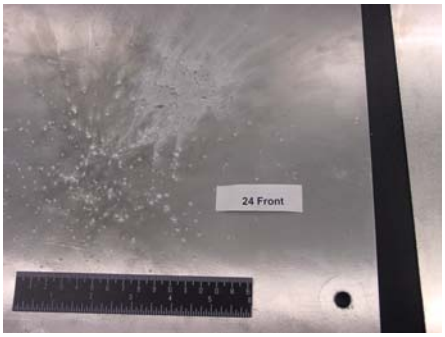

(b) 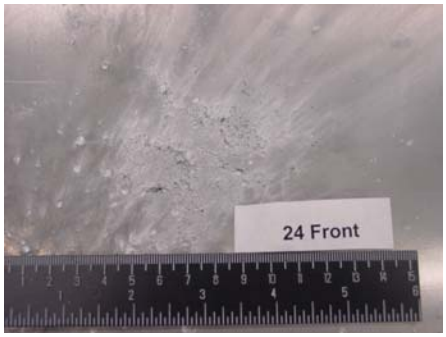

(c) 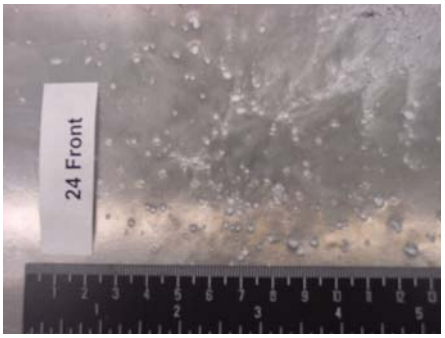

(d) 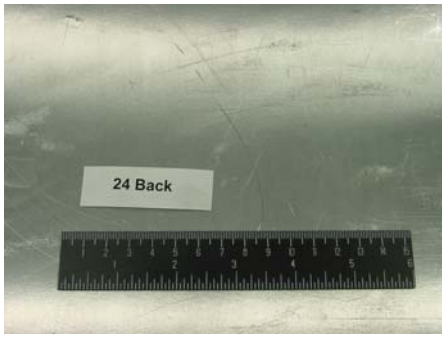

Figure D25. Sample 24 Views of Rear Wall Front (a,b, & c) and Back (d) Faces after Hypervelocity Impact.

(a) 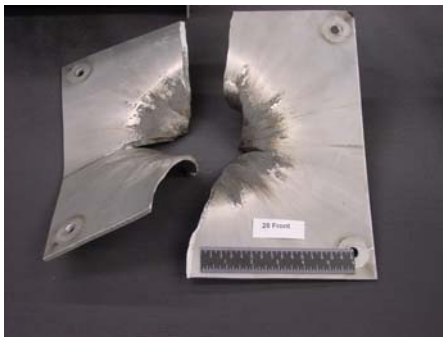

(b) 

(c) 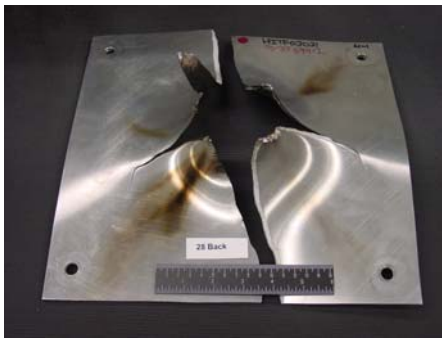

Figure D26. Sample 28 Views of Rear Wall Front (a & b) and Back (c) Faces after Hypervelocity Impact.

(a) 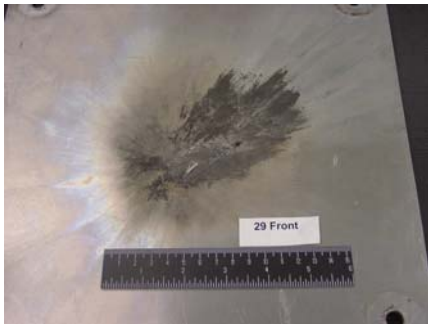

(b) 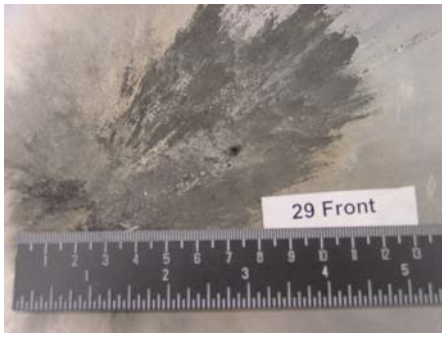

(c) 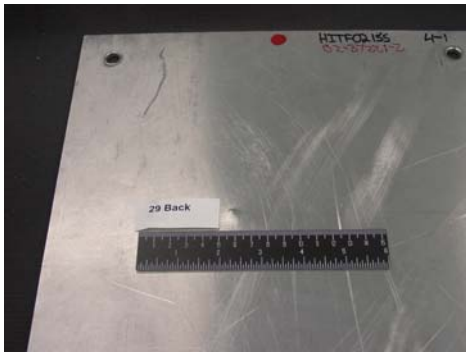

Figure D27. Sample 29 Views of Rear Wall Front (a & b) and Back (c) Faces after Hypervelocity Impact.

(a) 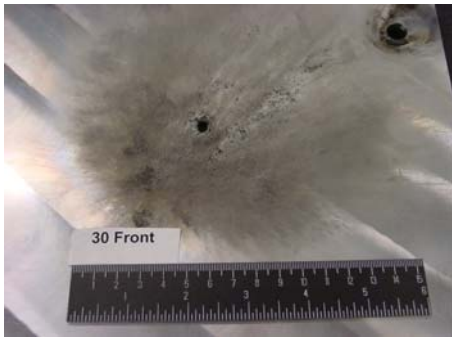

(b) 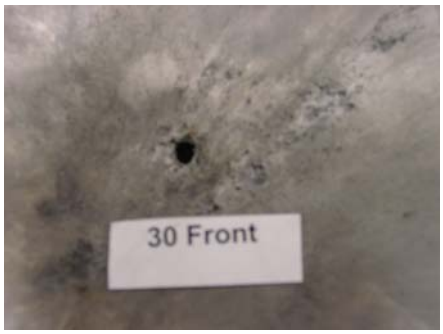

(c) 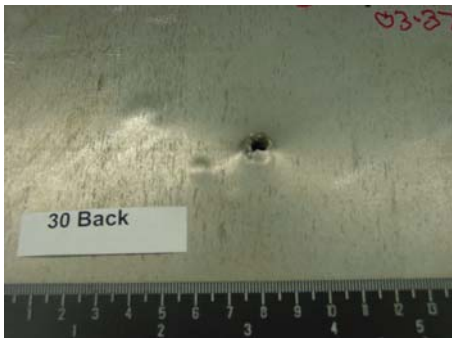

Figure D28. Sample 30 Views of Rear Wall Front (a & b) and Back (c) Faces after Hypervelocity Impact.

(a) 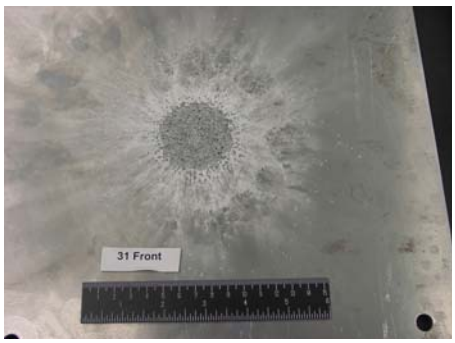

(b) 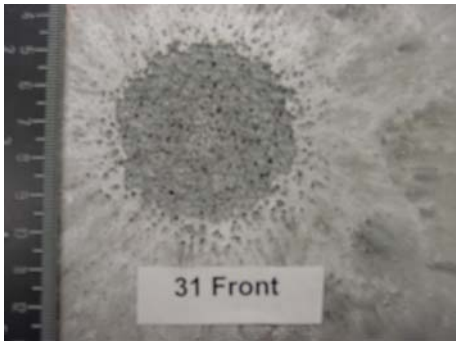

(c) 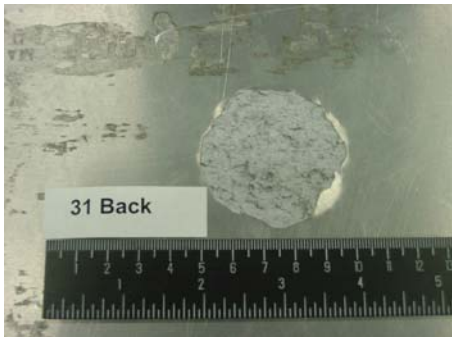

Figure D29. Sample 31 Views of Rear Wall Front (a & b) and Back (c) Faces after Hypervelocity Impact.

(a) 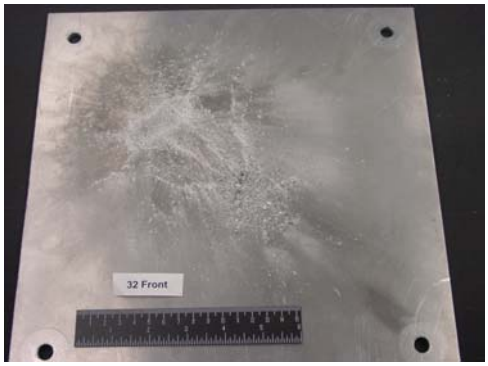

(b) 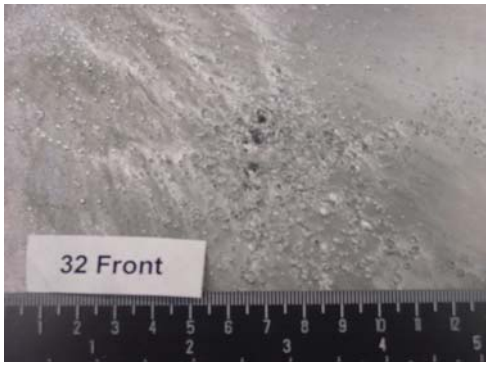

(c) 

Figure D30. Sample 32 Views of Rear Wall Front (a & b) and Back (c) Faces after Hypervelocity Impact.

(a) 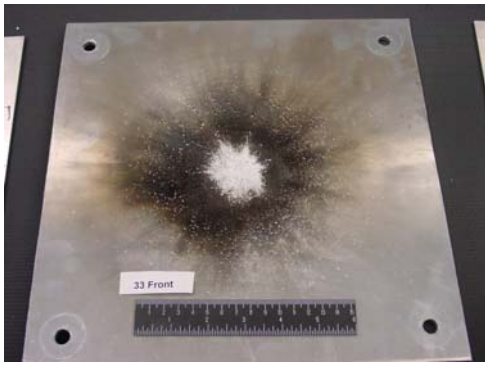

(b) 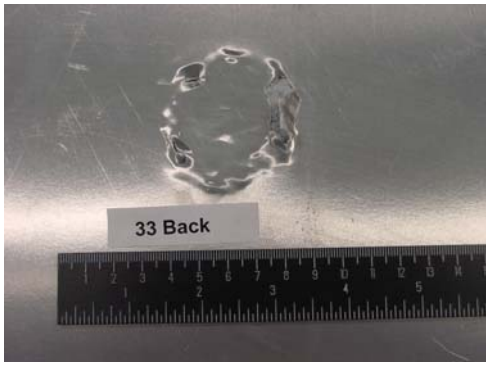

Figure D31. Sample 33 Views of Rear Wall Front (a) and Back (b) Faces after Hypervelocity Impact.

(a) 

(b) 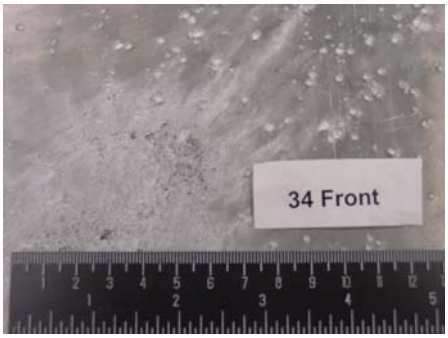

(c) 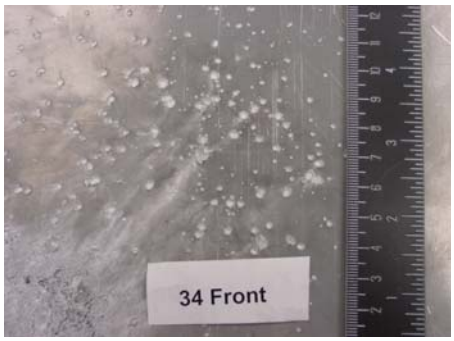

(d) 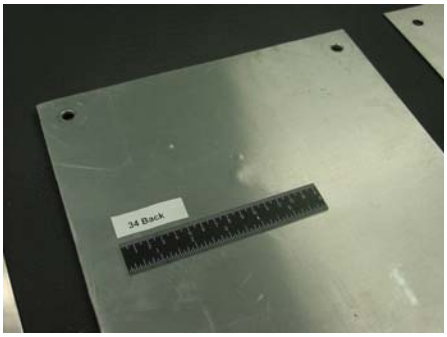

Figure D32. Sample 34 Views of Rear Wall Front (a,b, & c) and Back (d) Faces after Hypervelocity Impact.

(a) 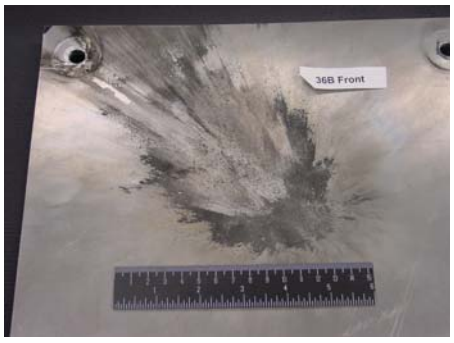

(b) 

Figure D33. Sample 36B Views of Rear Wall Front (a) and Back (b) Faces after Hypervelocity Impact.

(a) 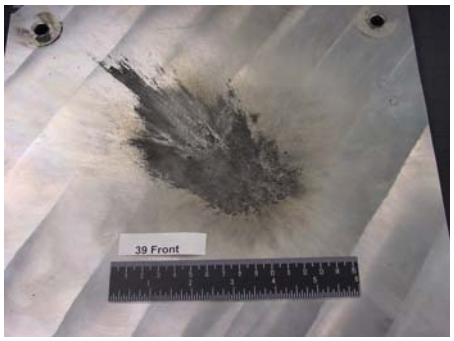

(b) 

Figure D34. Sample 39 Views of Rear Wall Front (a) and Back (b) Faces after Hypervelocity Impact.

(a) 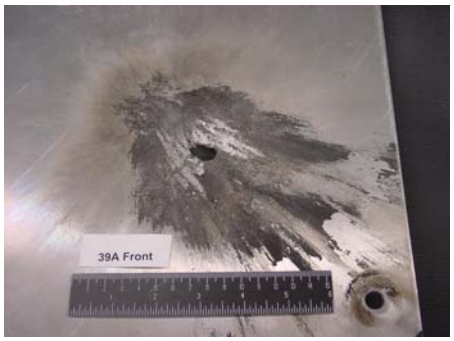

(b) 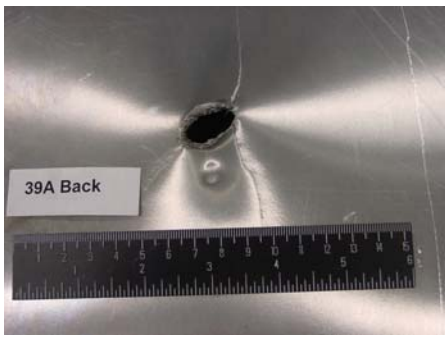

Figure D35. Sample 39A Views of Rear Wall Front (a) and Back (b) Faces after Hypervelocity Impact.

(a) 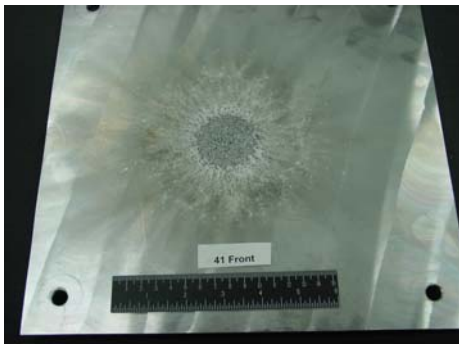

(b) 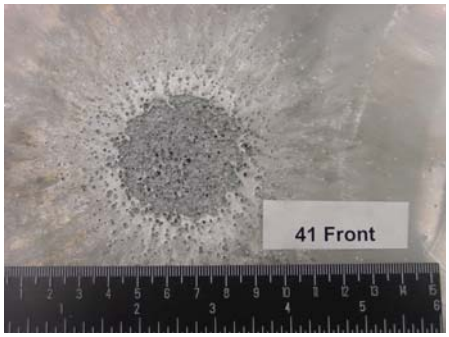

(c) 

(d) 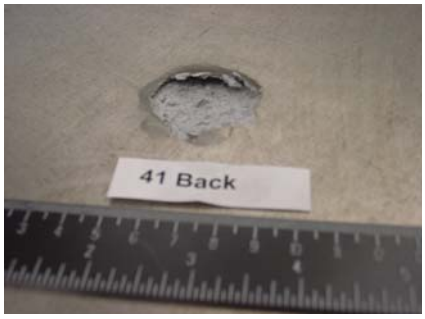

Figure D36. Sample 41 Views of Rear Wall Front (a & b) and Back (c & d) Faces after Hypervelocity Impact.

(a) 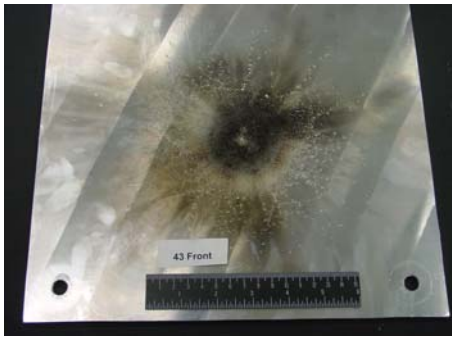

(b) 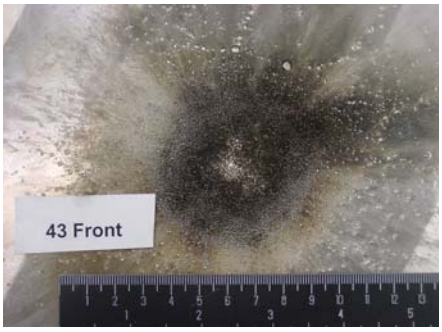

(c) 

Figure D37. Sample 43 Views of Rear Wall Front (a & b) and Back (c) Faces after Hypervelocity Impact.

(a) 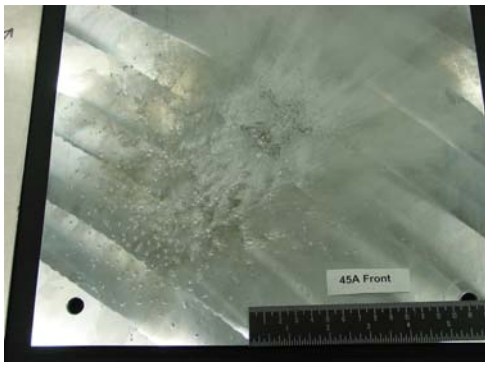

(b) 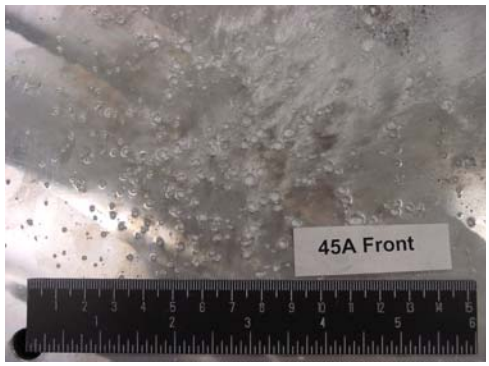

(c) 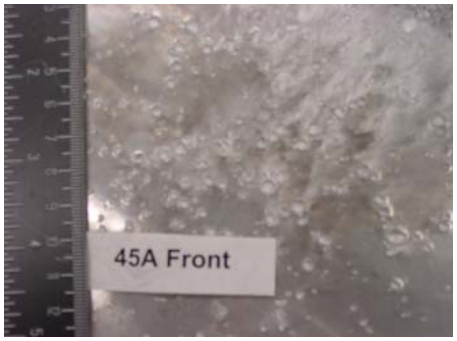

(d) 

Figure D38. Sample 45A Views of Rear Wall Front (a, b & c) and Back Faces (d) after Hypervelocity Impact.

THIS PAGE INTENTIONALLY LEFT BLANK

APPENDIX E - ENTERING BALLISTIC LIMIT CURVES

1. WHIPPLE SHIELDS

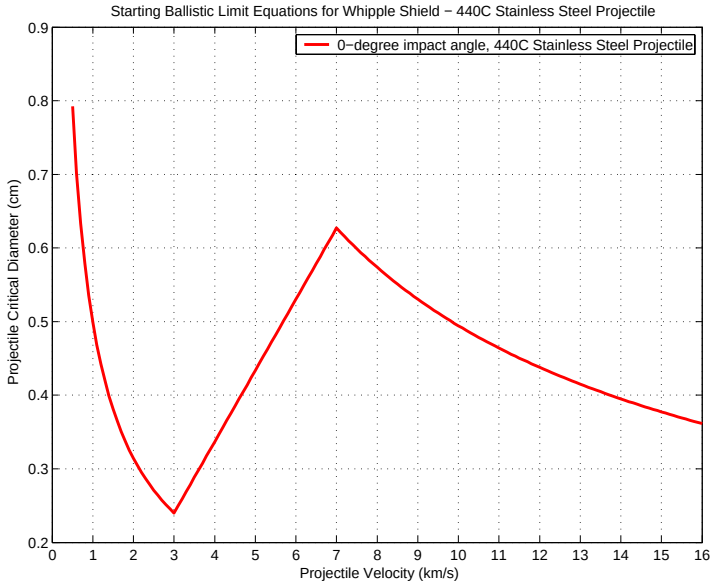

Figure E1. Entering Whipple Shield Ballistic Limit Equations for 440C Stainless Steel Projectiles at 0-degree Impact Angle.

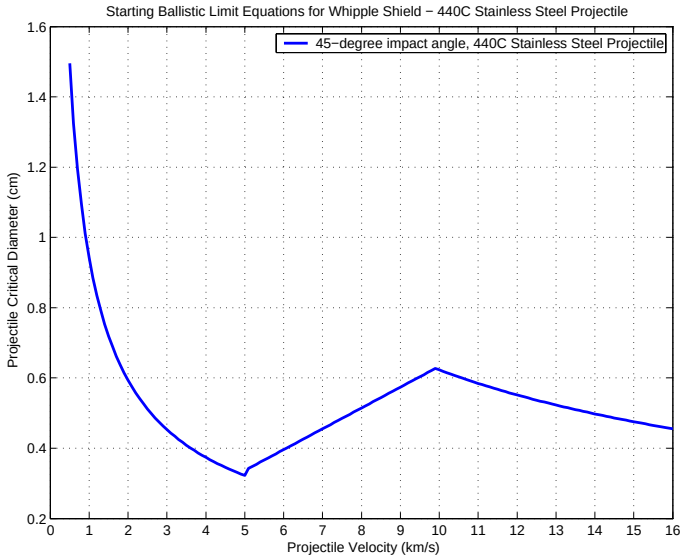

Figure E2. Entering Whipple Shield Ballistic Limit Equations for 440C Stainless Steel Projectiles at 45-degree Impact Angle.

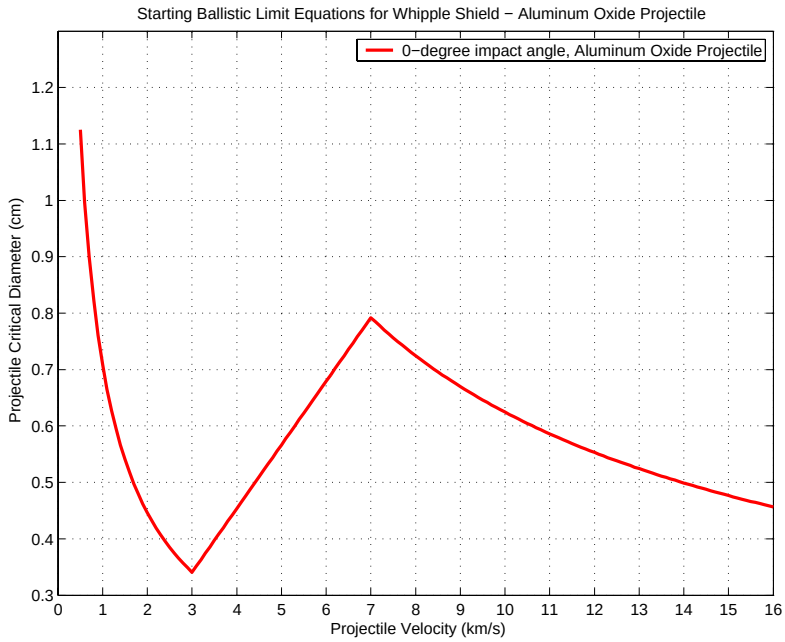

Figure E3. Entering Whipple Shield Ballistic Limit Equations for Aluminum Oxide Projectiles at 0-degree Impact Angle.

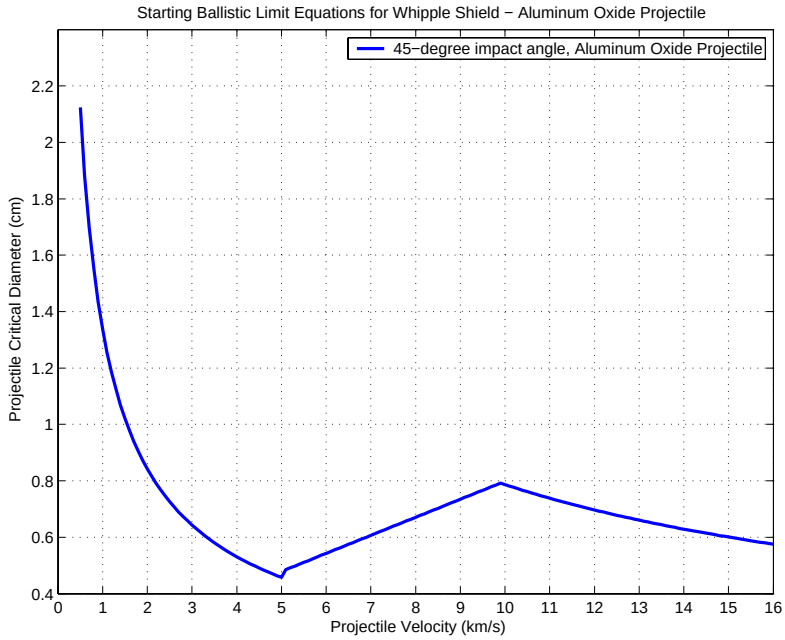

Figure E4. Entering Whipple Shield Ballistic Limit Equations for Aluminum Oxide Projectiles at 45-degree Impact Angle.

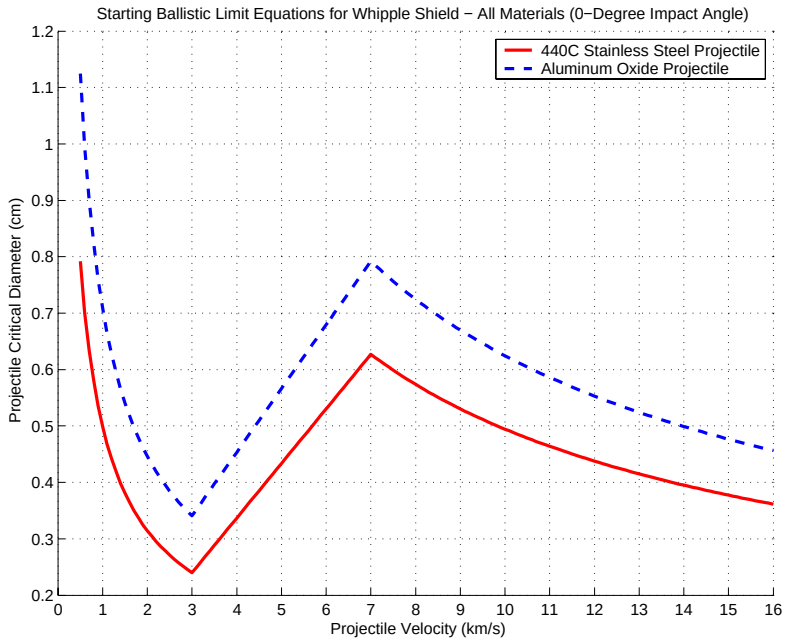

Figure E5. Entering Whipple Shield Ballistic Limit Equations for Projectiles at 0-degree Impact Angle.

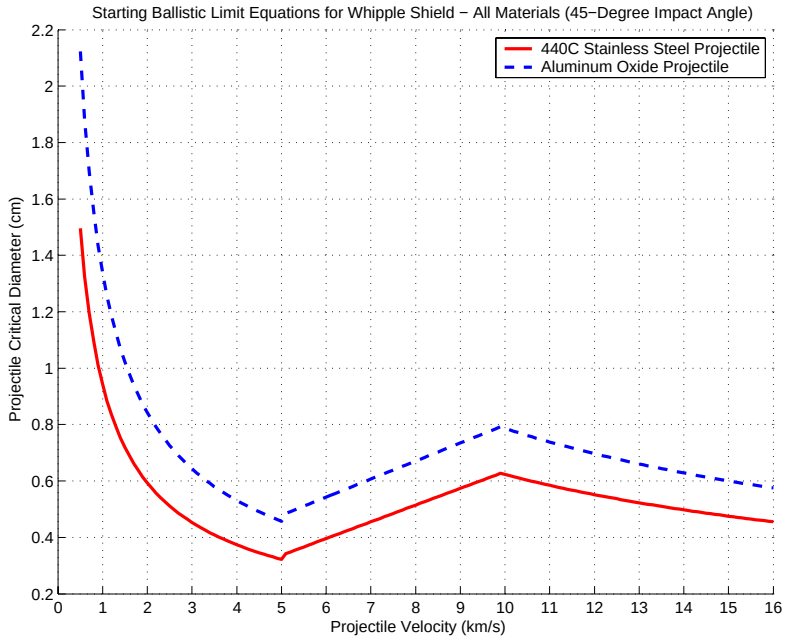

Figure E6. Entering Whipple Shield Ballistic Limit Equations for Projectiles at 45-degree Impact Angle.

2. ENHANCED STUFFED WHIPPLE SHIELDS

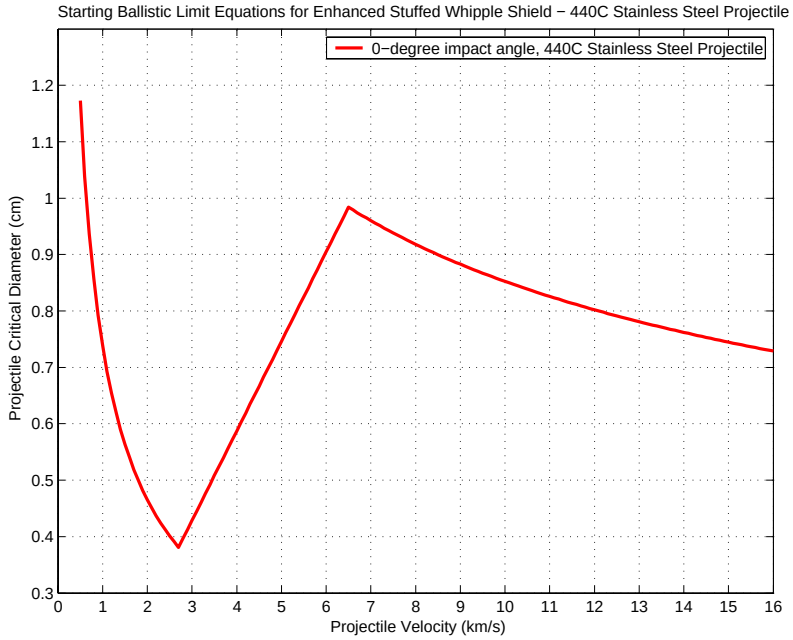

Figure E7. Entering Enhanced Stuffed Whipple Shield Ballistic Limit Equations for 440C Stainless Steel Projectiles at 0-degree Impact Angle.

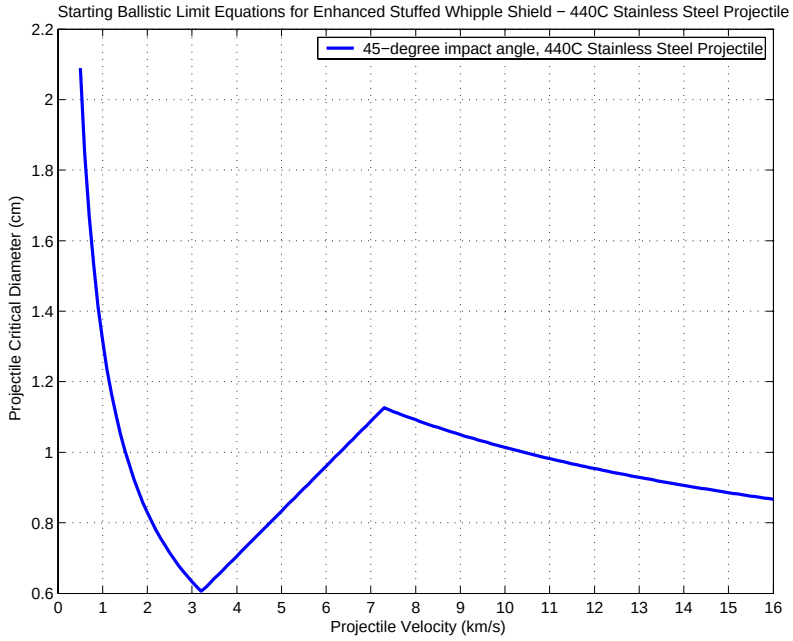

Figure E8. Entering Enhanced Stuffed Whipple Shield Ballistic Limit Equations for 440C Stainless Steel Projectiles at 45-degree Impact Angle.

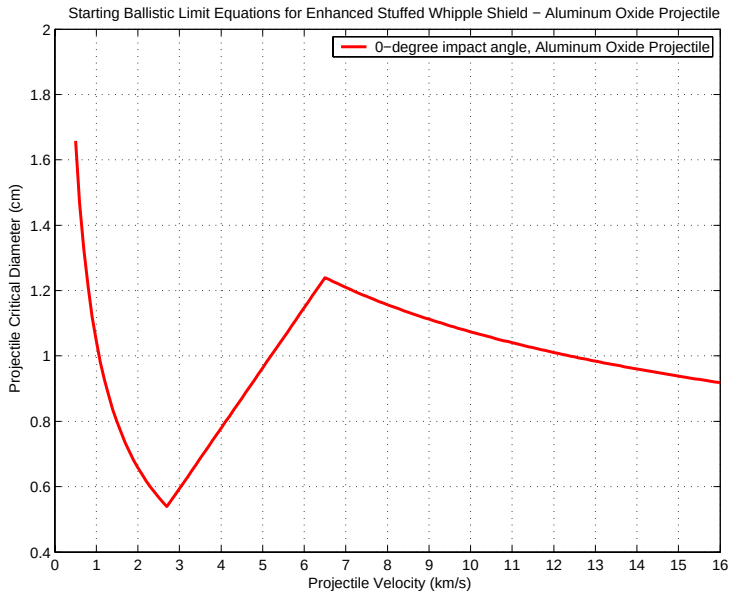

Figure E9. Entering Enhanced Stuffed Whipple Shield Ballistic Limit Equations for Aluminum Oxide Projectiles at 0-degree Impact Angle.

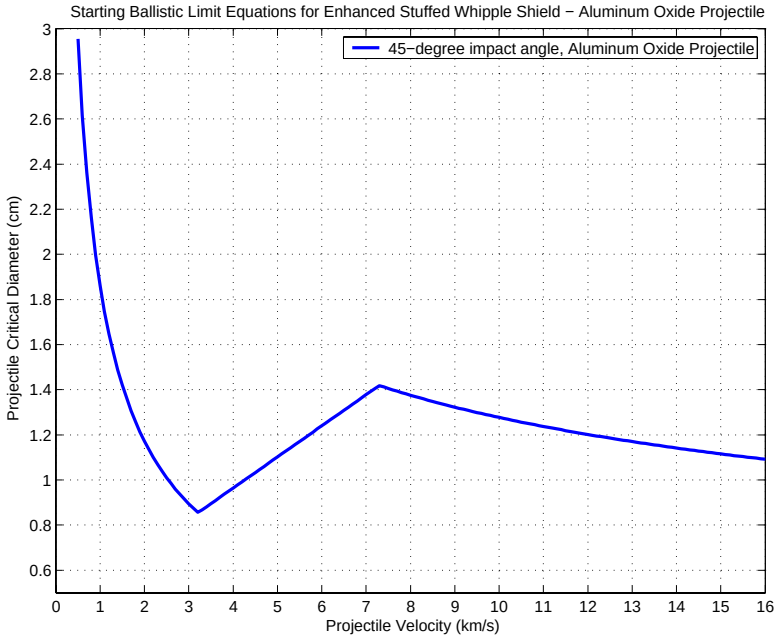

Figure E10. Entering Enhanced Stuffed Whipple Shield Ballistic Limit Equations for Aluminum Oxide Projectiles at 45-degree Impact Angle.

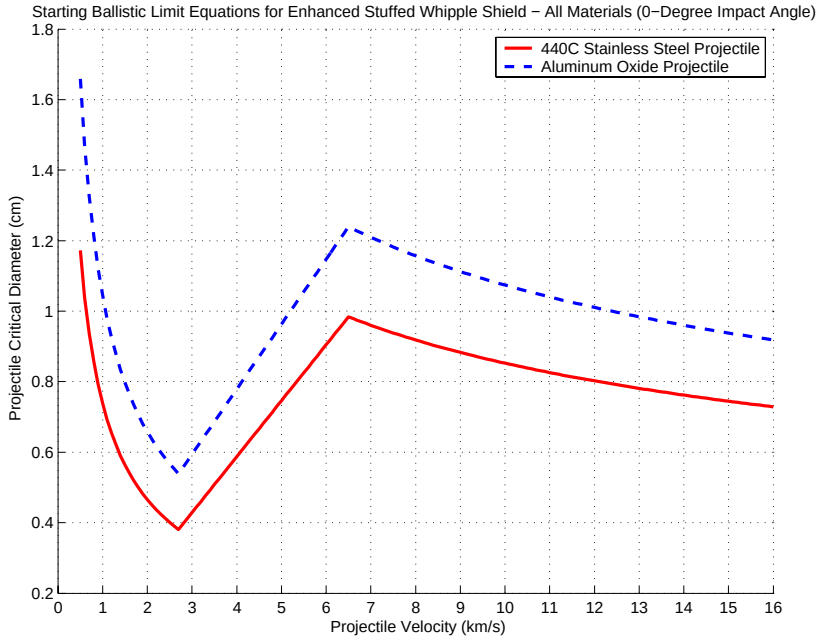

Figure E11. Entering Enhanced Stuffed Whipple Shield Ballistic Limit Equations Projectiles at 0-degree Impact Angle.

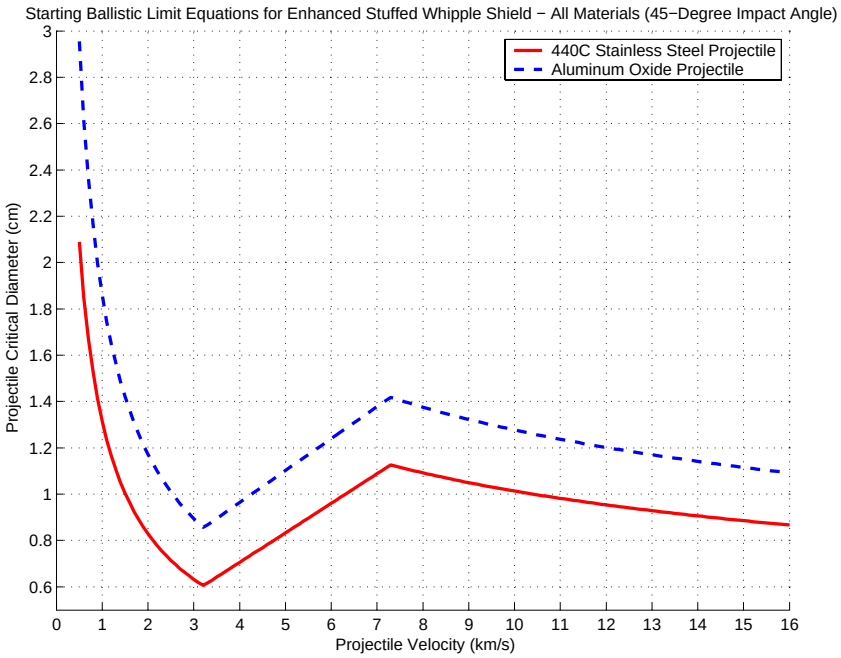

Figure E12. Entering Enhanced Stuffed Whipple Shield Ballistic Limit Equations Projectiles at 45-degree Impact Angle

APPENDIX F - ENTERING BALLISTIC LIMIT CURVES WITH RAW DATA OVERLAY

1. WHIPPLE SHIELDS

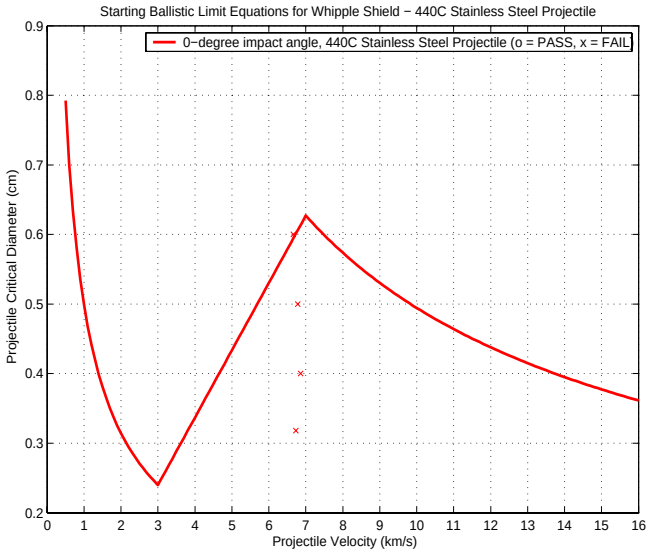

Figure F1. Entering Whipple Shield Ballistic Limit Equations for 440C Stainless Steel Projectiles at 0-degree Impact Angle with Density Effects Test Series Data Overlay.

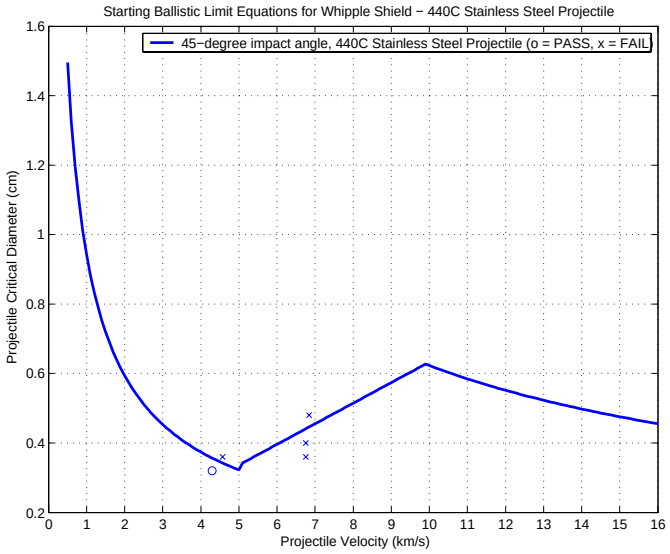

Figure F2. Entering Whipple Shield Ballistic Limit Equations for 440C Stainless Steel Projectiles at 45-degree Impact Angle with Density Effects Test Series Data Overlay.

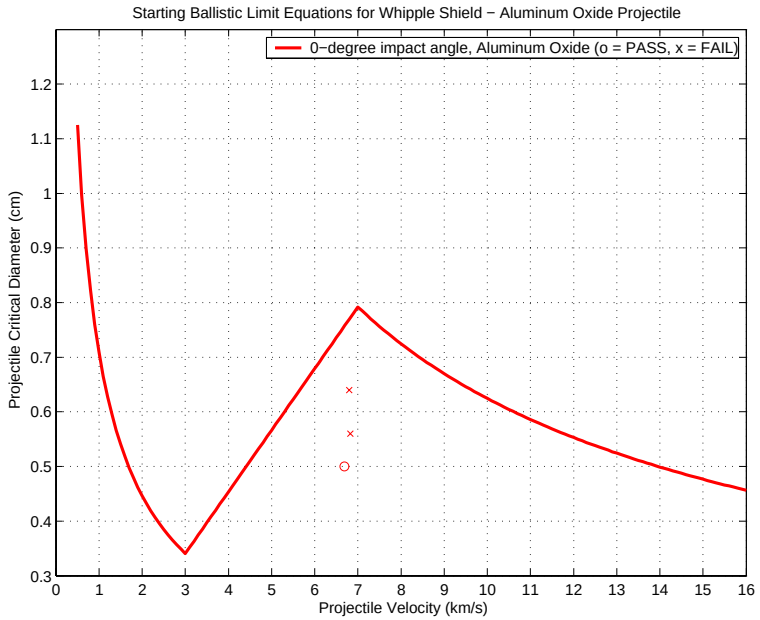

Figure F3. Entering Whipple Shield Ballistic Limit Equations for Aluminum Oxide Projectiles at 0-degree Impact Angle with Density Effects Test Series Data Overlay.

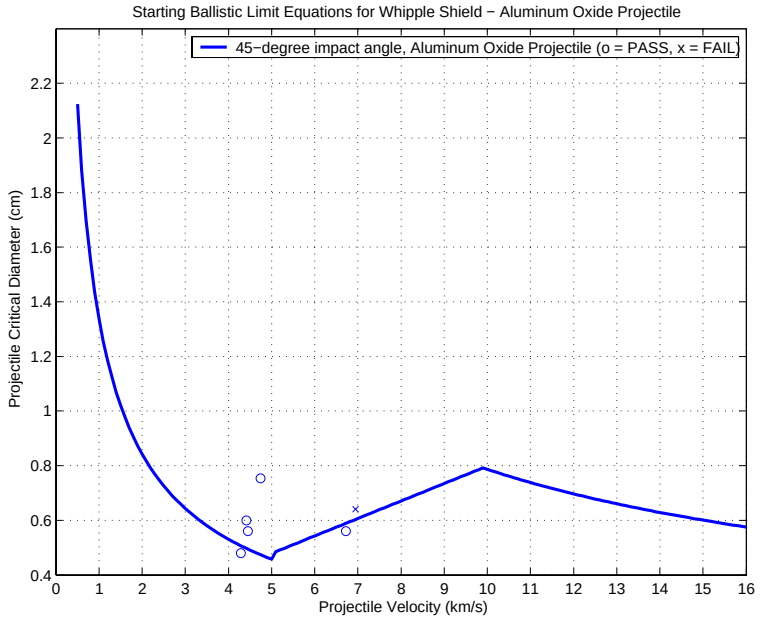

Figure F4. Entering Whipple Shield Ballistic Limit Equations for Aluminum Oxide Projectiles at 45-degree Impact Angle with Density Effects Test Series Data Overlay.

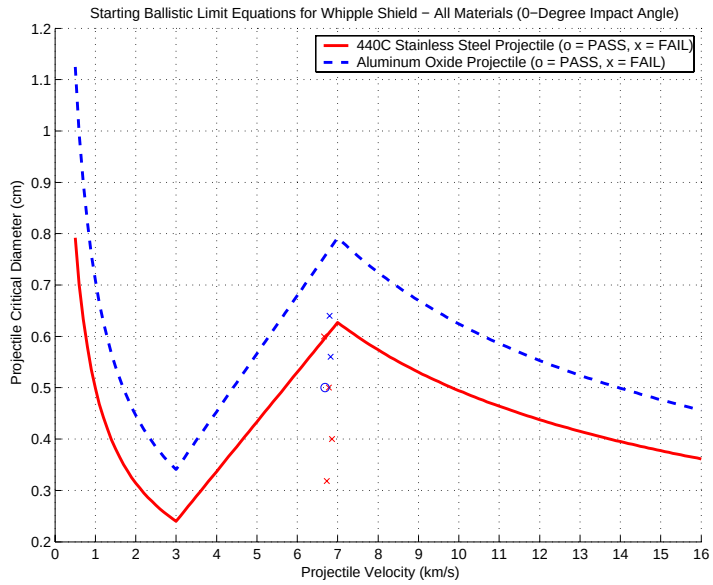

Figure F5. Entering Whipple Shield Ballistic Limit Equations for Projectiles at 0-degree Impact Angle with Density Effects Test Series Data Overlay.

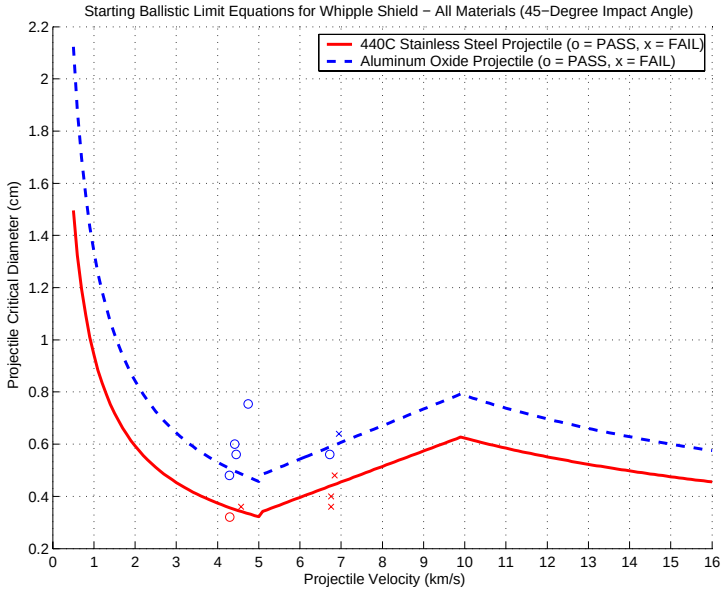

Figure F6. Entering Whipple Shield Ballistic Limit Equations for Projectiles at 45-degree Impact Angle with Density Effects Test Series Data Overlay.

2. ENHANCED STUFFED WHIPPLE SHIELDS

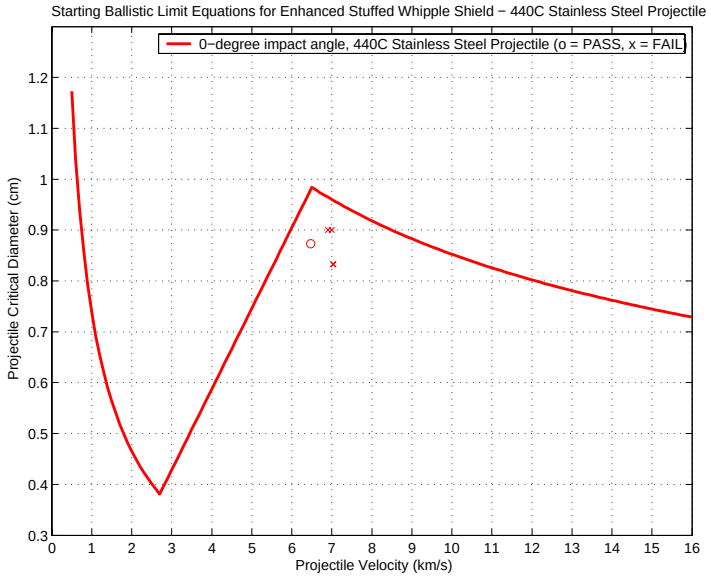

Figure F7. Entering Enhanced Stuffed Whipple Shield Ballistic Limit Equations for 440C Stainless Steel Projectiles at 0-degree Impact Angle with Density Effects Test Series Data Overlay.

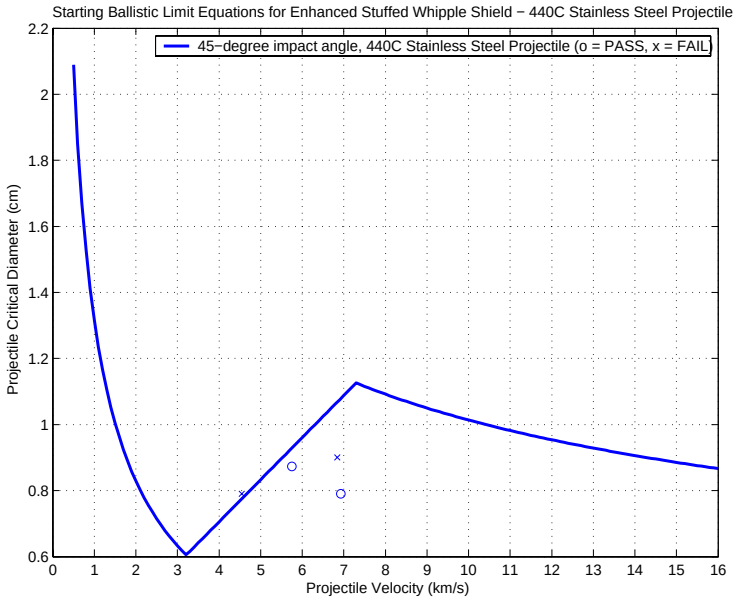

Figure F8. Entering Enhanced Stuffed Whipple Shield Ballistic Limit Equations for 440C Stainless Steel Projectiles at 45-degree Impact Angle with Density Effects Test Series Data Overlay.

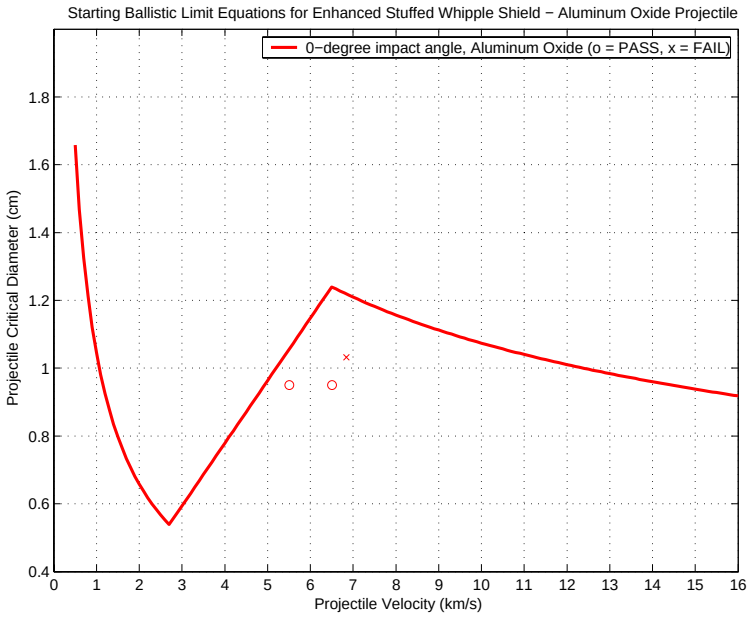

Figure F9. Entering Enhanced Stuffed Whipple Shield Ballistic Limit Equations for Aluminum Oxide Projectiles at 0-degree Impact Angle with Density Effects Test Series Data Overlay.

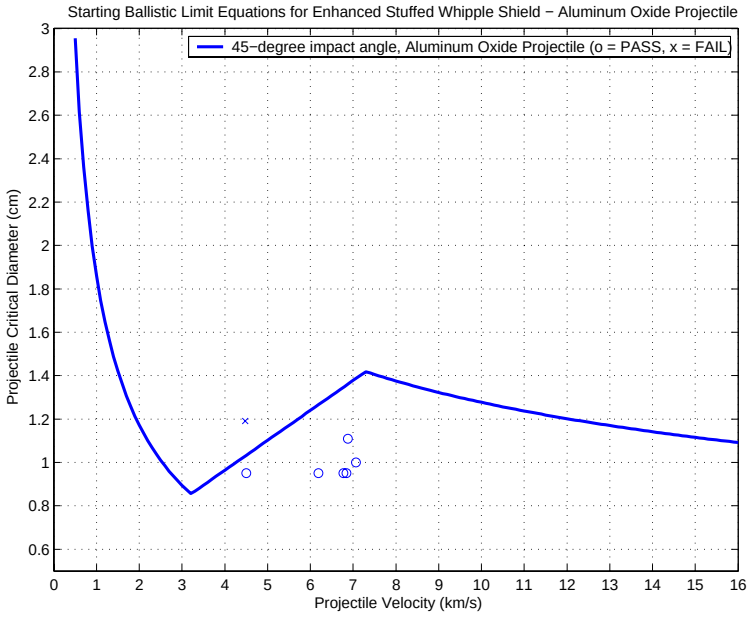

Figure F10. Entering Enhanced Stuffed Whipple Shield Ballistic Limit Equations for Aluminum Oxide Projectiles at 45-degree Impact Angle with Density Effects Test Series Data Overlay.

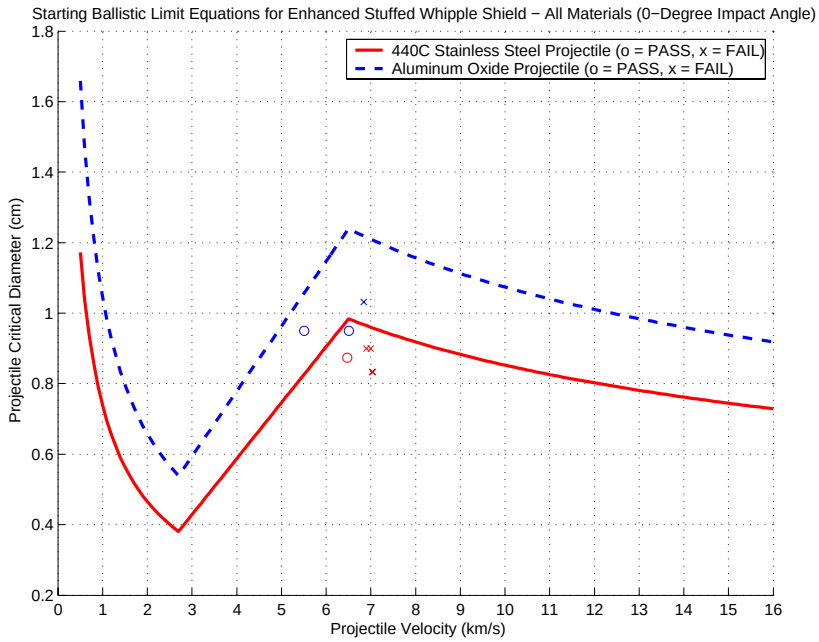

Figure F11. Entering Enhanced Stuffed Whipple Shield Ballistic Limit Equations for Projectiles at 0-degree Impact Angle with Density Effects Test Series Data Overlay.

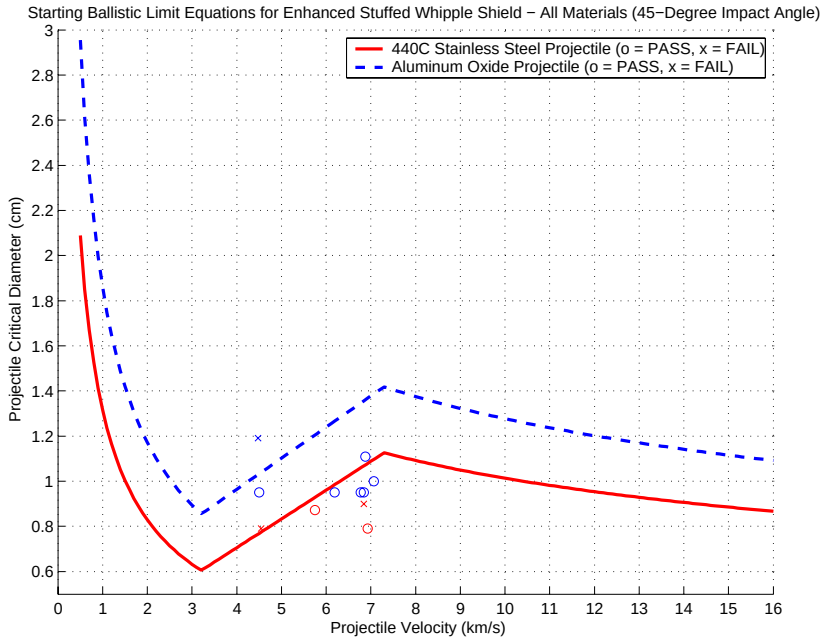

Figure F12. Entering Enhanced Stuffed Whipple Shield Ballistic Limit Equations for Projectiles at 45-degree Impact Angle with Density Effects Test Series Data Overlay.

APPENDIX G - MATLAB CODE FOR ENTERING BALLISTIC LIMIT EQUATIONS, RAW DATA, AND GRAPHICAL OVERLAYS

```
%%%%%%%%%%%%%%%%%%%%%%%%%%%%%%%%%%%%%%%%%%%%%%%%%%%%%%%%%%%%%%%%%%%%%%%%%%%%%%%%
%                                                                                 %
%                                  Thesis Work                                    %
%                Experimental Data Overlay with Ballistic Limit Curves            %
%                          (Generated by Formula used in MS Excel)                %
%                                                                                 %
%                                  Whipple Shield                                 %
%                Aluminum Oxide & 440C Stainless Steel Projectiles                %
%                                LT Michael E. Kalinski, USN                      %
%                                Last Updated: 8/11/04                            %
%                                                                                 %
%%%%%%%%%%%%%%%%%%%%%%%%%%%%%%%%%%%%%%%%%%%%%%%%%%%%%%%%%%%%%%%%%%%%%%%%%%%%%%%%
clear all;
close all;
%
% Include all reference data and constants to be used later.
%
format long;
%
t_bumper = 0.2032;                  % Bumper Thickness in cm.
rho_bumper = 2.713;     % Bumper Density in g/cm^3.
mBumper = t_bumper * rho_bumper;    % Bumper Areal Density in g/cm^2.
%
t_rearwall = .47625;    %0.4826; % Rear Wall Thickness in cm.
rho_rearwall = 2.851;   % Rear Wall Density in g/cm^3.
mRearWall = t_rearwall * rho_rearwall;       % Rear Wall Areal Density in g/cm^2.
%
Sigma_yield = 58;     % Yield Stress of Rear Wall in ksi.
S = (4.5 * 2.54) - t_bumper - t_rearwall;      % Shield separation distance in cm.
%
rho_proj_Al2O3 = 3.9;  % Projectile Density in g/cm^3 for Al2O3 Ruby Sapphire Projectile.
rho_proj_440C_SS =7.86;% Projectile Density in g/cm^3 for 440C Stainless Steel Projectile.
```

```
%
Vhi = 7.0;     % Default values in Excel Spreadsheet.
Vlo = 3.0;     % Default Values in Excel Spreadsheet.
%
Xhi = -1;        % Default Values in Excel Spreadsheet.
Xlo = -1.5;      % Default Values in Excel Spreadsheet.
%
KL = 1.8;       % Default Values in Excel Spreadsheet.
KH = 1.35;      % Default Values in Excel Spreadsheet.
%               % If t_bumper/(t_rearwall^(2/3)*S^(1/3)), then KH =
%               % 7.451*(t_bumper/(t_rearwall^(2/3)*S^(1/3))+0.411, or else KH = 1.35.  For our
%                % cases of study in the Density Effect Series, KH always equals 1.35.
%
Cell_A8 = (1/3);  % Default Value in Excel.
% (Sigma_yield/70)*exp(hi-vel)????? What is hi-vel? hi-vel = -0.910560057.
%
angle =  [0; 45];   % In FOR loop, we just do two loops, one for 0 degrees and one for 45 degrees.
% The angles are explicitly stated in the equations in the loop. However, this variable is used in
% the formulations in the lines below.
%
cos_ang = cos (angle .* pi/180);
%
%%%%%%%%%%%%%%%%%%%%%%%%%%%%%%%%%%%%%%%%%%%%%%%%%%%%%%%
%
% Input experimentally obtained velocities and projectile diameters from the HITF ISS Density
% Effects Test Series  for the Al2O3 Ruby Sapphire & the 440C Stainless Steel Projectiles on the
% Whipple Shield.
%
% Aluminum Oxide (0-degree impact angle) - PASSING samples
%
vel_exp_0_Al2O3_PASS = [6.69];     % projectile velocity in km/s
diam_exp_0_Al2O3_PASS = [0.50];    % projectile diameter in cm
%
% Aluminum Oxide (0-degree impact angle) - FAILING samples
%
vel_exp_0_Al2O3_FAIL = [6.80; 6.83];       % projectile velocity in km/s
```

```
diam_exp_0_Al2O3_FAIL = [0.640;0.560];     % projectile diameter in cm
%
% Aluminum Oxide (45-degree impact angle) - PASSING samples
%
vel_exp_45_Al2O3_PASS = [6.72;4.29;4.45;4.42;4.74]; % projectile velocity in km/s
diam_exp_45_Al2O3_PASS = [0.560;0.480;0.560;0.600;0.754]; % projectile diameter in cm
%
% Aluminum Oxide (45-degree impact angle) - FAILING samples
%
vel_exp_45_Al2O3_FAIL = [6.95];      % projectile velocity in km/s
diam_exp_45_Al2O3_FAIL = [0.640];    % projectile diameter in cm
%
% 440C Stainless Steel (0-degree impact angle) - PASSING samples
%
vel_exp_0_440C_SS_PASS = [];     % projectile velocity in km/s
diam_exp_0_440C_SS_PASS = [];    % projectile diameter in cm
%
% 440C Stainless Steel (0-degree impact angle) - FAILING samples
%
vel_exp_0_440C_SS_FAIL = [6.66;6.78;6.86;6.73];        % projectile velocity in km/s
diam_exp_0_440C_SS_FAIL = [0.600;0.500;0.400;0.318];   % projectile diameter in cm
%
% 440C Stainless Steel (45-degree impact angle) - PASSING samples
%
vel_exp_45_440C_SS_PASS = [4.30];      % projectile velocity in km/s
diam_exp_45_440C_SS_PASS = [0.320];    % projectile diameter in cm
%
% 440C Stainless Steel (45-degree impact angle) - FAILING samples
%
vel_exp_45_440C_SS_FAIL = [6.84;4.57;6.76;6.76];      % projectile velocity in km/s
diam_exp_45_440C_SS_FAIL = [0.480;0.360;0.400;0.360];     % projectile diameter in cm
%
% We now have all the Starting Ballistic Limit Equation (BLE) Data to plot
% the Whipple Shields Equations for the Aluminum Oxide and Stainless Steel case.
%
%%%%%%%%%%%%%%%%%%%%%%%%%%%%%%%%%%%%%%%%%%%%%%%%%%%%%%%%%%%%%%%%%%%%%%%%%%%%%%%
```

```
% Setup Initial Velocity Increment
%
increment = 0.01;    % Velocity Increment in km/s.
%
velocity = [0.01:increment:16]; % Define Velocities for which we will find theoretical Critical
% Projectile Diameters. We will read these into FOR statements, copied from the MS Excel
% Spreadsheet IF-THEN statements into MATLAB code. Velocity in km/s.
%
%%%%%%%%%%%%%%%%%%%%%%%%%%%%%%%%%%%%%%%%%%%%%%%%%%%%%%%%%%%%%%%%%%%%%%%%%%%%%%%%
%
% 440C Stainless Steel Projectiles (440C_SS):
%
% Loop to create starting BLE for 0-degree impact angle. d_crit_0_440C_SS is projectile critical
% diameter in cm.
%
for n = 1 : ((Vlo*(cos_ang(1)).^ Xlo) / increment)
  d_crit_0_440C_SS(n) = KL * (t_rearwall * (Sigma_yield / 40)^(1/2) + (0.37 * t_bumper * ...
     rho_bumper)) * (cos_ang(1))^(-11/6) * rho_proj_440C_SS^(-1/2) * velocity(n).^(-2/3);
end
%
for n = (((Vlo*(cos_ang(1))^ Xlo)/increment) + 1) : (((Vhi*(cos_ang(1))^ Xhi)/increment) - 1)
  d_crit_0_440C_SS(n) = KH * Vhi^(-2/3) * rho_proj_440C_SS^(-1/3) * S^(1/2) * ...
     (t_rearwall * rho_rearwall)^(2/3) * (Sigma_yield/70)^(Cell_A8) * ...
     rho_bumper^(-1/9) * (velocity(n) - Vlo*(cos_ang(1))^Xlo)/(Vhi*(cos_ang(1))^Xhi - ...
     Vlo*(cos_ang(1))^Xlo) + KL * Vlo^(-2/3) * (t_rearwall*(Sigma_yield / 40)^(1/2) + ...
     0.37*t_bumper*rho_bumper) * (cos_ang(1))^((-11/6)-(2/3)-Xlo) * ...
     rho_proj_440C_SS^(-1/2) * (Vhi * (cos_ang(1))^Xhi - velocity(n)) / ...
     (Vhi * (cos_ang(1))^Xhi - Vlo * (cos_ang(1))^Xlo);
end
%
for n = ((Vhi*(cos_ang(1))^ Xhi) / increment) : (max(velocity) / increment)
  d_crit_0_440C_SS(n) = KH * rho_proj_440C_SS^(-1/3) * (velocity(n).*(cos_ang(1)))^(-2/3)
*...
     S^(1/2) * (t_rearwall * rho_rearwall)^(2/3) * (Sigma_yield / 70)^(Cell_A8) *  rho_bumper^(-
1/9);
end
%
```

```
d_crit_0_440C_SS = d_crit_0_440C_SS(10:10:1600);
%
%%%%%%%%%%%%%%%%%%%%%%%%%%%%%%%%%%%%%%%%%%%%%%%%%%%%%%%%%%%%%%%%%%%%%%%%%%%%%%%%
%
% Loop to create starting BLE for 45-degree impact angle. d_crit_45_440C_SS is projectile
% critical diameter in cm.
%
for n = 1 : (5.05 / increment)    %((Vlo*(cos_ang(2)).^ Xlo) / increment)
  d_crit_45_440C_SS(n) = KL * (t_rearwall * (Sigma_yield / 40)^(1/2) + (0.37 * t_bumper * ...
     rho_bumper)) * (cos_ang(2))^(-11/6) * rho_proj_440C_SS^(-1/2) * velocity(n).^(-2/3);
end
%
for n = ((5.05 / increment)+ 1) : ((9.9 / increment) - 1)
% for n = 1 :(((Vlo*(cos_ang(2))^ Xlo)/increment) + 1) : (((Vhi*(cos_ang(2))^ Xhi)/increment) -
1)
  d_crit_45_440C_SS(n) = KH * Vhi^(-2/3) * rho_proj_440C_SS^(-1/3) * S^(1/2) * ...
     (t_rearwall * rho_rearwall)^(2/3) * (Sigma_yield/70)^(Cell_A8) * ...
     rho_bumper^(-1/9) * (velocity(n) - Vlo*(cos_ang(2))^Xlo)/(Vhi*(cos_ang(2))^Xhi - ...
     Vlo*(cos_ang(2))^Xlo) + KL * Vlo^(-2/3) * (t_rearwall*(Sigma_yield / 40)^(1/2) + ...
     0.37*t_bumper*rho_bumper) * (cos_ang(2))^((-11/6)-(2/3)-Xlo) * ...
     rho_proj_440C_SS^(-1/2) * (Vhi * (cos_ang(2))^Xhi - velocity(n)) / ...
     (Vhi * (cos_ang(2))^Xhi - Vlo * (cos_ang(2))^Xlo);
end
%
for n =  (9.9 / increment) : (max(velocity) / increment)
% for n = ((Vhi*(cos_ang(2))^ Xhi) / increment) : (max(velocity) / increment)
  d_crit_45_440C_SS(n) = KH * rho_proj_440C_SS^(-1/3) * (velocity(n).*(cos_ang(2)))^(-2/3)
*...
      S^(1/2) * (t_rearwall * rho_rearwall)^(2/3) * (Sigma_yield / 70)^(Cell_A8) *  rho_bumper^(-
1/9);
end
%
d_crit_45_440C_SS = d_crit_45_440C_SS(10:10:1600);
%
%%%%%%%%%%%%%%%%%%%%%%%%%%%%%%%%%%%%%%%%%%%%%%%%%%%%%%%%%%%%%%%%%%%%%%%%%%%%%%%%
%
% Aluminum Oxide Projectiles (Al2O3):
```

```
%
% Loop to create starting BLE for 0-degree impact angle. d_crit_0_Al2O3 is projectile critical
% diameter in cm. Due to values of for statements in equations, I had to make numerical
% approximations to make the loops work. For the 0-degree impact, the results were nice round
% numbers, however, the 45-degree impact resulted in ranges from 0 to 5.045 to 9.899 to 16.
%
for n = 1 : ((Vlo*(cos_ang(1)).^ Xlo) / increment)
  d_crit_0_Al2O3(n) = KL * (t_rearwall * (Sigma_yield / 40)^(1/2) + (0.37 * t_bumper * ...
     rho_bumper)) * (cos_ang(1))^(-11/6) * rho_proj_Al2O3^(-1/2) * velocity(n).^(-2/3);
end
%
for n = (((Vlo*(cos_ang(1))^ Xlo)/increment) + 1) : (((Vhi*(cos_ang(1))^ Xhi)/increment) - 1)
  d_crit_0_Al2O3(n) = KH * Vhi^(-2/3) * rho_proj_Al2O3^(-1/3) * S^(1/2) * ...
     (t_rearwall * rho_rearwall)^(2/3) * (Sigma_yield/70)^(Cell_A8) * ...
     rho_bumper^(-1/9) * (velocity(n) - Vlo*(cos_ang(1))^Xlo)/(Vhi*(cos_ang(1))^Xhi - ...
     Vlo*(cos_ang(1))^Xlo) + KL * Vlo^(-2/3) * (t_rearwall*(Sigma_yield / 40)^(1/2) + ...
     0.37*t_bumper*rho_bumper) * (cos_ang(1))^((-11/6)-(2/3)-Xlo) * ...
     rho_proj_Al2O3^(-1/2) * (Vhi * (cos_ang(1))^Xhi - velocity(n)) / ...
     (Vhi * (cos_ang(1))^Xhi - Vlo * (cos_ang(1))^Xlo);
end
%
for n = ((Vhi*(cos_ang(1))^ Xhi) / increment) : (max(velocity) / increment)
  d_crit_0_Al2O3(n) = KH * rho_proj_Al2O3^(-1/3) * (velocity(n).*(cos_ang(1)))^(-2/3) *...
      S^(1/2) * (t_rearwall * rho_rearwall)^(2/3) * (Sigma_yield / 70)^(Cell_A8) *  rho_bumper^(-
1/9);
end
%
d_crit_0_Al2O3 = d_crit_0_Al2O3(10:10:1600);
%
%%%%%%%%%%%%%%%%%%%%%%%%%%%%%%%%%%%%%%%%%%%%%%%%%%%%%%%%%%%%%%%%%%%%%%%%%%%%%%%%%%%%%%%%%%%%
% Loop to create starting BLE for 45-degree impact angle. d_crit_45_Al2O3 is projectile critical
% diameter in cm.
%
for n = 1 : (5.05 / increment)    %((Vlo*(cos_ang(2)).^ Xlo) / increment)
  d_crit_45_Al2O3(n) = KL * (t_rearwall * (Sigma_yield / 40)^(1/2) + (0.37 * t_bumper * ...
     rho_bumper)) * (cos_ang(2))^(-11/6) * rho_proj_Al2O3^(-1/2) * velocity(n).^(-2/3);
```

```
end
%
for n = ((5.05 / increment) + 1) : ((9.9 / increment) - 1)
% for n = 1 :(((Vlo*(cos_ang(2))^Xlo)/increment)+1) : (((Vhi*(cos_ang(2))^Xhi)/increment)-1)
  d_crit_45_Al2O3(n) = KH * Vhi^(-2/3) * rho_proj_Al2O3^(-1/3) * S^(1/2) * ...
     (t_rearwall * rho_rearwall)^(2/3) * (Sigma_yield/70)^(Cell_A8) * ...
     rho_bumper^(-1/9) * (velocity(n) - Vlo*(cos_ang(2))^Xlo)/(Vhi*(cos_ang(2))^Xhi - ...
     Vlo*(cos_ang(2))^Xlo) + KL * Vlo^(-2/3) * (t_rearwall*(Sigma_yield / 40)^(1/2) + ...
     0.37*t_bumper*rho_bumper) * (cos_ang(2))^((-11/6)-(2/3)-Xlo) * ...
     rho_proj_Al2O3^(-1/2) * (Vhi * (cos_ang(2))^Xhi - velocity(n)) / ...
     (Vhi * (cos_ang(2))^Xhi - Vlo * (cos_ang(2))^Xlo);
end
%
for n =  (9.9 / increment) : (max(velocity) / increment)
% for n = ((Vhi*(cos_ang(2))^ Xhi) / increment) : (max(velocity) / increment)
  d_crit_45_Al2O3(n) = KH * rho_proj_Al2O3^(-1/3) * (velocity(n).*(cos_ang(2)))^(-2/3) *...
      S^(1/2) * (t_rearwall * rho_rearwall)^(2/3) * (Sigma_yield / 70)^(Cell_A8) *  rho_bumper^(-
1/9);
end
%
d_crit_45_Al2O3 = d_crit_45_Al2O3(10:10:1600);
%
velocity = velocity(10:10:1600);
%
%%%%%%%%%%%%%%%%%%%%%%%%%%%%%%%%%%%%%%%%%%%%%%%%%%%%%%%%%%%%%%%%%%%%%%%%%%%%%%%%
% Plot Velocity versus Projectile Critical Diameter to establish Theoretical Ballistic Limit Curves.
%Then, overlay the experimental results from HITF's ISS Density Effects Test Series. Notice how
% I have incremented the velocity steps in 0.01 km/s before the iterations, but scaled the plotting
% increments down to 0.1 km/s steps.  I have done  this for ease and to scale the graphs in a
% meaningful away as the early velocity points have huge critical  diameters. this would cause the
% areas of interest to not be clearly defined if we let these high value numbers stay  on the plot.
% Since these impact velocity regimes are not expected on orbit, I threw them out here.
%
%%%%%%%%%%%%%%%%%%%%%%%%%%%%%%%%%%%%%%%%%%%%%%%%%%%%%%%%%%%%%%%%%%%%%%%%%%%%%%%%
%
% Aluminum Oxide Plots
```

```
%
figure(1);clf reset
plot(velocity(5:160),d_crit_0_Al2O3(5:160),'r-','LineWidth',2),...
  xlabel('Projectile Velocity (km/s)'), ylabel('Projectile Critical Diameter (cm)'), ...
  title('Starting Ballistic Limit Equations for Whipple Shield - Aluminum Oxide Projectile'),...
  set (gca, 'XTick',[0:1:16], 'YTick',[0:0.10:1.2]),...
  legend('0-degree impact angle, Aluminum Oxide Projectile'),...
  grid on
  print -depsc -tiff -r300 StartBLEAl2O30
%
figure(2);clf reset
plot(velocity(5:160),d_crit_45_Al2O3(5:160),'b-','LineWidth',2),...
  xlabel('Projectile Velocity (km/s)'), ylabel('Projectile Critical Diameter (cm)'), ...
  title('Starting Ballistic Limit Equations for Whipple Shield - Aluminum Oxide Projectile'),...
  set (gca, 'XTick',[0:1:16], 'YTick',[0:0.20:10.2]),...
  legend('45-degree impact angle, Aluminum Oxide Projectile'),...
  grid on
  print -depsc -tiff -r300 StartBLEAl2O345
%
figure(3);clf reset
hold on
plot(velocity(5:160),d_crit_0_Al2O3(5:160),'r-','LineWidth',2),...
hold on
plot(velocity(5:160),d_crit_45_Al2O3(5:160),'b--','LineWidth',2),...
  xlabel('Projectile Velocity (km/s)'), ylabel('Projectile Critical Diameter (cm)'), ...
  title('Starting Ballistic Limit Equations for Whipple Shield - Aluminum Oxide Projectile'),...
  set (gca, 'XTick',[0:1:16], 'YTick',[0:0.20:10.2]),...
  legend('0-degree impact angle, Aluminum Oxide Projectile', ...
        '45-degree impact angle, Aluminum Oxide Projectile'),...
  grid on
  print -depsc -tiff -r300 StartBLEAl2O3
%
%%%%%%%%%%%%%%%%%%%%%%%%%%%%%%%%%%%%%%%%%%%%%%%
%
% 440C Stainless Steel Plots
%
```

```
figure(4);clf reset
plot(velocity(5:160),d_crit_0_440C_SS(5:160),'r-','LineWidth',2),...
  xlabel('Projectile Velocity (km/s)'), ylabel('Projectile Critical Diameter (cm)'), ...
  title('Starting Ballistic Limit Equations for Whipple Shield - 440C Stainless Steel Projectile'),...
  set (gca, 'XTick',[0:1:16], 'YTick',[0:0.10:1.0]),...
  legend('0-degree impact angle, 440C Stainless Steel Projectile'),...
  grid on
  print -depsc -tiff -r300 StartBLE440CSS0
%
figure(5);clf reset
plot(velocity(5:160),d_crit_45_440C_SS(5:160),'b-','LineWidth',2),...
  xlabel('Projectile Velocity (km/s)'), ylabel('Projectile Critical Diameter (cm)'), ...
  title('Starting Ballistic Limit Equations for Whipple Shield - 440C Stainless Steel Projectile'),...
  set (gca, 'XTick',[0:1:16], 'YTick',[0:0.20:10.2]),...
  legend('45-degree impact angle, 440C Stainless Steel Projectile'),...
  grid on
  print -depsc -tiff -r300 StartBLE440CSS45
%
figure(6);clf reset
hold on
plot(velocity(5:160),d_crit_0_440C_SS(5:160),'r-','LineWidth',2),...
hold on
plot(velocity(5:160),d_crit_45_440C_SS(5:160),'b--','LineWidth',2),...
  xlabel('Projectile Velocity (km/s)'), ylabel('Projectile Critical Diameter (cm)'), ...
  title('Starting Ballistic Limit Equations for Whipple Shield - 440C Stainless Steel Projectile'),...
  set (gca, 'XTick',[0:1:16], 'YTick',[0:0.20:10.2]),...
  legend('0-degree impact angle, 440C Stainless Steel Projectile',...
        '45-degree impact angle, 440C Stainless Steel Projectile'),...
  grid on
  print -depsc -tiff -r300 StartBLE440CSS
%
%%%%%%%%%%%%%%%%%%%%%%%%%%%%%%%%%%%%%%%%%%%%%%%%%%%%%%%%%%%%%%%%%%%%%%%%%%%%%%%%
%
% 2 Curves per Plot - All Materials at 0-degree and 45-degree impact angle
%
figure(7);clf reset
```

```
hold on
plot(velocity(5:160),d_crit_0_440C_SS(5:160),'r-','LineWidth',2),...
hold on
plot(velocity(5:160),d_crit_0_Al2O3(5:160),'b--','LineWidth',2),...
  xlabel('Projectile Velocity (km/s)'), ylabel('Projectile Critical Diameter (cm)'), ...
  title('Starting Ballistic Limit Equations for Whipple Shield - All Materials (0-Degree Impact Angle)'),...
  set (gca, 'XTick',[0:1:16], 'YTick',[0:0.1:1.2]),...
  legend('440C Stainless Steel Projectile','Aluminum Oxide Projectile'),...
  grid on
  print -depsc -tiff -r300 StartBLE0
%
%%%%%%%%%%%%%%%%%%%%%%%%%%%%%%%%%%%%%%%%%%%%%%%%%%
%
figure(8);clf reset
hold on
plot(velocity(5:160),d_crit_45_440C_SS(5:160),'r-','LineWidth',2),...
hold on
plot(velocity(5:160),d_crit_45_Al2O3(5:160),'b--','LineWidth',2),...
  xlabel('Projectile Velocity (km/s)'), ylabel('Projectile Critical Diameter (cm)'), ...
  title('Starting Ballistic Limit Equations for Whipple Shield - All Materials (45-Degree Impact Angle)'),...
  set (gca, 'XTick',[0:1:16], 'YTick',[0:0.20:10.2]),...
  legend('440C Stainless Steel Projectile','Aluminum Oxide Projectile'),...
  grid on
  print -depsc -tiff -r300 StartBLE45
%
%%%%%%%%%%%%%%%%%%%%%%%%%%%%%%%%%%%%%%%%%%%%%%%%%%
%
% Next create Starting BLE Plots with the ISS Density Effects Test Overlays.
%
% Plots of the Ballistic Limit Equations with which we start. There will be three plots for each of
% the TWO material  types tested in the DENSITY EFFECTS series (Al2O3, 440C SS):
%
%   1) 0-degree impact angle,
%   2) 45-degree impact angle, and
%   3) a combination plot.
```

```
%
% Also plotted are a combined 0-degree impact angle plot for each of the TWO materials and a
% similar 45-degree impact angle plot.
%
% Common Notation for all graphical overlays is as follows:
%
%         o = Passing Sample
%         x = Failing Sample
%
%%%%%%%%%%%%%%%%%%%%%%%%%%%%%%%%%%%%%%%%%%%%%%%%%
%
% Aluminum Oxide Plots
%
figure(9);clf reset
plot(velocity(5:160),d_crit_0_Al2O3(5:160),'r-','LineWidth',2),...
hold on
plot(vel_exp_0_Al2O3_PASS,diam_exp_0_Al2O3_PASS,'ro'),...
hold on
plot(vel_exp_0_Al2O3_FAIL,diam_exp_0_Al2O3_FAIL,'rx'),...
  xlabel('Projectile Velocity (km/s)'), ylabel('Projectile Critical Diameter (cm)'), ...
  title('Starting Ballistic Limit Equations for Whipple Shield - Aluminum Oxide Projectile'),...
  set (gca, 'XTick',[0:1:16], 'YTick',[0:0.1:1.2]),...
  legend('0-degree impact angle, Aluminum Oxide (o = PASS, x = FAIL)'),...
  grid on
  print -depsc -tiff -r300 OverlayStartBLEAl2O30
%
figure(10);clf reset
plot(velocity(5:160),d_crit_45_Al2O3(5:160),'b-','LineWidth',2),...
hold on
plot(vel_exp_45_Al2O3_PASS,diam_exp_45_Al2O3_PASS,'bo'),...
hold on
plot(vel_exp_45_Al2O3_FAIL,diam_exp_45_Al2O3_FAIL,'bx'),...
  xlabel('Projectile Velocity (km/s)'), ylabel('Projectile Critical Diameter (cm)'), ...
  title('Starting Ballistic Limit Equations for Whipple Shield - Aluminum Oxide Projectile'),...
  set (gca, 'XTick',[0:1:16], 'YTick',[0:0.2:10.2]),...
  legend('45-degree impact angle, Aluminum Oxide Projectile (o = PASS, x = FAIL)'),...
```

```
  grid on
  print -depsc -tiff -r300 OverlayStartBLEAl2O345
%
figure(11);clf reset
hold on
plot(velocity(5:160),d_crit_0_Al2O3(5:160),'r-','LineWidth',2),...
hold on
plot(velocity(5:160),d_crit_45_Al2O3(5:160),'b--','LineWidth',2),...
hold on
plot(vel_exp_45_Al2O3_PASS,diam_exp_45_Al2O3_PASS,'bo'),...
hold on
plot(vel_exp_45_Al2O3_FAIL,diam_exp_45_Al2O3_FAIL,'bx'),...
hold on
plot(vel_exp_0_Al2O3_PASS,diam_exp_0_Al2O3_PASS,'ro'),...
hold on
plot(vel_exp_0_Al2O3_FAIL,diam_exp_0_Al2O3_FAIL,'rx'),...
  xlabel('Projectile Velocity (km/s)'), ylabel('Projectile Critical Diameter (cm)'), ...
  title('Starting Ballistic Limit Equations for Whipple Shield - Aluminum Oxide Projectile'),...
  set (gca, 'XTick',[0:1:16], 'YTick',[0:0.2:10.2]),...
  legend('0-degree impact angle, Aluminum Oxide Projectile (o = PASS, x = FAIL)', ...
        '45-degree impact angle, Aluminum Oxide Projectile (o = PASS, x = FAIL)'),...
  grid on
  print -depsc -tiff -r300 OverlayStartBLEAl2O3
%
%%%%%%%%%%%%%%%%%%%%%%%%%%%%%%%%%%%%%%%%%%%%%%%%%%%%%%%%%%%%%%%%%%%%%%%%%%%%%%%%
%
% 440C Stainless Steel Plots
%
figure(12);clf reset
plot(velocity(5:160),d_crit_0_440C_SS(5:160),'r-','LineWidth',2),...
hold on
plot(vel_exp_0_440C_SS_PASS,diam_exp_0_440C_SS_PASS,'ro'),...
hold on
plot(vel_exp_0_440C_SS_FAIL,diam_exp_0_440C_SS_FAIL,'rx'),...
  xlabel('Projectile Velocity (km/s)'), ylabel('Projectile Critical Diameter (cm)'), ...
  title('Starting Ballistic Limit Equations for Whipple Shield - 440C Stainless Steel Projectile'),...
```

```
  set (gca, 'XTick',[0:1:16], 'YTick',[0:0.1:1.0]),...
  legend('0-degree impact angle, 440C Stainless Steel Projectile (o = PASS, x = FAIL)'),...
  grid on
  print -depsc -tiff -r300 OverlayStartBLE440CSS0
%
figure(13);clf reset
plot(velocity(5:160),d_crit_45_440C_SS(5:160),'b-','LineWidth',2),...
hold on
plot(vel_exp_45_440C_SS_PASS,diam_exp_45_440C_SS_PASS,'bo'),...
hold on
plot(vel_exp_45_440C_SS_FAIL,diam_exp_45_440C_SS_FAIL,'bx'),...
  xlabel('Projectile Velocity (km/s)'), ylabel('Projectile Critical Diameter (cm)'), ...
  title('Starting Ballistic Limit Equations for Whipple Shield - 440C Stainless Steel Projectile'),...
  set (gca, 'XTick',[0:1:16], 'YTick',[0:0.2:10.2]),...
  legend('45-degree impact angle, 440C Stainless Steel Projectile (o = PASS, x = FAIL)'),...
  grid on
  print -depsc -tiff -r300 OverlayStartBLE440CSS45
%
figure(14);clf reset
hold on
plot(velocity(5:160),d_crit_0_440C_SS(5:160),'r-','LineWidth',2),...
hold on
plot(velocity(5:160),d_crit_45_440C_SS(5:160),'b--','LineWidth',2),...
hold on
plot(vel_exp_0_440C_SS_PASS,diam_exp_0_440C_SS_PASS,'ro'),...
hold on
plot(vel_exp_0_440C_SS_FAIL,diam_exp_0_440C_SS_FAIL,'rx'),...
hold on
plot(vel_exp_45_440C_SS_PASS,diam_exp_45_440C_SS_PASS,'bo'),...
hold on
plot(vel_exp_45_440C_SS_FAIL,diam_exp_45_440C_SS_FAIL,'bx'),...
  xlabel('Projectile Velocity (km/s)'), ylabel('Projectile Critical Diameter (cm)'), ...
  title('Starting Ballistic Limit Equations for Whipple Shield - 440C Stainless Steel Projectile'),...
  set (gca, 'XTick',[0:1:16], 'YTick',[0:0.2:10.2]),...
  legend('0-degree impact angle, 440C Stainless Steel Projectile (o = PASS, x = FAIL)',...
       '45-degree impact angle, 440C Stainless Steel Projectile (o = PASS, x = FAIL)'),...
```

```
  grid on
  print -depsc -tiff -r300 OverlayStartBLE440CSS
%
%%%%%%%%%%%%%%%%%%%%%%%%%%%%%%%%%%%%%%%%%%%%%%%%%%%%%%%%%%%%%%%%%%%%%%%%%%%%%%%%
% TWO Curves per Plot - All Materials at 0-degree and 45-degree impact angle
%
figure(15);clf reset
hold on
plot(velocity(5:160),d_crit_0_440C_SS(5:160),'r-','LineWidth',2),...
hold on
plot(velocity(5:160),d_crit_0_Al2O3(5:160),'b--','LineWidth',2),...
hold on
plot(vel_exp_0_440C_SS_PASS,diam_exp_0_440C_SS_PASS,'ro'),...
hold on
plot(vel_exp_0_440C_SS_FAIL,diam_exp_0_440C_SS_FAIL,'rx'),...
hold on
plot(vel_exp_0_Al2O3_PASS,diam_exp_0_Al2O3_PASS,'bo'),...
hold on
plot(vel_exp_0_Al2O3_FAIL,diam_exp_0_Al2O3_FAIL,'bx'),...
  xlabel('Projectile Velocity (km/s)'), ylabel('Projectile Critical Diameter (cm)'), ...
  title('Starting Ballistic Limit Equations for Whipple Shield - All Materials (0-Degree Impact
Angle)'),...
  set (gca, 'XTick',[0:1:16], 'YTick',[0:0.1:1.2]),...
  legend('440C Stainless Steel Projectile (o = PASS, x = FAIL)','Aluminum Oxide Projectile (o =
PASS, x = FAIL)'),...
  grid on
  print -depsc -tiff -r300 OverlayStartBLEAngle0
%
%%%%%%%%%%%%%%%%%%%%%%%%%%%%%%%%%%%%%%%%%%%%%%%%%%%%%%%%%%%%%%%%%%%%%%%%%%%%%%%%
%
figure(16);clf reset
hold on
plot(velocity(5:160),d_crit_45_440C_SS(5:160),'r-','LineWidth',2),...
hold on
plot(velocity(5:160),d_crit_45_Al2O3(5:160),'b--','LineWidth',2),...
hold on
plot(vel_exp_45_440C_SS_PASS,diam_exp_45_440C_SS_PASS,'ro'),...
```

```
hold on
plot(vel_exp_45_440C_SS_FAIL,diam_exp_45_440C_SS_FAIL,'rx'),...
hold on
plot(vel_exp_45_Al2O3_PASS,diam_exp_45_Al2O3_PASS,'bo'),...
hold on
plot(vel_exp_45_Al2O3_FAIL,diam_exp_45_Al2O3_FAIL,'bx'),...
  xlabel('Projectile Velocity (km/s)'), ylabel('Projectile Critical Diameter (cm)'), ...
  title('Starting Ballistic Limit Equations for Whipple Shield - All Materials (45-Degree Impact Angle)'),...
  set (gca, 'XTick',[0:1:16], 'YTick',[0:0.2:10.2]),...
  legend('440C Stainless Steel Projectile (o = PASS, x = FAIL)','Aluminum Oxide Projectile (o = PASS, x = FAIL)'),...
  grid on
  print -depsc -tiff -r300 OverlayStartBLEAngle45
%
% END
%%%%%%%%%%%%%%%%%%%%%%%%%%%%%%%%%%%%%%%%%%%%%%%%
%%%%%%%%%%%%%%%%%%%%%%%%%%%%%%%%%%%%%%%%%%%%%%%%
%                                                                              %
%                               Thesis Work                                    %
%     Experimental Data Overlaid with Theoretical Ballistic Limit Curves      %
%                 (Generated by Formula used in MS Excel)                      %
%                                                                              %
%                        Enhanced Stuffed Whipple Shield                       %
%     Ruby Sapphire Aluminum Oxide & 440C Stainless Steel Projectiles          %
%                                                                              %
%                         LT Michael E. Kalinski, USN                          %
%                                                                              %
%                           Last Updated:  8/10/04                             %
%                                                                              %
%%%%%%%%%%%%%%%%%%%%%%%%%%%%%%%%%%%%%%%%%%%%%%%%
%
clear all;
close all;
%
% Include all reference data and constants to be used later.
%
```

```
format long;
%
t_bumper = 0.2032;                    % Bumper Thickness in cm.
rho_bumper = 2.713;     % Bumper Density in g/cm^3.
mBumper = t_bumper * rho_bumper;    % Bumper Areal Density in g/cm^2.
%
t_rearwall = 0.4826;    % Rear Wall Thickness in cm.
rho_rearwall = 2.851;   % Rear Wall Density in g/cm^3.
mRearWall = 1.3758926;  % Rear Wall Areal Density in g/cm^2.
%
mNextel = 0.6;       % Areal Density in g/cm^2 for 6 layers of Nextel.  (0.1 x 6 layers).
mKevlar = 0.204;   % Areal Density in g/cm^2 for 6 layers of Kevlar. (0.034 x 6 layers).
                     % May want to use 0.032 instead.
mMesh = 0;           % Areal Density in g/cm^2 for mesh material (not used in this run).
mmli = 0.06;        % Areal Density in g/cm^2.
%
% Total Areal Density in g/cm^2.
%
mTotal = mBumper + mNextel + mKevlar + mMesh + mmli;
%
Sigma_yield = 58;       % Yield Stress of Rear Wall in ksi.
S = 4.5 * 2.54;         % Shield separation distance in cm.
%
CH_generic = 0.6;               % Generic CH Coefficient.
CL_generic = 2;                 % Generic CL Coefficient.
%
% Calculate a refined CH  and CL Coefficient.
%
CH_calc = CH_generic * (mRearWall^(0.3333333)) * (S^(2/3)) *  ((Sigma_yield/40)^(1/6));
CL_calc = CL_generic * (t_rearwall * (Sigma_yield/40)^0.5 + 0.37 * mTotal);
%
rho_proj_Al2O3 =3.9;   % Projectile Density in g/cm^3 for Al2O3 Ruby Sapphire Projectile.
rho_proj_440C_SS =7.8; % Projectile Density in g/cm^3 for 440C Stainless Steel Projectile.
%
Vhi_0 = 6.5;  Vhi_45 = 6.5;  % Default values in Excel Spreadsheet.
Vlo_0 = 2.7;  Vlo_45 = 2.7;  % Default Values in Excel Spreadsheet.
```

```
%
CH = 3.642;                          % Default values in Excel Spreadsheet.
CL = 2.063;                                % Default values in Excel Spreadsheet.
Chi_0 = CH * Vhi_0^(-1/3);           % Should be  1.952.
Chi_45 = CH * Vhi_45^(-1/3);  % Should be 1.952.
Cli_0 = CL * Vlo_0^(-2/3);    % Should be 1.064.
Cli_45 = CL * Vlo_45^(-2/3);  % Should be 1.064.
%
angle =   [0; 45];   % In IF-ELSEIF-ELSE loop, we just do two loops, one for 0 degrees and one
for
%                    % 45 degrees. The
%                    % angles are explicitly stated in the equations in the loop. However, this variable
%                     % is used in the formulations in the lines below.
%
cos_ang = cos (angle .* pi/180);
%
Vhi_div_0 = Vhi_0/((cos_ang(1))^(1/3));          % Vhi/cos_ang^(1/3).
Vhi_div_45 = Vhi_45/((cos_ang(2))^(1/3));   % Vhi/cos_ang^(1/3).
Vlo_div_0 = Vlo_0/((cos_ang(1))^(1/2));      % Vlo/cos ang^0.5 .
Vlo_div_45 = Vlo_45/((cos_ang(2))^(1/2));    % Vlo/cos ang^0.5 .
%
delta_0 =            Vhi_div_0 - Vlo_div_0;     % Simply Vhi_div - Vlo_div.
delta_45 =           Vhi_div_45 - Vlo_div_45;   % Simply Vhi_div - Vlo_div.
%
% Input experimentally obtained velocities and projectile diameters from the HITF ISS Density
% Effects Test Series for the Al2O3 Ruby Sapphire & the 440C Stainless Steel Projectiles on the
% Enhanced Stuffed Whipple Shield.
%
% Aluminum Oxide (0-degree impact angle) - PASSING samples
%
vel_exp_0_Al2O3_PASS = [6.51;5.51];   % projectile velocity in km/s
diam_exp_0_Al2O3_PASS = [0.95;0.95];  % projectile diameter in cm
%
% Aluminum Oxide (0-degree impact angle) - FAILING samples
%
vel_exp_0_Al2O3_FAIL = [6.84];    % projectile velocity in km/s
```

```
diam_exp_0_Al2O3_FAIL = [1.032];  % projectile diameter in cm
%
% Aluminum Oxide (45-degree impact angle) - PASSING samples
%
vel_exp_45_Al2O3_PASS = [6.77;6.84;4.50;6.19;7.07;6.88]; % projectile velocity in km/s
diam_exp_45_Al2O3_PASS = [0.95;0.95;0.95;0.95;1.00;1.11]; % projectile diameter in cm
%
% Aluminum Oxide (45-degree impact angle) - FAILING samples
%
vel_exp_45_Al2O3_FAIL = [4.48];      % projectile velocity in km/s
diam_exp_45_Al2O3_FAIL = [1.191];    % projectile diameter in cm
%
% 440C Stainless Steel (0-degree impact angle) - PASSING samples
%
vel_exp_0_440C_SS_PASS = [6.47];      % projectile velocity in km/s
diam_exp_0_440C_SS_PASS = [0.873];    % projectile diameter in cm
%
% 440C Stainless Steel (0-degree impact angle) - FAILING samples
%
vel_exp_0_440C_SS_FAIL = [6.9;7.0;7.04;7.03];    % projectile velocity in km/s
diam_exp_0_440C_SS_FAIL = [0.9; 0.9; 0.833;0.833];  % projectile diameter in cm
%
% 440C Stainless Steel (45-degree impact angle) - PASSING samples
%
vel_exp_45_440C_SS_PASS = [6.93;5.75];   % projectile velocity in km/s
diam_exp_45_440C_SS_PASS = [0.79;0.873]; % projectile diameter in cm
%
% 440C Stainless Steel (45-degree impact angle) - FAILING samples
%
vel_exp_45_440C_SS_FAIL = [6.84;4.55];   % projectile velocity in km/s
diam_exp_45_440C_SS_FAIL = [0.9; 0.79];  % projectile diameter in cm
%
% We now have all the Starting Ballistic Limit Equation (BLE) Data to plot the Enhanced Stuffed
% Whipple Shields Equations for the Aluminum Oxide and Stainless Steel case.
%
%%%%%%%%%%%%%%%%%%%%%%%%%%%%%%%%%%%%%%%%%%%%%%%%%%%%%%%%%%
```

```
%
velocity = [0.1:0.1:16]';  % Define Velocities for which we will calculate theoretical Critical
% Projectile Diameters.  We will read these into our FOR statements, copied from the MS Excel
% Spreadsheet IF-THEN statements into MATLAB code. Velocity in km/s.
%
% Setup Initial Velocity Increment
%
increment = 0.1;    % Velocity Increment in km/s.
%
%%%%%%%%%%%%%%%%%%%%%%%%%%%%%%%%%%%%%%%%%%%%%%%%%
%
% Aluminum Oxide Projectiles (Al2O3):
%
% Loop to create starting BLE for 0-degree impact angle. d_crit_0_Al2O3 is critical diameter in
% cm. We can use  this simple incrementing technique only because the division by COS(0)^1/3 =
% a nice round number.
%
for n = 1 : (Vlo_div_0 / increment)
  d_crit_0_Al2O3(n) = CL * cos_ang(1)^(-5/3) * rho_proj_Al2O3^(-1/2) *...
                velocity(n).^(-2/3);
end
%
for n = ((Vlo_div_0 / increment) + 1) : ((Vhi_div_0 / increment) - 1)
  d_crit_0_Al2O3(n) = (Cli_0 * rho_proj_Al2O3^(-1/2) * (cos_ang(1)^(-4/3)) * ...
                ((Vhi_div_0 - velocity(n))/ delta_0)) + ...
                (Chi_0 * (rho_proj_Al2O3^(-1/3)) * (cos_ang(1)^(-7/18)) *...
                ((velocity(n) - Vlo_div_0) / delta_0));
end
%
for n =  (Vhi_div_0 / increment) : (max(velocity) / increment)
  d_crit_0_Al2O3(n) = CH * cos_ang(1)^(-1/2) * rho_proj_Al2O3^(-1/3) * ...
                velocity(n).^(-1/3);
end
%
d_crit_0_Al2O3 = d_crit_0_Al2O3';
%
```

```
%%%%%%%%%%%%%%%%%%%%%%%%%%%%%%%%%%%%%%%%%%%%%%%%%%%%
%
% Loop to create starting BLE for 45-degree impact angle. d_crit_45_Al2O3 is projectile critical
% diameter in cm.
%
for n = 1 : (3.2 / increment)
% 3.2 is from Vlo_div_45 (rounded from 3.210859 due to incrementing difficulty)
   d_crit_45_Al2O3(n) = CL * cos_ang(2)^(-5/3) * rho_proj_Al2O3^(-1/2) * velocity(n).^(-2/3);
end
%
for n = ((3.2 / increment) + 1) : ((7.3 / increment) - 1)
   d_crit_45_Al2O3(n) = (Cli_45 * rho_proj_Al2O3^(-1/2) * (cos_ang(2)^(-4/3)) * ((Vhi_div_45 - velocity(n))/ delta_45)) + (Chi_45 * (rho_proj_Al2O3^(-1/3)) * (cos_ang(2)^(-7/18)) *((velocity(n) - Vlo_div_45) / delta_45));
end
%
for n = (7.3 / increment) : (max(velocity) / increment)
% 7.3 is from Vhi_div_45 (rounded from 7.296003 due to incrementing difficulty)
         d_crit_45_Al2O3(n) = CH * cos_ang(2)^(-1/2) * rho_proj_Al2O3^(-1/3) * velocity(n).^(-1/3);
end
%
d_crit_45_Al2O3 = d_crit_45_Al2O3';
%
%%%%%%%%%%%%%%%%%%%%%%%%%%%%%%%%%%%%%%%%%%%%%%%%%%%%
%
% 440C Stainless Steel Projectiles (440C_SS):
%
% Loop to create starting BLE for 0-degree impact angle. d_crit_0_440C_SS is projectile critical
% diameter in cm.
%
for n = 1 : (Vlo_div_0 / increment)
 d_crit_0_440C_SS(n) = CL * cos_ang(1)^(-5/3) * rho_proj_440C_SS^(-1/2) *  velocity(n).^(-2/3);
end
%
for n =  ((Vlo_div_0 / increment) + 1) : ((Vhi_div_0 / increment) - 1)
```

```
      d_crit_0_440C_SS(n) = (Cli_0 * rho_proj_440C_SS^(-1/2) * (cos_ang(1)^(-4/3)) * ...
                  ((Vhi_div_0 - velocity(n))/ delta_0)) + ...
                  (Chi_0 * (rho_proj_440C_SS^(-1/3)) * (cos_ang(1)^(-7/18)) * ((velocity(n) -
Vlo_div_0) / delta_0));
    end
    %
    for n =  (Vhi_div_0 / increment) : (max(velocity) / increment)
      d_crit_0_440C_SS(n) = CH * cos_ang(1)^(-1/2) * rho_proj_440C_SS^(-1/3) *  velocity(n).^(-
1/3);
    end
    %
    d_crit_0_440C_SS = d_crit_0_440C_SS';
    %
    %%%%%%%%%%%%%%%%%%%%%%%%%%%%%%%%%%%%%%%%%%%%%%%
    %
    % Loop to create starting BLE for 45-degree impact angle. d_crit_45_440C_SS is projectile
    % critical diameter in cm.
    %
    for n = 1 : (3.2 / increment)
    % 3.2 is from Vlo_div_45 (rounded from 3.210859 due to incrementing difficulty)
       d_crit_45_440C_SS(n) = CL * cos_ang(2)^(-5/3) * rho_proj_440C_SS^(-1/2) * velocity(n).^(-
2/3);
    end
    %
    for n =  ((3.2 / increment) + 1) : ((7.3 / increment) - 1)
      d_crit_45_440C_SS(n) = (Cli_45 * rho_proj_440C_SS^(-1/2) * (cos_ang(2)^(-4/3)) * ...
                  ((Vhi_div_45 - velocity(n))/ delta_45)) + ...
                  (Chi_45 * (rho_proj_440C_SS^(-1/3)) * (cos_ang(2)^(-7/18)) * ((velocity(n) -
Vlo_div_45) / delta_45));
    end
    %
    for n =  (7.3 / increment) : (max(velocity) / increment)
    % 7.3 is from Vhi_div_45 (rounded from 7.296003 due to incrementing difficulty)
      d_crit_45_440C_SS(n) = CH * cos_ang(2)^(-1/2) * rho_proj_440C_SS^(-1/3) *  velocity(n).^(-
1/3);
    end
    %
    d_crit_45_440C_SS = d_crit_45_440C_SS';
```

```
%
%%%%%%%%%%%%%%%%%%%%%%%%%%%%%%%%%%%%%%%%%%%%%%%%%%%
%
% Plot Velocity versus Projectile Critical Diameter to establish Theoretical Ballistic Limit Curves.
% Then, overlay the experimental results from HITF's ISS Density Effects Test Series.
%
%%%%%%%%%%%%%%%%%%%%%%%%%%%%%%%%%%%%%%%%%%%%%%%%%%%
%
% Aluminum Oxide Plots
%
figure(1);clf reset
plot(velocity(5:160),d_crit_0_Al2O3(5:160),'r-','LineWidth',2),...
  xlabel('Projectile Velocity (km/s)'), ylabel('Projectile Critical Diameter (cm)'), ...
  title('Starting Ballistic Limit Equations for Enhanced Stuffed Whipple Shield - Aluminum Oxide Projectile'),...
  set (gca, 'XTick',[0:1:16], 'YTick',[0:0.20:10.2]),...
  legend('0-degree impact angle, Aluminum Oxide Projectile'),...
  grid on
  print -depsc -tiff -r300 SWStartBLEAl2O30
%
figure(2);clf reset
plot(velocity(5:160),d_crit_45_Al2O3(5:160),'b-','LineWidth',2),...
  xlabel('Projectile Velocity (km/s)'), ylabel('Projectile Critical Diameter (cm)'), ...
  title('Starting Ballistic Limit Equations for Enhanced Stuffed Whipple Shield - Aluminum Oxide Projectile'),...
  set (gca, 'XTick',[0:1:16], 'YTick',[0:0.20:10.2]),...
  legend('45-degree impact angle, Aluminum Oxide Projectile'),...
  grid on
  print -depsc -tiff -r300 SWStartBLEAl2O345
%
figure(3);clf reset
hold on
plot(velocity(5:160),d_crit_0_Al2O3(5:160),'r-','LineWidth',2),...
hold on
plot(velocity(5:160),d_crit_45_Al2O3(5:160),'b--','LineWidth',2),...
  xlabel('Projectile Velocity (km/s)'), ylabel('Projectile Critical Diameter (cm)'), ...
```

```
         title('Starting Ballistic Limit Equations for Enhanced Stuffed Whipple Shield - Aluminum Oxide
Projectile'),...
         set (gca, 'XTick',[0:1:16], 'YTick',[0:0.20:10.2]),...
         legend('0-degree impact angle, Aluminum Oxide Projectile', ...
             '45-degree impact angle, Aluminum Oxide Projectile'),...
         grid on
         print -depsc -tiff -r300 SWStartBLEAl2O3
        %
        %%%%%%%%%%%%%%%%%%%%%%%%%%%%%%%%%%%%%%%%%%%%%%%%
        %
        % 440C Stainless Steel Plots
        %
        figure(4);clf reset
        plot(velocity(5:160),d_crit_0_440C_SS(5:160),'r-','LineWidth',2),...
         xlabel('Projectile Velocity (km/s)'), ylabel('Projectile Critical Diameter (cm)'), ...
         title('Starting Ballistic Limit Equations for Enhanced Stuffed Whipple Shield - 440C Stainless
Steel Projectile'),...
         set (gca, 'XTick',[0:1:16], 'YTick',[0:0.10:1.2]),...
         legend('0-degree impact angle, 440C Stainless Steel Projectile'),...
         grid on
         print -depsc -tiff -r300 SWStartBLE440CSS0
        %
        figure(5);clf reset
        plot(velocity(5:160),d_crit_45_440C_SS(5:160),'b-','LineWidth',2),...
         xlabel('Projectile Velocity (km/s)'), ylabel('Projectile Critical Diameter (cm)'), ...
         title('Starting Ballistic Limit Equations for Enhanced Stuffed Whipple Shield - 440C Stainless
Steel Projectile'),...
         set (gca, 'XTick',[0:1:16], 'YTick',[0:0.20:10.2]),...
         legend('45-degree impact angle, 440C Stainless Steel Projectile'),...
         grid on
          print -depsc -tiff -r300 SWStartBLE440CSS45
        %
        figure(6);clf reset
        hold on
        plot(velocity(5:160),d_crit_0_440C_SS(5:160),'r-','LineWidth',2),...
        hold on
        plot(velocity(5:160),d_crit_45_440C_SS(5:160),'b--','LineWidth',2),...
```

```
 xlabel('Projectile Velocity (km/s)'), ylabel('Projectile Critical Diameter (cm)'), ...
 title('Starting Ballistic Limit Equations for Enhanced Stuffed Whipple Shield - 440C Stainless Steel Projectile'),...
 set (gca, 'XTick',[0:1:16], 'YTick',[0:0.20:10.2]),...
 legend('0-degree impact angle, 440C Stainless Steel Projectile',...
     '45-degree impact angle, 440C Stainless Steel Projectile'),...
 grid on
  print -depsc -tiff -r300 SWStartBLE440CSS
%
%%%%%%%%%%%%%%%%%%%%%%%%%%%%%%%%%%%%%%%%%%%%%%%%%%
%
% 2 Curves per Plot - All Materials at 0-degree and 45-degree impact angle
%
figure(7);clf reset
hold on
plot(velocity(5:160),d_crit_0_440C_SS(5:160),'r-','LineWidth',2),...
hold on
plot(velocity(5:160),d_crit_0_Al2O3(5:160),'b--','LineWidth',2),...
 xlabel('Projectile Velocity (km/s)'), ylabel('Projectile Critical Diameter (cm)'), ...
 title('Starting Ballistic Limit Equations for Enhanced Stuffed Whipple Shield - All Materials (0-Degree Impact Angle)'),...
 set (gca, 'XTick',[0:1:16], 'YTick',[0:0.20:10.2]),...
 legend('440C Stainless Steel Projectile','Aluminum Oxide Projectile'),...
 grid on
 print -depsc -tiff -r300 SWStartBLEAngle0
%
%%%%%%%%%%%%%%%%%%%%%%%%%%%%%%%%%%%%%%%%%%%%%%%%%%
%
figure(8);clf reset
hold on
plot(velocity(5:160),d_crit_45_440C_SS(5:160),'r-','LineWidth',2),...
hold on
plot(velocity(5:160),d_crit_45_Al2O3(5:160),'b--','LineWidth',2),...
 xlabel('Projectile Velocity (km/s)'), ylabel('Projectile Critical Diameter (cm)'), ...
 title('Starting Ballistic Limit Equations for Enhanced Stuffed Whipple Shield - All Materials (45-Degree Impact Angle)'),...
 set (gca, 'XTick',[0:1:16], 'YTick',[0:0.20:10.2]),...
```

```
  legend('440C Stainless Steel Projectile','Aluminum Oxide Projectile'),...
  grid on
  print -depsc -tiff -r300 SWStartBLEAngle45
%
%%%%%%%%%%%%%%%%%%%%%%%%%%%%%%%%%%%%%%%%%%%%%%%%%%%%%%%%%%%%%%%%%%%%%%%%
%
% Next create Starting BLE Plots with the ISS Density Effects Test Overlays.
%
% Plots of the Ballistic Limit Equations with which we start. There will be three plots for each of
% the TWO material  types tested in the DENSITY EFFECTS series (Al2O3, 440C SS):
%
%   1) 0-degree impact angle,
%   2) 45-degree impact angle, and
%   3) a combination plot.
%
% Also plotted are a combined 0-degree impact angle plot for each of the TWO materials and a
% similar 45-degree impact angle plot.
%
% Common Notation for all graphical overlays is as follows:
%
%          o = Passing Sample
%          x = Failing Sample
%
%%%%%%%%%%%%%%%%%%%%%%%%%%%%%%%%%%%%%%%%%%%%%%%%%%%%%%%%%%%%%%%%%%%%%%%%
%
% Aluminum Oxide Plots
%
figure(9);clf reset
plot(velocity(5:160),d_crit_0_Al2O3(5:160),'r-','LineWidth',2),...
hold on
plot(vel_exp_0_Al2O3_PASS,diam_exp_0_Al2O3_PASS,'ro'),...
hold on
plot(vel_exp_0_Al2O3_FAIL,diam_exp_0_Al2O3_FAIL,'rx'),...
  xlabel('Projectile Velocity (km/s)'), ylabel('Projectile Critical Diameter (cm)'), ...
  title('Starting Ballistic Limit Equations for Enhanced Stuffed Whipple Shield - Aluminum Oxide
Projectile'),...
```

```
  set (gca, 'XTick',[0:1:16], 'YTick',[0:0.2:10.2]),...
  legend('0-degree impact angle, Aluminum Oxide (o = PASS, x = FAIL)'),...
  grid on
  print -depsc -tiff -r300 SWOverlayStartBLEAl2O30
%
figure(10);clf reset
plot(velocity(5:160),d_crit_45_Al2O3(5:160),'b-','LineWidth',2),...
hold on
plot(vel_exp_45_Al2O3_PASS,diam_exp_45_Al2O3_PASS,'bo'),...
hold on
plot(vel_exp_45_Al2O3_FAIL,diam_exp_45_Al2O3_FAIL,'bx'),...
  xlabel('Projectile Velocity (km/s)'), ylabel('Projectile Critical Diameter (cm)'), ...
  title('Starting Ballistic Limit Equations for Enhanced Stuffed Whipple Shield - Aluminum Oxide
Projectile'),...
  set (gca, 'XTick',[0:1:16], 'YTick',[0:0.2:10.2]),...
  legend('45-degree impact angle, Aluminum Oxide Projectile (o = PASS, x = FAIL)'),...
  grid on
  print -depsc -tiff -r300 SWOverlayStartBLEAl2O345
%
figure(11);clf reset
hold on
plot(velocity(5:160),d_crit_0_Al2O3(5:160),'r-','LineWidth',2),...
hold on
plot(velocity(5:160),d_crit_45_Al2O3(5:160),'b--','LineWidth',2),...
hold on
plot(vel_exp_45_Al2O3_PASS,diam_exp_45_Al2O3_PASS,'bo'),...
hold on
plot(vel_exp_45_Al2O3_FAIL,diam_exp_45_Al2O3_FAIL,'bx'),...
hold on
plot(vel_exp_0_Al2O3_PASS,diam_exp_0_Al2O3_PASS,'ro'),...
hold on
plot(vel_exp_0_Al2O3_FAIL,diam_exp_0_Al2O3_FAIL,'rx'),...
  xlabel('Projectile Velocity (km/s)'), ylabel('Projectile Critical Diameter (cm)'), ...
  title('Starting Ballistic Limit Equations for Enhanced Stuffed Whipple Shield - Aluminum Oxide
Projectile'),...
  set (gca, 'XTick',[0:1:16], 'YTick',[0:0.2:10.2]),...
  legend('0-degree impact angle, Aluminum Oxide Projectile (o = PASS, x = FAIL)', ...
```

```
        '45-degree impact angle, Aluminum Oxide Projectile (o = PASS, x = FAIL)'),...
  grid on
  print -depsc -tiff -r300 SWOverlayStartBLEAl2O3
%
%%%%%%%%%%%%%%%%%%%%%%%%%%%%%%%%%%%%%%%%%%%%%%%%%%%%%%%%%%%%%%%%%%%%%%%%%%%%%%%%
%
% 440C Stainless Steel Plots
%
figure(12);clf reset
plot(velocity(5:160),d_crit_0_440C_SS(5:160),'r-','LineWidth',2),...
hold on
plot(vel_exp_0_440C_SS_PASS,diam_exp_0_440C_SS_PASS,'ro'),...
hold on
plot(vel_exp_0_440C_SS_FAIL,diam_exp_0_440C_SS_FAIL,'rx'),...
  xlabel('Projectile Velocity (km/s)'), ylabel('Projectile Critical Diameter (cm)'), ...
  title('Starting Ballistic Limit Equations for Enhanced Stuffed Whipple Shield - 440C Stainless Steel Projectile'),...
  set (gca, 'XTick',[0:1:16], 'YTick',[0:0.1:1.2]),...
  legend('0-degree impact angle, 440C Stainless Steel Projectile (o = PASS, x = FAIL)'),...
  grid on
  print -depsc -tiff -r300 SWOverlayStartBLE440CSS0
%
figure(13);clf reset
plot(velocity(5:160),d_crit_45_440C_SS(5:160),'b-','LineWidth',2),...
hold on
plot(vel_exp_45_440C_SS_PASS,diam_exp_45_440C_SS_PASS,'bo'),...
hold on
plot(vel_exp_45_440C_SS_FAIL,diam_exp_45_440C_SS_FAIL,'bx'),...
  xlabel('Projectile Velocity (km/s)'), ylabel('Projectile Critical Diameter (cm)'), ...
  title('Starting Ballistic Limit Equations for Enhanced Stuffed Whipple Shield - 440C Stainless Steel Projectile'),...
  set (gca, 'XTick',[0:1:16], 'YTick',[0:0.2:10.2]),...
  legend('45-degree impact angle, 440C Stainless Steel Projectile (o = PASS, x = FAIL)'),...
  grid on
  print -depsc -tiff -r300 SWOverlayStartBLE440CSS45
%
figure(14);clf reset
```

```
hold on
plot(velocity(5:160),d_crit_0_440C_SS(5:160),'r-','LineWidth',2),...
hold on
plot(velocity(5:160),d_crit_45_440C_SS(5:160),'b--','LineWidth',2),...
hold on
plot(vel_exp_0_440C_SS_PASS,diam_exp_0_440C_SS_PASS,'ro'),...
hold on
plot(vel_exp_0_440C_SS_FAIL,diam_exp_0_440C_SS_FAIL,'rx'),...
hold on
plot(vel_exp_45_440C_SS_PASS,diam_exp_45_440C_SS_PASS,'bo'),...
hold on
plot(vel_exp_45_440C_SS_FAIL,diam_exp_45_440C_SS_FAIL,'bx'),...
  xlabel('Projectile Velocity (km/s)'), ylabel('Projectile Critical Diameter (cm)'), ...
  title('Starting Ballistic Limit Equations for Enhanced Stuffed Whipple Shield - 440C Stainless
Steel Projectile'),...
  set (gca, 'XTick',[0:1:16], 'YTick',[0:0.2:10.2]),...
  legend('0-degree impact angle, 440C Stainless Steel Projectile (o = PASS, x = FAIL)',...
      '45-degree impact angle, 440C Stainless Steel Projectile (o = PASS, x = FAIL)'),...
  grid on
  print -depsc -tiff -r300 SWOverlayStartBLE440CSS
%
%%%%%%%%%%%%%%%%%%%%%%%%%%%%%%%%%%%%%%%%%%%%
%
% TWO Curves per Plot - All Materials at 0-degree & 45-degree impact angle
%
figure(15);clf reset
hold on
plot(velocity(5:160),d_crit_0_440C_SS(5:160),'r-','LineWidth',2),...
hold on
plot(velocity(5:160),d_crit_0_Al2O3(5:160),'b--','LineWidth',2),...
hold on
plot(vel_exp_0_440C_SS_PASS,diam_exp_0_440C_SS_PASS,'ro'),...
hold on
plot(vel_exp_0_440C_SS_FAIL,diam_exp_0_440C_SS_FAIL,'rx'),...
hold on
plot(vel_exp_0_Al2O3_PASS,diam_exp_0_Al2O3_PASS,'bo'),...
```

```
hold on
plot(vel_exp_0_Al2O3_FAIL,diam_exp_0_Al2O3_FAIL,'bx'),...
  xlabel('Projectile Velocity (km/s)'), ylabel('Projectile Critical Diameter (cm)'), ...
  title('Starting Ballistic Limit Equations for Enhanced Stuffed Whipple Shield - All Materials (0-Degree Impact Angle)'),...
  set (gca, 'XTick',[0:1:16], 'YTick',[0:0.2:10.2]),...
  legend('440C Stainless Steel Projectile (o = PASS, x = FAIL)','Aluminum Oxide Projectile (o = PASS, x = FAIL)'),...
  grid on
  print -depsc -tiff -r300 SWOverlayStartBLEAngle0
%
%%%%%%%%%%%%%%%%%%%%%%%%%%%%%%%%%%%%%%%%%%%%%%%%%%%%%%%%%%
figure(16);clf reset
hold on
plot(velocity(5:160),d_crit_45_440C_SS(5:160),'r-','LineWidth',2),...
hold on
plot(velocity(5:160),d_crit_45_Al2O3(5:160),'b--','LineWidth',2),...
hold on
plot(vel_exp_45_440C_SS_PASS,diam_exp_45_440C_SS_PASS,'ro'),...
hold on
plot(vel_exp_45_440C_SS_FAIL,diam_exp_45_440C_SS_FAIL,'rx'),...
hold on
plot(vel_exp_45_Al2O3_PASS,diam_exp_45_Al2O3_PASS,'bo'),...
hold on
plot(vel_exp_45_Al2O3_FAIL,diam_exp_45_Al2O3_FAIL,'bx'),...
  xlabel('Projectile Velocity (km/s)'), ylabel('Projectile Critical Diameter (cm)'), ...
  title('Starting Ballistic Limit Equations for Enhanced Stuffed Whipple Shield - All Materials (45-Degree Impact Angle)'),...
  set (gca, 'XTick',[0:1:16], 'YTick',[0:0.2:10.2]),...
  legend('440C Stainless Steel Projectile (o = PASS, x = FAIL)','Aluminum Oxide Projectile (o = PASS, x = FAIL)'),...
  grid on
  print -depsc -tiff -r300 SWOverlayStartBLEAngle45
%
% END
%%%%%%%%%%%%%%%%%%%%%%%%%%%%%%%%%%%%%%%%%%%%%%%%%%%%%%%%%%
```

THIS PAGE INTENTIONALLY LEFT BLANK

APPENDIX H - REVISED BALLISTIC LIMIT CURVES WITH DENSITY EFFECTS RAW DATA OVERLAYS

1. WHIPPLE SHIELDS

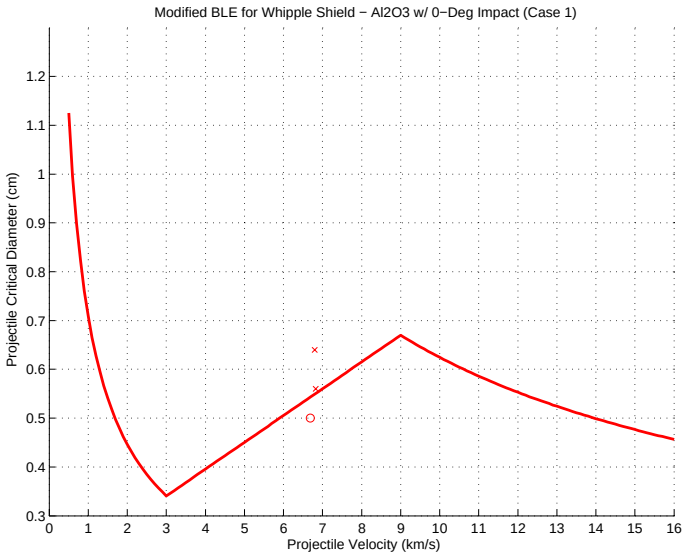

Figure H1. Improved Ballistic Limit Equation for Whipple Shield with Aluminum Oxide Projectile at 0-degree Impact (Case 1).

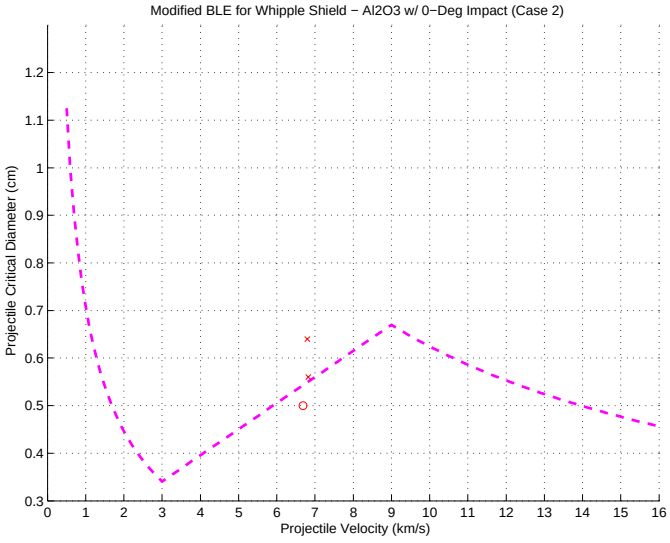

Figure H2. Improved Ballistic Limit Equation for Whipple Shield with Aluminum Oxide Projectile at 0-degree Impact (Case 2).

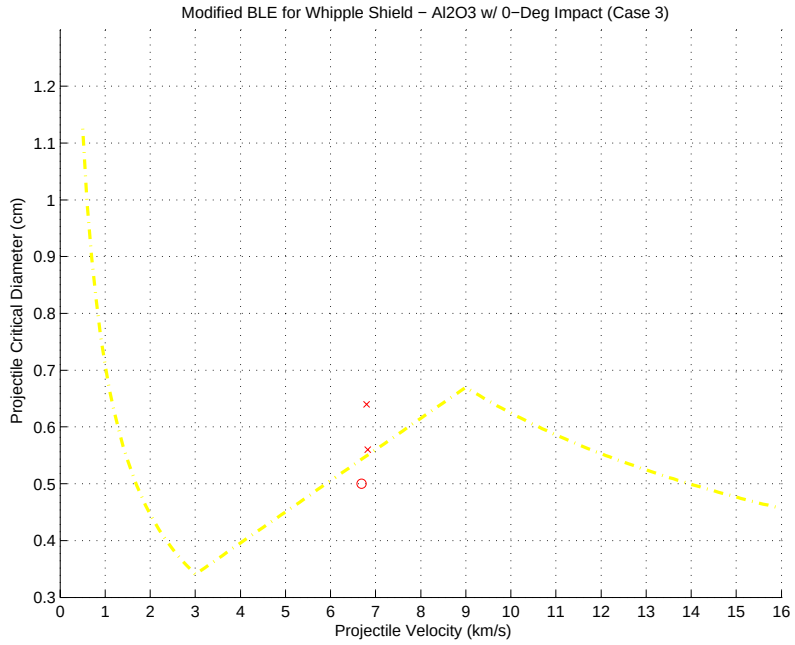

Figure H3. Improved Ballistic Limit Equation for Whipple Shield with Aluminum Oxide Projectile at 0-degree Impact. (Case 3)

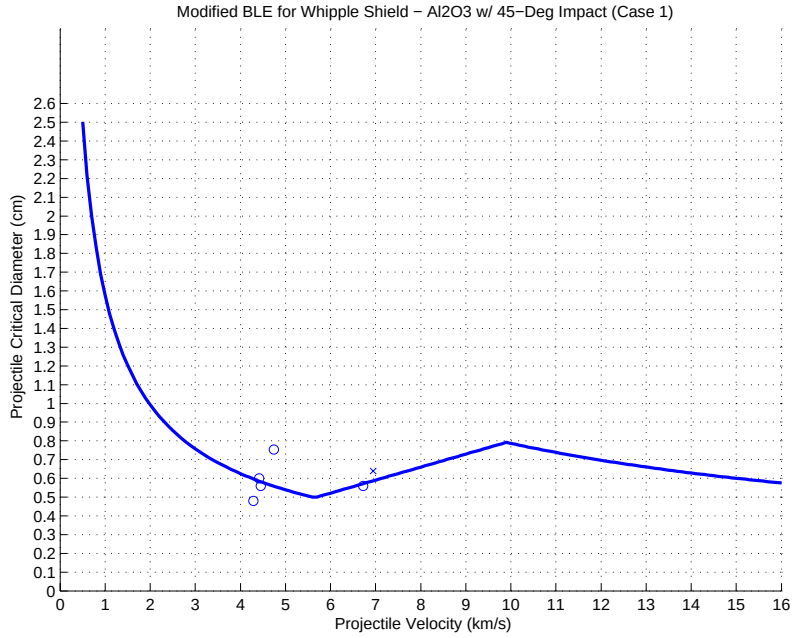

Figure H4. Improved Ballistic Limit Equation for Whipple Shield with Aluminum Oxide Projectile at 45-degree Impact. (Case 1)

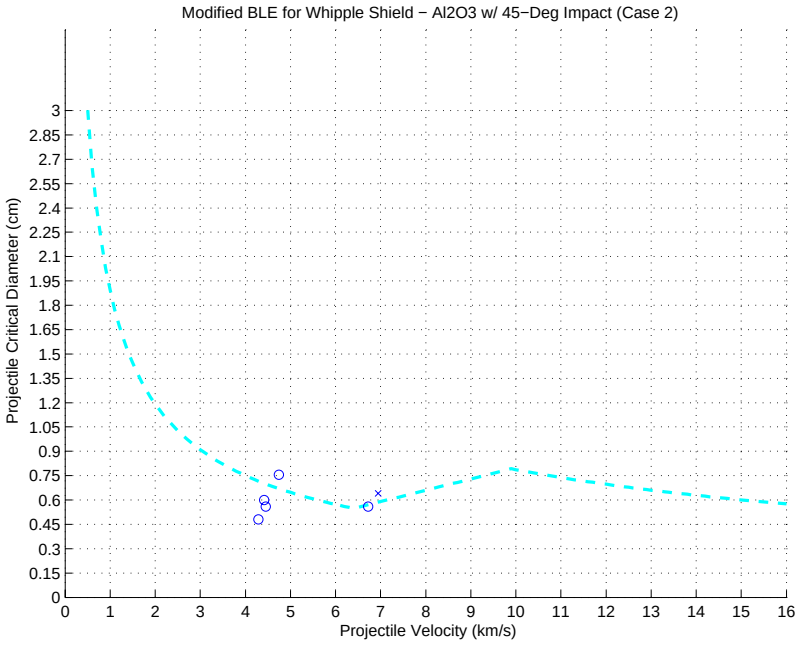

Figure H5. Improved Ballistic Limit Equation for Whipple Shield with Aluminum Oxide Projectile at 45-degree Impact. (Case 2)

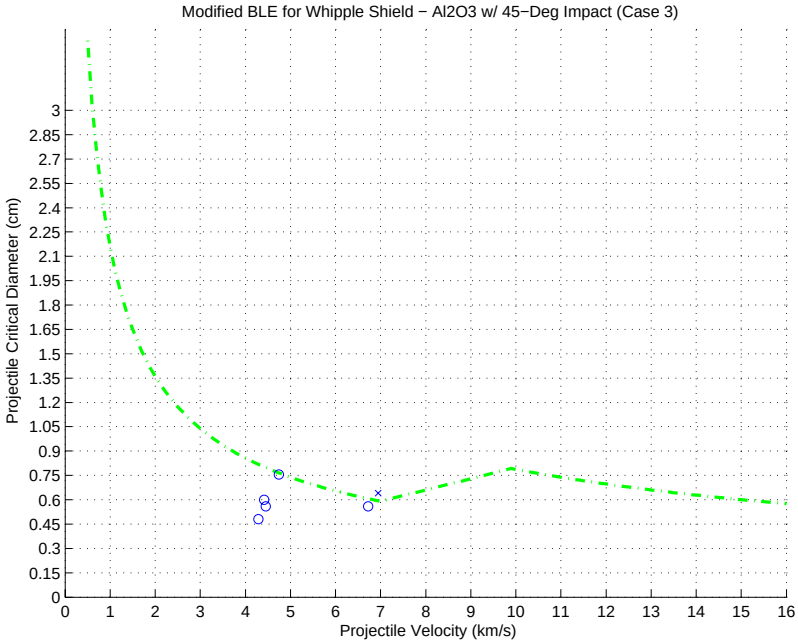

Figure H6. Improved Ballistic Limit Equation for Whipple Shield with Aluminum Oxide Projectile at 45-degree Impact. (Case 3)

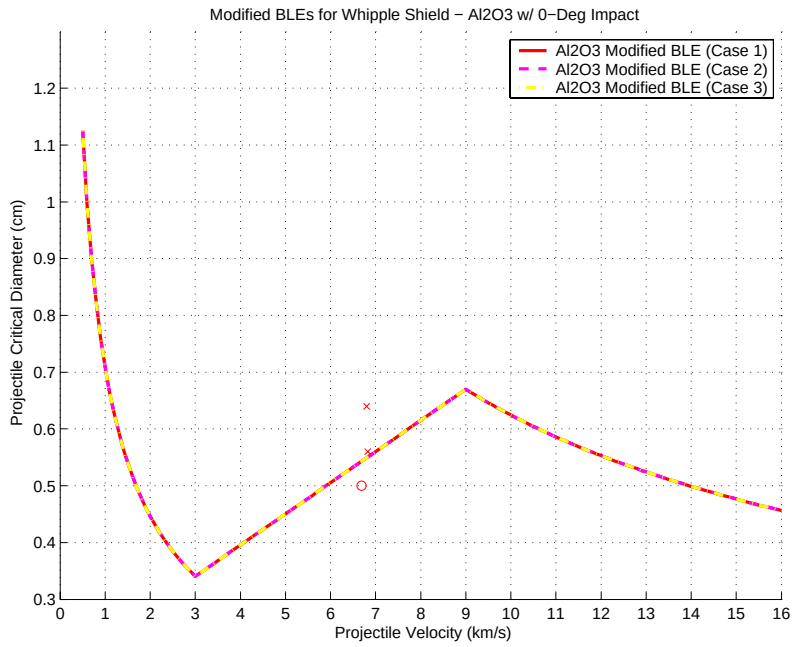

Figure H7. Composite of Improved Ballistic Limit Equations for Whipple Shield with Aluminum Oxide Projectile at 0-degree Impact.

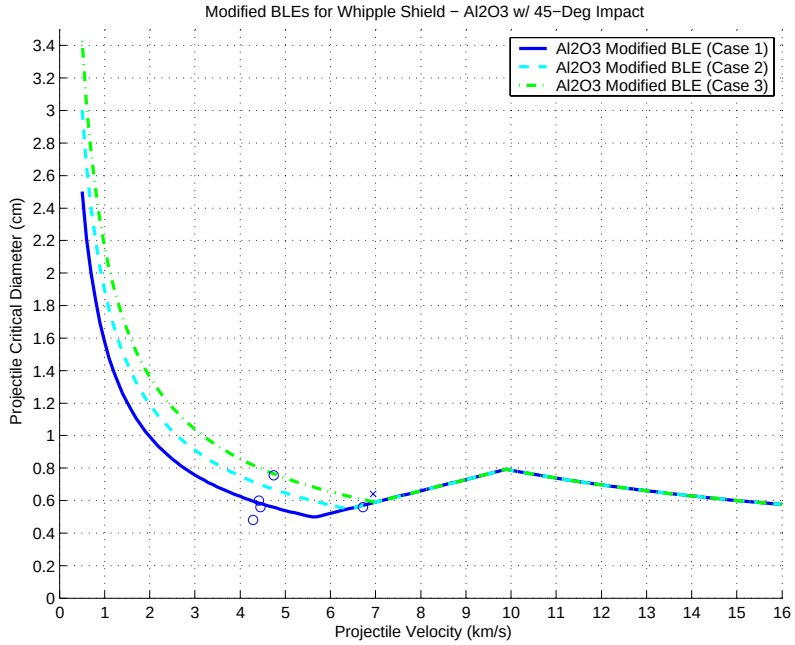

Figure H8. Composite of Improved Ballistic Limit Equations for Whipple Shield with Aluminum Oxide Projectile at 45-degree Impact.

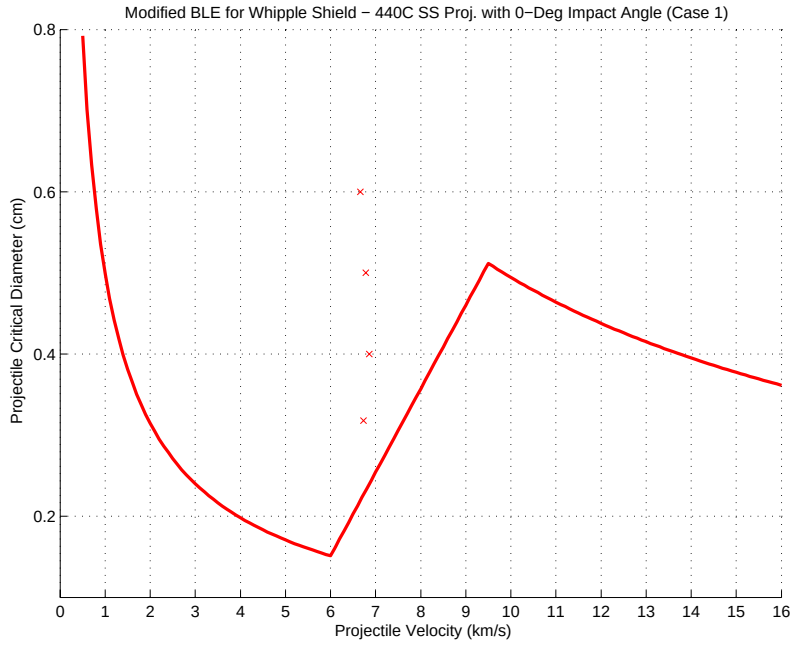

Figure H9. Improved Ballistic Limit Equation for Whipple Shield with 440C Stainless Steel Projectile at 0-degree Impact (Case 1).

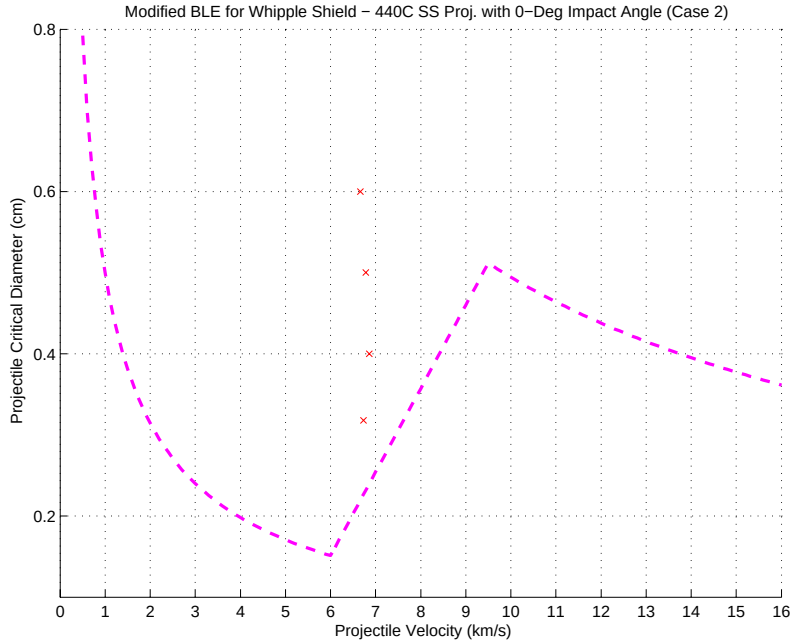

Figure H10. Improved Ballistic Limit Equation for Whipple Shield with 440C Stainless Steel Projectile at 0-degree Impact (Case 2).

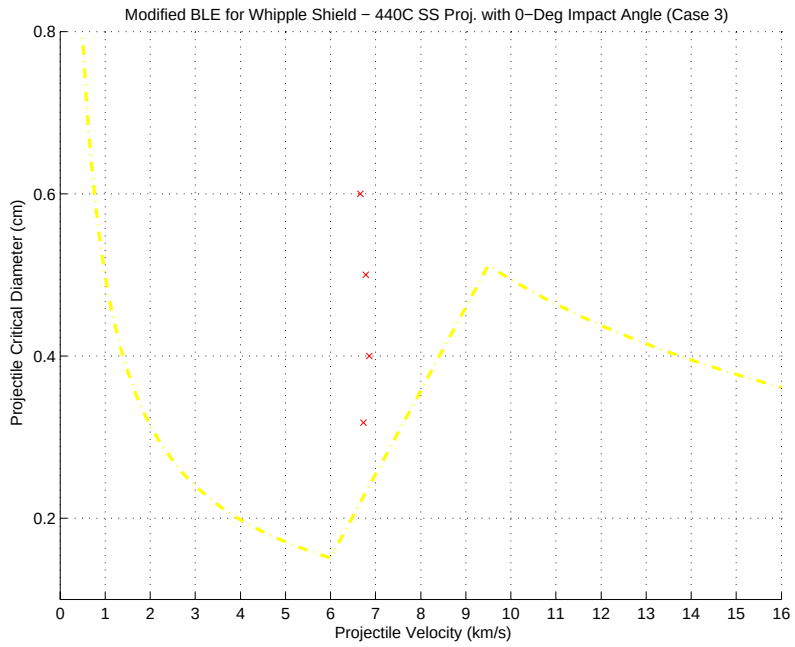

Figure H11. Improved Ballistic Limit Equation for Whipple Shield with 440C Stainless Steel Projectile at 0-degree Impact (Case 3).

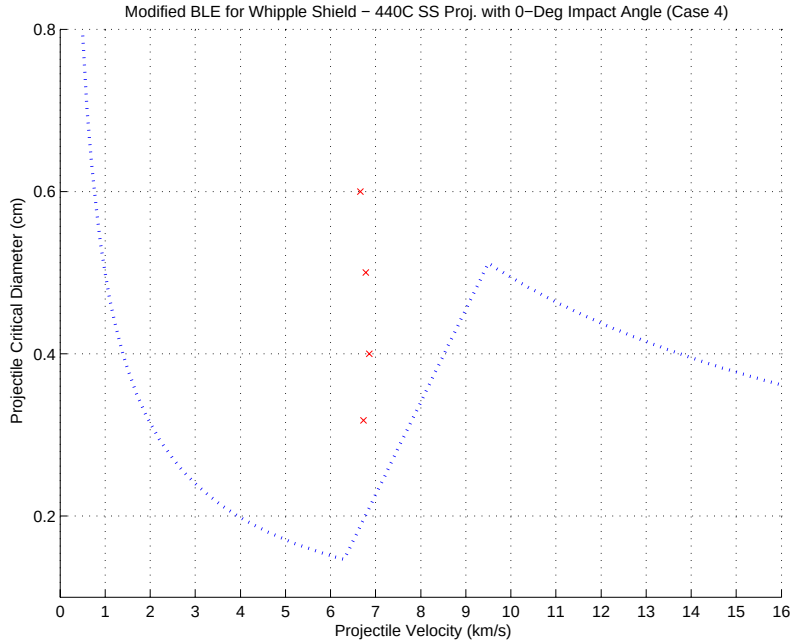

Figure H12. Improved Ballistic Limit Equation for Whipple Shield with 440C Stainless Steel Projectile at 0-degree Impact (Case 4).

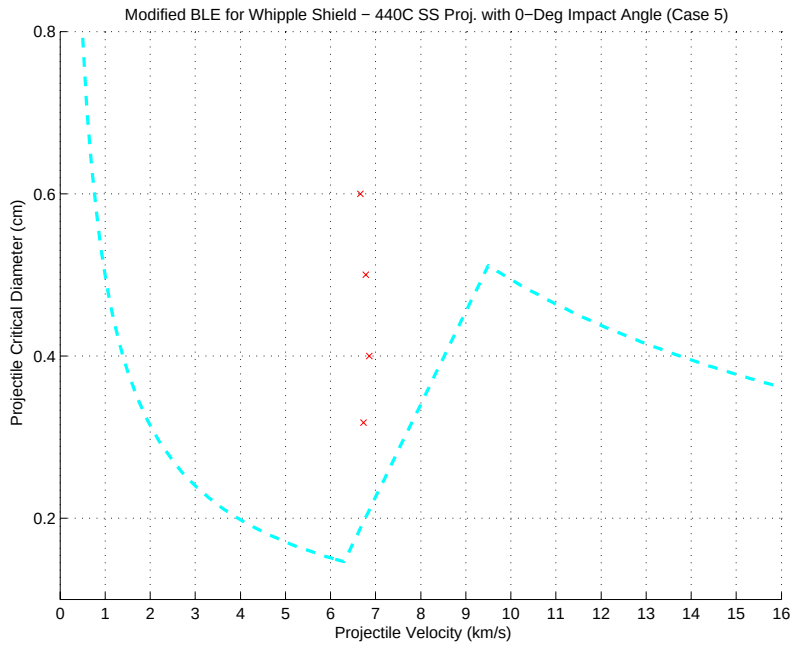

Figure H13. Improved Ballistic Limit Equation for Whipple Shield with 440C Stainless Steel Projectile at 0-degree Impact (Case 5).

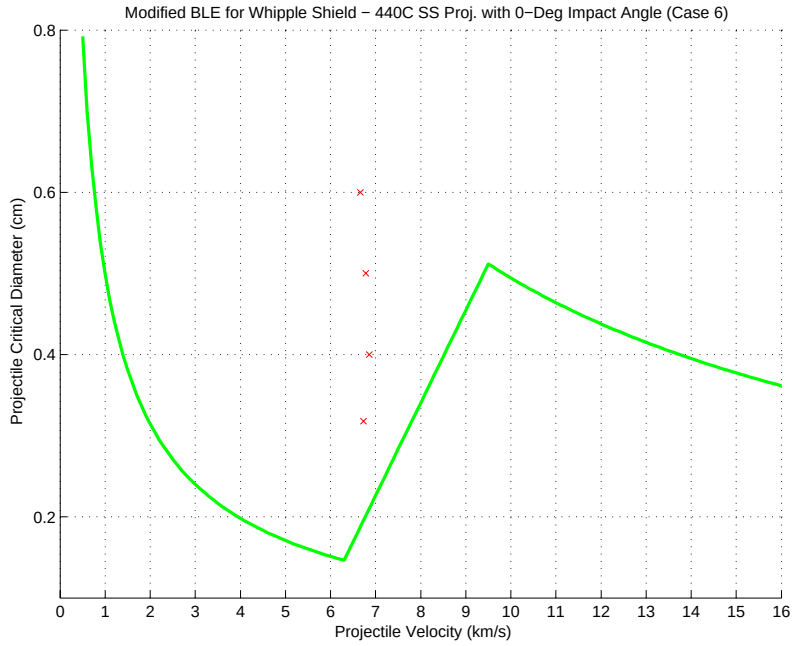

Figure H14. Improved Ballistic Limit Equation for Whipple Shield with 440C Stainless Steel Projectile at 0-degree Impact (Case 6).

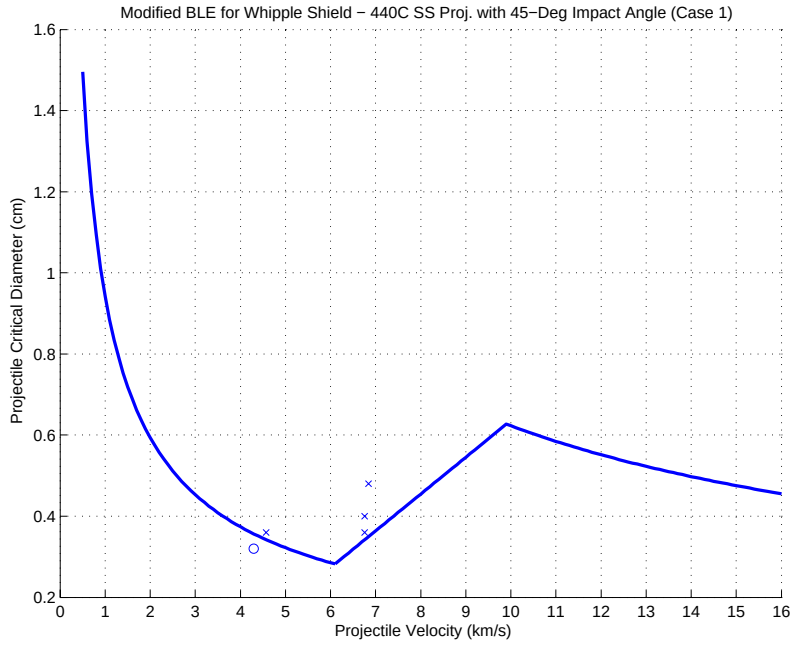

Figure H15. Improved Ballistic Limit Equation for Whipple Shield with 440C Stainless Steel Projectile at 45-degree Impact (Case 1).

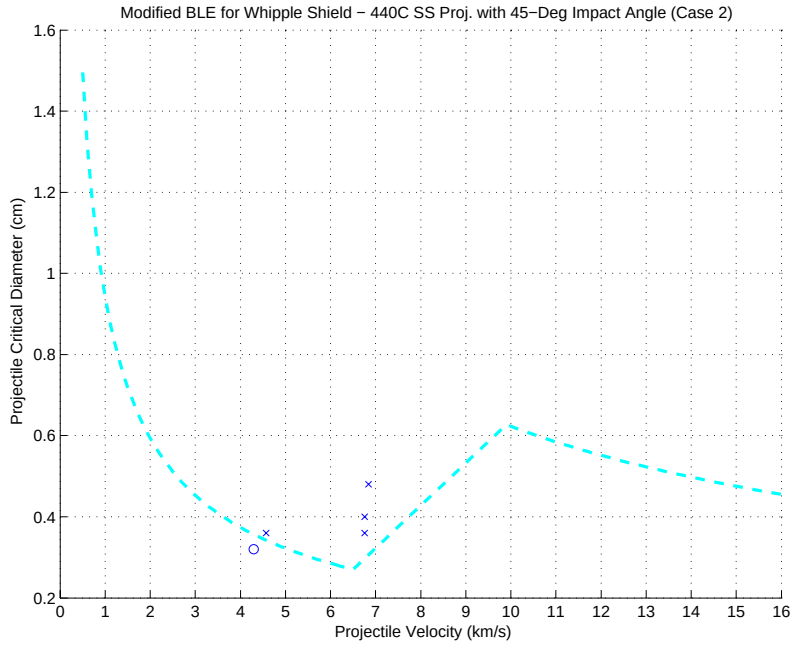

Figure H16. Improved Ballistic Limit Equation for Whipple Shield with 440C Stainless Steel Projectile at 45-degree Impact (Case 2).

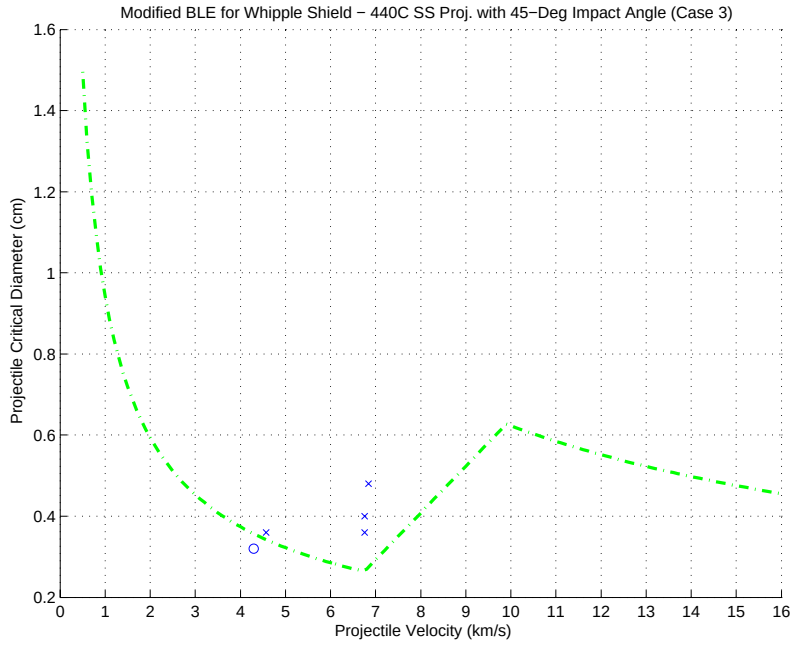

Figure H17. Improved Ballistic Limit Equation for Whipple Shield with 440C Stainless Steel Projectile at 45-degree Impact (Case 3).

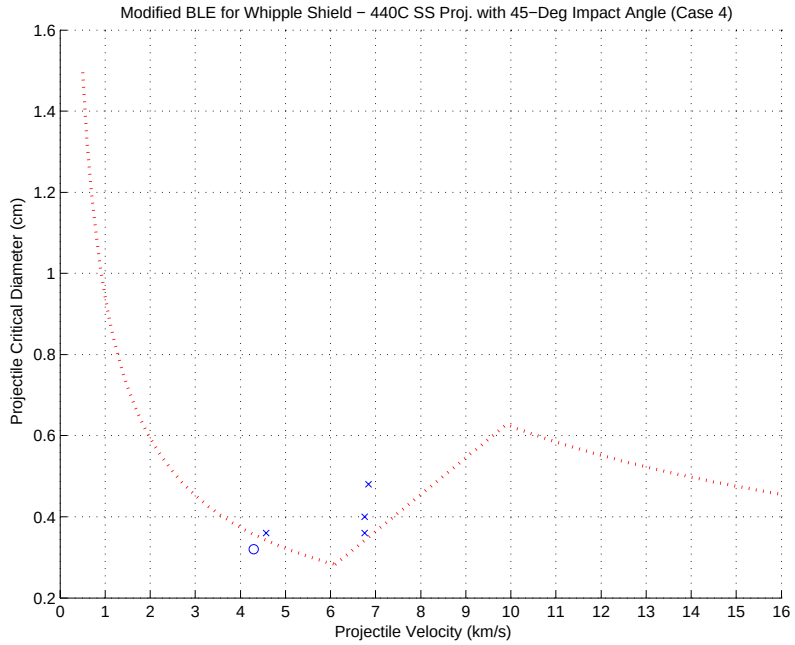

Figure H18. Improved Ballistic Limit Equation for Whipple Shield with 440C Stainless Steel Projectile at 45-degree Impact (Case 4).

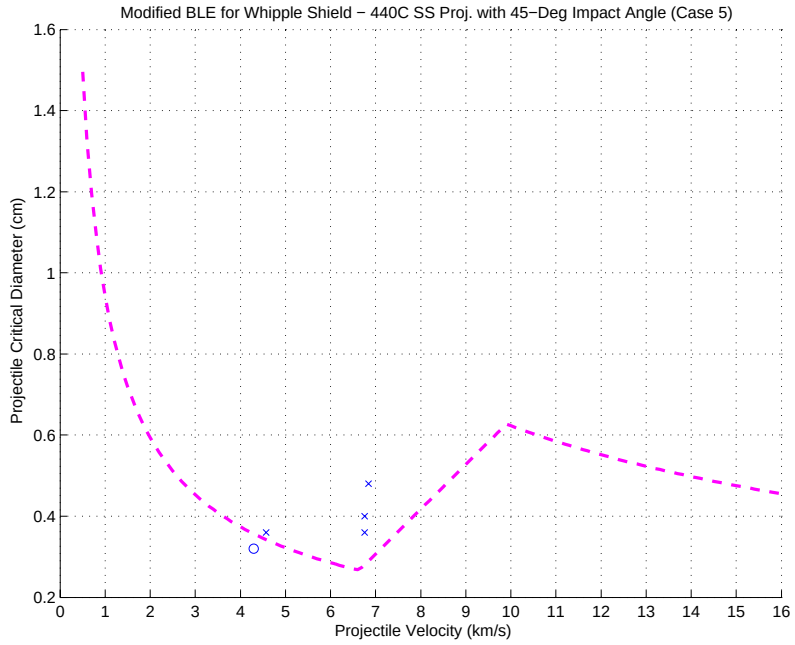

Figure H19. Improved Ballistic Limit Equation for Whipple Shield with 440C Stainless Steel Projectile at 45-degree Impact (Case 5).

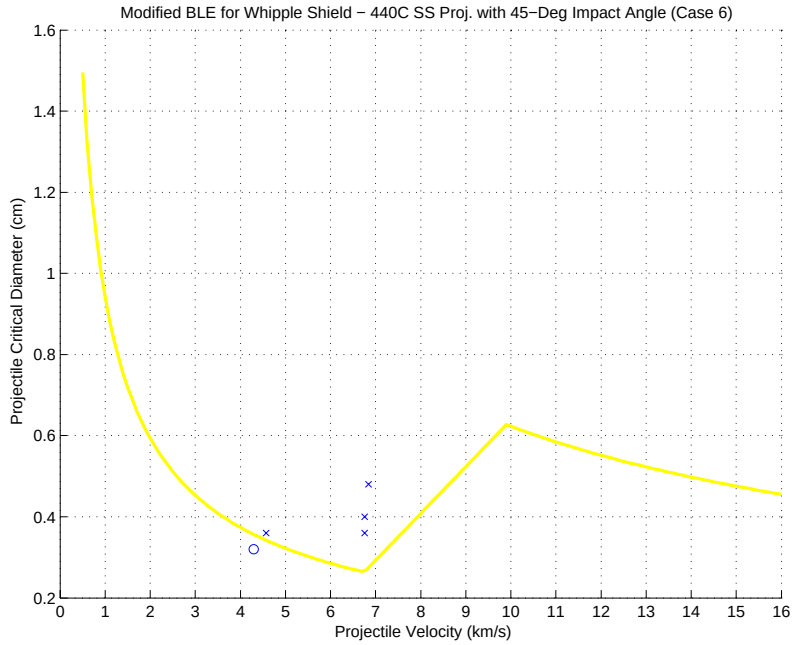

Figure H20. Improved Ballistic Limit Equation for Whipple Shield with 440C Stainless Steel Projectile at 45-degree Impact (Case 6).

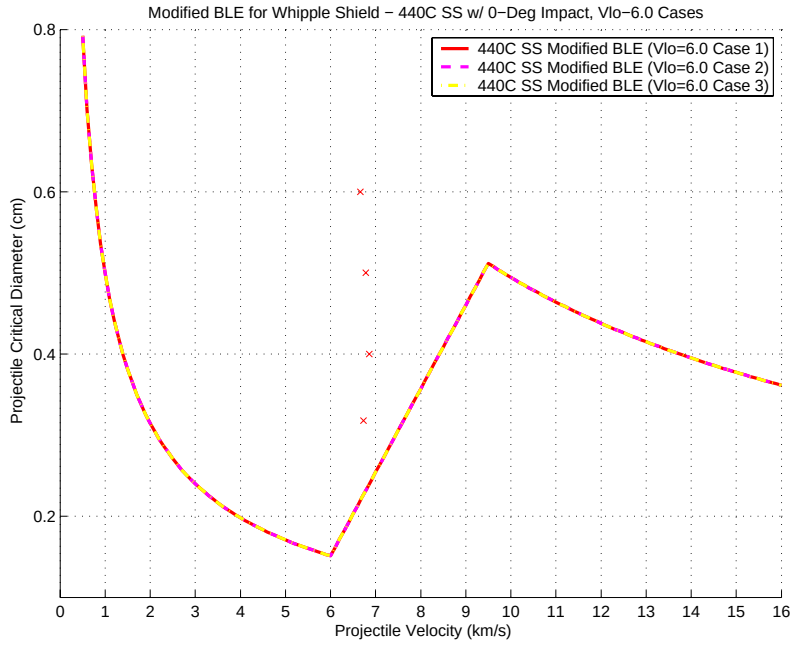

Figure H21. Composite of Improved Ballistic Limit Equations for Whipple Shield with 440C Stainless Steel Projectile at 0-degree Impact (Cases 1-3, Vlo=6.0).

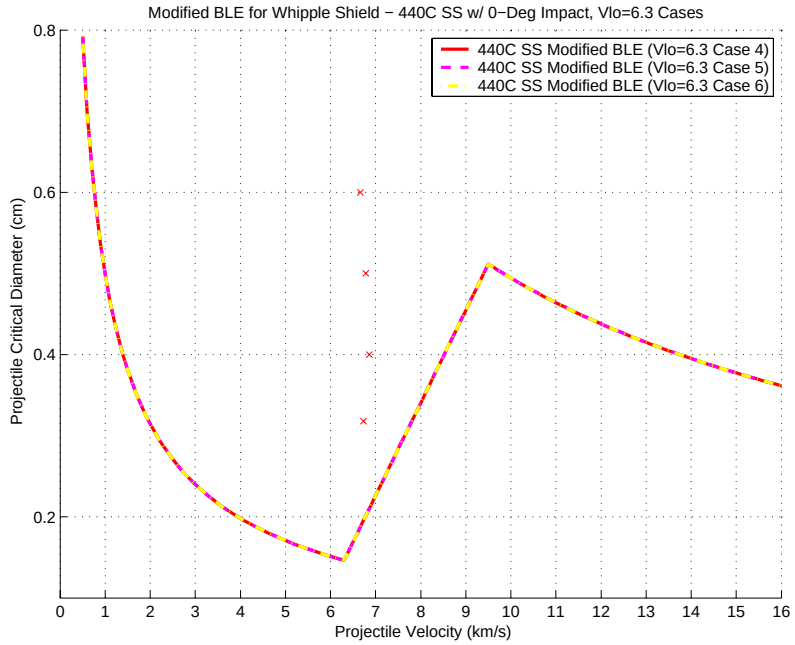

Figure H22. Composite of Improved Ballistic Limit Equations for Whipple Shield with 440C Stainless Steel Projectile at 0-degree Impact (Cases 4-6, Vlo=6.3).

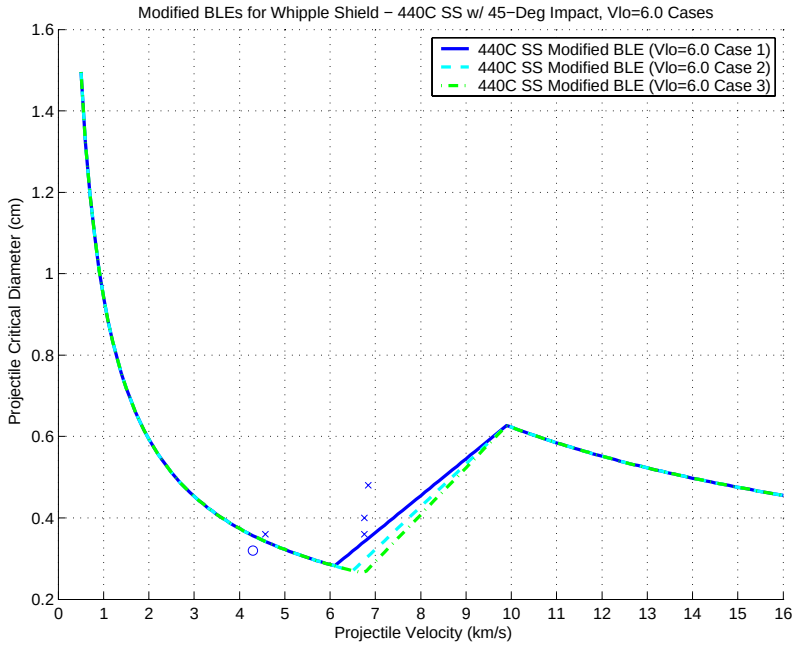

Figure H23. Composite of Improved Ballistic Limit Equations for Whipple Shield with 440C Stainless Steel Projectile at 45-degree Impact (Cases 1-3, Vlo=6.0).

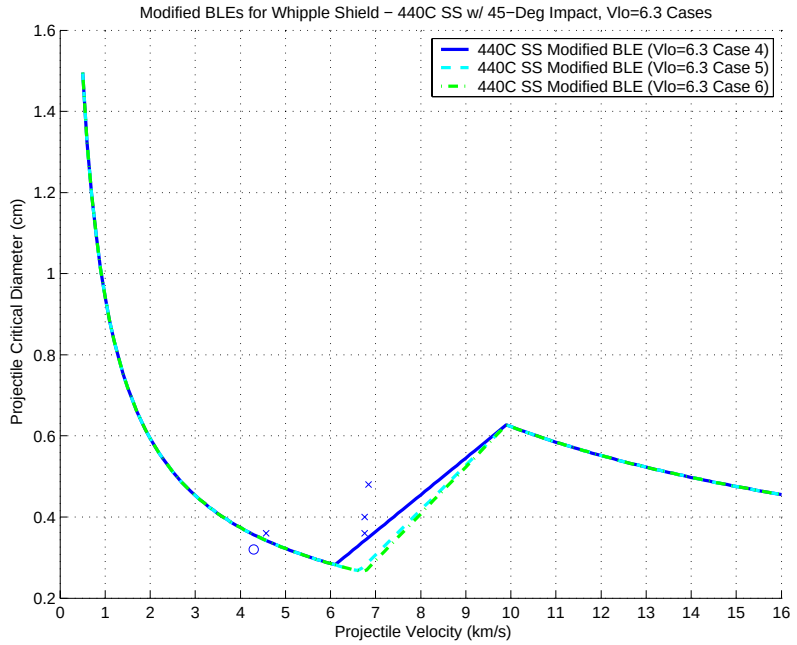

Figure H24. Composite of Improved Ballistic Limit Equations for Whipple Shield with 440C Stainless Steel Projectile at 45-degree Impact (Cases 4-6, Vlo=6.3).

2. ENHANCED STUFFED WHIPPLE SHIELDS

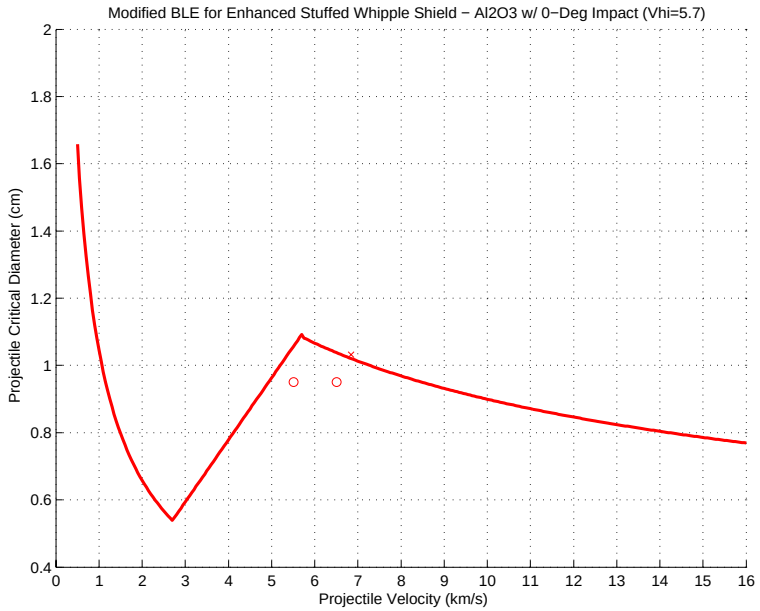

Figure H25. Improved Ballistic Limit Equation for Stuffed Whipple Shield with Aluminum Oxide Projectile at 0-degree Impact (Case 1, Vhi = 5.7).

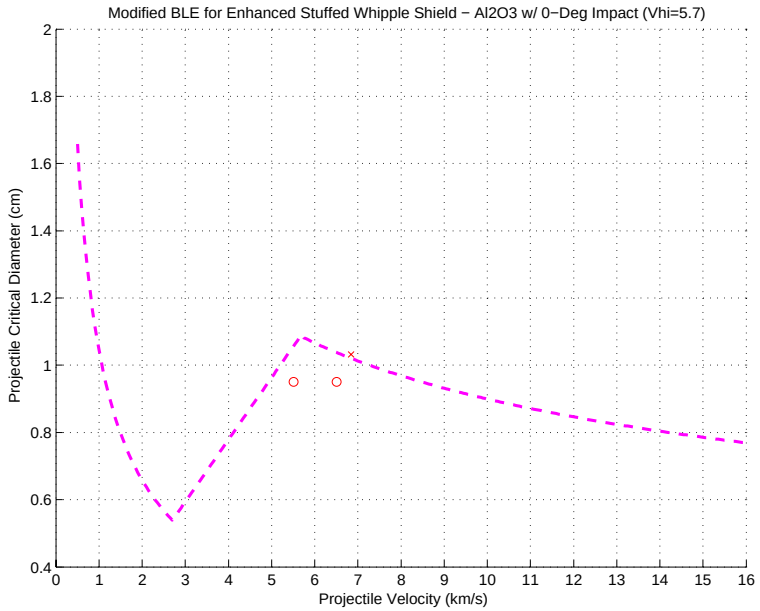

Figure H26. Improved Ballistic Limit Equation for Stuffed Whipple Shield with Aluminum Oxide Projectile at 0-degree Impact (Case 2).

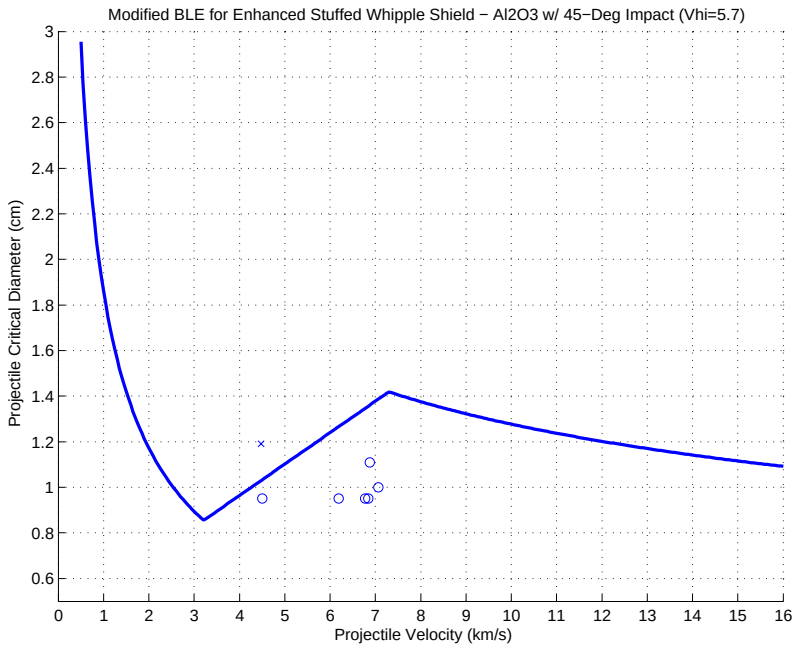

Figure H27. Improved Ballistic Limit Equation for Stuffed Whipple Shield with Aluminum Oxide Projectile at 45-degree Impact (Case 1, Vhi = 5.7).

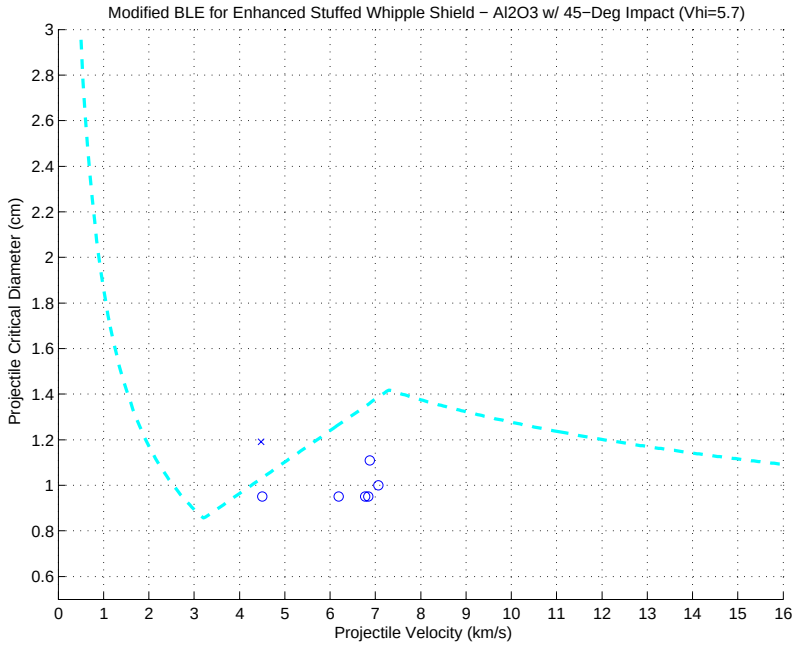

Figure H28. Improved Ballistic Limit Equation for Stuffed Whipple Shield with Aluminum Oxide Projectile at 45-degree Impact (Vhi = 5.7).

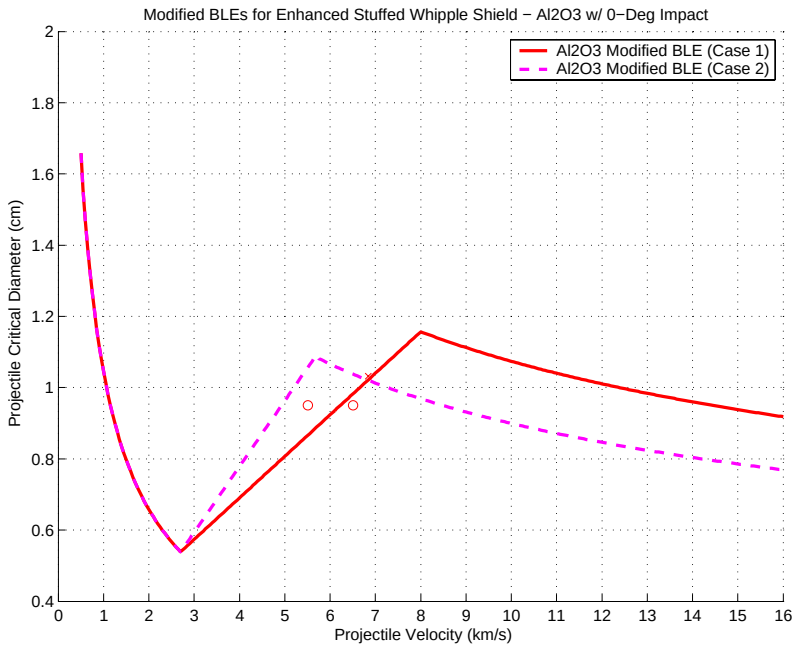

Figure H29. Combined Improved Ballistic Limit Equations for Stuffed Whipple Shield with Aluminum Oxide Projectile at 0-degree Impact.

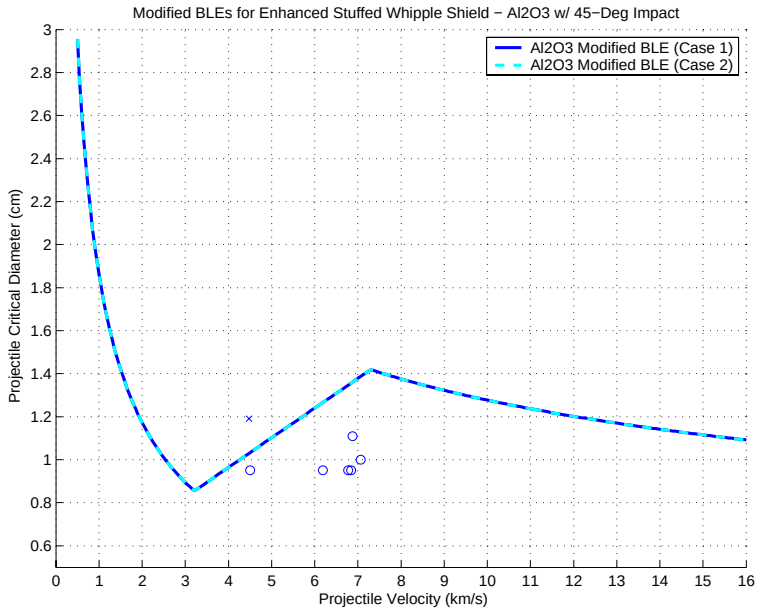

Figure H30. Combined Improved Ballistic Limit Equations for Stuffed Whipple Shield with Aluminum Oxide Projectile at 0-degree Impact.

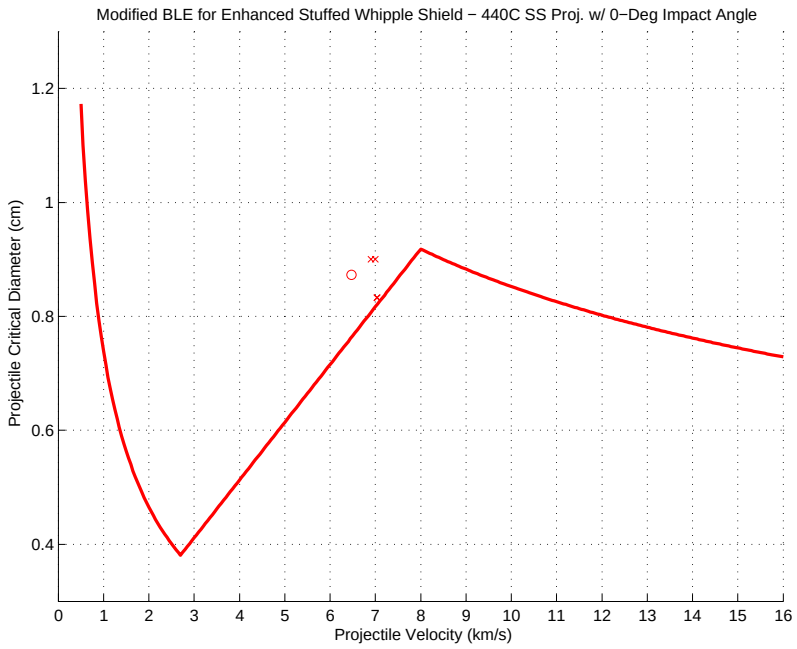

Figure H31. Improved Ballistic Limit Equation for Stuffed Whipple Shield with 440C Stainless Steel Projectile at 0-degree Impact (Case 1).

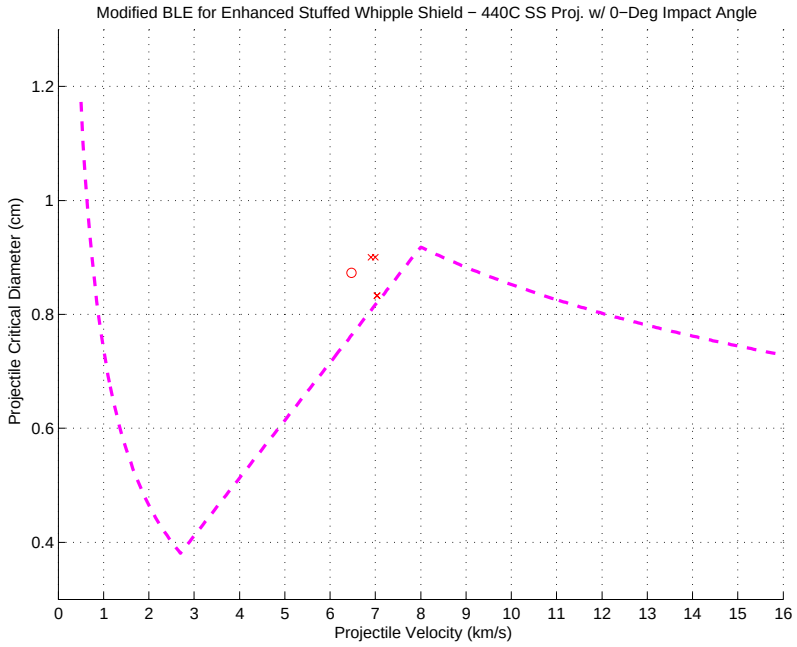

Figure H32. Improved Ballistic Limit Equation for Stuffed Whipple Shield with 440C Stainless Steel Projectile at 0-degree Impact (Case 2).

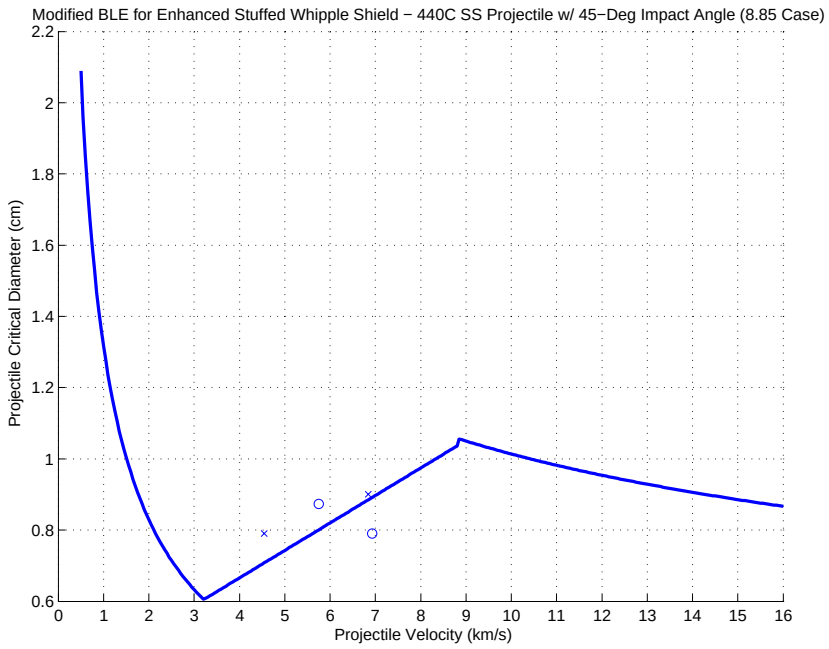

Figure H33. Improved Ballistic Limit Equation for Stuffed Whipple Shield with 440C Stainless Steel Projectile at 45-degree Impact (Case 1, Vhi = 8.85).

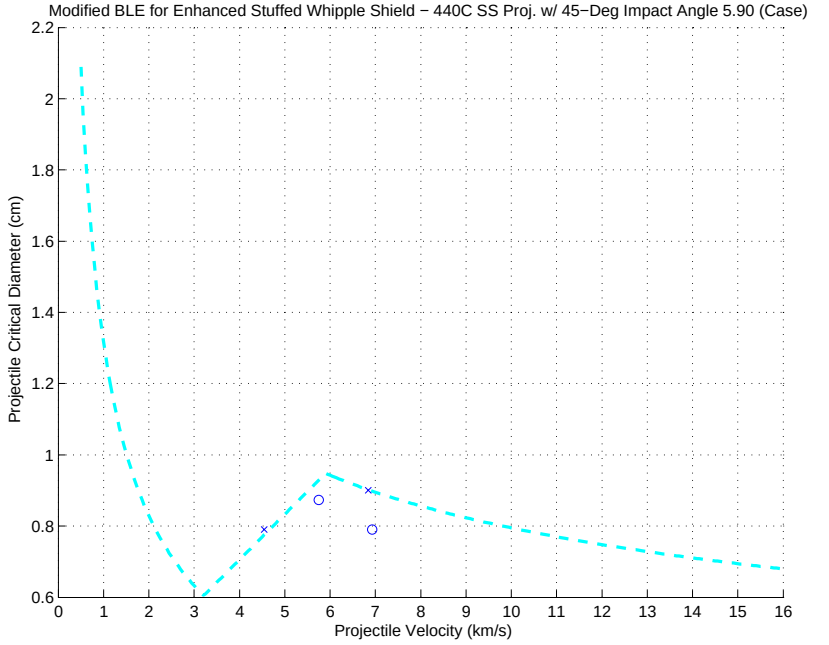

Figure H34. Improved Ballistic Limit Equation for Stuffed Whipple Shield with 440C Stainless Steel Projectile at 45-degree Impact (Case 2, Vhi = 5.9).

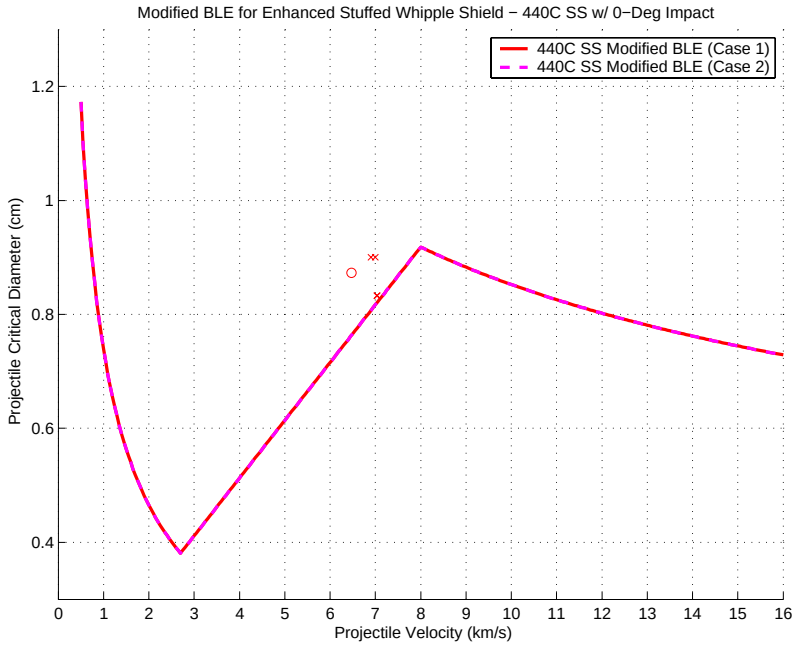

Figure H35. Combined Improved Ballistic Limit Equations for Stuffed Whipple Shield with 440C Stainless Steel Projectile at 0-degree Impact.

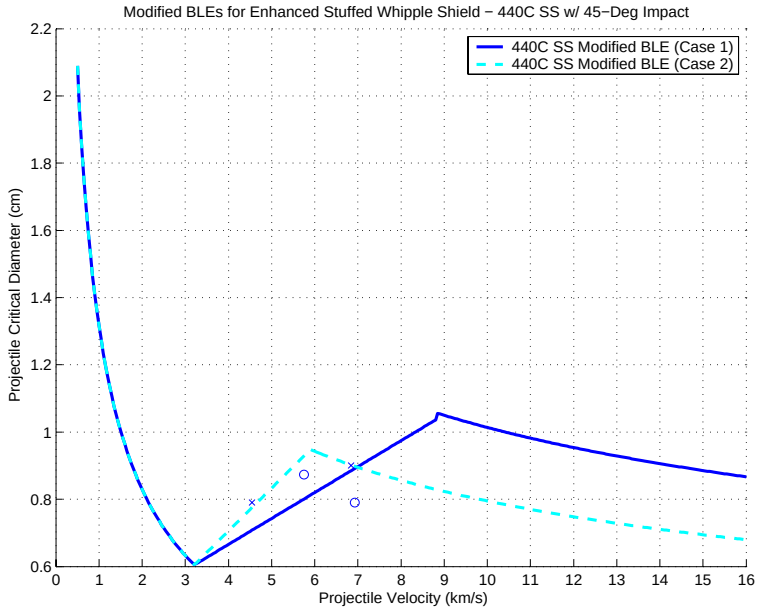

Figure H36. Combined Improved Ballistic Limit Equations for Stuffed Whipple Shield with 440C Stainless Steel Projectile at 45-degree Impact.

APPENDIX I - REVISED BALLISTIC LIMIT CURVES WITH ENTERING CURVES

1. WHIPPLE SHIELDS

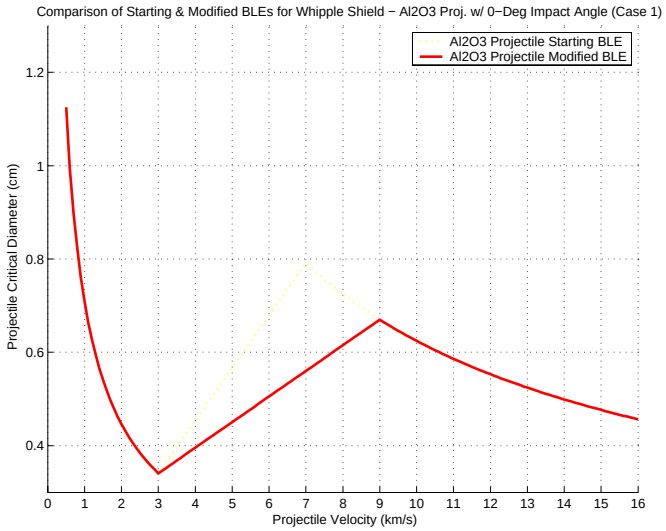

Figure I1. Starting vs. Improved Ballistic Limit Equation for Whipple Shield with Aluminum Oxide Projectile at 0-degree Impact (Case 1).

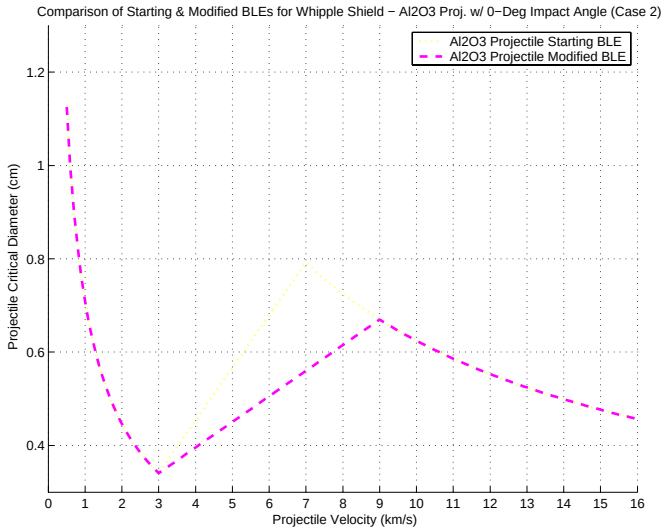

Figure I2. Starting vs. Improved Ballistic Limit Equation for Whipple Shield with Aluminum Oxide Projectile at 0-degree Impact (Case 2).

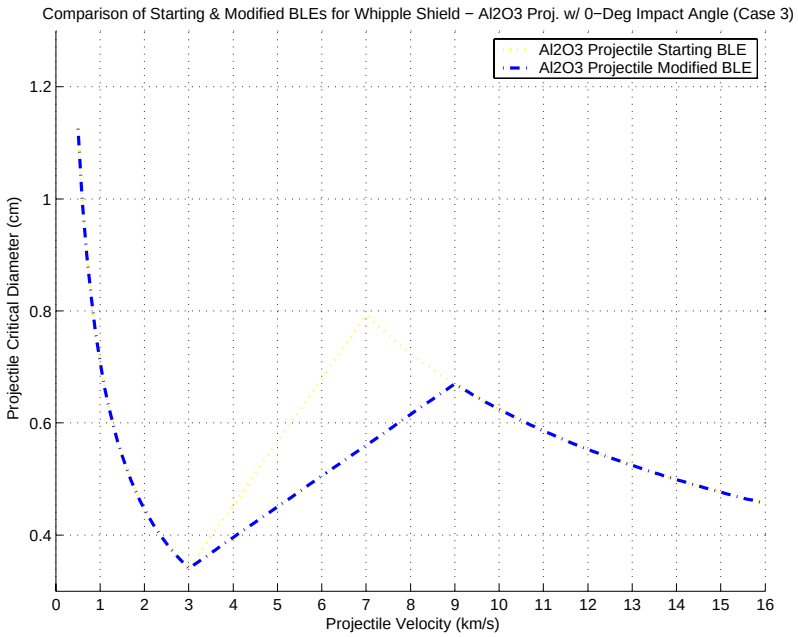

Figure I3. Starting vs. Improved Ballistic Limit Equation for Whipple Shield with Aluminum Oxide Projectile at 0-degree Impact (Case 3).

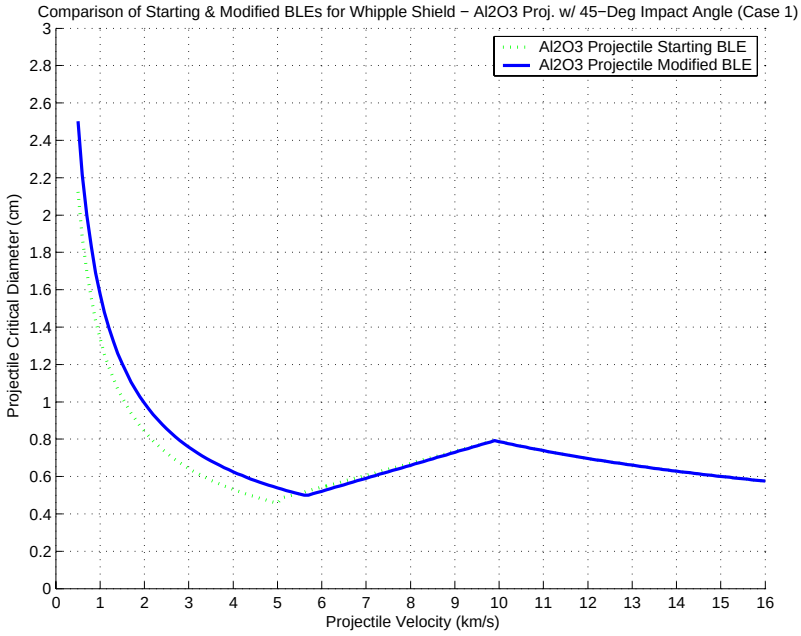

Figure I4. Starting vs. Improved Ballistic Limit Equation for Whipple Shield with Aluminum Oxide Projectile at 45-degree Impact (Case 1).

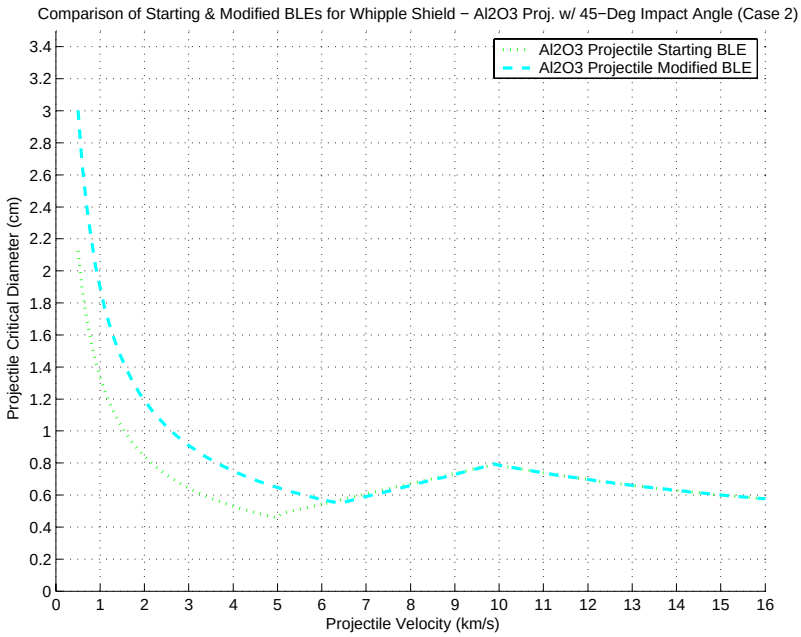

Figure I5. Starting vs. Improved Ballistic Limit Equation for Whipple Shield with Aluminum Oxide Projectile at 45-degree Impact (Case 2).

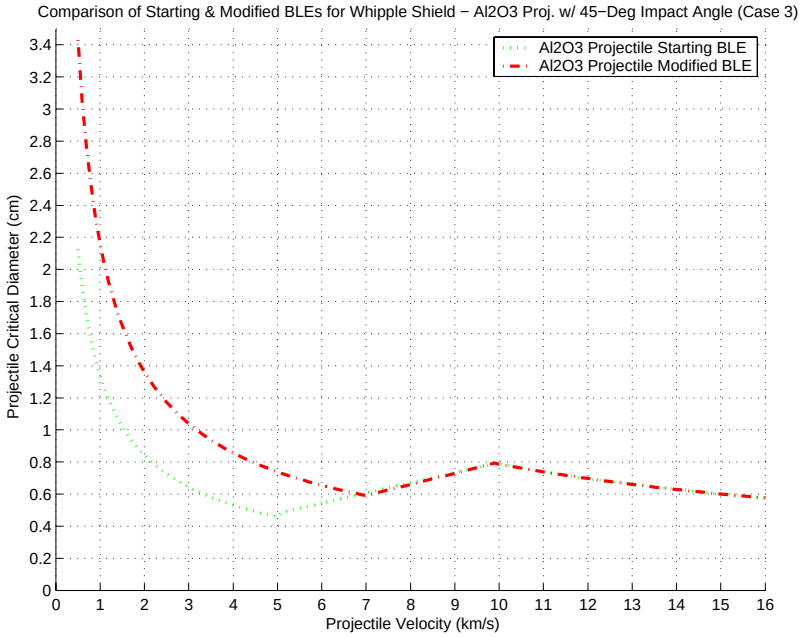

Figure I6. Starting vs. Improved Ballistic Limit Equation for Whipple Shield with Aluminum Oxide Projectile at 45-degree Impact (Case 3).

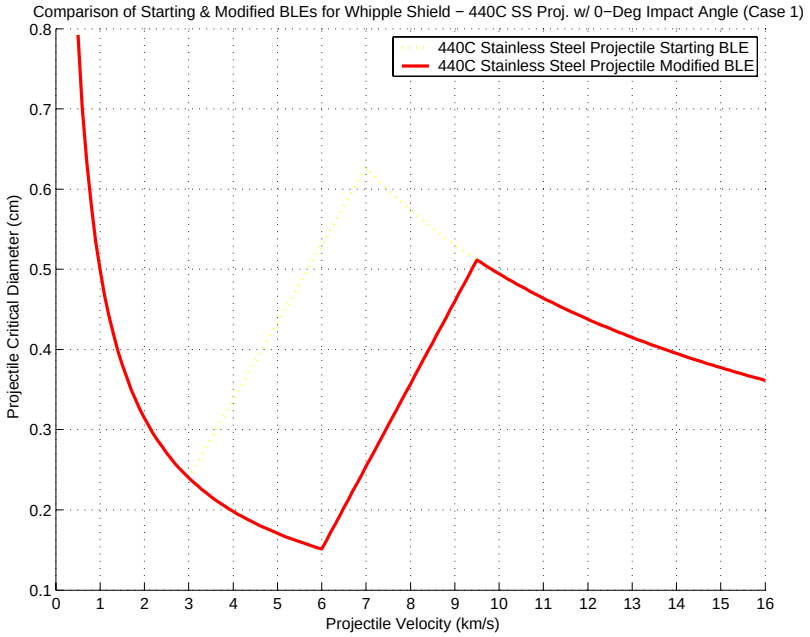

Figure I7. Starting vs. Improved Ballistic Limit Equation for Whipple Shield with 440C Stainless Steel Projectile at 0-degree Impact (Case 1).

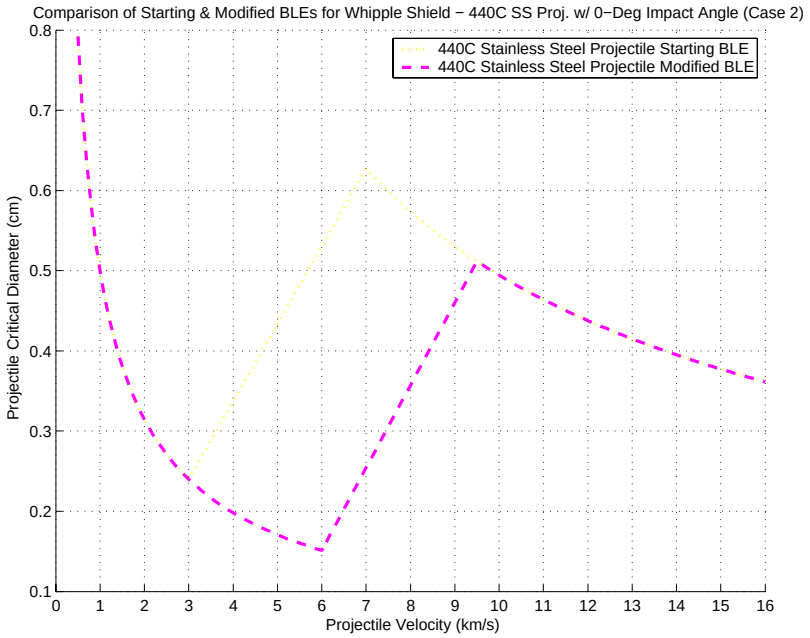

Figure I8. Starting vs. Improved Ballistic Limit Equation for Whipple Shield with 440C Stainless Steel Projectile at 0-degree Impact (Case 2).

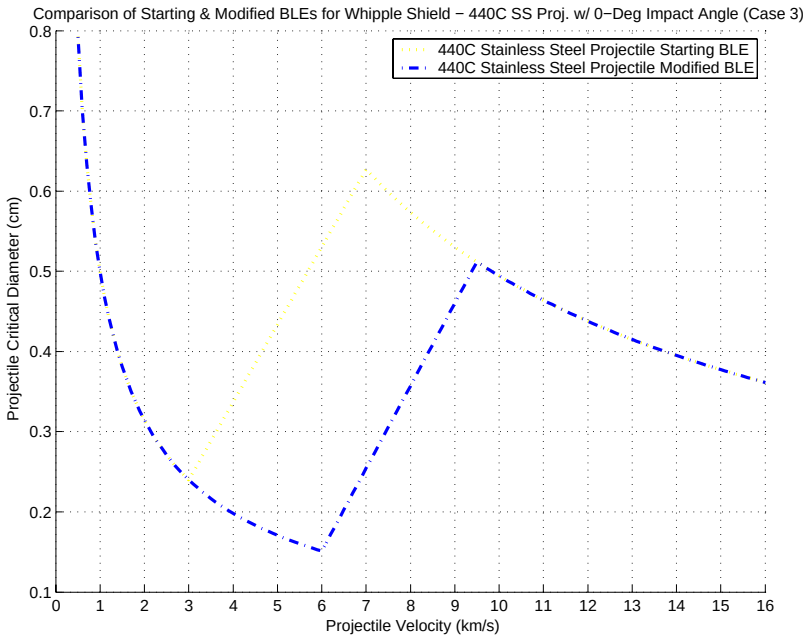

Figure I9. Starting vs. Improved Ballistic Limit Equation for Whipple Shield with 440C Stainless Steel Projectile at 0-degree Impact (Case 3).

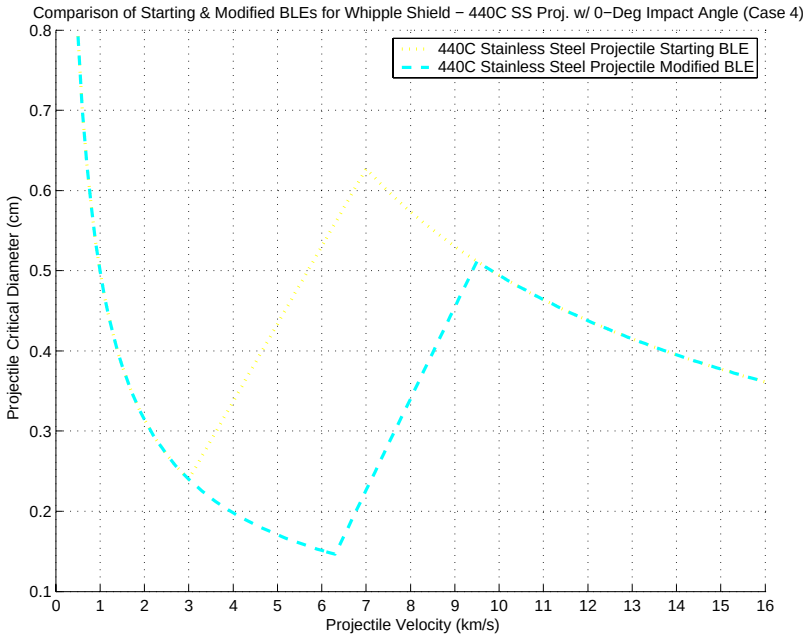

Figure I10. Starting vs. Improved Ballistic Limit Equation for Whipple Shield with 440C Stainless Steel Projectile at 0-degree Impact (Case 4).

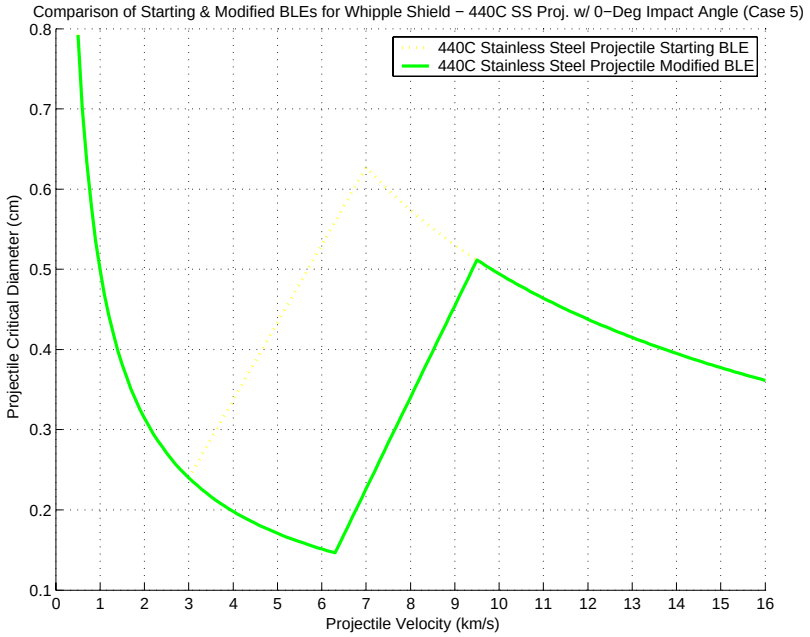

Figure I11. Starting vs. Improved Ballistic Limit Equation for Whipple Shield with 440C Stainless Steel Projectile at 0-degree Impact (Case 5).

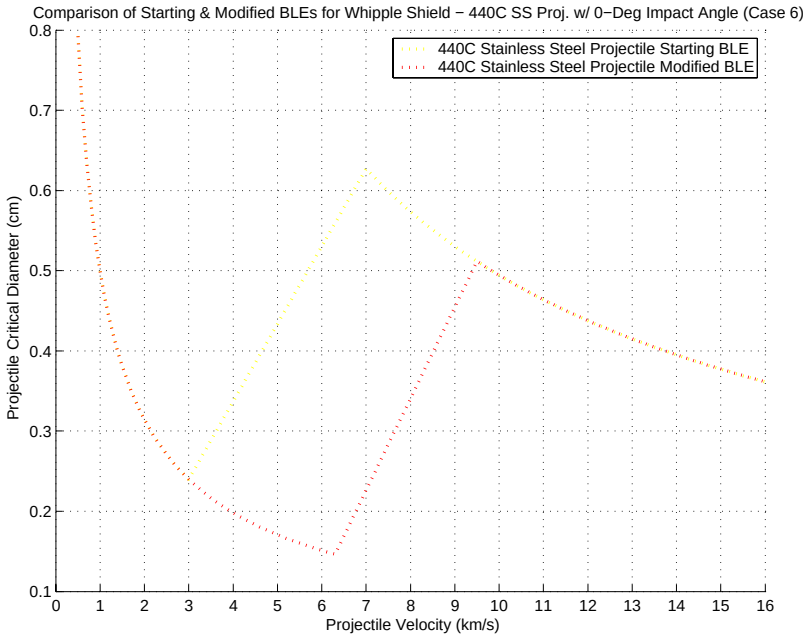

Figure I12. Starting vs. Improved Ballistic Limit Equation for Whipple Shield with 440C Stainless Steel Projectile at 0-degree Impact (Case 6).

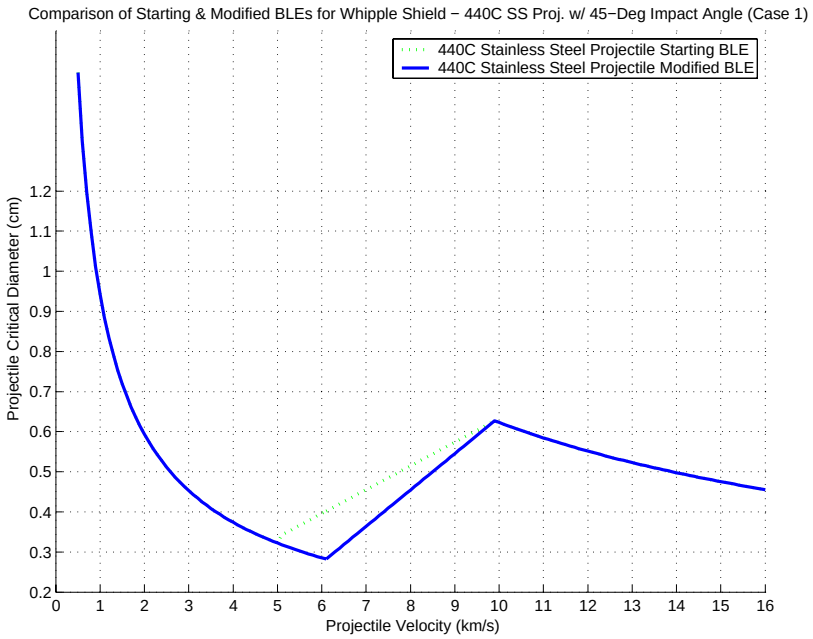

Figure I13. Starting vs. Improved Ballistic Limit Equation for Whipple Shield with 440C Stainless Steel Projectile at 45-degree Impact (Case 1).

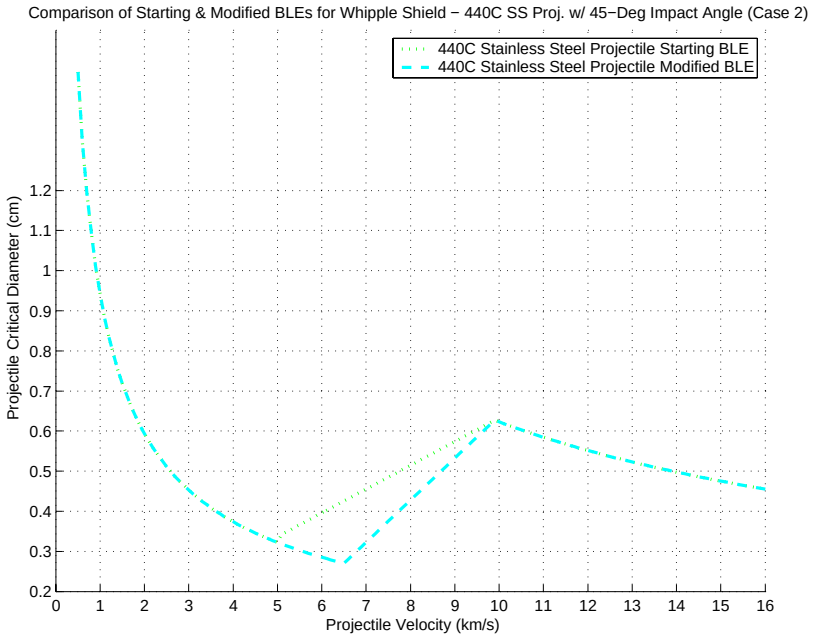

Figure I14. Starting vs. Improved Ballistic Limit Equation for Whipple Shield with 440C Stainless Steel Projectile at 45-degree Impact (Case 2).

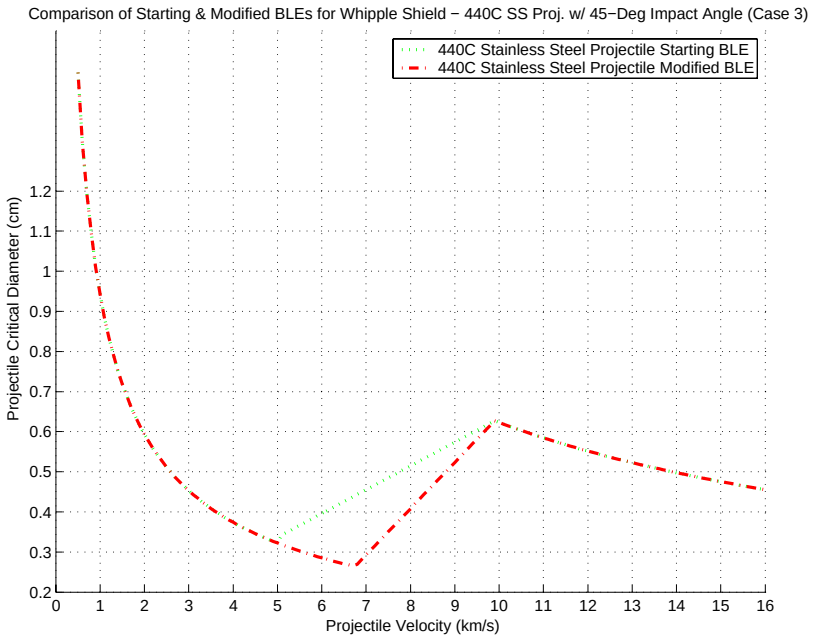

Figure I15. Starting vs. Improved Ballistic Limit Equation for Whipple Shield with 440C Stainless Steel Projectile at 45-degree Impact (Case 3).

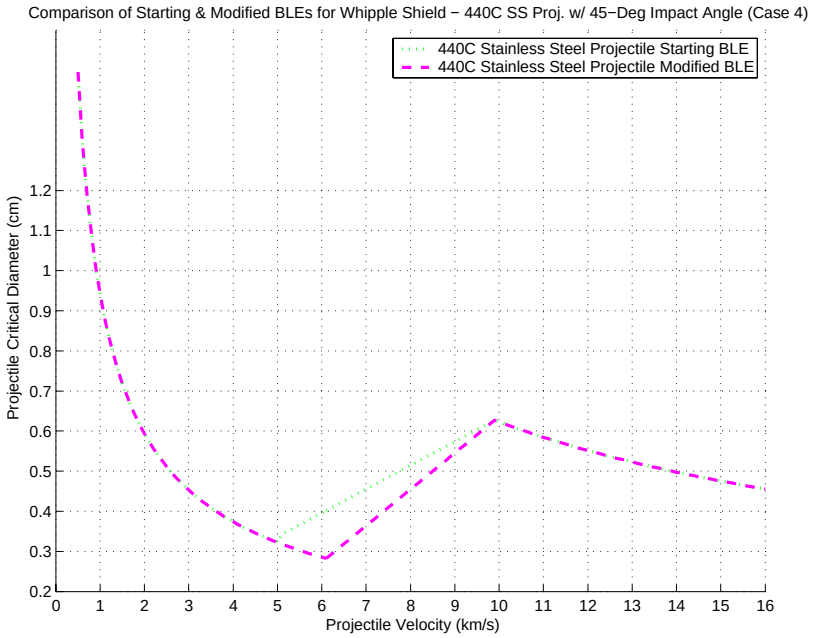

Figure I16. Starting vs. Improved Ballistic Limit Equation for Whipple Shield with 440C Stainless Steel Projectile at 45-degree Impact (Case 4).

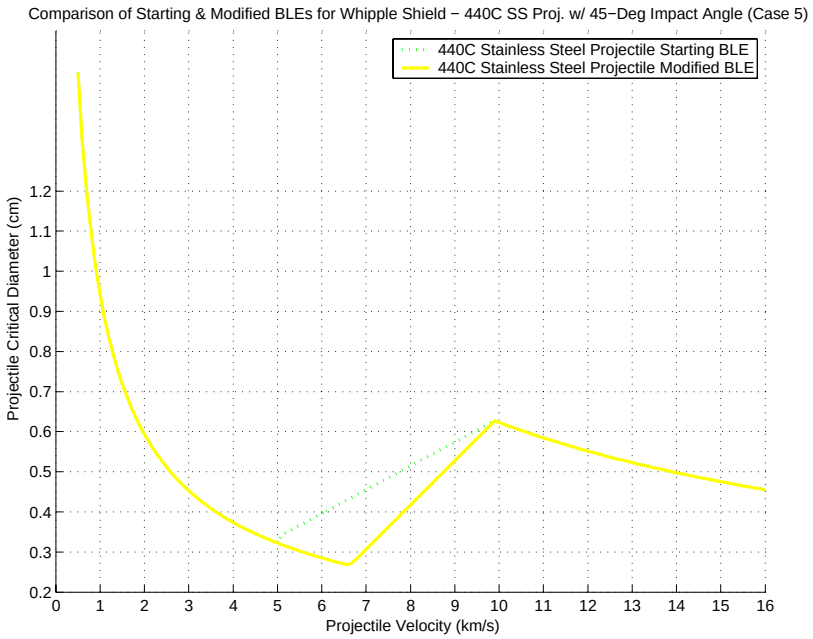

Figure I17. Starting vs. Improved Ballistic Limit Equation for Whipple Shield with 440C Stainless Steel Projectile at 45-degree Impact (Case 5).

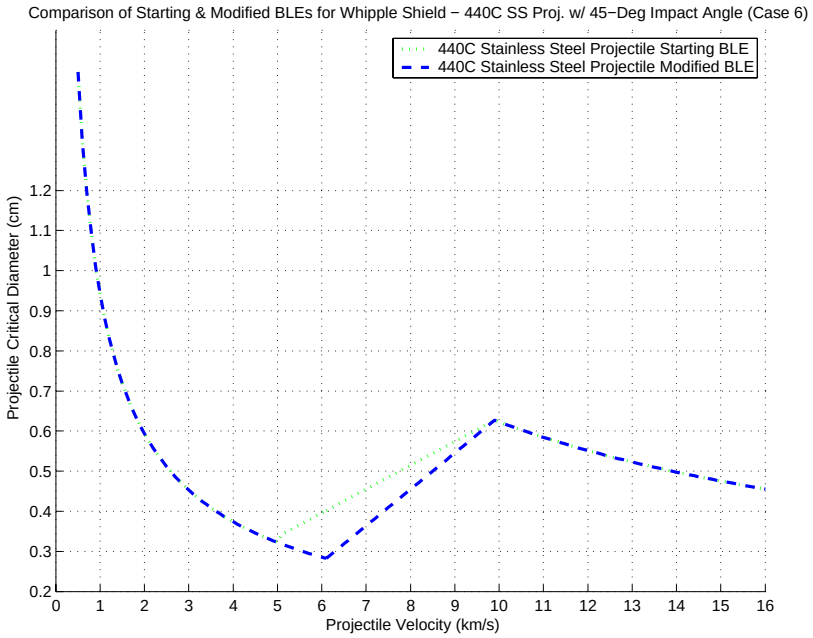

Figure I18. Starting vs. Improved Ballistic Limit Equation for Whipple Shield with 440C Stainless Steel Projectile at 45-degree Impact (Case 6).

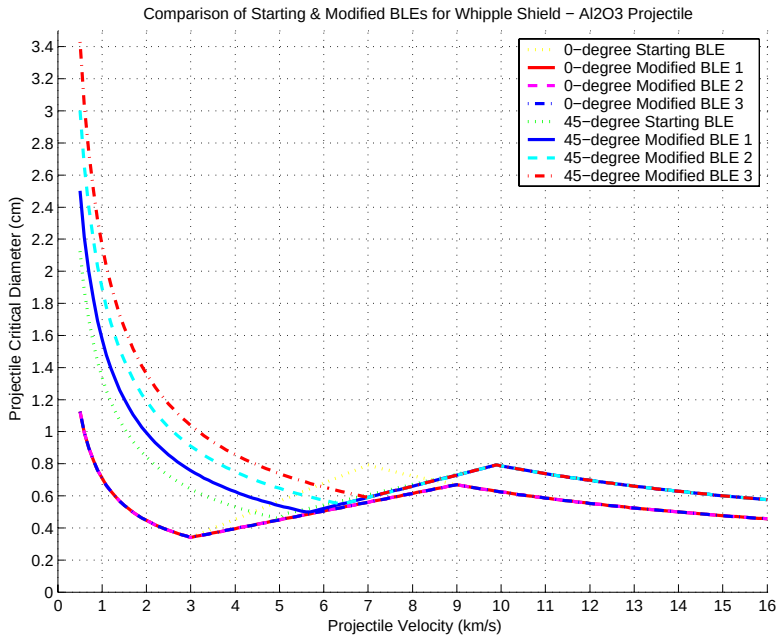

Figure I19. Combined Starting vs. Improved Ballistic Limit Equations for Whipple Shield with Aluminum Oxide Projectile (Cases 1-3).

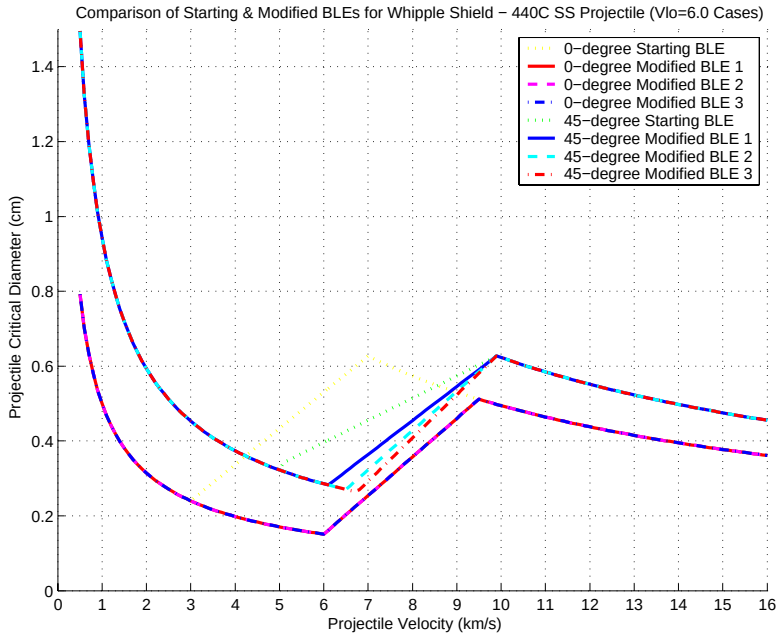

Figure I20. Combined Starting vs. Improved Ballistic Limit Equations for Whipple Shield with 440C Stainless Steel Projectile (Cases 1-3, Vhi = 6.0).

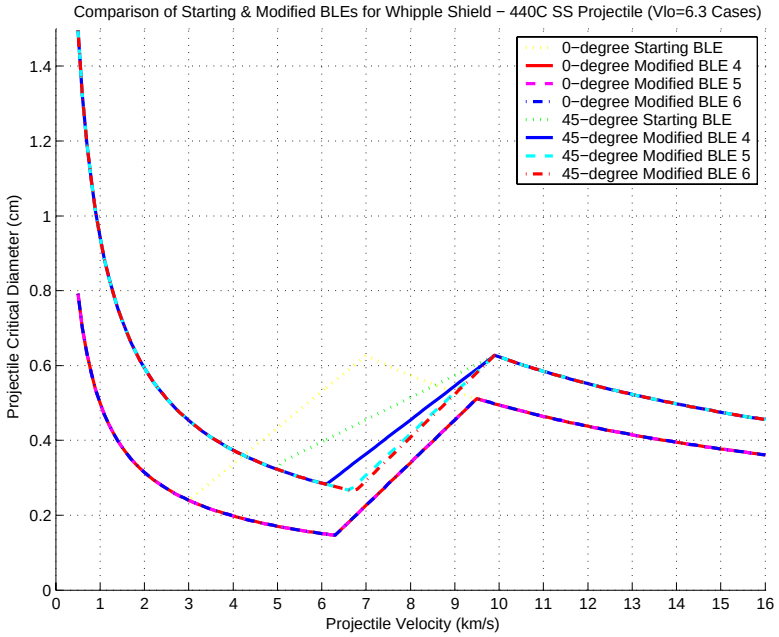

Figure I21. Combined Starting vs. Improved Ballistic Limit Equations for Whipple Shield with 440C Stainless Steel Projectile (Cases 4-6, Vhi = 6.3).

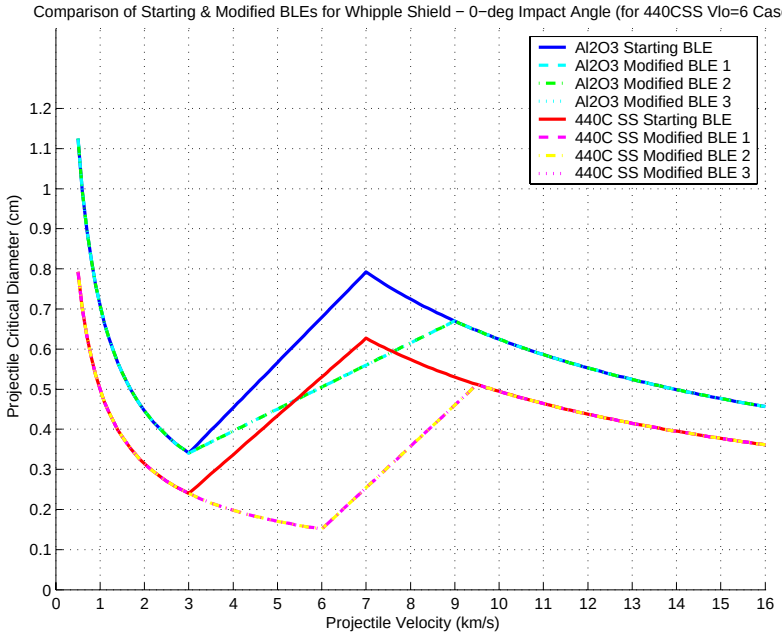

Figure I22. Combined Starting vs. Improved Ballistic Limit Equations for Whipple Shield with 0-degree Impacts (Cases 1-3, Where 440C SS Vlo = 6.0).

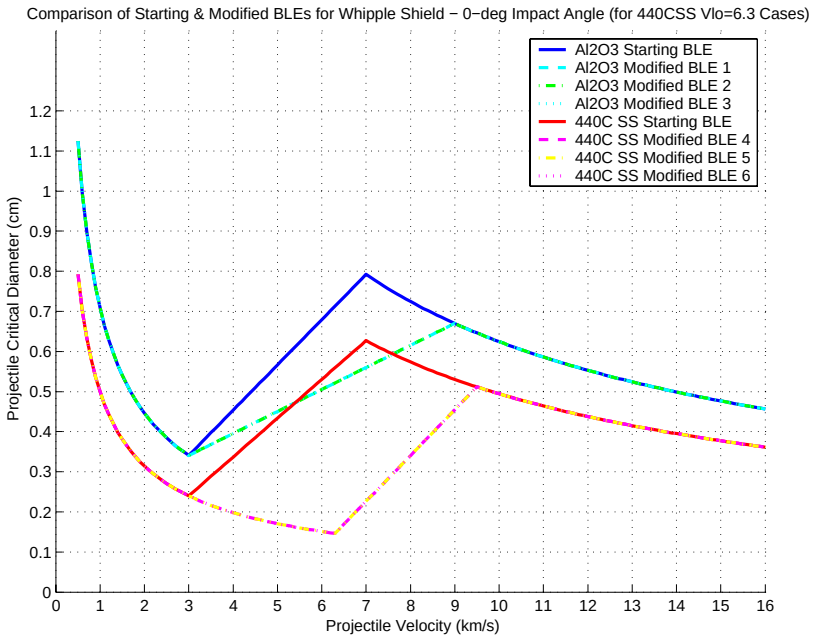

Figure I23. Combined Starting vs. Improved Ballistic Limit Equations for Whipple Shield with 0-degree Impacts (Cases 4-6, Where 440C SS Vlo = 6.3).

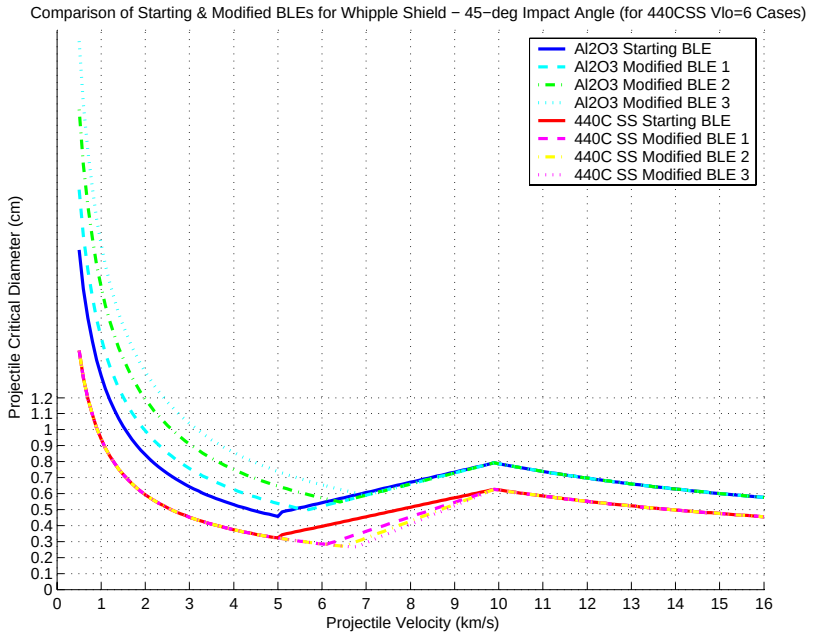

Figure I24. Combined Starting vs. Improved Ballistic Limit Equations for Whipple Shield with 45-degree Impacts (Cases 1-3, Where 440C SS Vlo = 6.0).

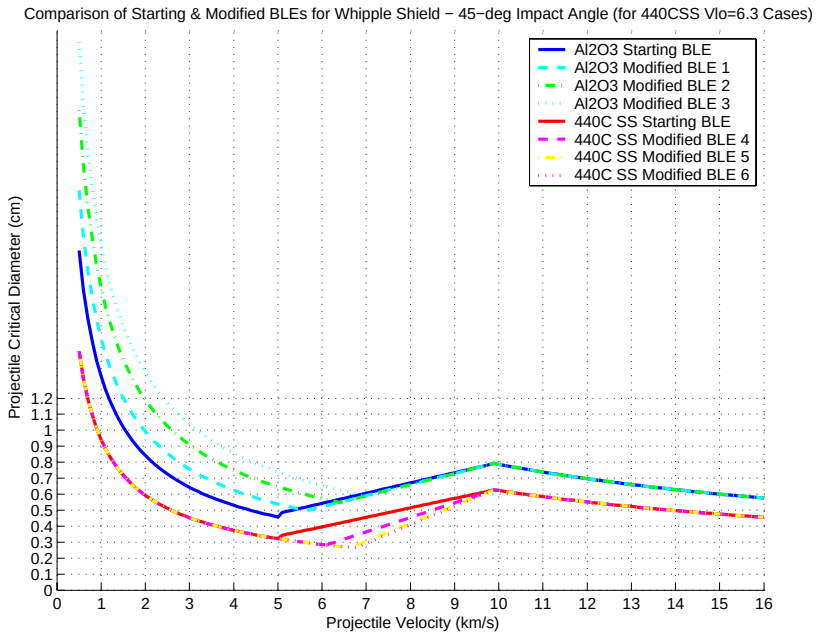

Figure I25. Combined Starting vs. Improved Ballistic Limit Equations for Whipple Shield with 45-degree Impacts (Cases 4-6, Where 440C SS Vlo = 6.3).

2. ENHANCED STUFFED WHIPPLE SHIELDS

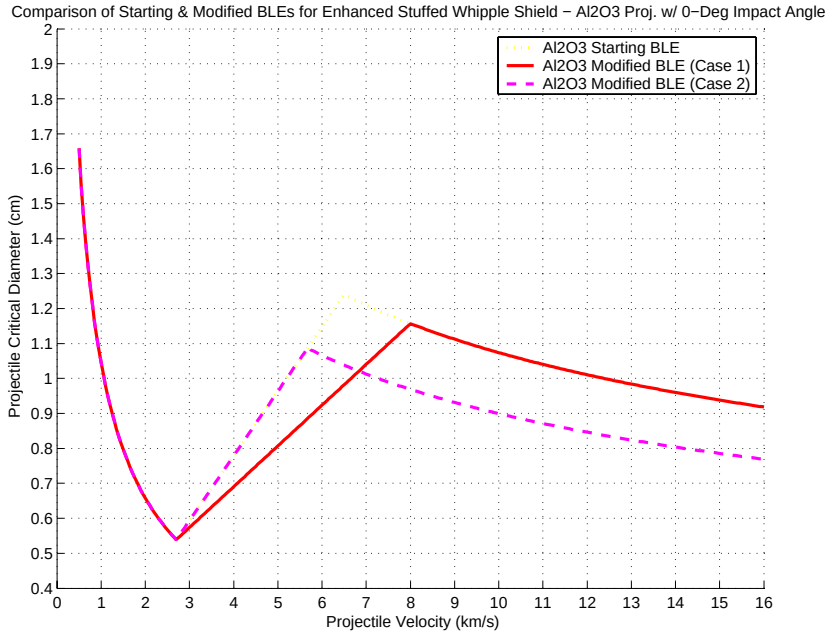

Figure I26. Starting vs. Improved Ballistic Limit Equation for Stuffed Whipple Shield with Aluminum Oxide Projectile at 0-degree Impact (Cases 1 & 2).

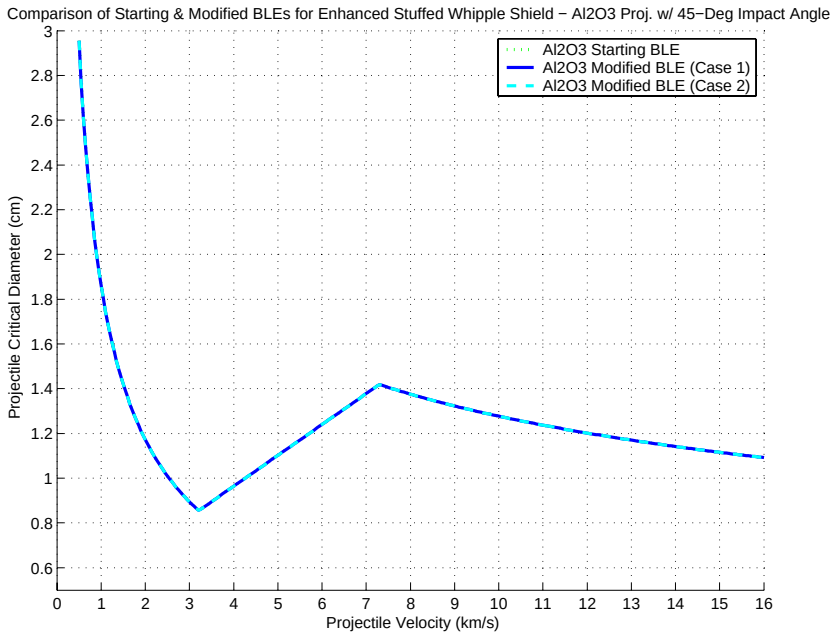

Figure I27. Starting vs. Improved Ballistic Limit Equation for Stuffed Whipple Shield with Aluminum Oxide Projectile at 45-degree Impact (Cases 1 & 2).

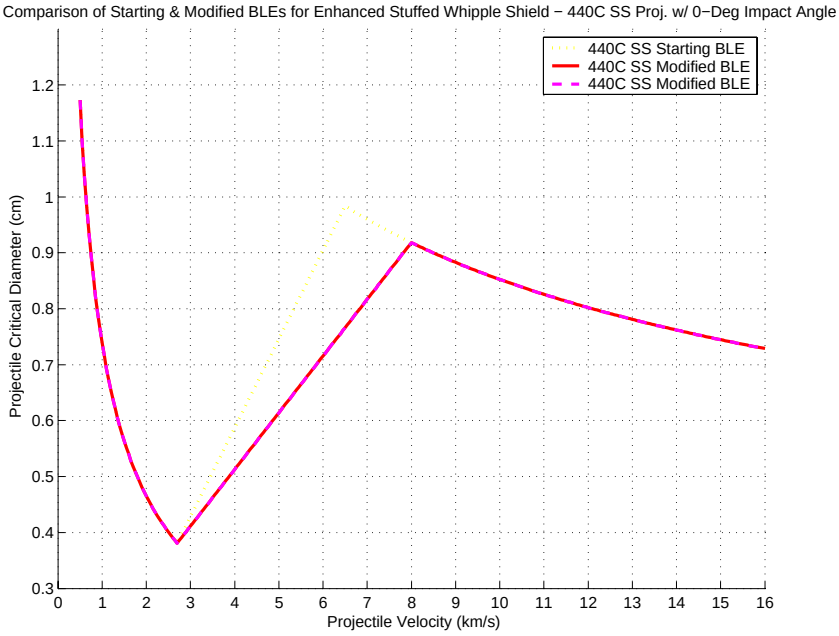

Figure I28. Starting vs. Improved Ballistic Limit Equation for Stuffed Whipple Shield with 440C Stainless Steel Projectile at 0-degree Impact (Cases 1 & 2).

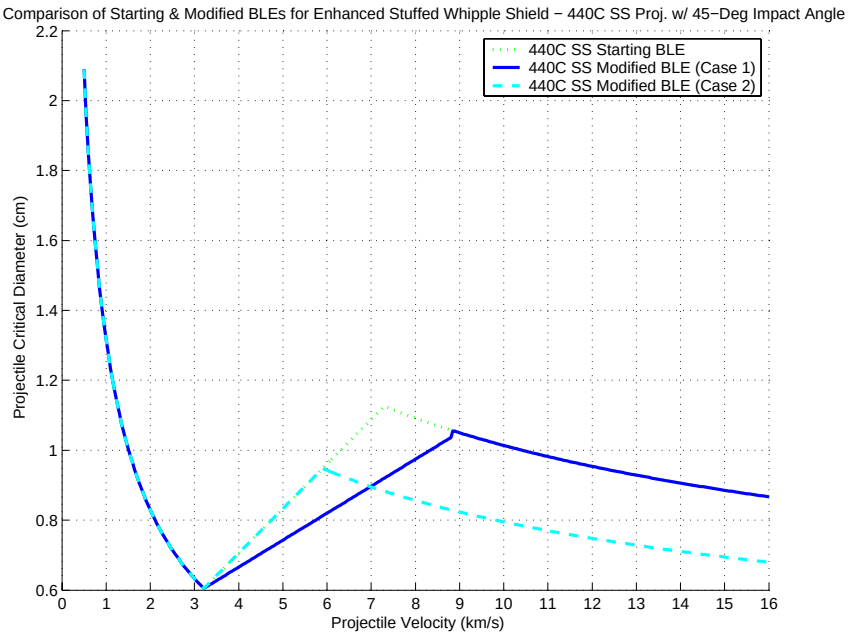

Figure I29. Starting vs. Improved Ballistic Limit Equation for Stuffed Whipple Shield with 440C Stainless Steel Projectile at 45-degree Impact (Cases 1 & 2).

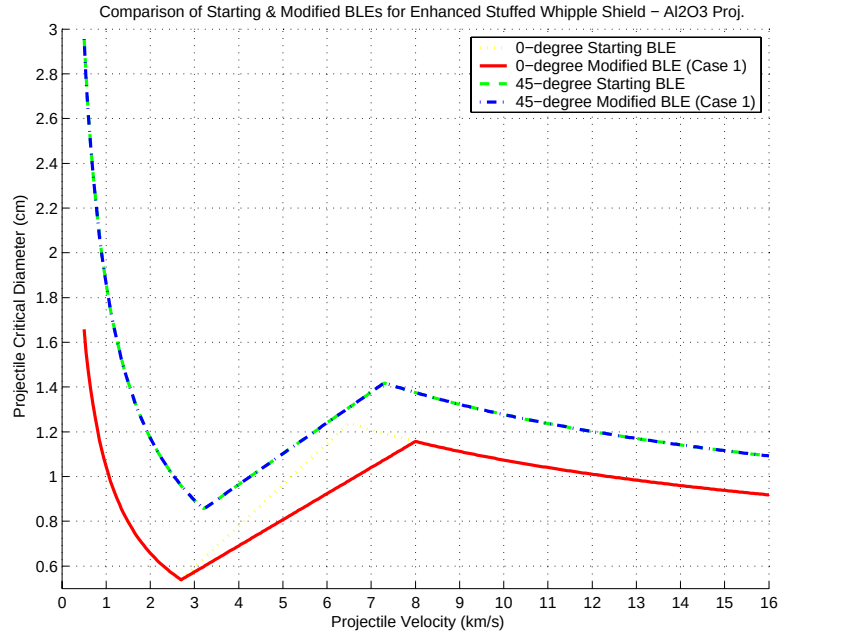

Figure I30. Combined Starting vs. Improved Ballistic Limit Equation for Stuffed Whipple Shield with Aluminum Oxide Projectile at 45-degree Impact (Case 1).

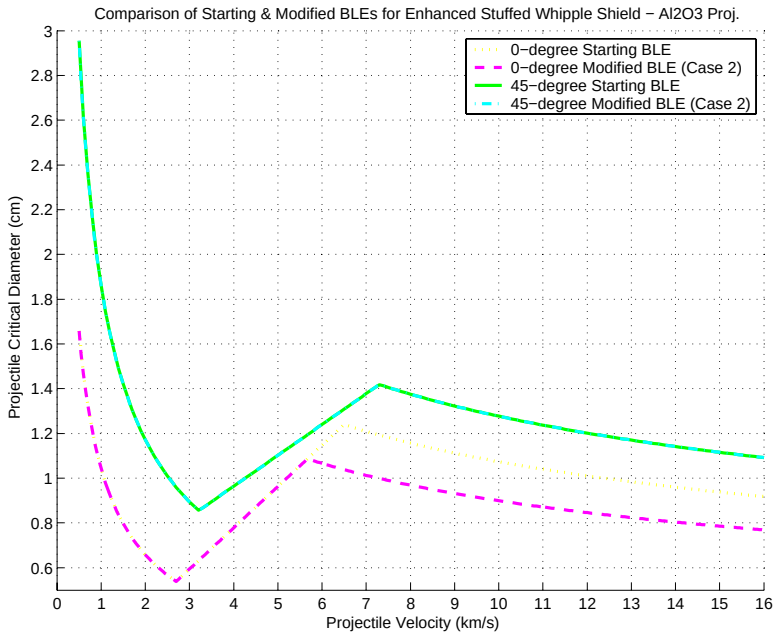

Figure I31. Combined Starting vs. Improved Ballistic Limit Equation for Stuffed Whipple Shield with Aluminum Oxide Projectile at 45-degree Impact (Case 2).

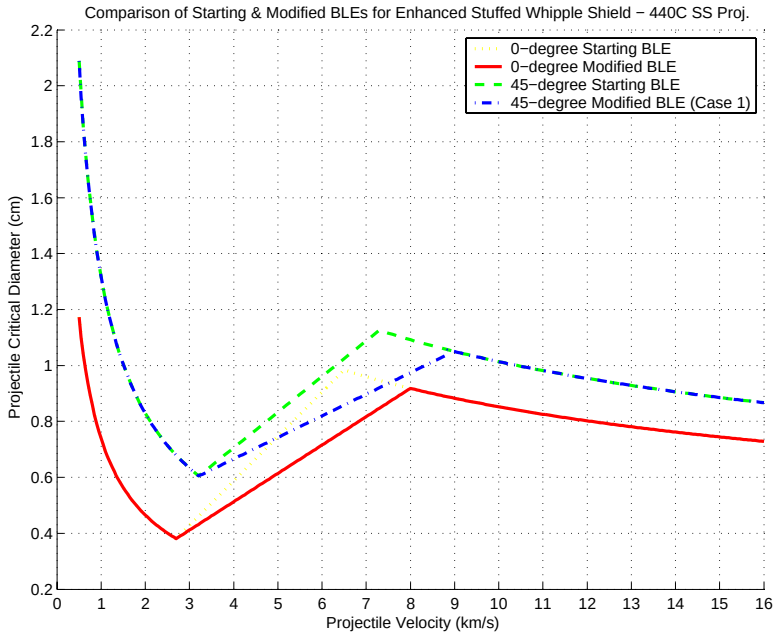

Figure I32. Combined Starting vs. Improved Ballistic Limit Equation for Stuffed Whipple Shield with 440C Stainless Steel Projectile (Case 1).

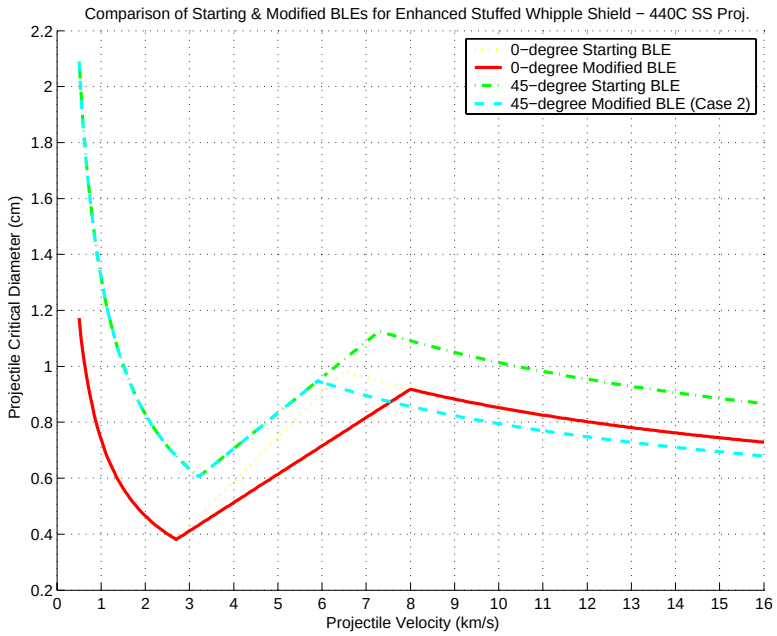

Figure I33. Combined Starting vs. Improved Ballistic Limit Equation for Stuffed Whipple Shield with 440C Stainless Steel Projectile (Case 2).

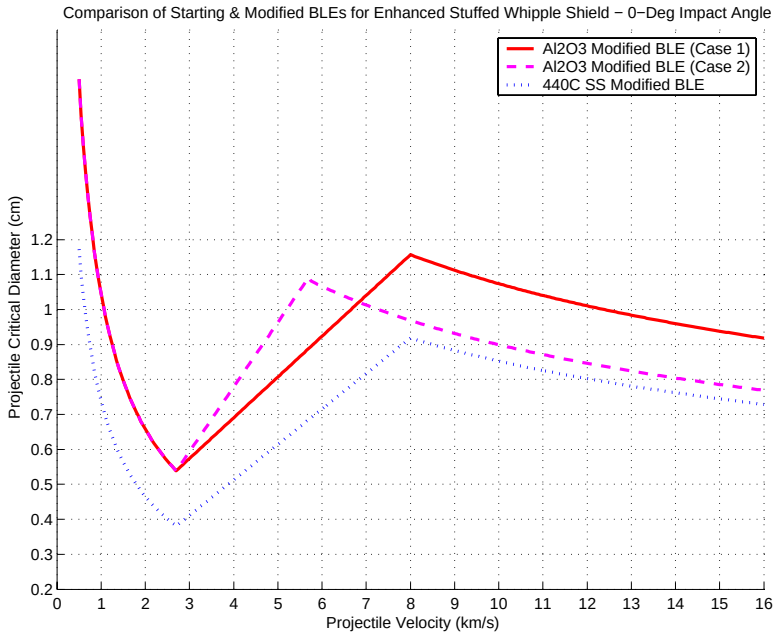

Figure I34. Combined Starting vs. Improved Ballistic Limit Equation for Stuffed Whipple Shield with 0-degree Impact (All Cases).

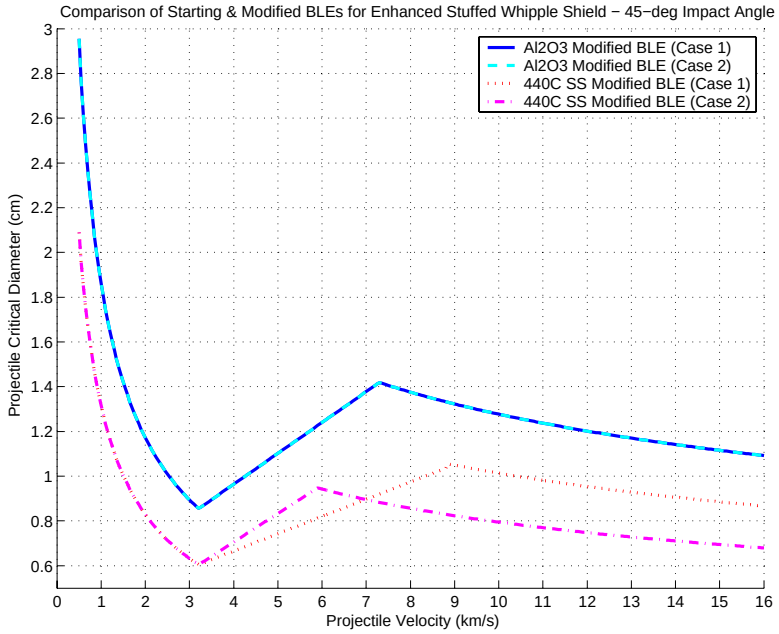

Figure I35. Combined Starting vs. Improved Ballistic Limit Equation for Stuffed Whipple Shield with 45-degree Impact (All Cases).

APPENDIX J - MATLAB CODE FOR REVISED BALLISTIC LIMIT EQUATIONS, RAW DATA, AND GRAPHICAL OVERLAYS

The complete MATLAB codes used to create all plots of the improved ballistic limit equations is quite lengthy and merely recreates the data contained in the MSEXCEL spreadsheets and graphs, representing the original analytical code. These original MSEXCEL spreadsheets have been passed to JSC HITF. The MATLAB codes are available from the author of this report upon request. Requests for electronic copies of the MATLAB m-files should be made to:

LT Michael E. Kalinski, USN

558 Manhattan Place

San Jose, CA 95136

THIS PAGE INTENTIONALLY LEFT BLANK

APPENDIX K - SHIELD MATERIAL CHARACTERISTICS TABLES

Candidate Aluminum Alloy Materials		
Bumper Material	**Density (g/cm^3)**	**Yield Strength (ksi)**
Al 2024 T3	2.768	50
Al 2024 T351	2.770	47
Al 2024 T361	2.768	57
Al 2024 T81	2.768	65.3
Al 2024 T86	2.768	63.8
Al 2124 T351	2.768	47.1
Al 6061 T6	**2.713**	**40**
Al 6061 T91	2.699	57.3
Al 6061 T913	2.699	66
Al 6066 T6	2.721	52
Al 6070 T6	2.710	51
Al 6262 T9	2.721	55

Table K1. Candidate Bumper Materials to Replace Current Rear Wall Aluminum 6061 T6 for U.S. Laboratory Module Whipple and Enhanced Stuffed Whipple Shields.

Candidate Aluminum Alloy Materials		
Rear Wall Material	**Density (g/cm^3)**	**Yield Strength (ksi)**
Al 2024 T86	2.768	63.8
Al 2090 T84	2.591	68.2
Al 2124 T81	2.768	65.3
Al 2124 T851	2.768	64
Al 2219 T87	**2.851**	**58**
Al 5056 H191	2.641	63.1
Al 6061 T913	2.699	66
Al 7001 T75	2.851	71.8
Al 7050 T7451	2.823	68
Al 7075 T6	2.823	73
Al 7175 T6	2.823	78
Al 7175 T66	2.796	75.4
Al 7178 T6	2.823	78

Table K2. Candidate Rear Wall Materials to Replace Current Rear Wall Aluminum 2219 T87 for U.S. Laboratory Module Whipple and Enhanced Stuffed Whipple Shields.

THIS PAGE INTENTIONALLY LEFT BLANK

APPENDIX L - BALLISTIC LIMIT CURVES FOR ALTERNATE SHIELD MATERIALS AND CONFIGURATIONS WITH OVERLAY OF REVISED BALLISTIC LIMIT CURVES

1. ALTERNATE STANDOFF DISTANCE TRIALS

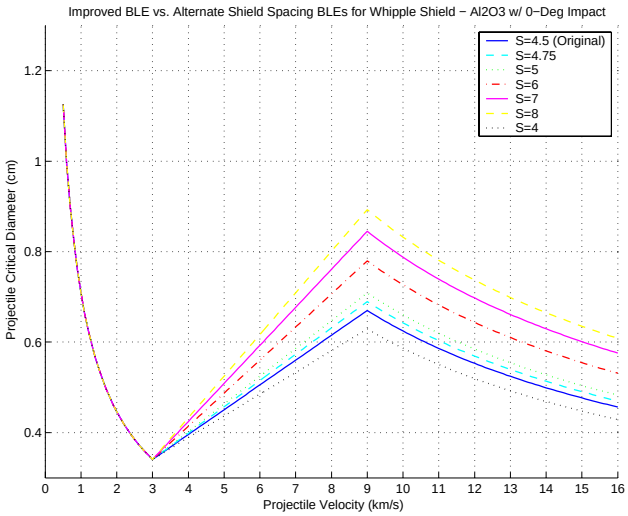

Figure L1. Plot of Improved Whipple BLE vs. Alternate Shield Spacing Trials for Aluminum Oxide Projectiles at 0-degree Impact Angles.

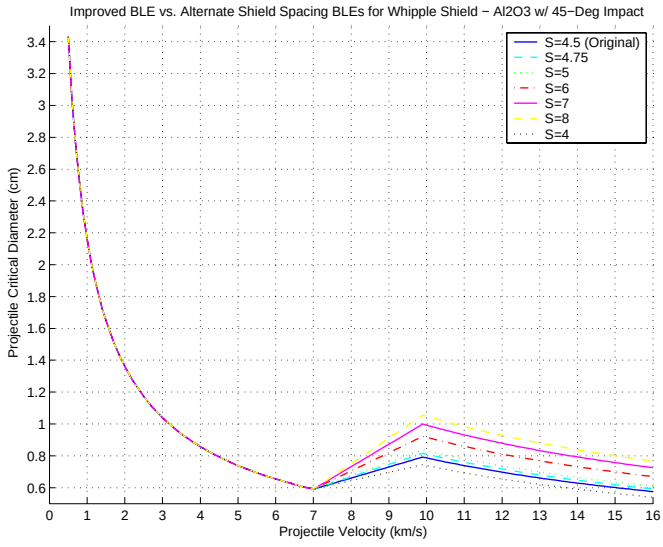

Figure L2. Plot of Improved Whipple BLE vs. Alternate Shield Spacing Trials for Aluminum Oxide Projectiles at 45-degree Impact Angles.

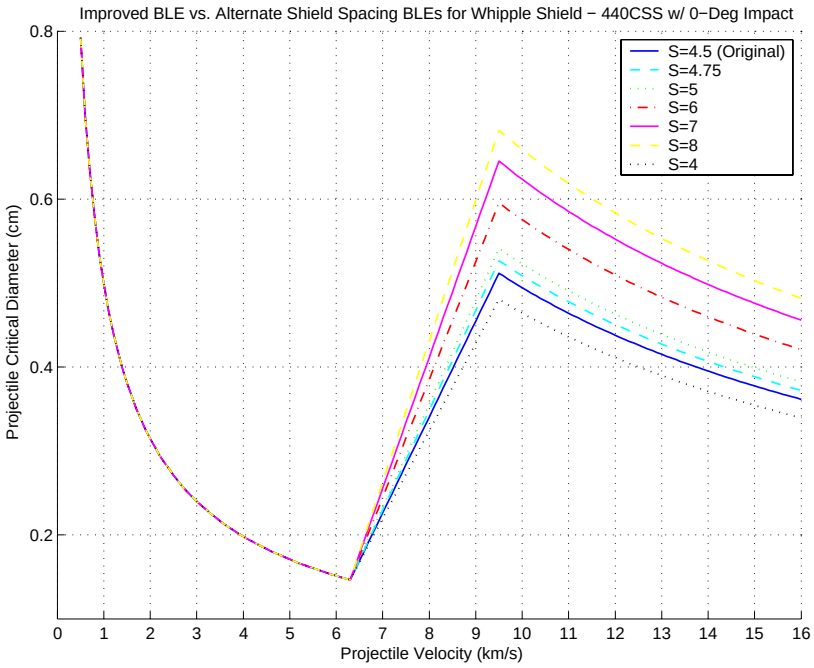

Figure L3. Plot of Improved Whipple BLE vs. Alternate Shield Spacing Trials for 440C Stainless Steel Projectiles at 0-degree Impact Angles.

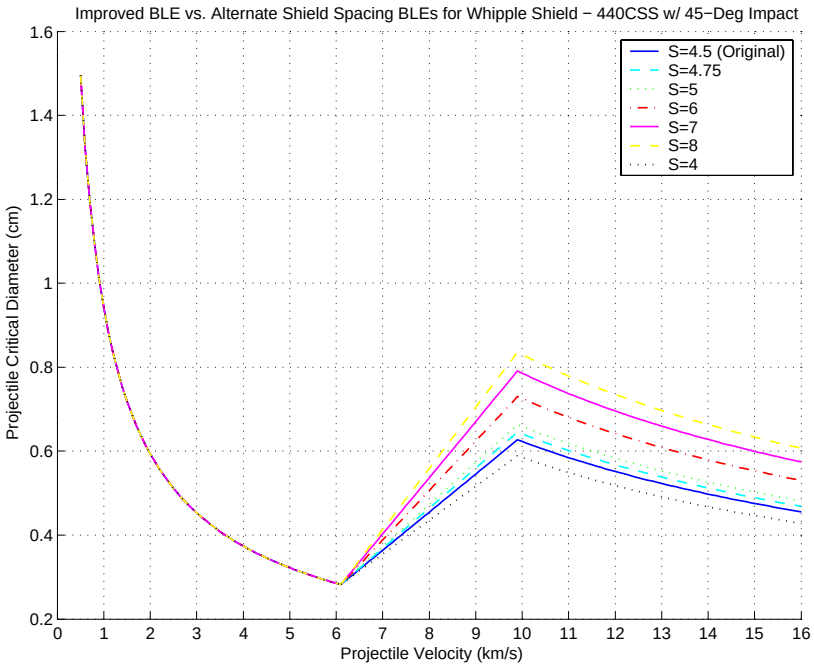

Figure L4. Plot of Improved Whipple BLE vs. Alternate Shield Spacing Trials for 440C Stainless Steel Projectiles at 45-degree Impact Angles.

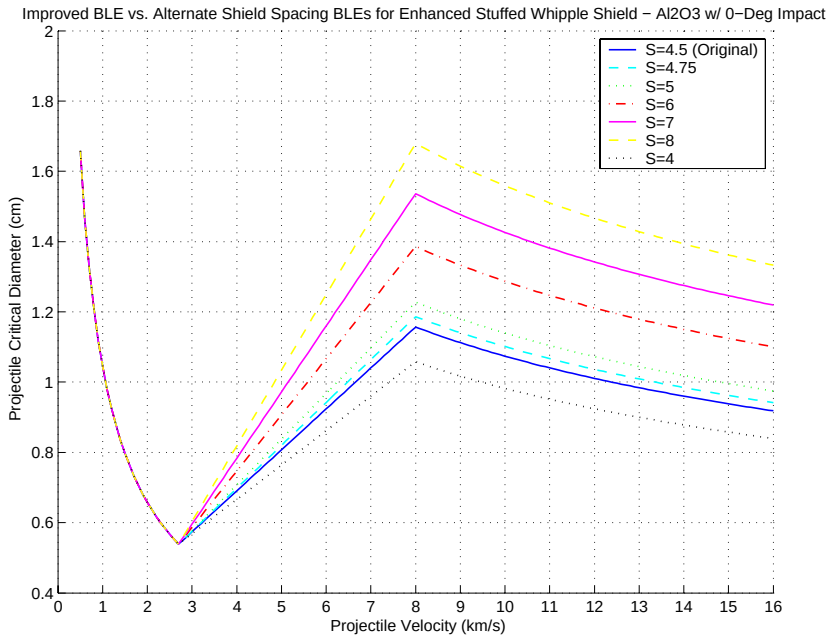

Figure L5. Plot of Improved Enhanced Stuffed Whipple BLE vs. Alternate Shield Spacing Trials for Aluminum Oxide Projectiles at 0-degree Impact Angles.

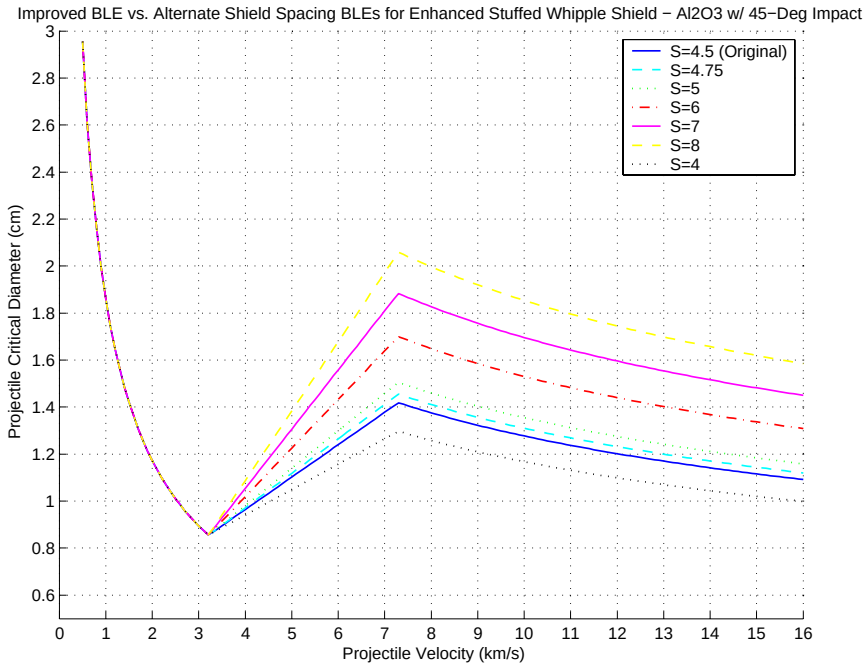

Figure L6. Plot of Improved Enhanced Stuffed Whipple BLE vs. Alternate Shield Spacing Trials for Aluminum Oxide Projectiles at 0-degree Impact Angles.

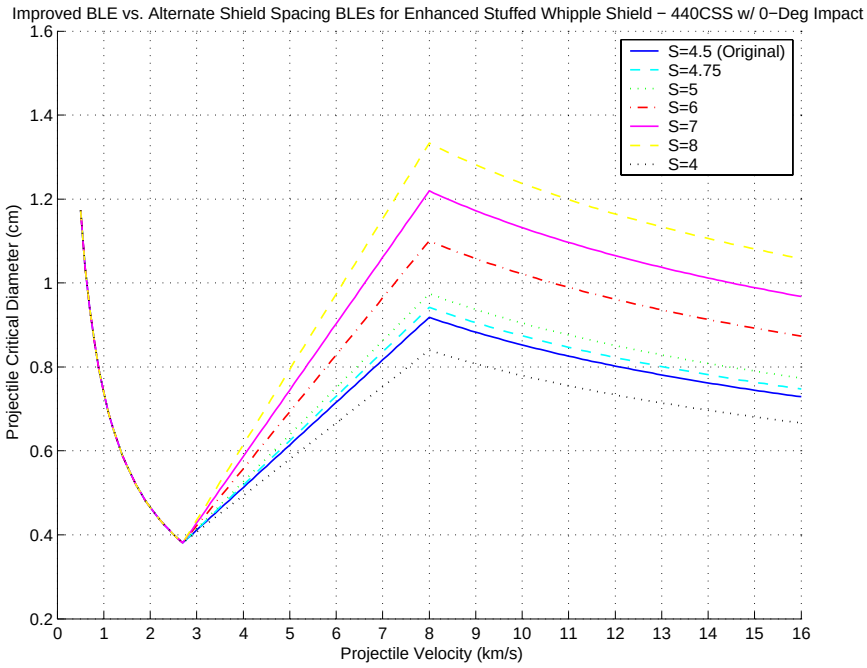

Figure L7. Plot of Improved Whipple BLE vs. Alternate Shield Spacing Trials for 440C Stainless Steel Projectiles at 0-degree Impact Angles.

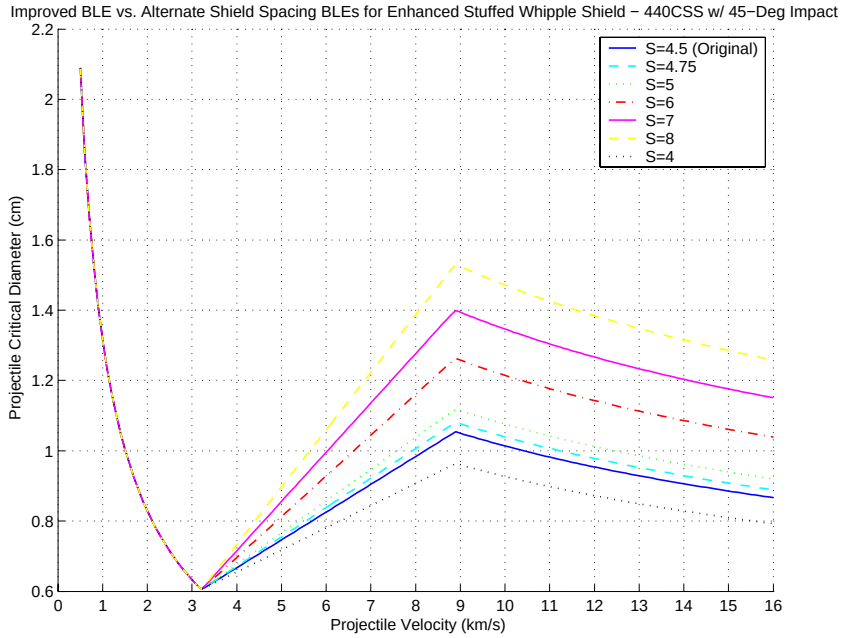

Figure L8. Plot of Improved Whipple BLE vs. Alternate Shield Spacing Trials for 440C Stainless Steel Projectiles at 0-degree Impact Angles

.

2. ALTERNATE BUMPER SHIELD THICKNESS TRIALS

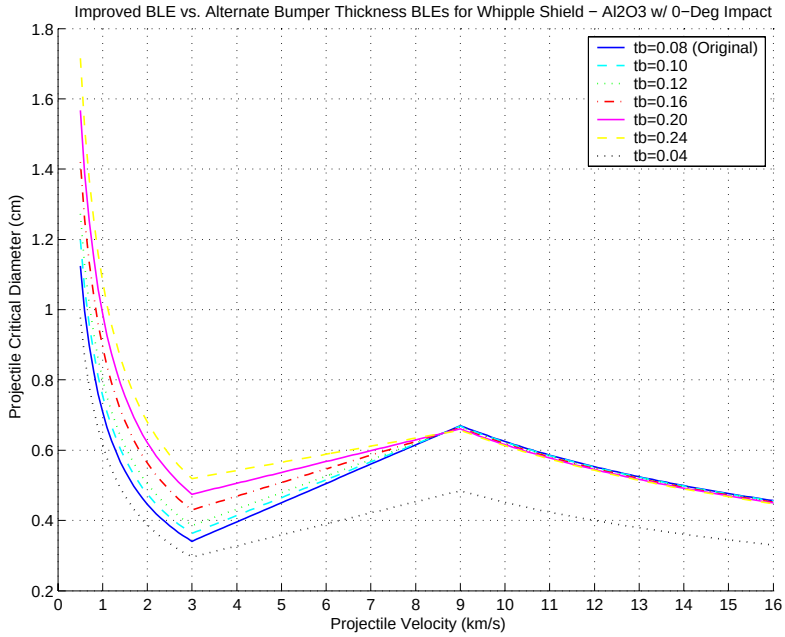

Figure L9. Plot of Improved Whipple BLE vs. Alternate Bumper Shield Thickness Trials for Aluminum Oxide Projectiles at 0-degree Impact Angles.

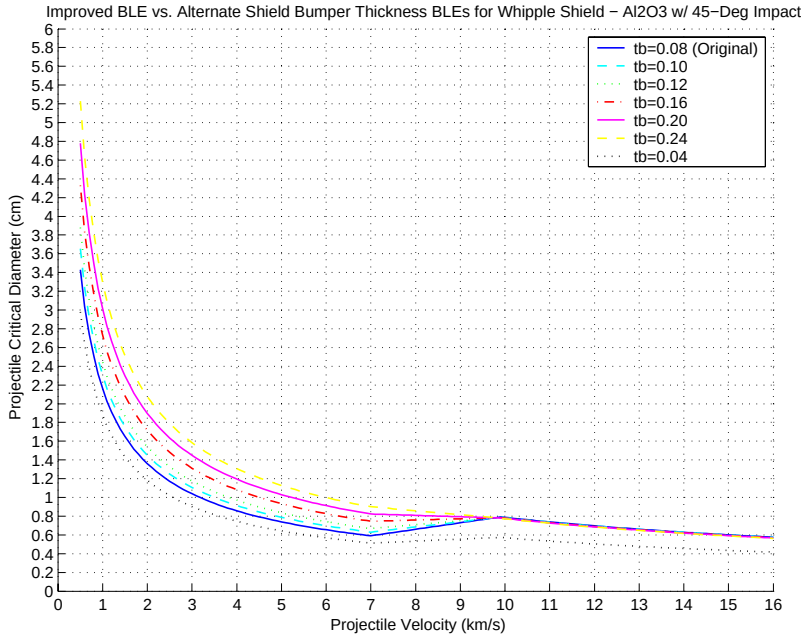

Figure L10. Plot of Improved Whipple BLE vs. Alternate Bumper Shield Thickness Trials for Aluminum Oxide Projectiles at 45-degree Impact Angles

.

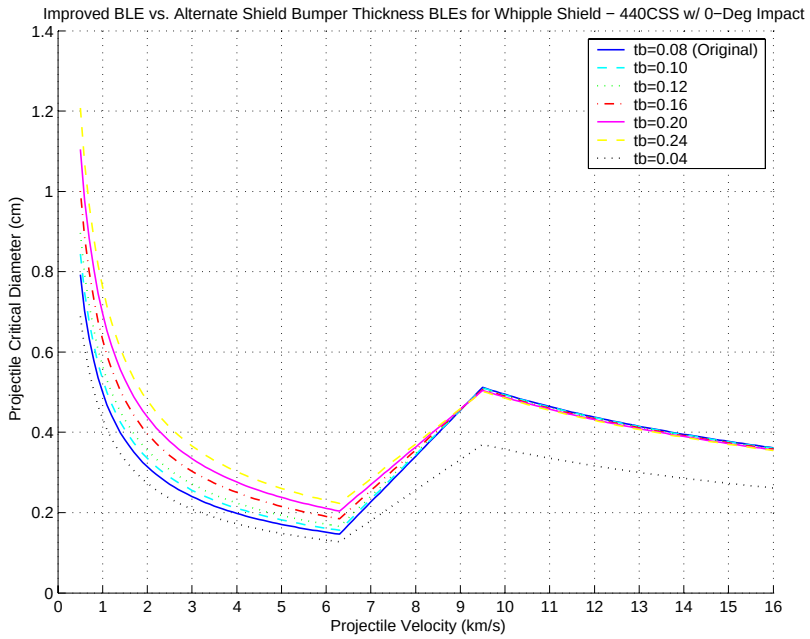

Figure L11. Plot of Improved Whipple BLE vs. Alternate Bumper Shield Thickness Trials for 440C Stainless Steel Projectiles at 0-degree Impact Angles.

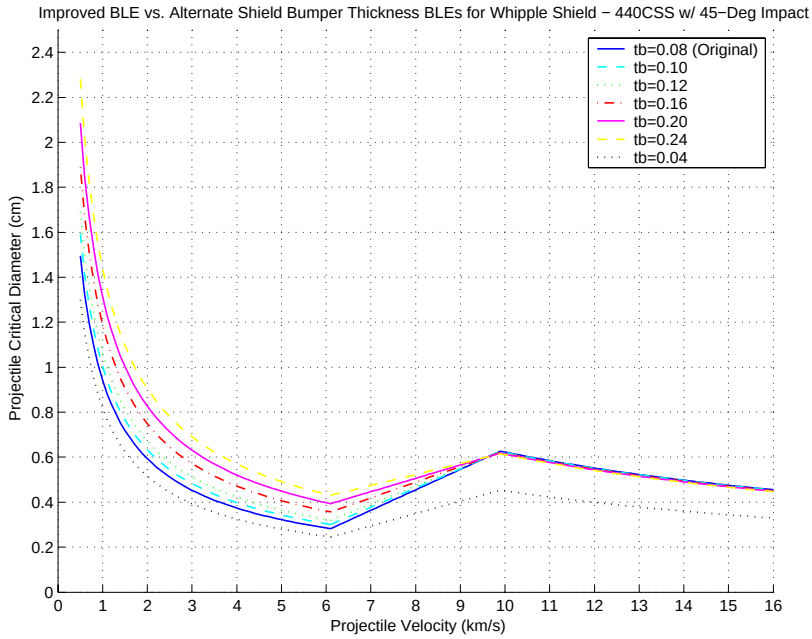

Figure L12. Plot of Improved Whipple BLE vs. Alternate Bumper Shield Thickness Trials for 440C Stainless Steel Projectiles at 45-degree Impact Angles.

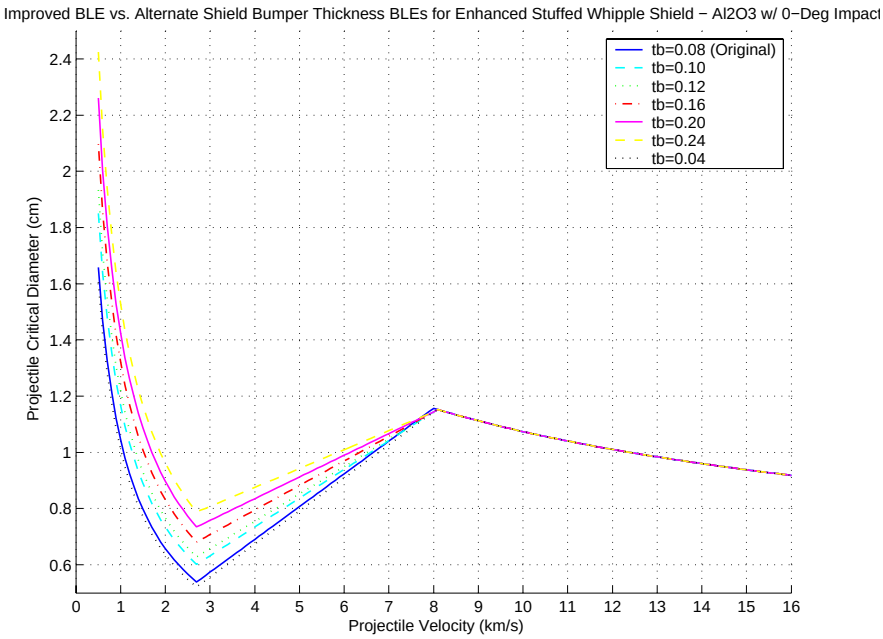

Figure L13. Plot of Improved Enhanced Stuffed Whipple BLE vs. Alternate Bumper Shield Thickness Trials for Aluminum Oxide Projectiles at 0-degree Impact Angles.

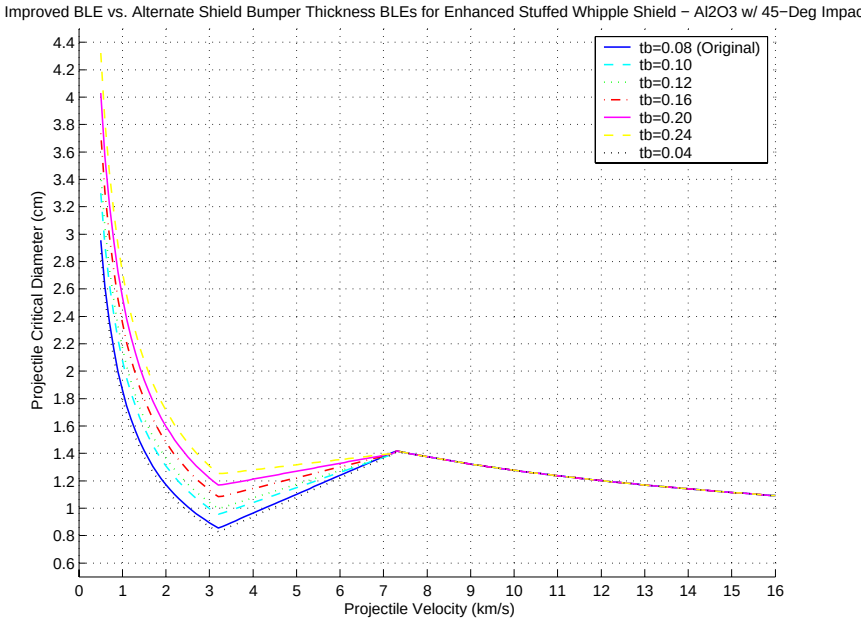

Figure L14. Plot of Improved Enhanced Stuffed Whipple BLE vs. Alternate Bumper Shield Thickness Trials for Aluminum Oxide Projectiles at 45-degree Impact Angles.

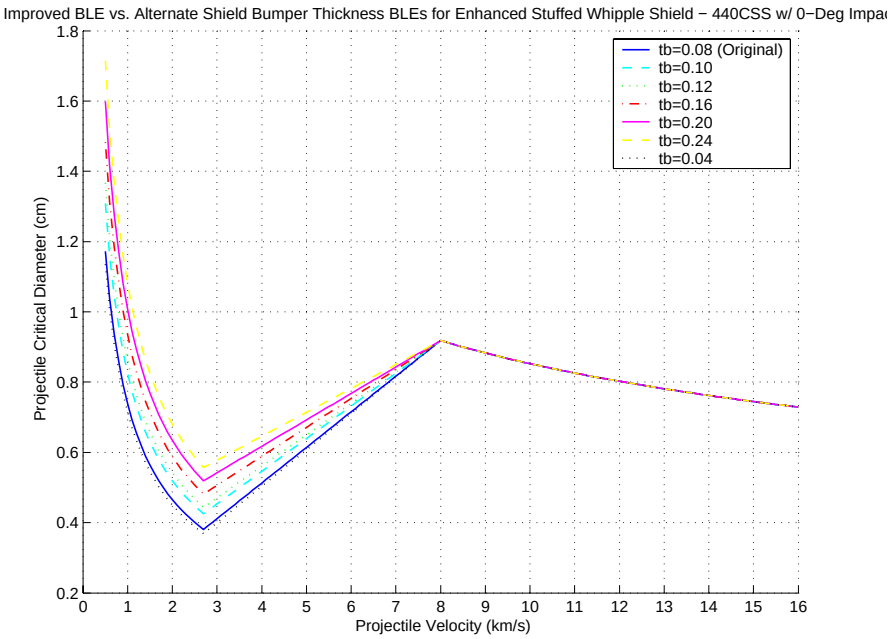

Figure L15. Plot of Improved Enhanced Stuffed Whipple BLE vs. Alternate Bumper Shield Thickness Trials for 440C Stainless Steel Projectiles at 0-degree Impact Angles.

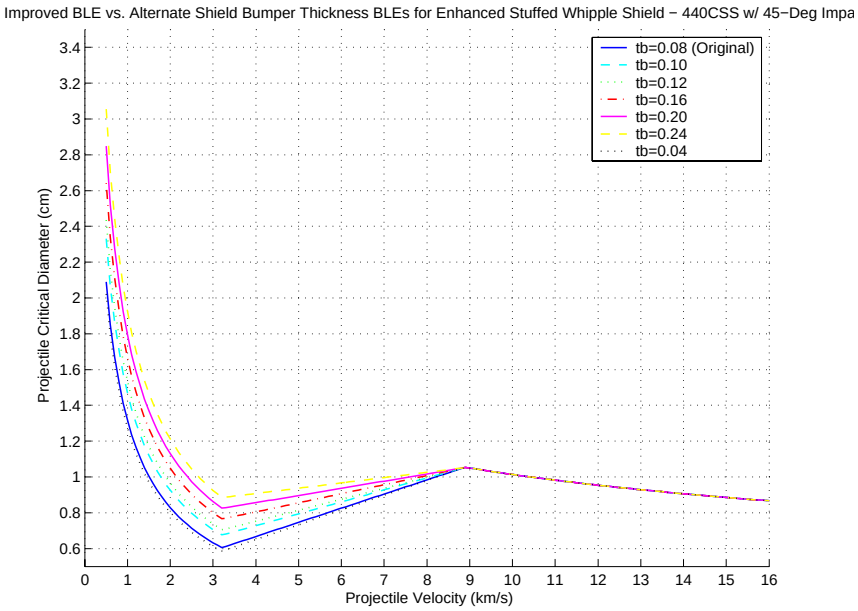

Figure L16. Plot of Improved Enhanced Stuffed Whipple BLE vs. Alternate Bumper Shield Thickness Trials for 440C Stainless Steel Projectiles at 45-degree Impact Angles

.

3. ALTERNATE REAR WALL THICKNESS TRIALS

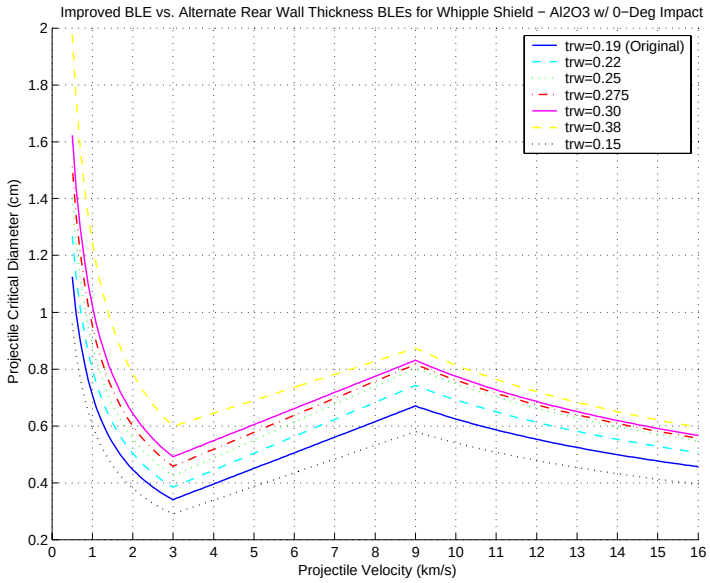

Figure L17. Plot of Improved Whipple BLE vs. Alternate Rear Wall Thickness Trials for Aluminum Oxide Projectiles at 0-degree Impact Angles.

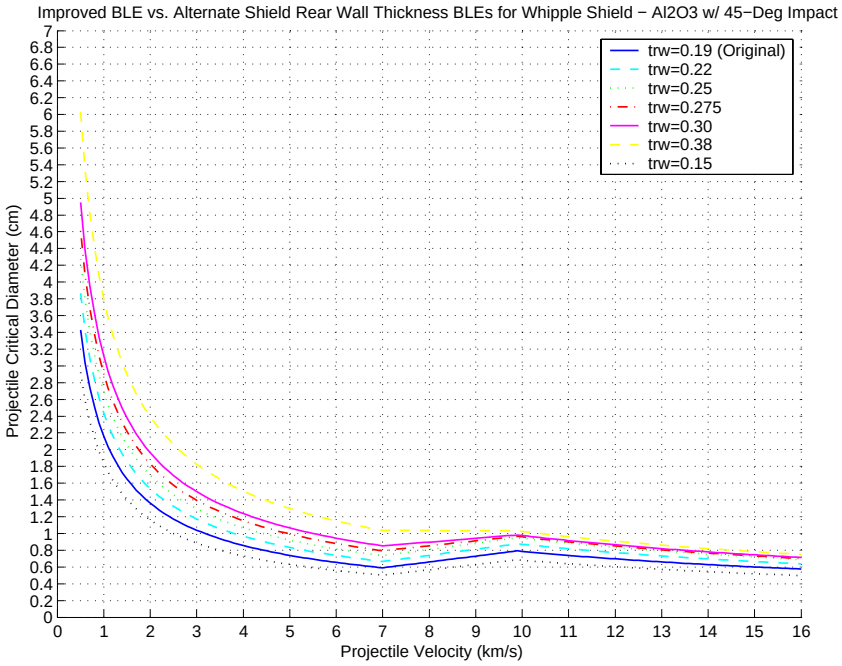

Figure L18. Plot of Improved Whipple BLE vs. Alternate Rear Wall Thickness Trials for Aluminum Oxide Projectiles at 45-degree Impact Angles.

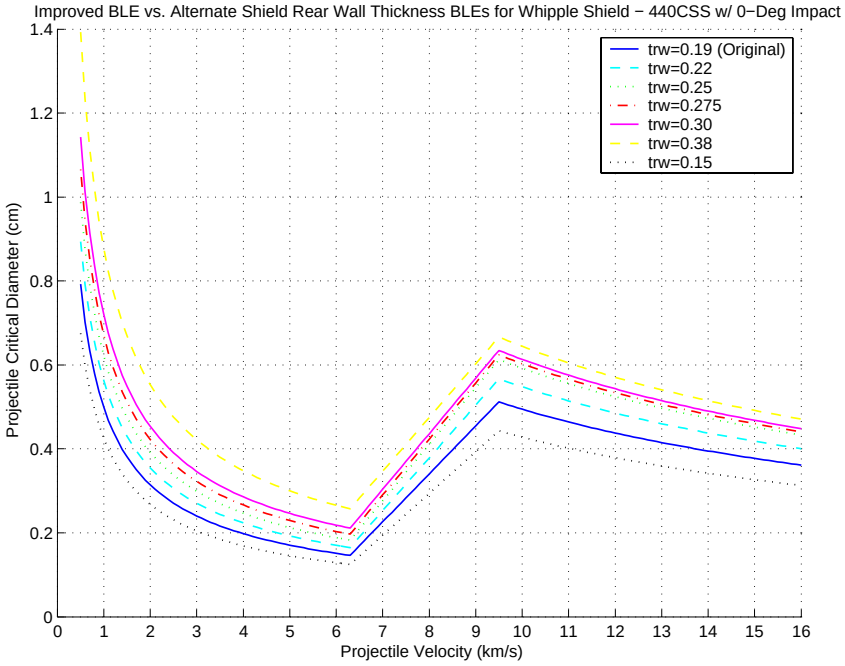

Figure L19. Plot of Improved Whipple BLE vs. Alternate Rear Wall Thickness Trials for 440C Stainless Steel Projectiles at 0-degree Impact Angles.

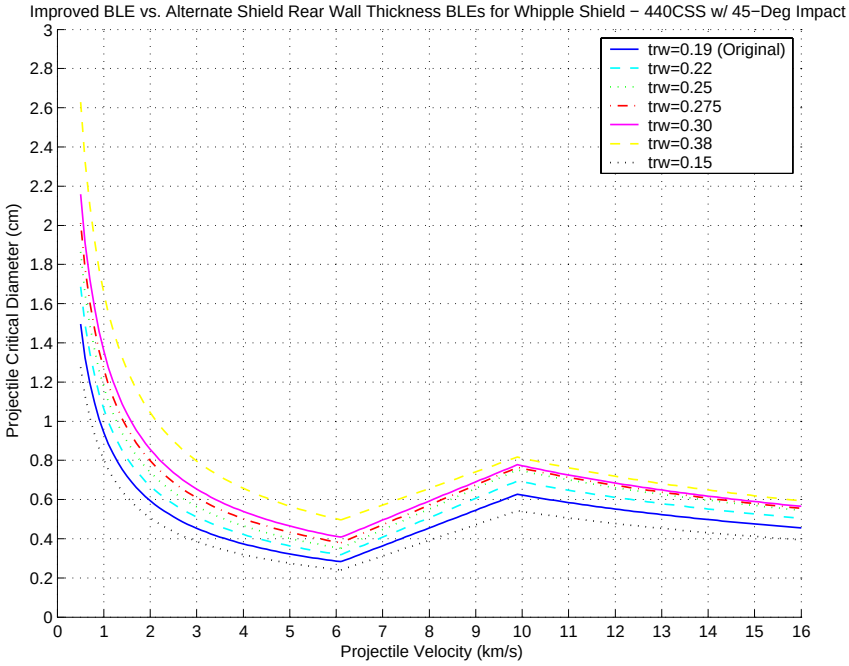

Figure L20. Plot of Improved Whipple BLE vs. Alternate Rear Wall Thickness Trials for 440C Stainless Steel Projectiles at 45-degree Impact Angles.

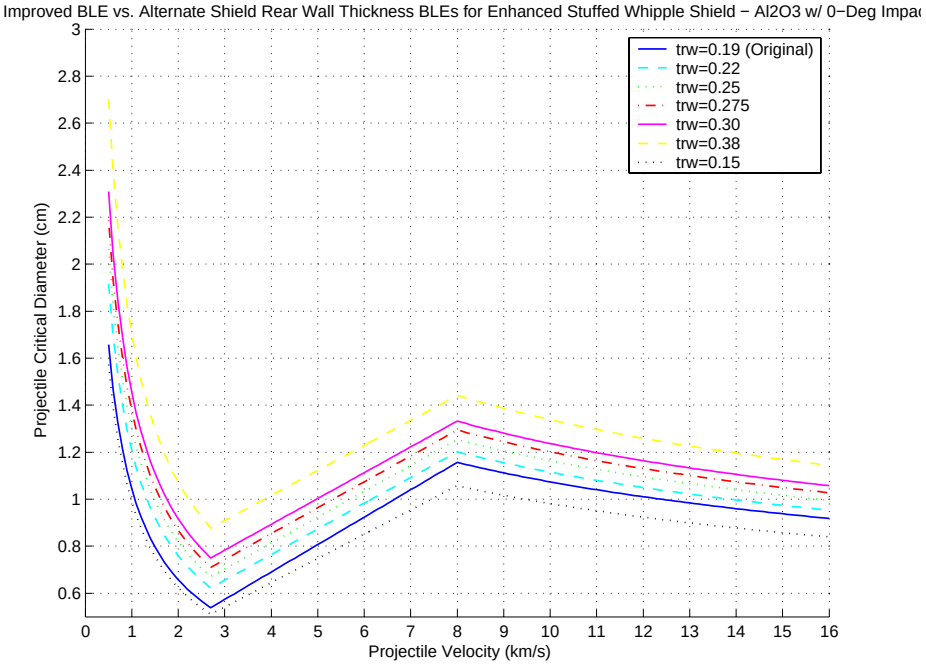

Figure L21. Plot of Improved Enhanced Stuffed Whipple BLE vs. Alternate Rear Wall Thickness Trials for Aluminum Oxide Projectiles at 0-degree Impact Angles

.

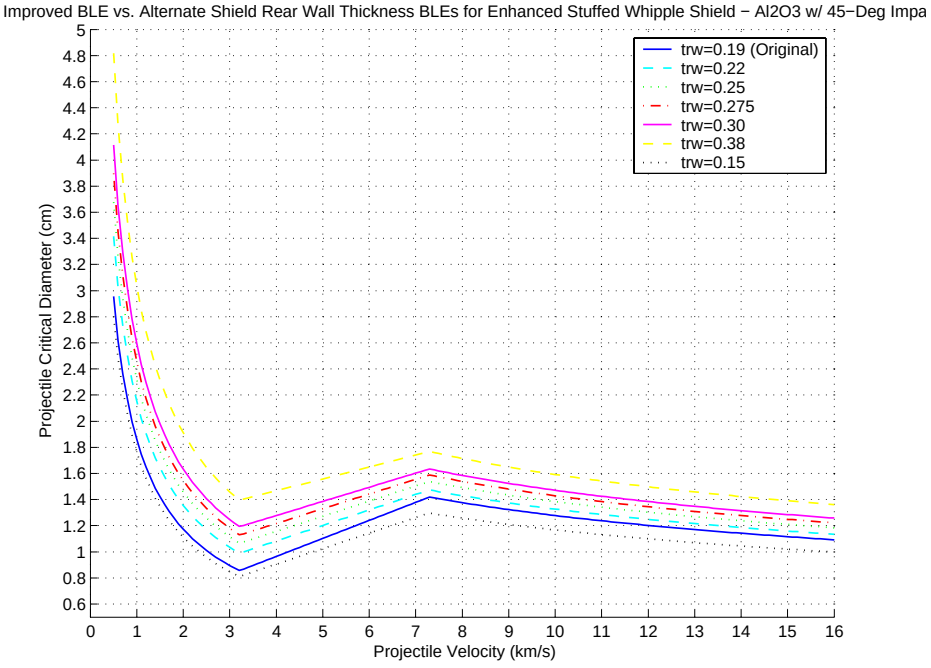

Figure L22. Plot of Improved Enhanced Stuffed Whipple BLE vs. Alternate Rear Wall Thickness Trials for Aluminum Oxide Projectiles at 45-degree Impact Angles.

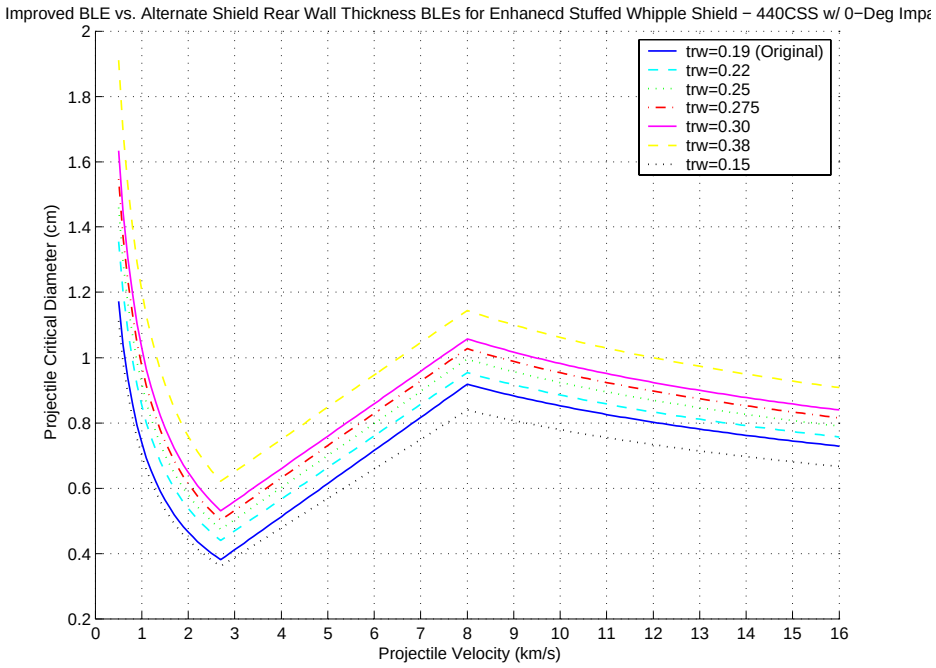

Figure L23. Plot of Improved Enhanced Stuffed Whipple BLE vs. Alternate Rear Wall Thickness Trials for 440C Stainless Steel Projectiles at 0-degree Impact Angles.

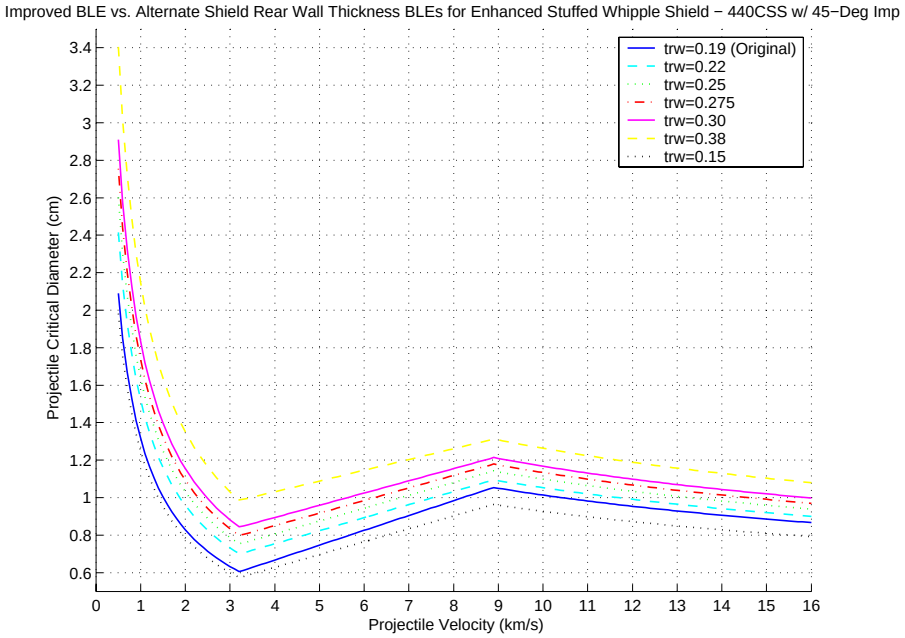

Figure L24. Plot of Improved Enhanced Stuffed Whipple BLE vs. Alternate Rear Wall Thickness Trials for 440C Stainless Steel Projectiles at 45-degree Impact Angles.

4. ALTERNATE BUMPER MATERIALS TRIALS

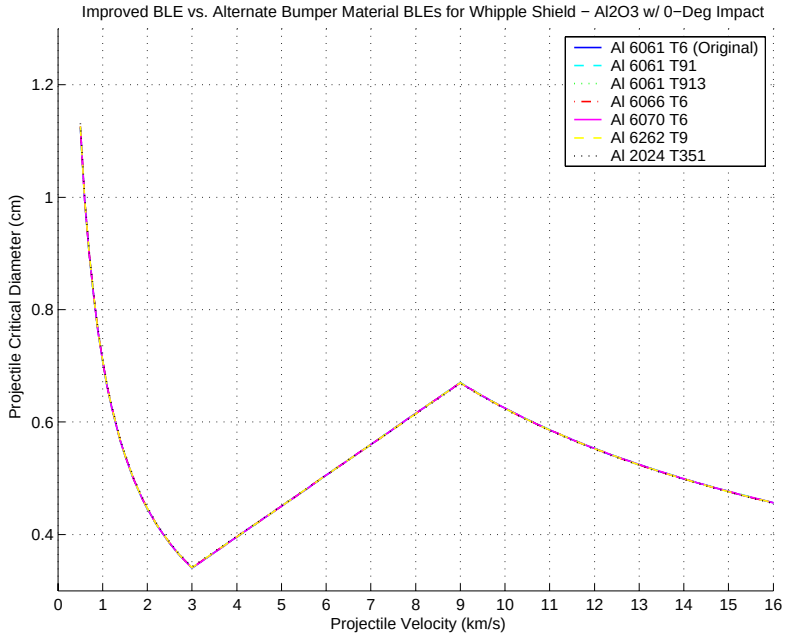

Figure L25. Plot of Improved Whipple BLE vs. Alternate Bumper Material Trials for Aluminum Oxide Projectiles at 0-degree Impact Angles.

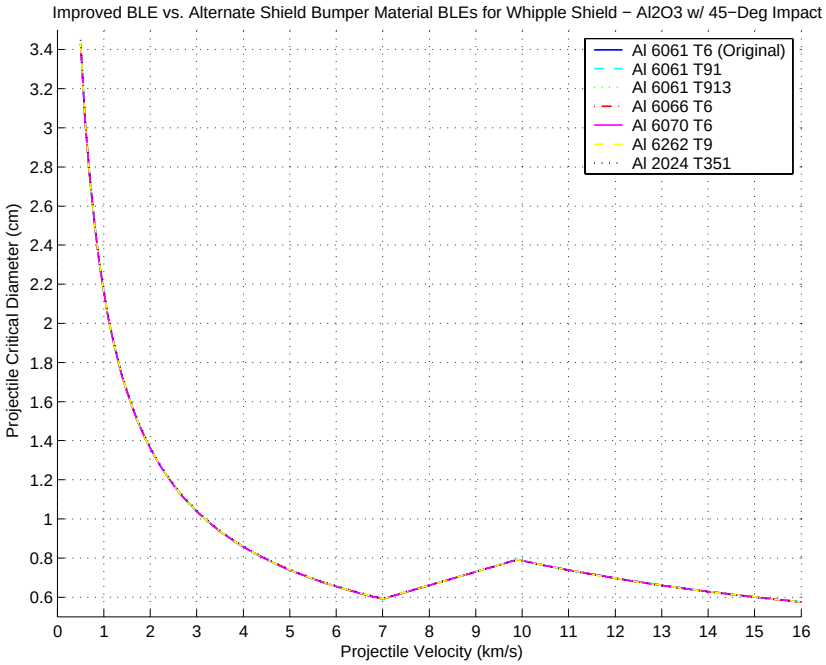

Figure L26. Plot of Improved Whipple BLE vs. Alternate Bumper Material Trials for Aluminum Oxide Projectiles at 45-degree Impact Angles.

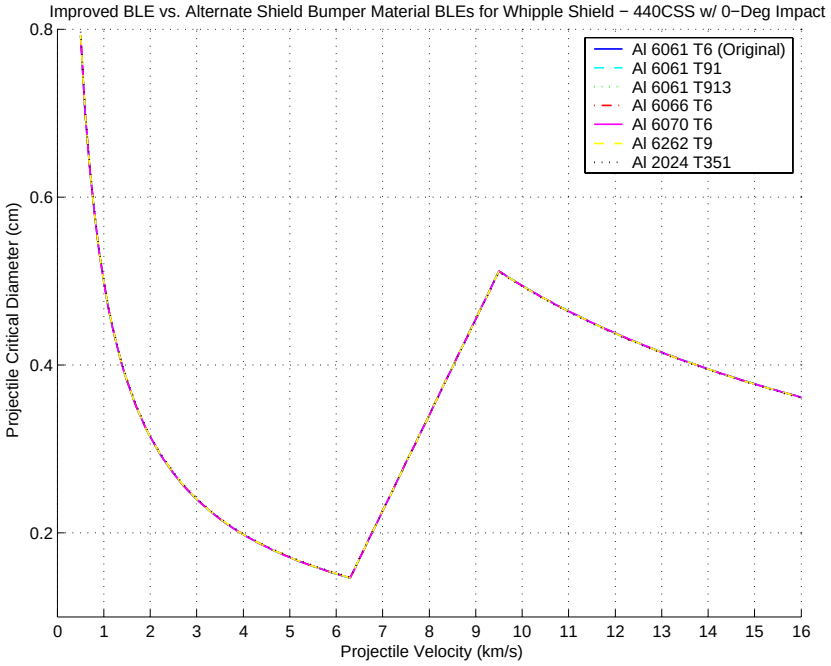

Figure L27. Plot of Improved Whipple BLE vs. Alternate Bumper Material Trials for 440C Stainless Steel Projectiles at 0-degree Impact Angles.

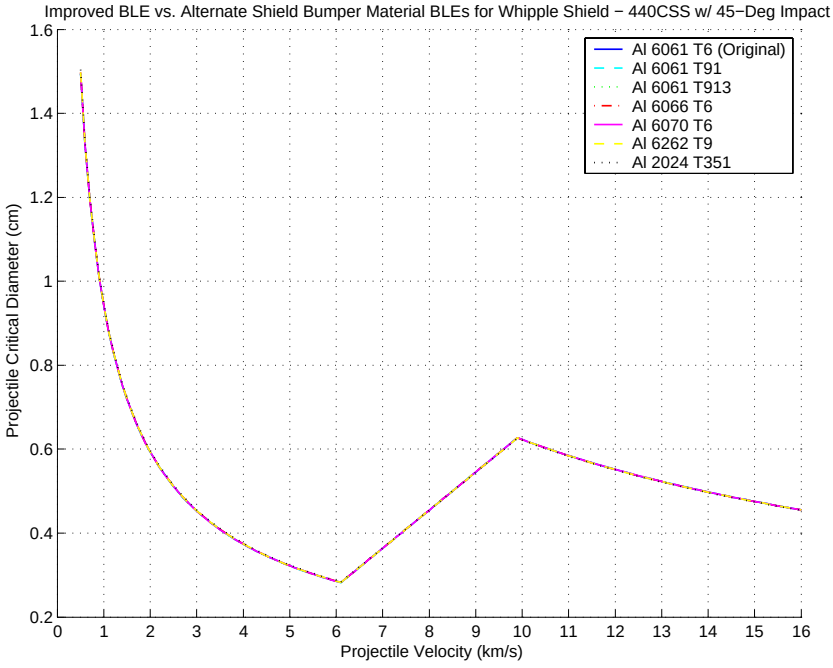

Figure L28. Plot of Improved Whipple BLE vs. Alternate Bumper Material Trials for 440C Stainless Steel Projectiles at 45-degree Impact Angles.

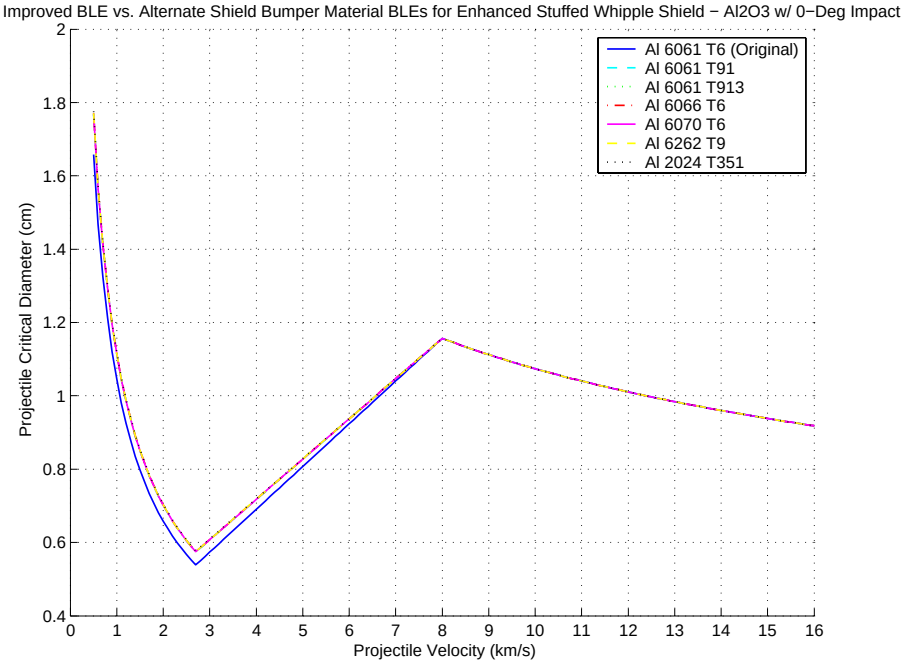

Figure L29. Plot of Improved Enhanced Stuffed Whipple BLE vs. Alternate Bumper Material Trials for Aluminum Oxide Projectiles at 0-degree Impact Angles.

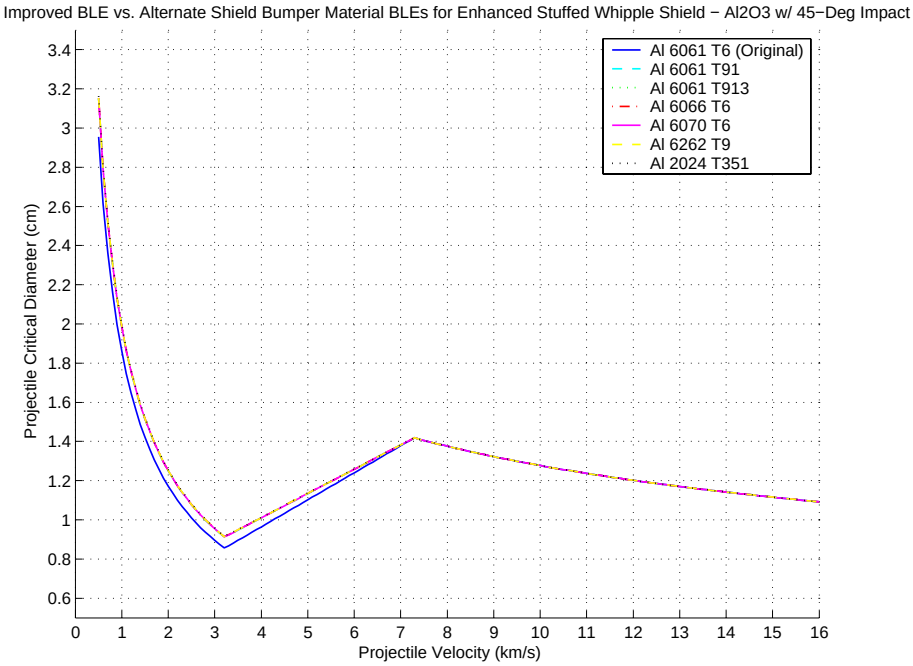

Figure L30. Plot of Improved Enhanced Stuffed Whipple BLE vs. Alternate Bumper Material Trials for Aluminum Oxide Projectiles at 45-degree Impact Angles.

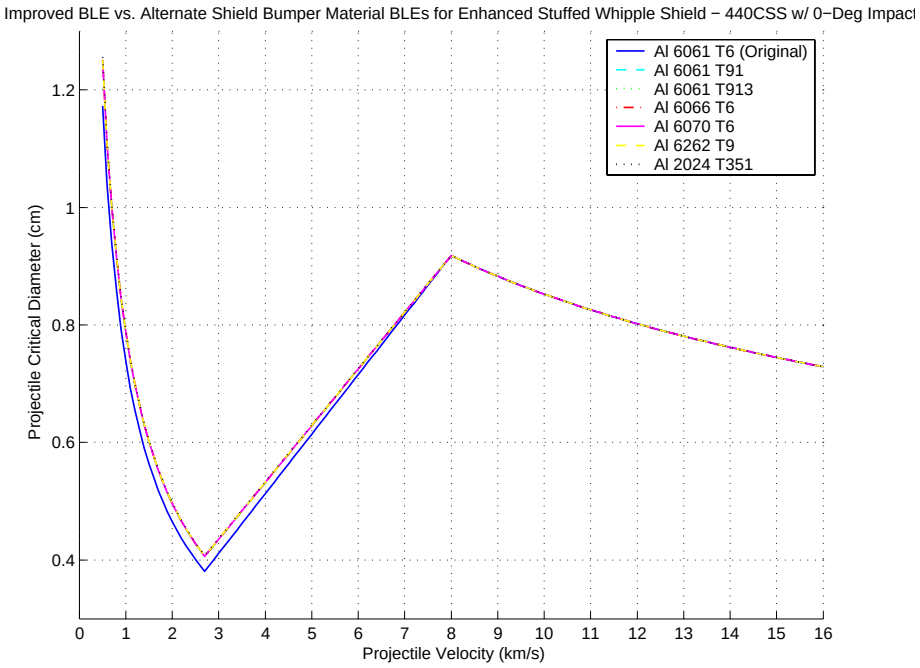

Figure L31. Plot of Improved Enhanced Stuffed Whipple BLE vs. Alternate Bumper Material Trials for 440C Stainless Steel Projectiles at 0-degree Impact Angles.

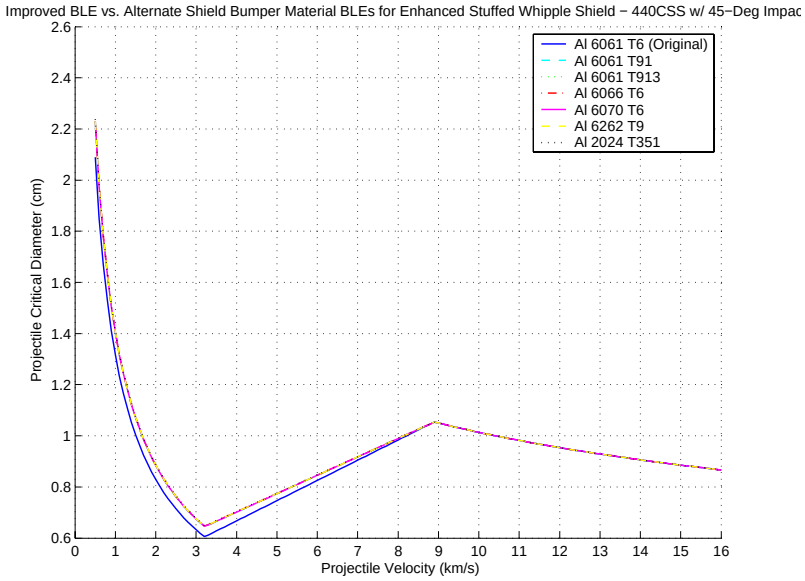

Figure L32. Plot of Improved Enhanced Stuffed Whipple BLE vs. Alternate Bumper Material Trials for 440C Stainless Steel Projectiles at 45-degree Impact Angles.

5. ALTERNATE REAR WALL MATERIALS TRIALS

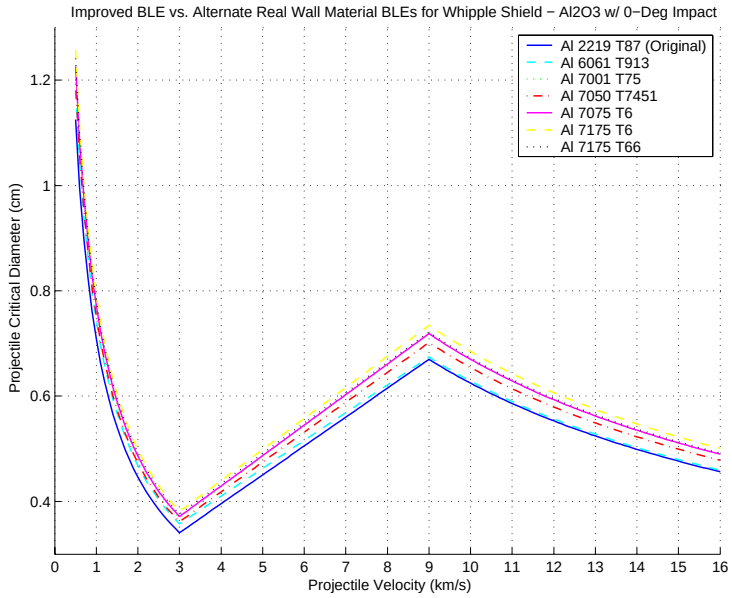

Figure L33. Plot of Improved Whipple BLE vs. Alternate Rear Wall Material Trials for Aluminum Oxide Projectiles at 0-degree Impact Angles.

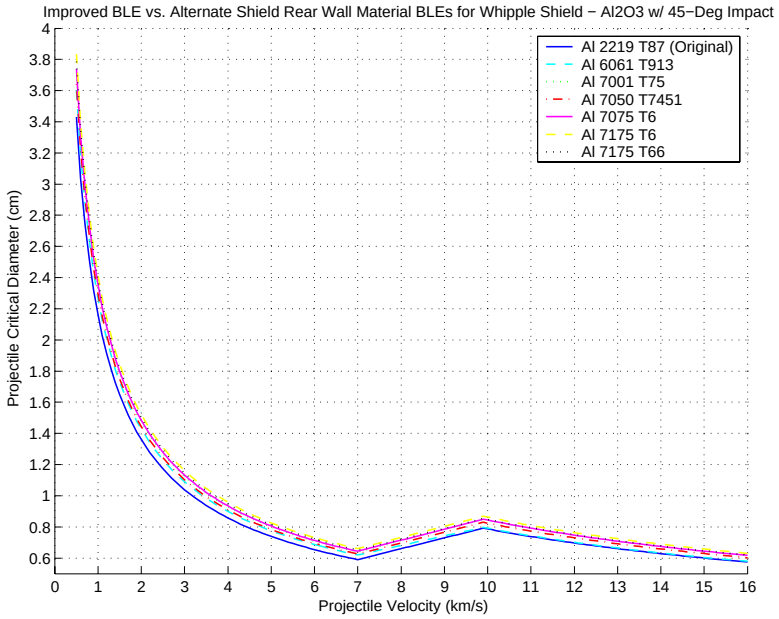

Figure L34. Plot of Improved Whipple BLE vs. Alternate Rear Wall Material Trials for Aluminum Oxide Projectiles at 45-degree Impact Angles.

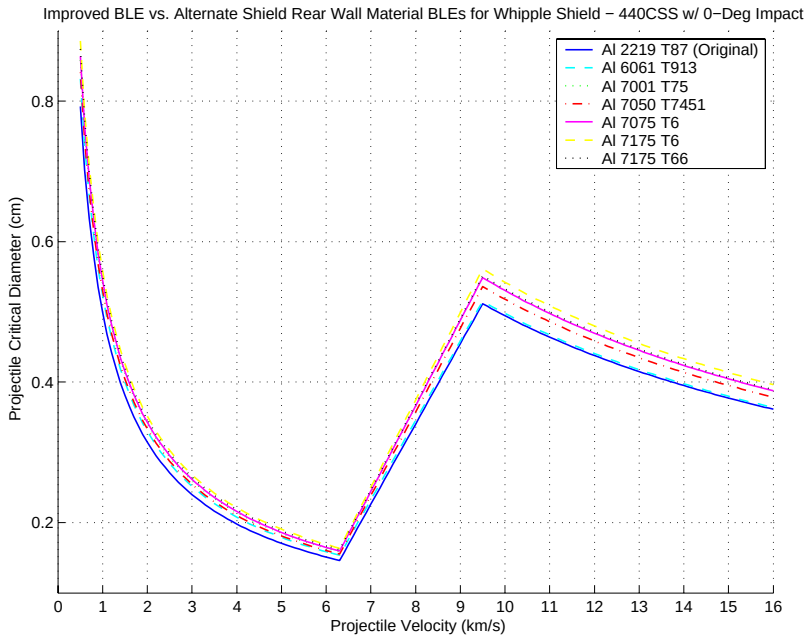

Figure L35. Plot of Improved Whipple BLE vs. Alternate Rear Wall Material Trials for 440C Stainless Steel Projectiles at 0-degree Impact Angles.

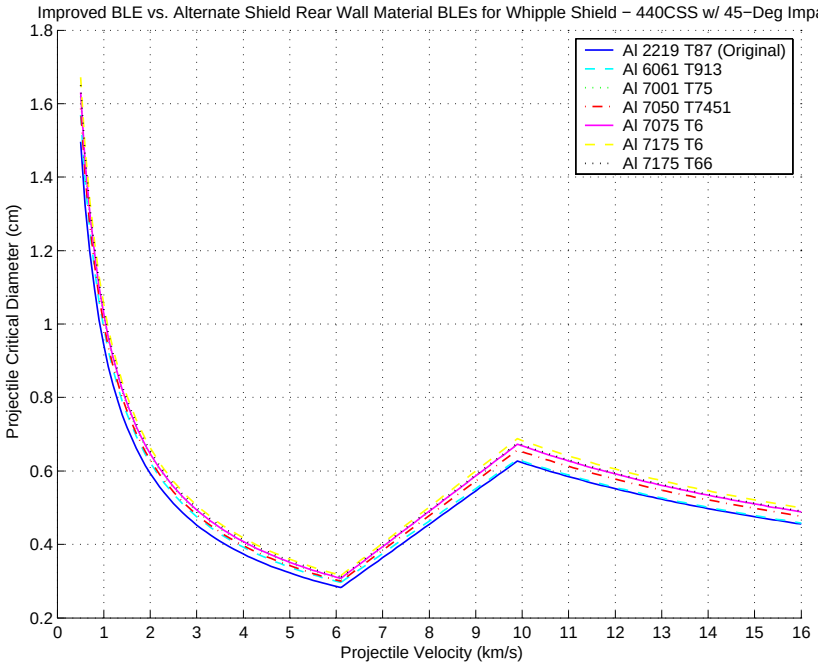

Figure L36. Plot of Improved Whipple BLE vs. Alternate Rear Wall Material Trials for 440C Stainless Steel Projectiles at 45-degree Impact Angles.

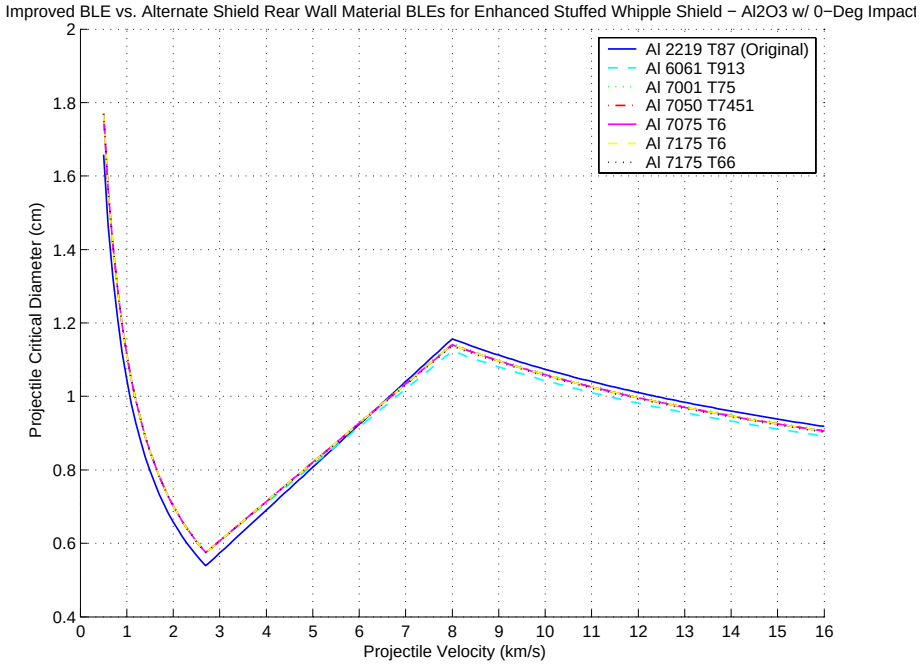

Figure L37. Plot of Improved Enhanced Stuffed Whipple BLE vs. Alternate Rear Wall Material Trials for Aluminum Oxide Projectiles at 0-degree Impact Angles.

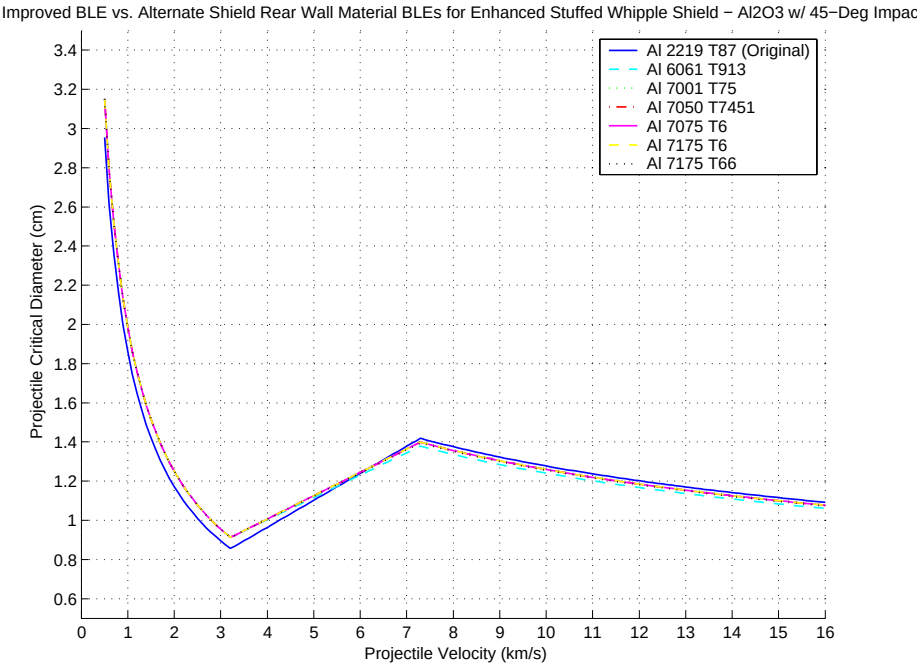

Figure L38. Plot of Improved Enhanced Stuffed Whipple BLE vs. Alternate Rear Wall Material Trials for Aluminum Oxide Projectiles at 45-degree Impact Angles.

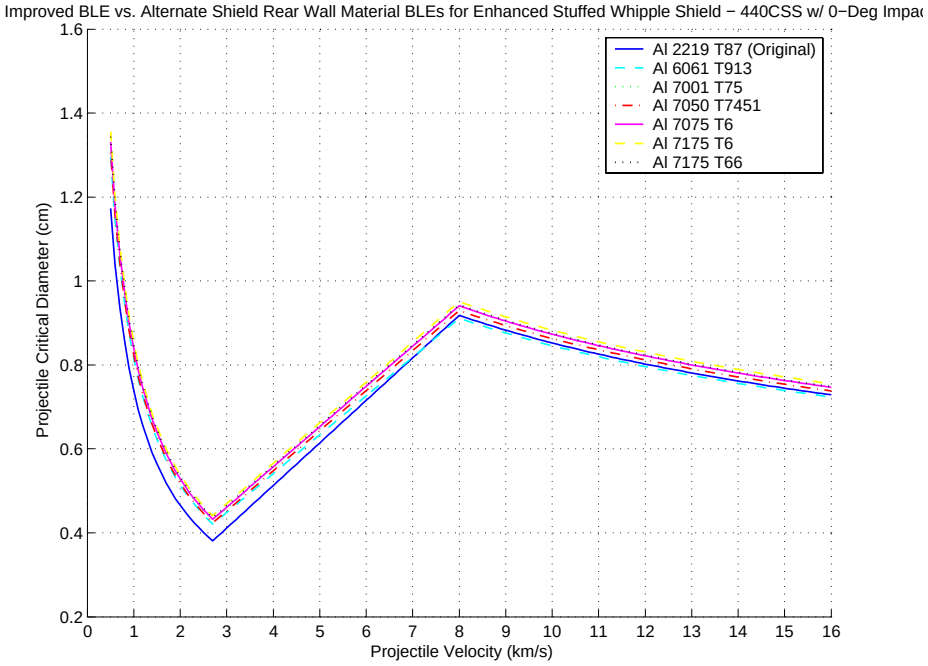

Figure L39. Plot of Improved Enhanced Stuffed Whipple BLE vs. Alternate Rear Wall Material Trials for 440C Stainless Steel Projectiles at 0-degree Impact Angles.

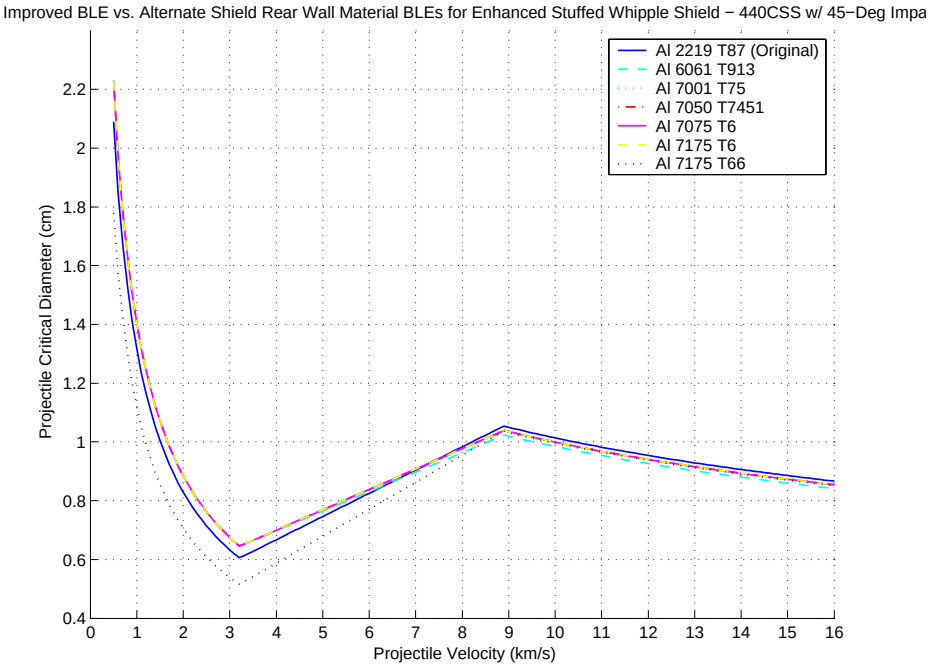

Figure L40. Plot of Improved Enhanced Stuffed Whipple BLE vs. Alternate Rear Wall Material Trials for 440C Stainless Steel Projectiles at 45-degree Impact Angles.

APPENDIX M – MATLAB CODES FOR ANALYZING ALTERNATE SHIELD CONFIGURATIONS WITH COMPARISONS TO THE BASELINE SHIELD CONFIGURATION

The MATLAB codes used to produce the plots in Chapter VI merely recreate the raw data and plots originally created in MSExcel and passed to JSC HITF in their electronic format. They are available from the author of this report upon request, but are excluded here in the interest of limiting the length of this Appendix. Requests for electronic copies of the MATLAB m-files should be made to:

LT Michael E. Kalinski, USN

558 Manhattan Place

San Jose, CA 95136

THIS PAGE LEFT INTENTIONALLY BLANK

LIST OF REFERENCES

1. *Caution: Falling Debris*. (2001). Retrieved March 17, 2004, from http://www.NASAexplores.com

2. Christiansen, E. L. (2002, April). *Density Effects Hypervelocity Impact (HVI) Test Plan, version 3.* Provided for the White Sands Test Facility, White Sands, New Mexico.

3. Christiansen, E. L. (2003, September). *Shuttle Meteoroid/Debris Risk Overview*. Provided for the Space Shuttle Safety and Mission Assurance Group, Houston, Texas.

4. Flury, W. (1994). *Space Debris*. Retrieved March 17, 2004, from European Space Agency, Mission Analysis Section website: http://www.esapub.esrin.esa.it/pff/pffv4n4/ppfflunr4.htm

5. Foust, Jeff. (1997, March). The Dangers of Orbital Debris *SpaceViews*. Retrieved from http://see/msfc.nasa.gov/sparkman/Section_Docs/article_1.htm

6. Lockheed-Martin Space Operations and NASA Hypervelocity Impact Technology Facility, NASA Johnson Space Center. (2003). International Space Station Meteoroid and Orbital Debris Integrated Threat Assessment #10, Revision C (ITA-10C), JSC 29951/ LMSEAT 34102. Houston, TX: Thomas G. Prior.

7. *NASA Hypervelocity Impact Technology Facility*. (n.d.). Retrieved March 17, 2004, from http://www.hitf.jsc.nasa.gov/hitfpub/main/

8. *NASA-White Sands Test Facility*. (2002). Retrieved March 17, 2004, from http://www.wstf.nasa.gov/Hazard/Hyper/Default.htm

9. National Aeronautics and Space Administration, Hypervelocity Impact Technology Facility, Johnson Space Center. (1999). International Space Station Ballistic Limit Study - Hypervelocity Impact Testing, JSC28837. Houston, TX: U.S. Government Printing Office.

10. National Aeronautics and Space Administration, Hypervelocity Impact Technology Facility, Johnson Space Center. (2003). Meteoroid/ Debris Shielding, TP-2003-210788. Houston, TX: U.S. Government Printing Office.

11. National Aeronautics and Space Administration, Johnson Space Center. (1999). Orbital Debris: A Chronology, NASA/TP-1999-208856. Houston, TX: U.S. Government Printing Office.

12. National Aeronautics and Space Administration, Johnson Space Center. *The Orbital Debris Quarterly News, Volume 3, Issue 4*. (1998, October). Houston, TX: U.S. Government Printing Office.

13. National Aeronautics and Space Administration, Marshall Space Flight Center. (2000). Double-Plate Penetration Equations, NASA/TM-2000-209907. Huntsville, AL: U.S. Government Printing Office.

14. National Aeronautics and Space Administration, Marshall Space Flight Center. (1997). Meteoroids and Orbital Debris: Effects on Spacecraft, NASA Reference Publication 408. Huntsville, AL: U.S. Government Printing Office.

15. *NASA Orbital Debris Program Office*. (2002). Retrieved March 17, 2004, from http://www.sn-callisto.jsc.nasa.gov/index.html

16. *Orbital Debris*. (1997). Retrieved March 17, 2004, from http://www-sn.jsc.nasa.gov/space.htm

17. Phipps, C. (1997, July). Orion: A Solution To The Orbital Debris Problem. *SpaceViews*. Retrieved from http://www.seds.org/spaceviews/9707/articles.html

18. Scientific and Technical Subcommittee of the United Nations Committee on the Peaceful Uses of Outer Space. (1999). Technical Report on Space Debris. New York, New York: United Nations Printing Office.

19. *Solutions for Hot Situations*. (2003). Retrieved March 17, 2004, from http://www.sti.nasa.gov/tto/spinoff2003/ip_3.html

20. *Space Debris Basics*. (2002). Retrieved March 17, 2004 from http://www.aero.org/cords/orbdebris.html

21. United Nations Committee on the Peaceful Uses of Outer Space. (2001). National Research On Space Debris, Safety Of Space Objects With Nuclear Power Sources Onboard And Problems Relating To Their Collision With Space Debris. New York, New York: United Nations Printing Office.

22. *What is Kevlar?* (n.d.). Retrieved March 17, 2004, from http://www.southbendclutch.com/kevlar.html

23. 3M Nextel Ceramic Fabric Offers Space Age Protection. (1997). Retrieved March 17, 2004, from http://www.mmm.com/ceramics

24. 3M Nextel Textiles Ceramic Fibers for Outerspace Applications. (2003). Retrieved March 17, 2004, from http://www.mmm.com

INITIAL DISTRIBUTION LIST

1. Defense Technical Information Center
   Ft. Belvoir, Virginia

2. Dudley Knox Library
   Naval Postgraduate School
   Monterey, California

3. Dr. Eric Christiansen
   NASA Johnson Space Center, Hypervelocity Impact Technology Facility
   Houston, Texas

4. Mr. Ronald P. Bernhard
   NASA Johnson Space Center, Hypervelocity Impact Technology Facility
   Houston, Texas

5. Mr. Thomas G. Prior
   NASA Johnson Space Center, Hypervelocity Impact Technology Facility
   Houston, Texas

6. LT Michael E. Kalinski, USN
   Naval Program Management Office, Strategic Systems Program
   Sunnyvale, California

7. CAPT Daniel Bursch, USN
   Graduate School of Engineering and Applied Science, Naval Postgraduate School
   Monterey, California

8. Dr. Terry McNelley
   Department of Mechanical and Astronautical Engineering, Naval Postgraduate School
   Monterey, CA